M.L. "Bob" Emiliani

PEER-REVIEWED PAPERS

Materials Science and Engineering

1. "Characterization and Oxidation Resistance of Hot-Pressed Chromium Diboride," *Mat. Sci. Eng.* A172(1993)111.
2. "Fiber Coating Concepts for Brittle-Matrix Composites," with J.B. Davis, J.P.A. Löfvander, A.G. Evans, E. Bischoff, *J. Amer. Ceram. Soc.* 76(1993)1249.
3. "Debond Coating Requirements for Brittle Matrix Composites," *J. Mat. Sci.* 28(1993)5280. **Featured Paper**.
4. "Assessment of Oxide Debond Coatings for Metal-Toughened Intermetallics," with H.E. Dève, *J. Amer. Ceram. Soc.* 75(1992)1935.
5. "Characterization of Sputtered Inconel 617, Part 2: Coatings in Cross-Section," with M. Richman, and R. Brown, *J. Mat. Sci.* 25(1990)144.
6. "Characterization of Sputtered Inconel 617, Part 1: Coatings in Plan Section," with M. Richman, and R. Brown, *J. Mat. Sci.* 25(1990)137.
7. "Diffusion of Sputtered Inconel 617 Coatings in Titanium," with M. Richman, and R. Brown, *Metall. Trans. A.* 21A(1990)1613.
8. "Ductile Reinforcement Toughening of γ-TiAl: Effects on Debond and Ductility," with H.E. Dève, A.G. Evans, G.R. Odette, R. Mehrabian, and R.J. Hecht, *Acta metall. mater.* 38(1990)1491.
9. "Sputter-Coating of Ti-6Al-4V with Inconel 617 for Erosion Resistance," with M. Richman, R. Brown, and O. Gregory, *Surf. Coatings Technol.* 33(1987)267.
10. "The Effect of Microstructure on Erosion of Ti-6Al-4V by Spherical Particles at 90º Impact Angles," with R. Brown, *Wear* 94(1984)323.

V_s peripheral wheel velocity
V_w workpiece velocity
V' chip velocity
V_s' shear velocity
U cutting velocity
x displacement in the direction of motion
X $xV/2\kappa$, dimensionless quantity in eqn. (1)
y displacement transverse to the direction of motion
$(y/b)_T$ normalized width of the temperature profile
Y $yV/2\kappa$, dimensionless quantity in eqn. (1)
z depth below the surface
Z $zV/2\kappa$, dimensionless quantity in eqn. (1)
α rake angle
$\bar{\alpha}$ mean rake angle for a normal distribution of α
α_c critical rake angle
β proportion of heat dissipated at the plane AB (Fig. 2) conducted into the workpiece
ζ dummy variable in eqn. (1)
η dummy variable in eqn. (1)
κ $k/\rho c$, thermal diffusivity
ρ density
Π_T $\Delta T \pi k V/\kappa q$, normalized temperature
σ_h standard deviation for a normal distribution of h
σ_α standard deviation for a normal distribution of α
ϕ shear angle

THE EFFECT OF MICROSTRUCTURE ON THE EROSION OF Ti-6Al-4V BY SPHERICAL PARTICLES AT 90° IMPACT ANGLES

M. EMILIANI and R. BROWN

Materials Laboratory, Department of Chemical Engineering, University of Rhode Island, Kingston, RI 02881 (U.S.A.)

Summary

Ti-6Al-4V alloy in two microstructural forms, equiaxed $\alpha + \beta$ and a basketweave $\alpha + \beta$ structure, was eroded. The erosion conditions utilized were an impact angle of 90°, spherical silica particles 210 μm in diameter and a velocity of 61 m s^{-1}. Examination of the eroded surfaces indicated that both microstructures were extensively covered by a layer of glass approximately 2 μm thick prior to the onset of steady state erosion. Thermal softening and plastic flow of erodent on impact formed the glass layer. In this way a large area of the target was protected from direct impact. Consequently little evidence of subsurface damage during erosion was found for either structure. Material loss during steady state erosion was possible only at discontinuities in the glass layer or when it was removed to reveal a fresh metallic surface. The primary mechanism of metal removal was found to be the same in incubation and steady state irrespective of the microstructure. Small platelets were formed from overlapping strain fields by several individual impacts. Other operating mechanisms were cutting due to fractured or preexisting irregular erodent and removal of lips from oblique impacts.

1. Introduction

The titanium alloy Ti-6Al-4V is commonly used in the low pressure stages of gas turbines. The in-service environment encountered in this location is well known for its deleterious effects on the aerodynamic profiles of blades and stators. The cause of this degradation is high velocity impact of ingested sand. Previous studies of the erosion behavior of Ti-6Al-4V under multiparticle impacts concentrated on quantification of erosion rates [1 - 3]. Little emphasis was placed on the mechanisms of material loss. Aluminium and its alloys [4 - 7], copper [8, 9], iron [10] and steels [11] are materials where mechanisms of material loss for multiparticle erosion were investigated. Ti-6Al-4V differs from these materials in at least one of the following aspects: strength, thermal conductivity, crystal structure and number of

phases. Therefore alternative erosion mechanisms may be expected, or different variations of previously observed mechanisms may operate.

Perhaps the most important parameter in controlling erosion is the low thermal conductivity of titanium alloys. This is emphasized by the fact that the first reports of melting during erosion were for Ti-6Al-4V eroded by Arizona road dust [2]. Furthermore, predictive models of erosion also utilized thermal properties with specific heat [12], thermal pressure [13], specific melting energy [14] and a parameter involving thermal conductivity [15] to predict the erosion resistance of alloys. The mechanisms of material loss for erosion at 90° impact angles are poorly understood but include extrusion of thin lips from craters by single impacts [16, 17], platelet formation from either overlapping strain fields [4] or forging of a thermally softened layer above a work-hardened layer [18], flaking from valley bottoms [8], adiabatic shear bands [7, 17] and surface melting [19]. The operation of these mechanisms may be modified by the low thermal conductivity of titanium alloys as reduced heat transfer into the bulk during erosion will result in a surface layer at elevated temperatures. The mechanical properties of Ti-6Al-4V are very temperature sensitive. For example, additional basal and pyramidal slip systems become active with increasing temperature [20]. The possibility of localized shear in the form of adiabatic shear bands, previously found for single impacts of titanium [21], is therefore unlikely during multiparticle erosion.

The objective of this work therefore was to investigate the erosion behavior of two microstructural forms of Ti-6Al-4V, at 90° impact angles, and to determine whether the mechanisms of material loss are different from these currently accepted for ductile metals.

2. Experimental details

2.1. Material

The target material chosen for this study was a Ti-6Al-4V alloy. Its chemical composition is given in Table 1. Two different microstructures were eroded: the first consisted of equiaxed α grains with second-phase β particles at grain boundaries (Fig. 1). The second was basketweave $\alpha + \beta$ platelet microstructure (Fig. 2). Equiaxed $\alpha + \beta$ erosion targets, 0.32 cm thick, were sectioned from rod 1.27 cm in diameter. While the surface to be eroded was equiaxed, metallographic sections perpendicular to the eroded surface showed that the β particles were aligned in the rolling direction of

TABLE 1

Chemical composition (weight per cent) of Ti-6Al-4V

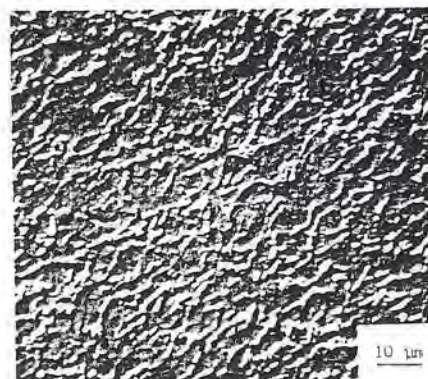| Al	V	Fe	C	O	N	H	Ti
6.07	3.93	0.09	0.02	—	—	45 ppm	Balance

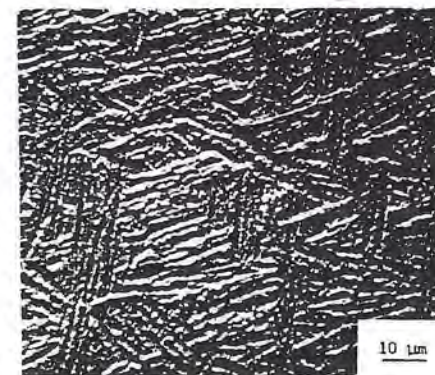Fig. 1. Equiaxed $\alpha + \beta$ structure of Ti-6Al-4V.

Fig. 2. Basketweave $\alpha + \beta$ structure of Ti-6Al-4V.

the rod. Basketweave targets 0.32 cm thick and 0.64 cm wide were sectioned from 0.64 cm sheet. All targets were metallographically prepared by the usual wet grinding and polishing techniques to a 0.3 μm Al_2O_3 finish. They were then washed in methanol and weighed to an accuracy of ±0.02 mg prior to erosion.

2.2. Erodent

The erodent utilized was mainly glass spheres with a nominal diameter of 210 μm produced by sieving between the size ranges of 180 and 240 μm. A small (less than 5%) volume fraction of irregular particles and microspheres was included with the large spheres. Figure 3 is a transmission light micrograph of the erodent showing a considerable amount of entrained air in large spheres. Some small spheres, about 10 μm in diameter, were attached to larger spheres.
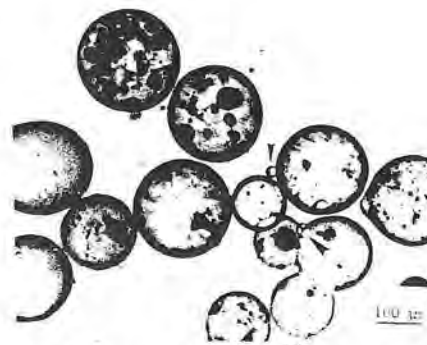

Fig. 3. Transmission electron micrograph of the silica erodent. The air entrapped in the spheres and the small spheres (arrowed) attached to the surfaces of larger spheres should be noted.

This particular erodent was chosen as earlier work on the erosion of aluminum alloy 1100 showed that the same major mechanisms of material removal operated when 210 μm silica spheres were utilized as when 210 μm angular quartz with different physical properties was utilized [22]. However, the rate of erosion was higher for quartz than for silica because of the enhanced cutting action of the angular particles. An additional feature of spherical erodent is the presence of moderately smooth eroded surfaces in comparison with the highly roughened surfaces from angular particles which increase the difficulty of interpretation of surface features and which may mask some operational mechanisms of erosion. Thus for this study of the mechanisms of erosion of Ti–6Al–4V spherical silica erodent was chosen.
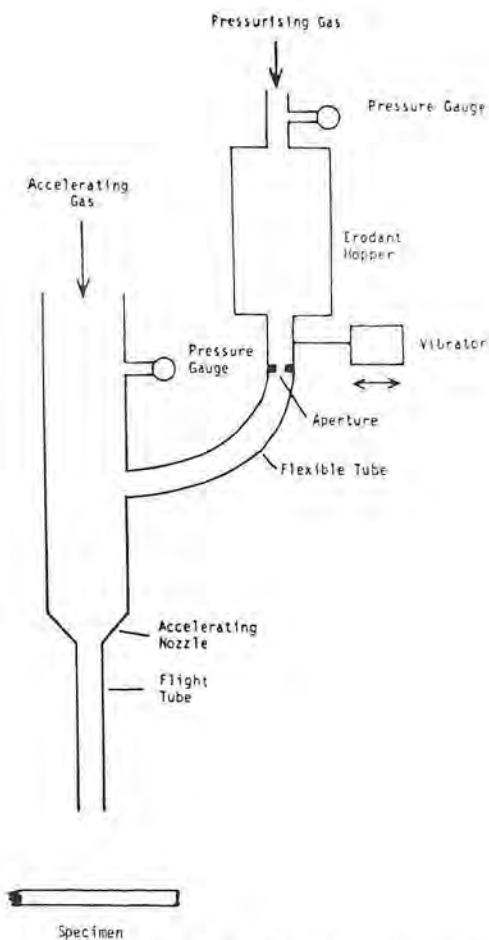
Pressurising Gas

Pressure Gauge

Accelerating Gas

Erodant Hopper

Pressure Gauge

Vibrator

Aperture

Flexible Tube

Accelerating Nozzle

Flight Tube

Specimen

Fig. 4. Schematic diagram of the erosion test equipment.

2.3. Test details

Erosion was performed at room temperature in a gas-blast rig. A schematic diagram of the apparatus is shown in Fig. 4. The particle velocity was calibrated by the double-disc technique [23]. To avoid humidity effects from compressed air and to provide a non-oxidizing atmosphere nitrogen was used as the accelerating gas to obtain a particle velocity of 61 m s^{-1} ($\pm$7.5%) at an impingement angle of 90°. 90° impact is the least understood erosion condition. The erodent concentration was maintained at 1.0 g cm^{-2} s^{-1}. Targets were weighed after specific periods of erosion to determine the mass change. The erosion rates were expressed in terms of mass change per unit area as a function of the concentration of erodent.

To characterize eroded surfaces specimens were examined in a scanning electron microscope equipped with an energy-dispersive X-ray analyzer. Erodent both before and after erosion was examined in a transmission light microscope.

3. Results

3.1. Equiaxed $\alpha + \beta$ microstructure

A single-impact crater on an equiaxed $\alpha + \beta$ target is shown in Fig. 5. No lips were found around craters for single impacts normal to the target. Instead there was only a slightly raised area around the crater periphery. This is consistent with earlier work on weaker and more ductile targets in surface conditions ranging from electropolished to ground, where a "threshold" number of impacts prior to material loss was reported [10, 4].

The erosion curve (Fig. 6) details the behavior of Ti–6Al–4V in the equiaxed $\alpha + \beta$ condition. For ductile targets such as aluminum, iron and copper, a continually increasing erosion rate from the start of erosion preceded a constant steady state of material loss [5, 8, 10]. For the equiaxed

10 μm

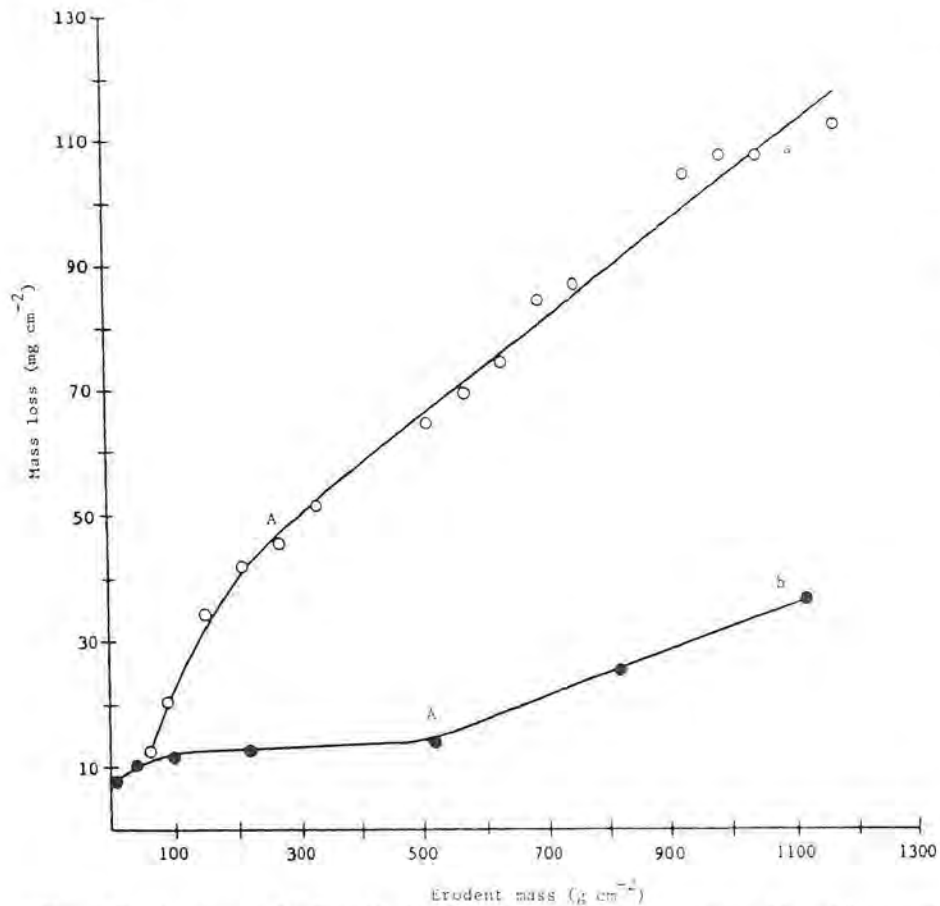Fig. 5. Single-impact crater on the equiaxed $\alpha + \beta$ structure. Only craters mirroring the erodent were found.

Fig. 6. Erosion curves for Ti–6Al–4V (210 μm silica spheres; velocity, 61 m s⁻¹; loading rate, 1 g cm⁻¹ s⁻¹; impingement angle, 90°): curve a, equiaxed α + β structure; curve b, basketweave α + β structure.

Fig. 7. Steady state eroded surface of the equiaxed α + β structure: A, large areas of the surface covered with a smooth glass layer.

Fig. 8. EDS spectrum from regions A of Fig. 7 (210 μm silica spheres). In addition to titanium and aluminum peaks, silicon and calcium peaks from the erodent were present.

α + β structure of Ti–6Al–4V, the incubation period was a region of gradually decreasing erosion rate until the lowest rate was found in the steady state.

Examination of eroded surfaces beyond incubation showed a smooth surface which did not exhibit much single-impact detail or a high density of thin lips around impact craters. The hill-and-valley topography previously reported in steady state for softer targets [5, 8] was not present. Figure 7 shows the surface of a target eroded by 1120 g cm⁻² of erodent. Large areas of the surface consisted of smooth regions marked A in Fig. 7. These were identified by X-ray analysis and found to contain silicon. Figure 8 is an energy-dispersive spectroscopy (EDS) X-ray trace of one of the areas marked A. An identical trace was found from EDS analysis of the erodent. It was concluded that the smooth r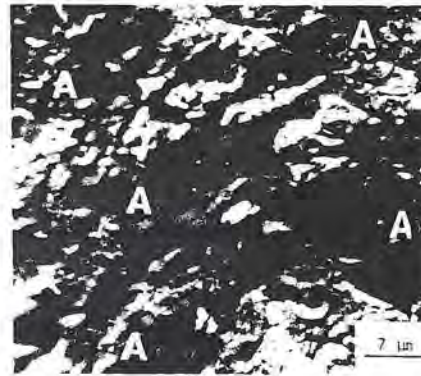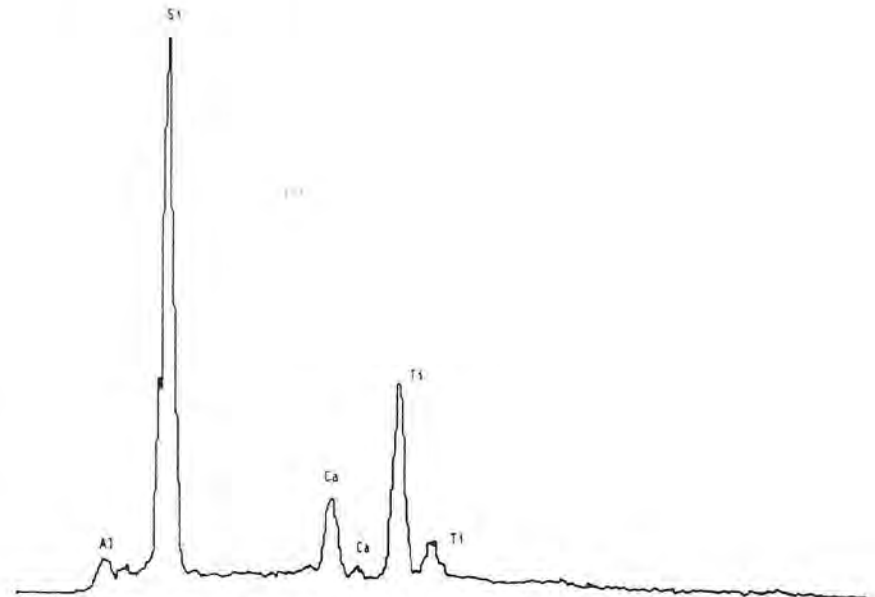egions were from erodent which remained on the target surface. However, the smooth morphology was not typical of fragmented angular embedded erodent.

Two different forms of evidence for melting were found in equiaxed α + β targets. Figure 9 shows an individual spherical droplet (arrowed) lying on the target surface, while Fig. 10 shows numerous small spheres lying on
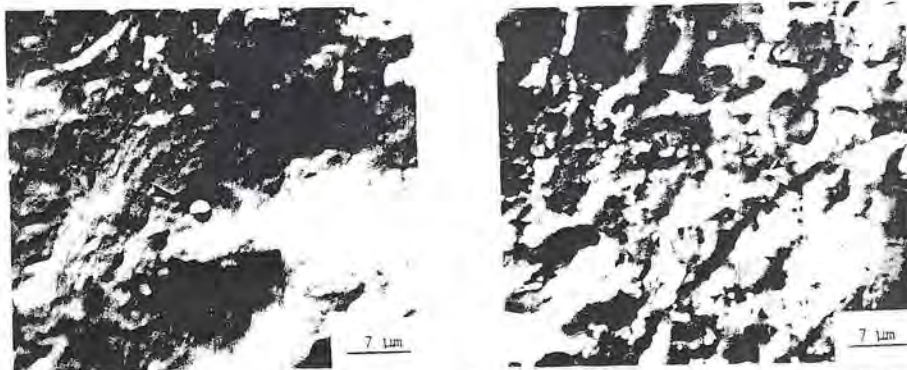
Fig. 9. The arrowed droplet, approximately 2 μm in diameter, has been shown by EDS to be titanium.

Fig. 10. The arrows indicate particles of titanium, about 0.5 μm in diameter, embedded in the glass layer.

smooth glass regions. Analysis of these droplets by EDS identified them as titanium alloy.

Examination of metallographic sections of steady state targets showed a layer of glass on the target surface 1 - 2 μm thick (Fig. 11). The layer exhibited no evidence of brittle fracture but was discontinuous over the target surface. This permitted metal to be exposed to erodent (Fig. 11, B). Below the glass, plastic deformation of the metallic substrate was indicated by the movement of β particles from their aligned rolling direction position,
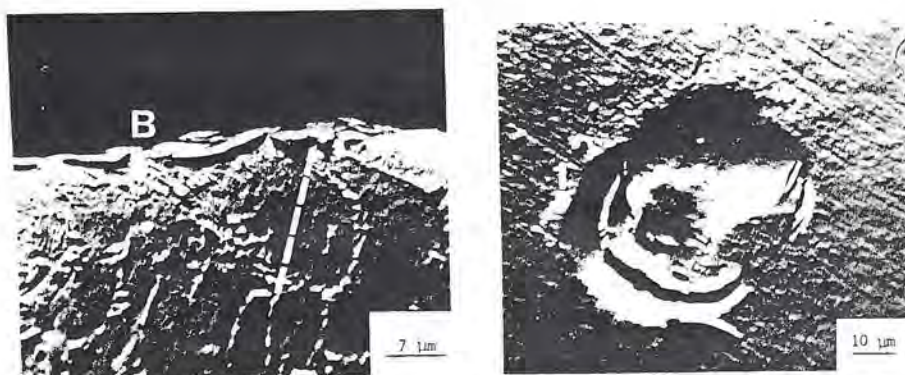

Fig. 11. Metallographic section of the steady state eroded equiaxed α + β structure showing a discontinuous layer of glass on the surface. A region of plastic deformation to a depth of 6 μm below the surface was evident from the movement of the β phase.

Fig. 12. Overlapping impact craters in the basketweave structure produced a small platelet within the initial impact crater during incubation.

as shown by the broken line in Fig. 11. The deformed layer was restricted to 5 - 6 μm below the surface for the erosion conditions used.

3.2. Basketweave α + β microstructure

Single-impact tests of Ti–6Al–4V with a basketweave microstructure showed no discernible difference from the equiaxed α + β structure. Although no lips were found for single impacts at the 90° impact angle, overlapping impacts formed platelets (Fig. 12). Two impacts, numbered 1 and 2 on Fig. 12, formed this platelet which is 30 μm long and 10 μm wide. The platelet, still attached to the target surface, was positioned where the two craters overlap. Similar features were found during incubation for the equiaxed α + β structure.

In the steady state the same high density of glass was found on the eroded surface of basketweave targets. A smooth surface with little single-impact detail was again observed. Platelets were evident on the eroded surface during the steady state. A small detached platelet which remained upon the surface is arrowed in Fig. 13. The size of this platelet was 30 μm long and 12 μm wide and is similar to that found for overlapping single impacts.

Evidence for melting was again found and was the same as that shown in Fig. 10 for the equiaxed structure.

Metallographic sections of the basketweave structure indicated that the glass layer was approximately 2 - 3 μm thick (Fig. 14). No evidence of brittle failure was found. From this micrograph it is clear that the glass layer covered the target surface more coherently and continuously and to a thicker depth than for the equiaxed α + β structure shown in Fig. 11. Below the
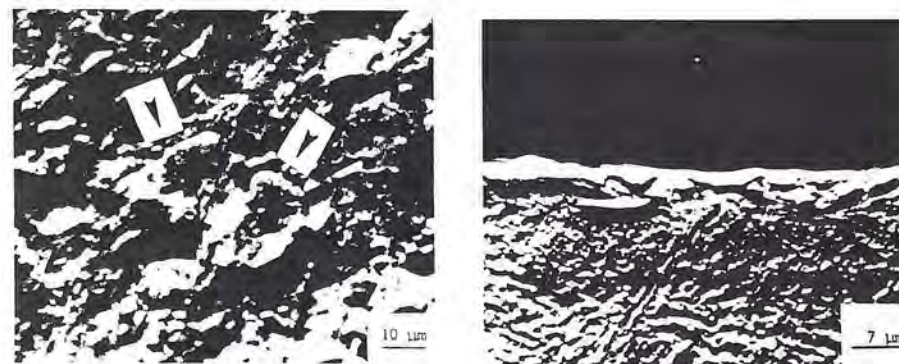

Fig. 13. Steady state eroded surface appearance of the basketweave structure target. A small platelet was found on the surface, and it was of similar size to that found in incubation.

Fig. 14. Metallographic section of the basketweave structure in the steady state. A continuous glass layer appeared on the surface, whereas no subsurface deformation was apparent.

glass layer, no evidence of plastic deformation in the form of β plate bending or colony movement was found.

The erosion curve for the basketweave structure is included in Fig. 6. An incubation period of decreasing rate of material loss was found. However, the initial material loss rate for the basketweave structure in this region was greater than for equiaxed $\alpha + \beta$ targets but for a much shorter period of erosion. After incubation there was a region of near-zero material loss preceding a constant steady state erosion period. As for equiaxed $\alpha + \beta$ targets, and contrary to that found for softer targets, the erosion rate in the steady state was lower than in incubation. The steady state erosion rate for equiaxed $\alpha + \beta$ and basketweave targets is given by the slope of the curves beyond A in Fig. 6. Equiaxed $\alpha + \beta$ targets had an erosion rate of 0.074 mg of material removed per g of erodent impacted, while the erosion rate of basketweave targets (0.038 mg g^{-1}) was nearly half that of equiaxed targets.

3.3. Erodent morphology after impact

Analysis of erodent by transmission light microscopy indicated that the volume fraction of erodent fragments was small, approximately 15%. The morphology of the erodent after impact was characterized into three categories: erodent that remained completely intact; erodent that was chipped (i.e. greater than 70% of the original particle remained); erodent that at least split in half or shattered into smaller pieces. In the last two cases the erodent exhibited cleavage fracture and was highly angular in shape. The maximum dimension of erodent fragments typically ranges from 25 to 210 μm for erodent which has split in two. Figure 15 shows fragmented erodent (arrowed) interspersed with intact erodent.

Another feature exhibited by the erodent during the erosion of Ti–6Al–4V was found by examination of single-impact sites. Single particles of erodent which had undergone a significant shape change on impact were often retained upon the surface. Figure 16 shows a particle of erodent about
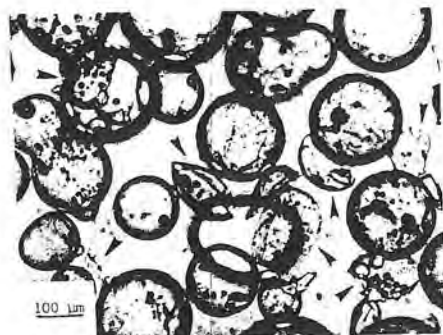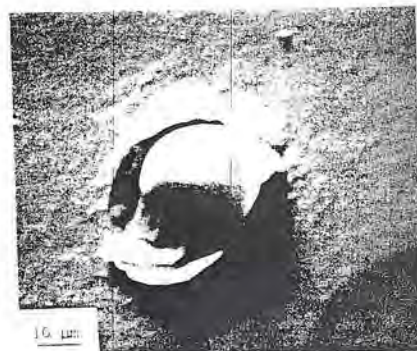

Fig. 15. Silica erodent after impact.

Fig. 16. Shape change of erodent due to high impact temperatures.

Fig. 17. The lip of glass formed by impact at less than 90° indicates that the glass is able to undergo significant plastic flow and hence to absorb impact energy.

25 μm in diameter embedded in the surface of an equiaxed $\alpha + \beta$ target. Further evidence of plastic deformation of erodent is shown in Fig. 17. The smooth glass layer was impacted by a silica sphere, and a lip formed typical of ductile metal impact. X-ray EDS analysis confirmed that the lip and most of the crater was glass.

4. Discussion

4.1. Material loss during incubation

Individual 90° impacts upon mechanically polished surfaces of Ti–6Al–4V were similar in features to those of iron and copper targets impacted under similar conditions [9, 10]. Lip formation by the extrusion around crater rims usually found for the high velocity impact of large spheres into ductile targets was absent [16]. Both mass loss data and surface examination by scanning electron microscopy indicated that the threshold required prior to material loss for b.c.c. [10] and f.c.c. [4] metals was clearly also present for the erosion of h.c.p. metals. Significant material loss in soft targets was not realized until sufficient surface "conditioning" occurred as a result of several impact events on a small area [4, 10]. Once this criterion was met, material was lost in the form of platelets. It should be noted that in this paper, material lost within craters by overlapping impacts will be referred to as platelets. This is in contrast with lips which are formed by single impacts and lie primarily outside the craters attached only to the periphery by a thin neck [14, 16] and "flakes" formed in the valleys of hill-and-valley topographies [8].

The primary mechanism of material loss for Ti–6Al–4V during incubation was platelet formation due to overlapping impacts. The two suggested mechanisms of formation of platelets are forging by continual impacts of existing lips formed by single impacts [18] and fracture of platelets by over-

lapping strain fields [4]. In the first mechanism, lip formation by single impacts is required and platelets would therefore be outside the initial crater but inside the second crater. The site of the platelet in Fig. 12, midway across the initial crater, suggests that the latter mechanism is the one applicable. With the strain-to-failure mechanism of platelet formation [4], the least ductile structure will erode at the larger rate in incubation. Figure 6 shows that the less ductile basketweave structure erodes at a higher rate than the equiaxed $\alpha + \beta$ structure. This is further evidence in support of the suggestion that the strain to failure controls erosion in incubation. A secondary mechanism of material loss during incubation was cutting due to pre-existing irregular and fragmented erodent. In this case, protruding lips are normally formed and later removed by subsequent impacts [17].

Evidence for the melting of Ti-6Al-4V during incubation was found, and it was similar to that found during steady state erosion. Areas of glass embedded in the surface during incubation were covered by small spheres of titanium. The mechanisms of melting will be discussed in Section 4.3.

4.2. Formation of the glassy layer and steady state material loss

Figures 7 and 11 reveal a different type of erodent behavior during erosion from that previously reported. The embedding of erodent was usually initiated by irregular erodent from either fragmented spheres or pre-existing irregular erodent. Plastic flow processes operating during hill and valley formation and stabilization provide a loop which pushes erodent fragments below valleys. A pocket is formed containing a high density of fragmented erodent which is continually driven further into the bulk of the target. This mechanism results in erodent being embedded primarily in valley floors [8]. Alternatively, individual fragments of erodent embed on the surface [24, 25] when no hills and valleys form. They may then be pushed further into the target by subsequent impacts. In either situation the erodent fragments maintain their sharp angular shape.

For Ti-6Al-4V a smooth layer of glass was found to cover large surface areas. The angularity typical of fragmented erodent was not found on the eroded surface or in the near-surface layers. Additionally, subsequent impacts often fractured embedded erodent below the surface [26]. This process was not apparent in the glass layer. It is suggested that the embedding phenomenon reported here is different from that reported in earlier work in that on impact the erodent reaches temperatures high enough to enable it to flow. Temperatures around 700 °C sufficient to soften the amorphous silica erodent were recently shown to be reached by smaller 70 μm spheres impacting aluminum alloy 6061 at higher velocities (122 m s^{-1}) [27]. Deposition of a smooth and continuous glassy layer is aided by the high strength, medium ductility and very low thermal conductivity of Ti-6Al-4V which contained thermal energy from impact to the very-near-surface layers. This explains why this phenomenon has not been observed in other target materials, all of which were softer, more or less ductile and/or had significantly higher thermal conductivities.

The importance of the glass layer will now be discussed in terms of its role in controlling the erosion rate of Ti-6Al-4V both in incubation and in the steady state. The embedding of erodent initiates as soon as erosion begins, and at the same time the surface temperature increases locally with each impact. It should be noted that each impact will input thermal energy, but not every impact will embed material. Material loss at this stage (incubation) is by platelet formation from overlapping impacts, as discussed above. Subsequent impacts by large spheres upon smaller embedded erodent cause fragments to soften and flow until large areas of the target surface become covered with a layer of glass. The target is partially protected from additional damage as impact energy is absorbed by the glass layer. Clear evidence of this process was given in Fig. 17, where a silica sphere impacted the glass layer at 90° and formed a lip along the crater periphery. No metal was removed, but the glass lip was vulnerable to removal or resoftening by subsequent impacts. In this way the glass layer provided good protection for the Ti-6Al-4V substrate.

The erosion rate during incubation decreased as the glass layer formed and platelet formation was increasingly suppressed. Clearly the mass lost in the incubation region will consist primarily of titanium, but it will include glass as it becomes more prevalent across the target surface. However, the nearly zero erosion rate after incubation for the basketweave Ti-6Al-4V indicates that sufficient glass was present to suppress metal removal almost totally and that the glass removal rate was itself low. This indicates that the glassy layer has the ability to undergo significant plastic deformation on impact.

The departure from incubation to steady state erosion was characterized differently for the two microstructures and as shown in Fig. 6. The equiaxed $\alpha + \beta$ structure exhibited one change in slope, while the basketweave structure showed two changes in slope. The difference is believed to be due to the characteristics of the glass layer for each microstructure, namely the layer thickness and the surface area covered by it.

After erosion into the steady state, equiaxed $\alpha + \beta$ targets retained a discontinuous layer of glass, thereby exposing metal to erodent. The basketweave structure exhibited a much more coherent and continuous glass layer. The movement of the β phase in the equiaxed material indicated subsurface deformation during erosion. Plastic flow in the near-surface layer immediately below the surface glass layer in the equiaxed $\alpha + \beta$ targets will hinder formation of a continuous glass layer, resulting in the spalling of glass as it cannot accommodate the plastic flow of the metal, which is calculated to be over 200% strain. The exposed metal was removed by subsequent impacts.

No subsurface deformation was apparent for the basketweave target in the steady state, and the glass layer was more uniform. With no spalling of glass from substrate plastic deformation, the less ductile basketweave targets formed a thicker and more continuous glass layer which provided considerably more protection of the target surface. The erosion rate decreased to nearly zero with more complete covering of the target, and it was much less than

for the equiaxed structure which did not exhibit such a uniform glass layer. After the near-zero erosion rate, the rate increased slightly and remained constant. It is suggested a critical glass layer thickness was reached after which subsequent impacts fractured glass from the surface. Such a process reduced the amount of protection, and an increased erosion rate in the steady state occurred. Once the metal was exposed the mechanism of material loss during steady state erosion was the same as that during incubation for both microstructures, namely platelet formation due to overlapping impacts. No adiabatic shear bands were found in Ti–6Al–4V during erosion. A critical strain is required for the presence of this deformation mode [28]. The glass layer present on the surface reduced the strain transmitted to the target to a level below which adiabatic shear was not possible. Reduced strain levels also blocked the plastic flow necessary for the formation of hills and valleys.

Figure 6 suggested that the increased ductility associated with the equiaxed $\alpha + \beta$ structure increased the steady state erosion rate under the present test conditions. This contrasts with earlier work [29] where it was found that increased ductility reduced erosion rates. However, the target materials used were Cu–4%Al and steel. A different erodent was also used. Clearly different mechanisms are at work when titanium is eroded with spherical glass beads. It is probable that the conclusions arrived at previously are indeed correct for soft targets with high thermal conductivities.

4.3. Melting of Ti–6Al–4V

Some evidence for melting was found in the form of single droplets 2 μm in diameter upon the eroded surface, and shown in Fig. 9, or alternatively a series of droplets about 0.5 μm in diameter lying upon and embedded within the glass on the target surface (Fig. 10). Both types of melting morphology have been previously observed but on much lower melting point materials. Direct melting of the surface with the ejection of drops from the molten pool produced similar individual drops in two low melting point materials [30].

In the second melting process small flakes of metal were dragged across low conductivity particles by erodent impact. The large input of thermal energy was absorbed by the metal flakes, thereby melting them [31]. Both processes are unlikely to produce significant amounts of material loss. Their importance lies in the indication that surface temperatures sufficient to melt Ti–6Al–4V were achieved during erosion. This confirms the earlier conclusion that Ti–6Al–4V melted when eroded by Arizona road dust [2]. In this respect, when considering erosion the mechanical properties of the surface will clearly not be those measured at ambient temperature but will be more representative of high near-melting-point temperatures.

5. Conclusion

A study of the behavior of Ti–6Al–4V eroded by silica spheres 210 μm in diameter at a 90° impact angle and a velocity of 61 m s⁻¹ has led to the following conclusions.

(1) During incubation, a smooth protective glass layer was formed on the target surface by thermal softening of the erodent on impact. This glass layer is believed to be unique to targets with high strength, low thermal conductivity and medium ductility.

(2) The erosion rate was highest in incubation and lowest in the steady state for both microstructures. The protective glass layer controlled the erosion rate by decreasing the incidence of direct impacts upon the metallic surface.

(3) The ductility of the microstructure controlled the relative erosion rates of the equiaxed and basketweave structures. The more ductile equiaxed structure permitted more spalling of the glass layer, thereby increasing the erosion in the steady state. The less ductile basketweave structure maintained a more consistent and uniform glass layer which reduced the erosion rate.

(4) Platelet formation from overlapping impact craters was the primary mechanism of material loss irrespective of the stage of erosion or microstructure. The mass loss due to melting of the target was considered to be negligible in both the incubation and the steady state.

References

1 J. E. Goodwin, W. Sage and G. P. Tilly, Proc., Inst. Mech. Eng., London, 184 (1969) 279 - 292.
2 C. E. Smeltzer, M. E. Gulden and W. A. Compton, J. Basic Eng., 92 (1970) 639 - 652.
3 N. Gat and W. Tabakoff, Wear, 50 (1978) 85 - 94.
4 D. G. Rickerby and N. H. Macmillan, Wear, 60 (1980) 369.
5 P. A. Doyle and A. Levy, Rep. LBL-7327, 1978 (Lawrence Berkeley Laboratory).
6 T. Christman and P. G. Shewmon, Wear, 52 (1979) 57 - 70.
7 T. Christman and P. G. Shewmon, Wear, 54 (1979) 145 - 155.
8 R. Brown and J. W. Edington, Wear, 69 (1981) 369 - 382.
9 R. Brown and J. W. Edington, Wear, 72 (1981) 377 - 381.
10 R. Brown, E. J. Jun and J. W. Edington, Wear, 70 (1981) 347 - 363.
11 A. V. Levy, Wear, 68 (1981) 269 - 287.
12 I. M. Hutchings, Wear, 35 (1975) 371 - 374.
13 P. Ascarelli, AMMRC Tech. Rep. 71-47, 1971 (Army Materials and Research Center, Watertown, MA).
14 S. Malkin, Wear, 68 (1981) 391 - 396.
15 T. Quadir and P. G. Shewmon, Metall. Trans. A, 12 (1981) 1163 - 1175.
16 D. G. Rickerby and N. H. Macmillan, Proc. 5th Int. Conf. on Erosion by Solid and Liquid Impact, Cambridge, Cambs., 1979, Cavendish Laboratory, Cambridge, Cambs., 1979, Paper 29.
17 I. M. Hutchings, R. E. Winter and J. E. Field, Proc. R. Soc. London, Ser. A, 348 (1976) 379 - 392.
18 A. Levy, The platelet mechanism of erosion of ductile metals, submitted to Wear.

19 M. E. Gulden, *Proc. 5th Int. Conf. on Erosion by Solid and Liquid Impact, Cambridge, Cambs., 1979*, Paper 31.
20 D. F. Neal and P. A. Blenkinsop, *Acta Metall.*, 24 (1976) 59 - 63.
21 R. E. Winter and I. M. Hutchings, *Wear*, 34 (1975) 141 - 148.
22 R. Brown, S. Kosco and E. J. Jun, *Wear*, 88 (1983) 181 - 193.
23 A. W. Ruff and L. K. Ives, *Wear*, 35 (1975) 195 - 199.
24 J. W. Edington and I. G. Wright, *Wear*, 48 (1978) 131 - 144.
25 R. O. Scattergood, T. H. Kosel and A. P. L. Turner, *Corrosion–Erosion Behavior of Materials, Proc. Fall Meeting of the AIME, 1978*, pp. 146 - 161.
26 L. K. Ives and A. W. Ruff, in W. F. Adler (ed.), *Erosion: Prevention and Useful Applications, ASTM Spec. Tech. Publ. 664*, 1979, pp. 5 - 35 (ASTM, Philadelphia, PA).
27 R. Brown and J. D. Ayers, in K. C. Ludema (ed.), *Proc. Int. Conf. on Wear of Materials, 1983*, American Society of Mechanical Engineers, New York, 1983, pp. 325 - 332.
28 S. P. Timothy and I. M. Hutchings, *Proc. 7th Int. Conf. on High Energy Rate Fabrication, Leeds, 1981*.
29 A. Levy, *Proc. 5th Int. Conf. on Erosion by Solid and Liquid Impact, Cambridge, Cambs., 1979*, Paper 39-1.
30 R. Brown and J. W. Edington, *Wear*, 71 (1981) 113 - 118.
31 R. Brown and J. W. Edington, *Wear*, 73 (1981) 193 - 200.

International Calendar

Date	Title and place	Further details from
May 1 - 3, 1984	Conference on Materials for Future Energy Systems Washington, DC, U.S.A.	J. E. Cunningham, Oak Ridge National Laboratory, P.O. Box X, Oak Ridge, TN 37831, U.S.A. (telephone number, 615 574 4067)
May 7 - 10, 1984	ASLE Annual Meeting Chicago, IL, U.S.A.	American Society of Lubrication Engineers, 838 Busse Highway, Park Ridge, IL 60068, U.S.A.
May 9 - 11, 1984	Tribology Offshore London, Gt. Britain	The Institution of Mechanical Engineers, 1 Birdcage Walk, Westminster, London SW1H 9JJ, Gt. Britain (telephone number, 01 222 7899)
June 4 - 7, 1984	8th IPMI International Precious Metals Conference and Exhibit Toronto, Canada	International Precious Metals Institute, Government Building, ABE Airport, Allentown, PA 18103, U.S.A.
June 13 - 15, 1984	2nd International Conference on Advances in Surface Coating Technology Brighton, Gt. Britain	John Sanders, The Welding Institute, Abington Hall, Abington, Cambridge CB1 6AL, Gt. Britain
June 25 - 29, 1984	Surface Treatment and Finishing Show Birmingham, Gt. Britain	Andry Montgomery Group, 49 Calthorpe Road, Edgbaston, Birmingham B15 1TH, Gt. Britain
August 5 - 9, 1984	3rd International Conference on Solid Lubrication Denver, CO, U.S.A.	American Society of Lubrication Engineers, 838 Busse Highway, Park Ridge, IL 60068, U.S.A.
September 4 - 7, 1984	11th Leeds–Lyons Symposium on Tribology (Mixed Lubrication and Lubricated Wear) Leeds, Gt. Britain	Dr. C. M. Taylor or Professor D. Dowson, Institute of Tribology, Department of Mechanical Engineering, University of Leeds, Leeds LS2 9JT, Gt. Britain (telephone number, 0532 431751, extension 6185 or 254)
September 5 - 14, 1984	High Productivity Machining — Materials and Processing Chicago, IL, U.S.A.	Lana M. Loar, Manager, Conferences and Expositions, American Society for Metals, Metals Park, OH 44073, U.S.A. (telephone number, 216 338 5151, extension 465 or 473)

SPUTTER-COATING OF Ti–6Al–4V WITH INCONEL 617 FOR EROSION RESISTANCE*

M. EMILIANI and M. H. RICHMAN

Division of Engineering, Brown University, Providence, RI 02912 (U.S.A.)

R. BROWN and O. GREGORY

Department of Chemical Engineering, University of Rhode Island, Kingston, RI 02881 (U.S.A.)

Summary

Inconel 617 and reactively sputtered Inconel 617 nitride coatings 26 - 28 μm thick were magnetron sputtered onto glass and titanium substrates at 1900 Å min^{-1} and 1400 Å min^{-1} respectively, and then characterized. Sputtered Inconel 617 coatings are smooth, adherent and ductile, with a b.c.c. structure. Equiaxed grains ranging in size from 300 to 1000 Å in diameter were found. Nitrided Inconel 617 is brittle, adherent, and has a two-phase structure consisting of fine crystallites, tentatively identified as f.c.c. Ni$_4$N, embedded in a semicrystalline matrix, and was found to be 38% harder than the non-nitrided coating. Sputtered Inconel 617 could not be compared with the Thornton zone model, but the nitrided coating corresponded well to a Zone T structure. Coatings deposited on Ti–6Al–4V were eroded at 90° with 15 μm SiC at a velocity of 67 m s^{-1} in order to examine the mechanisms of erosion. Both coatings exhibited ductile mechanical behavior at single impact sites. The cutting mechanism was prevalent. Embedded and fragmented erodent was also found.

1. Introduction

Solid particle erosion of gas turbine airfoils in vehicles operating near the ground and in dusty environments is a persistent problem. Engine weight has been reduced by the use of new materials, some of which have poor erosion or hot oxidation and/or erosion resistance. Various types of hard coatings have been deposited on titanium-based and nickel-based gas turbine airfoils for erosion resistance [1 - 4]. Some deposition techniques require

heating the substrate to temperatures in excess of 1000 °C, thus affecting the mechanical properties of the airfoils. Other factors which have limited the success of hard coatings in this application have been their poor erosion resistance at normal and near-normal impact angles, and spalling of the coating owing to thermal shock [1, 3, 5]. Studies of the fundamental aspects of erosion using angular particles have shown that ductile materials resist erosion at near 90° impact angles, whereas hard materials resist erosion at lower impact angles [6, 7]. Computer models have shown that gas turbine airfoils are subjected to erosive wear by particles impacting at all angles [8, 9]. Thus one type of coating cannot be expected to perform well under all conditions.

This study is concerned with the structure of sputtered Inconel 617 and reactively sputtered Inconel 617 nitride and the mechanisms of single-impact erosion. It is part of a larger program for investigating the feasibility of using composite soft-over-hard sputtered coatings on Ti–6Al–4V to resist erosive wear at all impact angles in the compressor section of gas turbine engines. A principal objective is to maintain the aerodynamic profile of the blades during erosive wear so as to minimize the power loss. Multiple-impact erosion studies will be presented in a separate publication. Magnetron sputtering was chosen as the coating method primarily because of low deposition temperatures, uniform coverage, good adhesion and ease of application.

2. Experimental details

2.1. Target material

Solution-annealed Inconel 617 was selected as the coating material because of its desirable bulk mechanical properties, high temperature stability and resistance to oxidation at elevated temperatures. It is an f.c.c. solid solution of nickel (52%), chromium (22%), cobalt (12.5%), molybdenum (9%) and iron (1.5%), and has a density of 8.36 g cm^{-3} and a lattice parameter of 3.25 Å. The microstructure consists of large equiaxed grains, and contains titanium carbides. Inconel 617 is not γ' or carbide strengthened in the solution-annealed condition, but will undergo slight strengthening after extended exposure to elevated temperatures owing to the small amount of aluminum (1.2%) and carbon (0.07%) present. Figure 1(a) is a transmission electron micrograph (TEM) of a typical Inconel 617 grain, and shows dislocations and bend contours. Figure 1(b) is an energy dispersive analysis by X-rays (EDAX) spectrum of the area shown in Fig. 1(a). Figures 1(c) and 1(d) are X-ray and electron diffraction patterns of bulk Inconel 617. Further characterizations of this alloy can be found elsewhere [10, 11].

2.2. Sputtering

Inconel 617 plate 0.64 cm thick was cut into a sputtering target 14 cm in diameter, and bonded to a copper magnetron backing plate with silver epoxy. Sputtering was performed in a Materials Research Corporation Model 8667

r.f. (13.56 MHz) sputtering unit. Commercial grades of pure α-Ti and Ti–6Al–4V with a Widmanstätten structure were used as substrates. The former were polished to 600 soft (30 μm SiC) and used for bend test specimens to evaluate adhesion, while the latter were polished to 0.05 μm alumina and used for erosion studies. Glass microscope slides 2 mm thick were also used as substrates.

The substrates were ultrasonically cleaned in trichloroethylene, acetone and ethanol and placed in the sputtering chamber. A vacuum better than 3×10^{-6} Torr was achieved. Argon (purity better than 99.999%) was then bled through the chamber for 30 min, and a similar vacuum level was re-established prior to sputtering. Samples were sputter-cleaned for 10 min in argon at a pressure of 15 mTorr and a forward r.f. power of 1000 W. The target was then sputter-cleaned on a shutter at 1000 W forward r.f. for 3 min using argon at a pressure of 2 mTorr. Samples were coated at normal incidence with Inconel 617 at a power level of 1000 W (6.5 W cm^{-2}) and at an argon pressure of 2 mTorr. Nitrided Inconel 617 coatings were prepared by reactive sputtering at 1000 W forward r.f. with a mixture of approximately 78% argon and 22% nitrogen (purity, 99.998%). The total gas pressure remained 2 mTorr. No bias or external heating was applied to the substrates during sputtering, and the substrates and target were water cooled. The target-to-substrate distance was 5.8 cm. A thermocouple was placed adjacent to the substrates during sputtering, and temperatures in excess of 400 °C were recorded. Inconel 617 and nitrided Inconel 617 were deposited at an average rate of 1900 Å min^{-1} and 1400 Å min^{-1} respectively. Coating thickness was measured using a Sloan Dektak profilometer. Inconel 617 and reactively sputtered Inconel 617 coatings were 28.7 and 26 μm thick respectively.

2.3. Transmission electron and scanning electron microscopy studies

Sputtered Inconel 617 was peeled from 0.45 mm commercially pure (c.p.) titanium sheet and punched into 3 mm discs; then jet polished at −10 °C in a Struers Tenupol using a standard solution for nickel alloys [12]. Additional samples were glued to thin c.p. titanium rings with Sicomet 50 adhesive and ion milled in a Gatan Dual Ion Mill. No external cooling was used during ion milling. A gun voltage of 5 kV and a specimen current of 18 μA resulted in specimens with the same structure as that obtained by jet polishing. Nitrided Inconel 617 samples were brittle and could only be prepared by ion milling. Samples which spalled off glass substrates were mounted on titanium rings and ion milled using the same conditions as previously described. TEM and energy-dispersive spectroscopy (EDS) characterizations were made using a Philips 420T SETM microscope at 120 kV. SEM studies were performed using an AMR 1000A.

2.4. Erosion

Single-impact tests were performed at room temperature on both Inconel 617 and nitrided Inconel 617 coatings deposited on polished Ti–6Al–4V using a nitrogen gas-blast erosion rig which has been previously described

12-FEB-87 22:37:47
RATE: CPS TIME   60LSEC
00-20KEV: 10EV/CH PRST: OFF
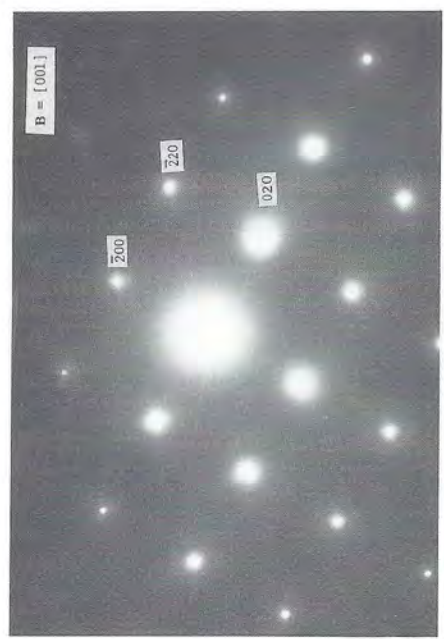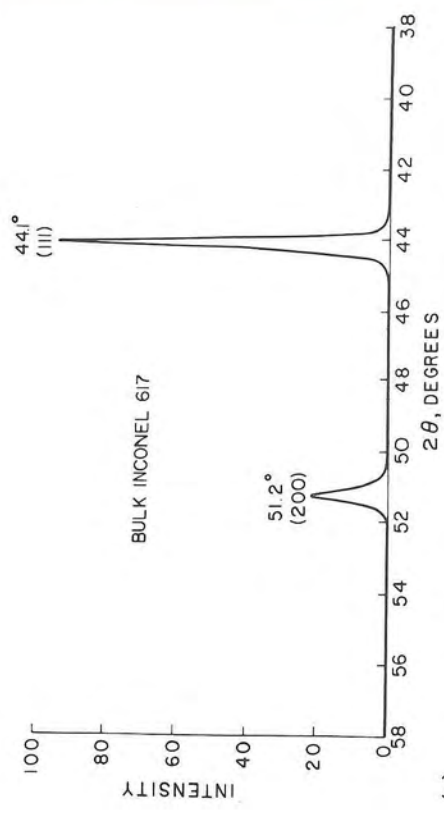A: INCO 617   B:
FS= 4672   MEM: A   FS=   200

Ni

Cr

Co   Cu

Mo

Ni

Al   Ti   Fe

Mo

EDAX

CURSOR (KEV) =10.240
(b)

1300 Å

(a)

Fig. 1 (continued).

(c)

(d)

BULK INCONEL 617

44,1°
(111)

51.2°
(200)

INTENSITY

100

80

60

40

20

0

58 56 54 52 50 48 46 44 42 40 38

2θ, DEGREES

B = [001]

$\overline{2}00$

$\overline{2}20$

020
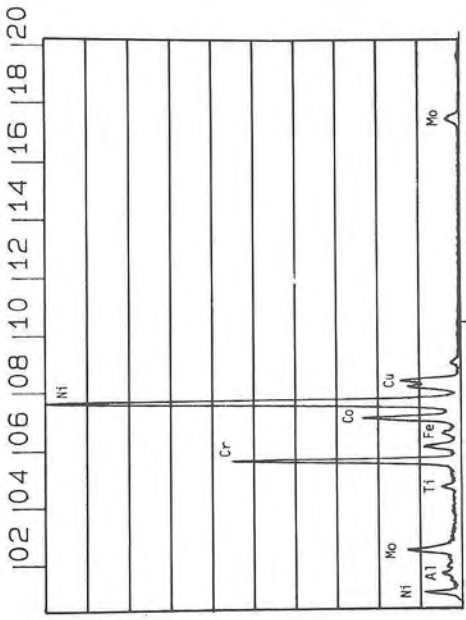
Fig. 1. Bulk Inconel 617: (a) transmission electron micrograph showing uniform arrays of straight dislocations and carbide particles; (b) EDAX spectrum (copper is an artifact); (c) X-ray diffraction pattern (Cu Kα radiation, λ = 1.54 Å); (d) electron diffraction pattern showing a [001] zone axis.

Fig. 2. Scanning electron micrograph of SiC erodent: note the range of particle sizes and shapes; 45° tilt.

[13]. Samples were briefly eroded at 90° using angular 15 μm SiC (Fig. 2) at a velocity of 67 m s^{-1}.

3. Results

3.1. Characterization of sputtered Inconel 617 and nitrided Inconel 617 coatings

Inconel 617 and nitrided Inconel 617 coatings deposited on thin c.p. titanium sheet were bent through 180° and examined using SEM. Both coatings were strongly adherent to titanium substrates. Scanning electron micrographs of the fracture morphology of sputtered Inconel 617 are shown in Figs. 3(a) and 3(b). Dimples on the fracture surfaces are indicative of ductile failure. The nitrided Inconel 617 coating failed in a brittle manner, as shown in Figs. 3(c) and 3(d). The hardness of coatings deposited on polished Ti–6Al–4V specimens was determined using a Buehler Micromet microhardness tester. The average Vickers hardness values of Inconel 617 and reactively sputtered Inconel 617 were 681 and 1104 respectively (200 gf load). EDAX spectra of sputtered Inconel 617 and reactively sputtered Inconel 617 coatings are nearly identical with that of the target material (Fig. 4). X-ray diffraction patterns show that the sputtered Inconel 617 is crystalline, whereas the reactively sputtered coating is either amorphous or has a very fine grain size (Fig. 5).

3.2. Transmission electron microscopy study of sputtered Inconel 617

Through-thickness transmission electron micrographs of sputtered Inconel 617 coatings are shown in Figs. 6(a) and 6(b). Like the target material, the sputtered coating is a solid solution. It is void free and equiaxed, and contains a bimodal distribution of grain sizes ranging from 300 to 1000 Å in diameter. Clusters of microtwinned grains are also shown. Grain boundaries are not easily visible owing to overlapping grains, high internal strain and a moderate dislocation density. A 5 μm selected area diffraction pattern

(a)

(b)

(c)

(d)
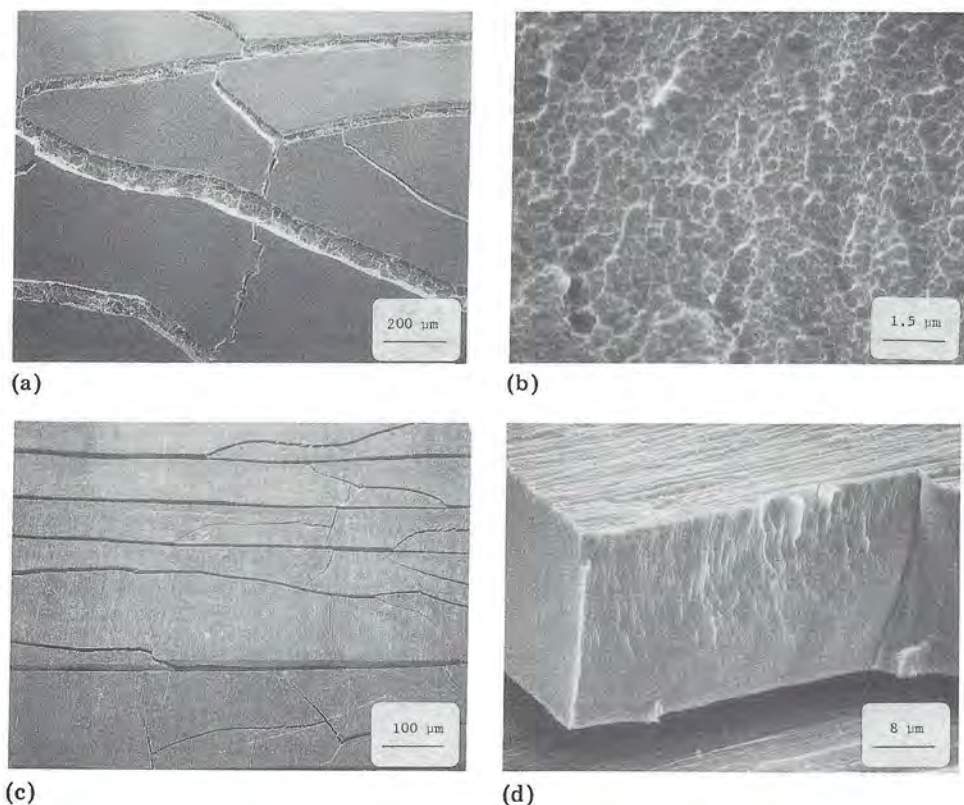
Fig. 3. Fracture morphology of sputtered Inconel 617 and reactively sputtered Inconel 617 nitride: (a) scanning electron micrograph of 180° bend test of sputtered Inconel 617 on c.p. titanium; (b) dimples on fracture surface; (c) 180° bend test of reactively sputtered Inconel 617 nitride on c.p. titanium; (d) fracture surface showing brittle fracture and densely packed fibrous columnar structure.

(Fig. 6(c)) shows evidence of texture. The structure is b.c.c. (with a lattice parameter of 3.02 Å), whereas the target material is f.c.c. Figure 6(d) is a microdiffraction pattern of the large grain shown in Fig. 6(b), and has a [111] zone axis.

3.3. Transmission electron microscopy study of reactively sputtered Inconel 617 nitride

Figures 7(a) and 7(b) show the through-thickness structure of the nitrided coating. It consists of zones of fine crystallites approximately 10 Å in diameter separated by featureless regions approximately 500 Å wide. No grain boundaries are apparent, and it is free of voids and dislocations. Figure 7(c) is a 5 μm selected area diffraction pattern of the region shown in Fig. 7(a). Its diffuse rings indicate that the structure is amorphous. Microdiffraction patterns of the matrix and crystallites using a 120 Å probe are shown in

274

12-FEB-87 08: 13: 59
RATE: CPS TIME   168LSEC
00-20KEV: 10EV/CH PRST: OFF
A: SR#24/C1   B:
FS=   4682   MEM: A   FS=   200

|02 |04 |06 |08 |10 |12 |14 |16 |18 |20

23-JAN-87 06: 45: 31
RATE: CPS TIME   60LSEC
00-20KEV: 10EV/CH PRST: OFF
A: SR#12/L3   B:
FS=   4587   MEM: A   FS=   299

|02 |04 |06 |08 |10 |12 |14 |16 |18 |20
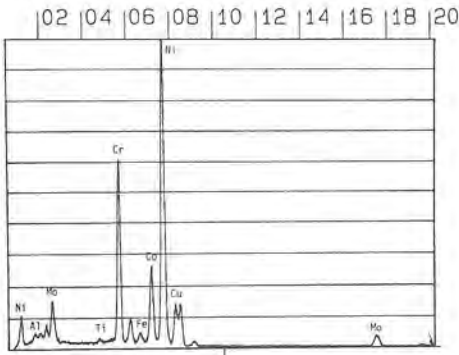
CURSOR (KEV)=10.240   EDAX

(a)
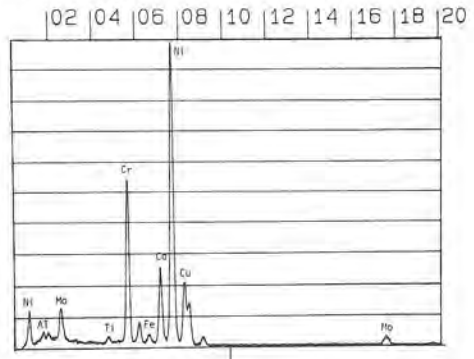
CURSOR (KEV)=10.160   EDAX

(b)

Fig. 4. EDAX spectrum of (a) sputtered Inconel 617 and (b) reactively sputtered Inconel 617 nitride (copper is an artifact).
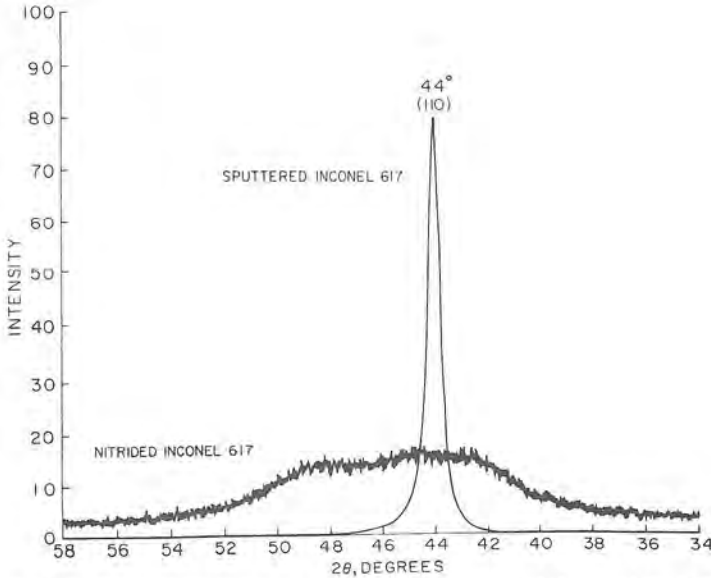
Fig. 5. X-ray diffraction spectrum of sputtered Inconel 617 and reactively sputtered Inconel 617 nitride (Cu Kα radiation, $\lambda = 1.54$ Å).

Fig. 7(d). The matrix is semicrystalline and appears to be cubic, but has not yet been completely characterized. The crystalline regions have a cubic structure with a [001] zone axis.

275

(a)

(b)
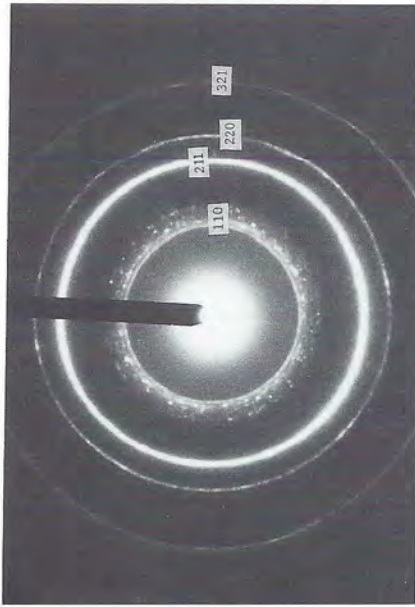
(c)
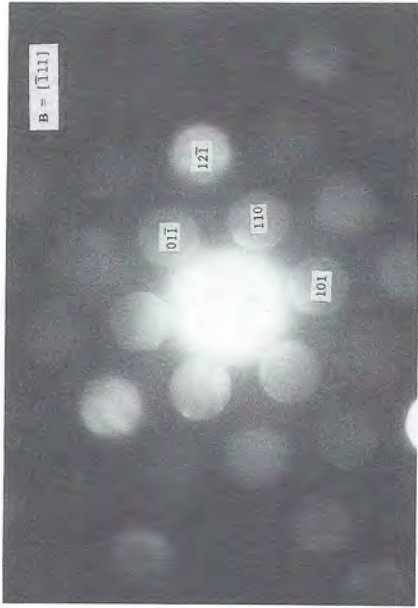
(d)

Fig. 6. Sputtered Inconel 617: (a) and (b) transmission electron micrographs of sputtered Inconel 617; (c) 5 μm selected area diffraction pattern showing a b.c.c. structure; (d) microdiffraction patterns of the large central grain in (b) with a [111] zone axis.

(a)

460 Å

(b)

460 Å
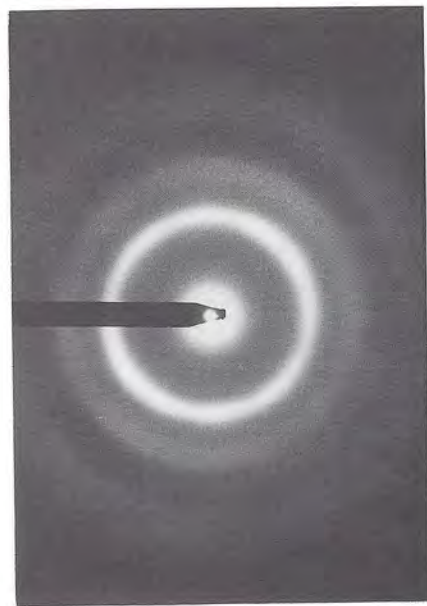
(c)

Fig. 7 (continued).
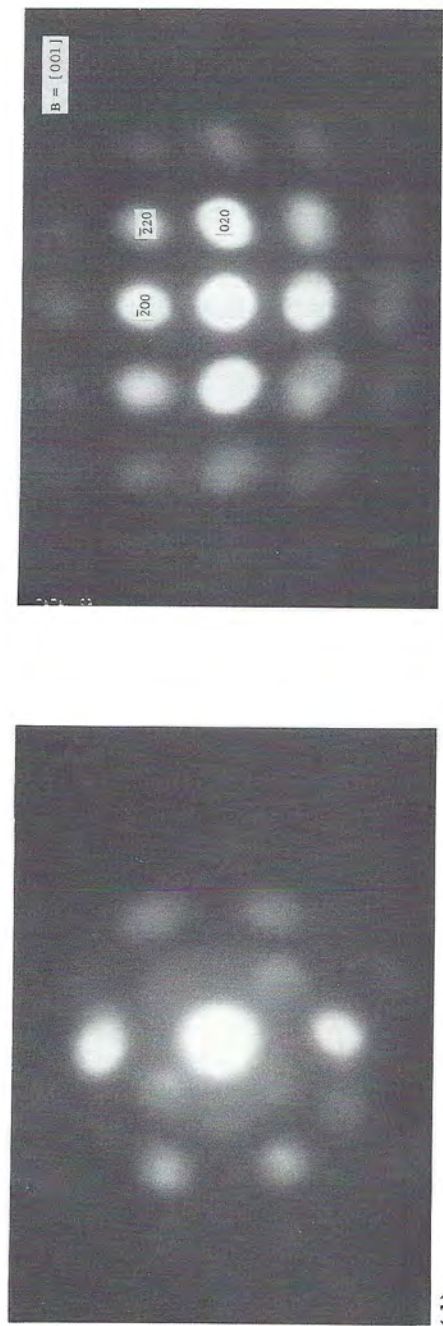
(d)

Fig. 7. Reactively sputtered Inconel 617 nitride: (a) TEM bright field image; (b) TEM dark field image; (c) 5 μm selected area diffraction pattern; (d) microdiffraction patterns of the matrix (left) and crystallites with a [001] zone axis (right).

(a)

(b)

(c)

(d)
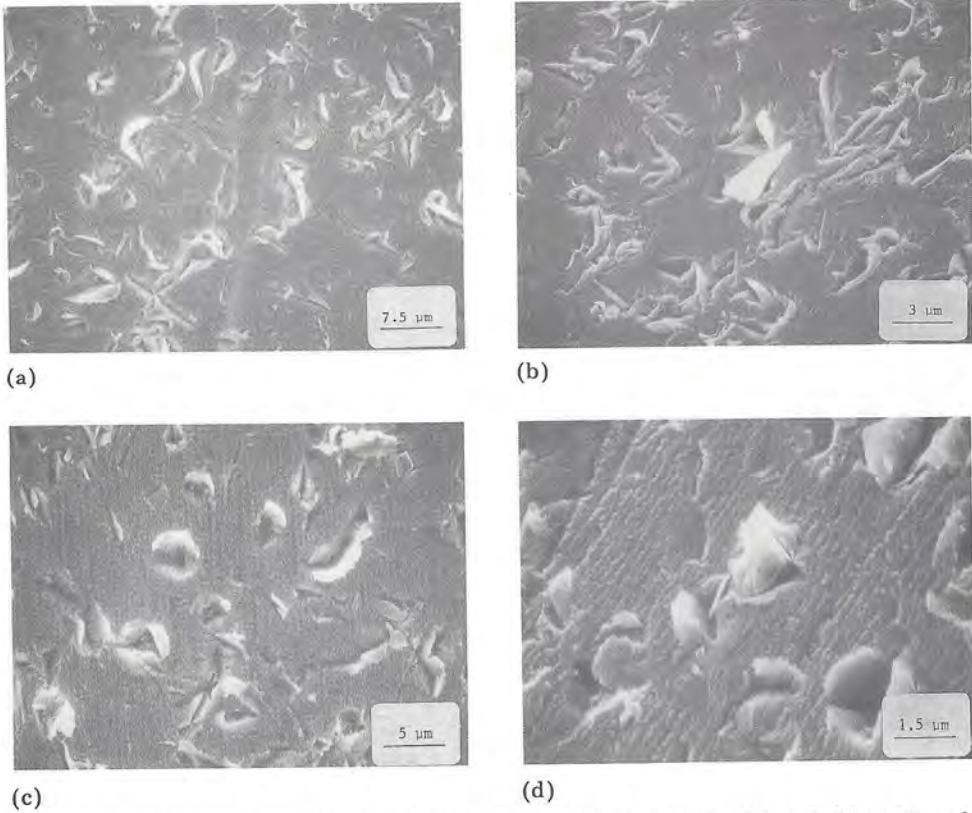
Fig. 8. Scanning electron micrographs of 90° single impact sites: (a) and (b) sputtered Inconel 617 (0°, 45° tilt); (c) and (d) reactively sputtered Inconel 617 nitride (0° and 45° tilt). Both coatings exhibit ductile behavior.

3.4. Erosion studies

Figure 8 shows the results of 90° single-impact tests on sputtered Inconel 617 and reactively sputtered Inconel 617. Both coatings exhibit ductile behavior when impacted by 15 μm SiC. No material loss was evident. However, the ductile lips indicate that the cutting mechanism was prevalent. Embedded and fragmented erodent was also found.

4. Discussion

4.1. Thornton zone model

A systematic investigation of the gross structural features of vapor-deposited coatings was first described by Movchan and Demchishin, and later revised by Thornton [14, 15]. This model has been widely accepted to describe the structural zones of thick (about 25 μm) vapor-deposited coatings as a function of homologous temperature and working gas pressure. Features

were found to be independent of substrate material, and are characteristic of deposition rates in the range 1000 - 2000 Å min^{-1}.

The sputtered Inconel 617 coatings deposited in this study should be Zone T, based upon the temperature measured during sputtering ($T/T_M = 0.3$, where T_M is the melting point of bulk Inconel 617) and working gas pressure (2 mTorr). However, they lack the fibrous columnar grains, high hardness, and brittle mechanical behavior characteristic of such coatings. Thus direct comparison with this model was not possible. The only surface features present are occasional nodular growth flaws, whose existence and mechanism of formation have been previously described [16]. The single reflection in Fig. 5 indicates that the coatings are textured and have a [110] preferred orientation perpendicular to the substrate. This is consistent with the [110] preferred orientation found in similar coatings sputtered from f.c.c. target materials [17, 18].

The surface finish of reactively sputtered Inconel 617 coatings was dull and rougher than that of sputtered Inconel 617. Further, the coatings were hard and brittle, and fracture surfaces showed evidence of a densely packed fibrous columnar grain structure (Fig. 3(d)). While this corresponds better to a Zone T structure, the homologous temperature of 0.3 does not apply since the melting point of the reactively sputtered coating may be higher or lower than that of bulk Inconel 617. Similarity to a Zone T structure suggests that the reactive gas may have influenced the gross structural morphology of the deposit. The mechanism by which this occurred may have been related to reduced adatom surface mobility caused by adsorbed nitrogen atoms [19]. X-ray and electron diffraction patterns do not indicate any preferred orientation (Figs. 5 and 7(c)).

4.2. Transmission electron microscopy studies

The microstructure of sputtered Inconel 617 coatings is similar to that found in other studies of similar sputtered materials [20, 21]. No external heat was applied to the specimens during sputtering, but a thermocouple placed above the platform and adjacent to the substrates recorded temperatures of 410 - 430 °C, depending on the sputtering rate. Similar temperatures were found in another study in which a thermocouple was used to control substrate temperature resulting from particle bombardment [22]. The temperatures measured during deposition of Inconel 617 are likely to be higher than the actual substrate surface temperature owing to the absence of thermal contact with the water-cooled platform. Since bulk Inconel 617 does not undergo any transformation at elevated temperatures, the b.c.c. structure of the coating may be attributed to rapid vapor quenching, limited atomic mobility at high sputtering rates, and local compositional differences between the coating and the bulk target material. The density of sputtered Inconel 617 was measured by weighing Ti–6Al–4V substrates before and after coating, and was found to be 8.29 g cm^{-3}, about 1% less than that of bulk Inconel 617.

Investigators recently studied the structure of 2 - 10 μm thick 304 stainless steel co-sputtered with carbon onto float glass, and found a crystalline-to-amorphous transition with increasing carbon content [23]. Pure sputtered 304 stainless steel was found to have the same chemical composition as the target material, but the structure was b.c.c. The authors attributed this to rapid vapor quenching of the condensate and a low substrate temperature (less than 375 °C) capable of retaining the b.c.c. phase. As the carbon content was increased, the size of the crystalline areas decreased, and amorphous regions approximately 500 Å wide were formed. At approximately 10 at.% C, the crystalline regions were composed of crystallites 10 - 30 Å in diameter. Neither the crystalline nor the amorphous phases were identified. The authors attributed the reduction in crystal size to grain refinement caused by carbon, and did not discuss the possibility of carbide formation. At a carbon concentration of 22.4 at.%, the coating was completely amorphous.

The structure and grain size of Inconel 617 sputtered onto c.p. titanium sheet (Figs. 6(a) and 6(b)) was similar to that of pure sputtered 304 stainless steel. The structure of reactively sputtered Inconel 617 (Figs. 7(a) and 7(b)) was similar to that of co-sputtered carbon–304 stainless steel at a carbon content near the transition to a completely amorphous structure, and nearly identical with that found in a study of Cr–C films [24]. Dark-field imaging and diffuse microdiffraction patterns indicate that the crystalline regions are composed of fine crystallites embedded in a semicrystalline matrix. The density of the nitrided Inconel 617 coating was 7.68 g cm^{-3}, about 7.3% less than that of sputtered Inconel 617. This corresponds to a nitrogen content of 27.8 at.% (8.5 wt.%).

The morphology of the crystalline and amorphous regions in co-sputtered carbon–304 stainless steel films was attributed to compositional variations caused by topographical differences on the substrates which produced shadowing relative to the position of the carbon target. In this study, however, the coating was reactively sputtered. Thus such shadowing effects could not have caused the observed microstructures. While sputtered coatings tend faithfully to replicate surface finishes, topographical variations are not a factor since the surface roughness of glass slides is not significant relative to the coating thickness [19]. Further, the coating was deposited at a homologous temperature where growth is dominated by surface diffusion. However, the mobility of adatoms was likely to be reduced because of adsorbed nitrogen atoms.

The literature contains reports of extensive work in the synthesis of nitrides of three of the four pure component metals found in Inconel 617. Various nitrides of nickel, chromium and molybdenum have been produced by reactive sputtering at different partial pressures of nitrogen [25 - 27]. Characterization of those coatings showed that they do not, in general, correspond well to that produced in this study. Thin nickel nitride coatings exhibiting sharp X-ray diffraction peaks were found to have f.c.c., f.c.t., b.c.t. and h.c.p. structures [25]. Line broadening of diffraction peaks was

attributed to interstitial nitrogen atoms resulting in a lattice parameter greater than that of pure nickel owing to an increased expansion of the lattice. Other investigators found both nondescript and highly oriented columnar grain structures in molybdenum nitride and chromium nitride films [26, 27]. In contrast with the study of nickel nitrides, nitrogen was found to be incorporated as a supersaturated solid solution for similar nitrogen partial pressures and at deposition temperatures below 400 °C. Higher deposition temperatures or subsequent annealing of both coatings produced discrete chromium and nickel nitrides detectable by X-ray diffraction. The Vickers hardness of these coatings was 3000 HV (50 gf load) at a nitrogen content of 10 at.%.

Reactive sputtering in an $Ar-N_2$ atmosphere would be expected to produce a variety of nitrides of the component metals in Inconel 617. The free energy of formation at 600 K is lowest for CrN, and this should thus be the favored compound [28]. Microdiffraction patterns of the crystallites indicate a cubic structure. The only binary nitrides with cubic structures are CrN, Mo_2N and Ni_4N [25, 29]. The lattice parameter measured in Fig. 7(d) is 3.72 Å, and corresponds well with f.c.c. Ni_4N. This is consistent with that expected as a result of lattice expansion caused by interstitial nitrogen in the f.c.c. unit cell, provided the regions in which the crystallites are embedded are rich in nickel. Thus the crystallites have been tentatively identified as f.c.c. Ni_4N.

4.3. Solid particle erosion studies

The angular dependence of solid particle erosion has been examined for many materials and found to be highest for ductile and brittle targets at impact angles of 15° - 30° and 80° - 90° respectively [5, 7, 30]. However, variations have been observed, particularly arising from the erodent shape. In one study it was found that the maximum erosion rate for ductile materials shifted from 20° to 90° as the erodent became less angular [31], while in another study similar erosion rates were found for 304 stainless steel eroded with angular particles at angles between 10° and 90° [32]. The mechanisms by which bulk ductile and brittle targets are eroded when impacted by angular particles has been well characterized [6, 30, 33]. Loss of material in ductile targets during steady state erosion is primarily by cutting. This may occur either through the formation of an indentation and subsequent removal of raised lips, or by the gouging of small volumes of material on impact. Through-thickness TEM studies of single impacts using 50 μm angular particles showed high dislocation densities surrounding impact craters [34]. No evidence of material loss was found because the particle velocity was low, but the large amount of strain at impact sites was believed to be a significant factor affecting the steady state erosion behavior of ductile targets. Particle fragmentation has also been shown to result in material loss [35]. Embedded erodent is often found in ductile targets at normal impact angles, and the resultant composite surface layer (made up of fragmented particles and target material) can decrease the erosion rate [36]. The mechanism of material loss

in brittle materials caused by angular particles is the initiation and propagation of cracks through repeated impacts above a threshold particle size and velocity [6, 30, 37]. Particles fragmenting on impact can cause additional material loss. Embedded erodent is not normally found in brittle materials.

Erosion of coatings deposited by physical vapour deposition (PVD) and other methods has also been examined. Hard silicon carbide and tungsten carbide coatings blended with 304 stainless steel 1 - 10 μm thick deposited on compressor blades showed an improvement in erosion resistance [1, 2]. However, erosive wear remained pronounced in leading edges and concave blade surfaces. Hard TiN coatings 1 μm thick deposited on quenched and tempered high-speed steel rod (grade M2) showed poor erosion resistance at 90° impact, partly owing to the large particle size relative to the coating thickness [38]. SEM studies showed deep craters and ductile lip formation in the steel substrate. A study of 20 - 25 μm thick TiB_2 deposited on Ti–6Al–4V by a pack cementation method showed greatly improved erosion resistance over other hard coatings and alloys [3]. The coating had a Knoop hardness value of 2800 - 3450 (50 gf load). Erosion tests utilized 75 μm angular silica. However, the tests were performed using a 45° impact angle.

Ductile PVD coatings should have good erosion resistance at 90° because of their small grain size, large amount of grain boundary area, and moderate dislocation density. Single-impact tests on sputtered Inconel 617 showed ductile lip formation and a variety of crater sizes and shapes (Figs. 8(a) and 8(b)). The latter is a common feature indicative of the range of particle sizes and shapes normally found in an angular erodent, and the fact that only a portion of the particle forms the crater. Fragmented particles were also found and may have caused many of the small irregularly shaped craters (Figs. 8(b) and 8(d)). The cutting mechanism is prevalent. Sharp lips indicative of glancing impacts and irregular particle trajectories and rotations are shown. No evidence of material loss was found. The ductile behavior observed in erosion tests is consistent with that of the bulk coating properties (Fig. 3(b)).

The fracture morphology of 180° bend test samples of nitrided Inconel 617 showed brittle failure. Thus this coating should have a maximum erosion rate at 90°. However, single-impact tests showed a response similar to that observed for sputtered Inconel 617 coatings. Indentations were smooth with ductile lips, and no evidence of cracking was found. The low dislocation density observed in nitride coatings may explain this behavior. However, the coating is likely to behave differently during repeated impacts owing to the formation of a work-hardened surface layer containing a high dislocation density. Further, Ni_4N crystallites may impede dislocation motion after steady state erosion has been achieved. Quasi-static microhardness indentations also showed ductile behavior. Other investigators have shown that brittle targets can exhibit features characteristic of ductile materials under certain conditions [35, 39]. Shear lips adjacent to impact craters and droplets inside craters indicative of localized melting have been found. However, no evidence of melting was observed in the nitrided coating.

5. Conclusion

Inconel 617 coatings 28 μm thick, magnetron sputtered on to titanium substrates, were adherent and ductile, and contained a bimodal distribution of equiaxed grains. The structure was b.c.c. with a [110] preferred orientation, whereas that of the target materials was f.c.c. The lattice parameter was found to be 3.02 Å. The coating did not correspond to a Thornton model Zone T structure, perhaps because of high surface diffusion. Reactively sputtered Inconel 617 nitride coatings 26 μm thick were also adherent to titanium substrates, but were brittle. The microstructure was two phase consisting of crystallites tentatively identified as f.c.c. Ni_4N, embedded in a semicrystalline matrix. The lattice parameter of the crystallites was 3.72 Å. No preferred orientation was evident. Nitrogen is believed to have influenced the formation of a Zone T structure through reduced adatom mobility. Single-impact erosion studies showed that both coatings exhibited ductile behavior when impacted by 15 μm SiC at 67 m s^{-1}. The cutting mechanism was prevalent.

Acknowledgments

References

1 K. Gentner and J. E. Newhart, in T. R. Shives and W. A. Ward (eds.), *The role of cavitation in mechanical failures, Proc. 19th Meet. Mechanical Failures Prevention Group, NBS Spec. Publ. 94,* 1974, p. 117.

2 K. Gentner, *Proc. 4th Int. Conf. on Rain Erosion and Associated Phenomena, May 1974,* Royal Aircraft Establishment, U.K., 1974, p. 701.

3 S. C. Singhal, *Thin Solid Films, 53* (1978) 375.

4 G. W. Goward, *Thin Solid Films, 53* (1978) 223.

5 P. F. Becher, R. W. Rice, C. CM. Wu and R. L. Jones, *Thin Solid Films, 53* (1978) 225.

6 G. P. Tilly, *Wear, 14* (1969) 63.

7 C. E. Smeltzer, M. E. Gulden and W. A. Compton, *J. Basic Eng., 92* (1970) 639.

8 B. Beacher, W. Tabakoff and A. Hamed, *Trans. ASME, 104* (1982) 64.

9 A. Hamed and S. Fowler, *J. Eng. Power, 105* (1983) 839.

10 *Inconel alloy 617,* Huntington Alloys, Inc., Huntington, WV, U.S.A., 1979.

11 W. L. Mankins, J. C. Hosier and T. H. Brassford, *Metall. Trans., 5* (1974) 2579.

12 P. W. Davies, J. P. Dennison and D. Sidey, *J. Inst. Met., 101* (1973) 153.

13 M. Emiliani and R. Brown, *Wear, 94* (1984) 323.

14 B. A. Movchan and A. V. Demchishin, *Fiz. Met. Metalloved., 28* (1969) 653.

15 J. A. Thornton, *J. Vac. Sci. Technol., 11* (1974) 666.

16 T. Spalvins and W. A. Brainard, *J. Vac. Sci. Technol., 11* (1974) 1186.

17 S. D. Dahlgren, *Metall. Trans.*, *1* (1970) 3095.

18 J. W. Patten, *Thin Solid Films*, *75* (1981) 205.

19 J. A. Thornton, *Ann. Rev. Mater. Sci.*, *7* (1977) 239.

20 S. D. Dahlgren, *J. Vac. Sci. Technol.*, *11* (1974) 832.

21 J. R. Spingarn, B. E. Jacobson and W. D. Nix, *Thin Solid Films*, *45* (1977) 507.

22 G. Cholvy, J. L. Derep and M. Gantios, *Thin Solid Films*, *126* (1985) 51.

23 T. W. Barbee, B. E. Jacobson and D. L. Keith, *Thin Solid Films*, *63* (1979) 143.

24 S. Komiya, S. Ono, N. Umezu and T. Narusawa, *Thin Solid Films*, *54* (1977) 433.

25 G. J. W. R. Dorman and M. Sikkens, *Thin Solid Films*, *105* (1981) 251.

26 A. Aubert, R. Gillet, A. Gaucher and J. P. Terrat, *Thin Solid Films*, *108* (1983) 165.

27 A. Aubert, J. Danroc, A. Gaucher and J. P. Terrat, *Thin Solid Films*, *126* (1985) 61.

28 J. F. Elliott and M. Gleiser, *Thermochemistry for Steelmaking*, Addison-Wesley, Reading, MA, 1960, pp. 151 - 155.

29 A. Taylor and B. J. Kagle, *Crystallographic Data on Metals and Alloy Structures*, Dover Publications, Inc., NY, 1963, pp. 214 - 219.

30 I. Finnie, *Wear*, *3* (1960) 87.

31 A. K. Cousens and I. M. Hutchings, in J. E. Field and N. S. Corney (eds.), *Proc. 6th Int. Conf. on Erosion by Liquid and Solid Impact, Cambridge, U.K., September 5 - 8, 1983*, Cavendish Laboratory, Cambridge, U.K., 1983, Paper 41.

32 C. T. Morrison, R. O. Scattergood and J. L. Routbort, *Wear*, *11* (1986) 1.

33 I. Finnie, *Wear*, *19* (1972) 81.

34 L. K. Ives and A. W. Ruff, *Wear*, *46* (1978) 149.

35 G. P. Tilly and W. Sage, *Wear*, *16* (1970) 447.

36 A. Venugopal Reddy and G. Sundararajan, *Wear*, *11* (1986) 313.

37 D. B. Marshall, A. G. Evans, M. E. Gulden, J. L. Routbort and R. O. Scattergood, *Wear*, *71* (1981) 363.

38 B. Jonsson, L. Akre, S. Johansson and S. Hogmark, *Thin Solid Films*, *137* (1986) 65.

39 C. S. Yust and R. S. Crouse, *Wear*, *51* (1978) 193.

DUCTILE REINFORCEMENT TOUGHENING OF γ-TiAl: EFFECTS OF DEBONDING AND DUCTILITY

H. E. DÈVE, A. G. EVANS, G. R. ODETTE and R. MEHRABIAN

Materials Department, College of Engineering, University of California, Santa Barbara, CA 93106, U.S.A.

and

M. L. EMILIANI and R. J. HECHT

Pratt & Whitney, United Technologies Corp., West Palm Beach, Fla, U.S.A.

Abstract—The effects of reinforcement debonding and work hardening on ductile reinforcement toughening of γ-TiAl have been examined. Debonding has been varied by either the development of a brittle reaction product layer or by depositing a thin oxide coating between the reinforement and matrix. The role of work hardening has been explored by comparing a Nb reinforcement that exhibits high work hardening with a solution hardened Ti–Nb alloy that exhibits negligible work hardening. It is demonstrated that a high work rupture is encouraged by extensive debonding when the reinforcement exhibits high work hardening. Conversely, debonding is not beneficial when the reinforcement exhibits low intrinsic ductility due to an absence of work hardening.

Résumé—On a étudié les effets de la décohésion et de l'ecrouissage du renfort sur le durcissement de TiAl γ par un renfort ductile. On a obtenu différents types de décohésion, soit en développant une couche fragile de produit de réaction, soit en déposant un mince revêtement d'oxyde entre le renfort et la matrice. On a exploré le rôle de l'écrouissage en comparant un renfort de Nb, qui présente un écrouissage élevé, avec un alliage de Ti–Nb durci en solution, qui présente un écrouissage négligeable. On démontre qu'un travail de rupture élevé est favorisé par une décohésion importante quand le renfort présente un écrouissage élevé. Réciproquement, la décohésion n'est pas avantageuse quand le renfort présente une ductilité intrinsèque faible due à une absence d'écrouissage.

Zusammenfassung—Der Einfluß der Ablösung und der Verfestigung auf die Härtung von einlagerungsverstärktem γ-TiAl wurde untersucht. Die Ablösung wurde variiert, indem zwischen Verstärkungsmittel und Matrix entweder eine spröde Reaktionsschicht erzeugt oder eine dünne Oxidschicht eingebracht wurde. Die Rolle der Verfestigung wurde untersucht, indem eine Nb-Verstärkung, welche hohe Verfestigung aufweist, mit einer mischkristallgehärteten Ti–Nb-Legierung verglichen wird, die nur eine vernachlässigbare Verfestigung aufweist. Es wird gezeigt, daß eine hohe Bruchenergie durch ausgedehntes Ablösen erzeugt wird, wenn das Verstärkungsmittel sich stark verfestigt. Umgekehrt ist Ablösen nicht hilfreich, wenn das Verstärkungsmittel eine geringe intrinsische Duktilität wegen fehlender Verfestigung aufweist.

1. INTRODUCTION

Substantial toughening of intermetallics and ceramics by ductile reinforcements has been established [1–5]. It has also been demonstrated that the toughening due to bridging, ΔG_c, has a steady-state magnitude given by [6, 7]

$$\Delta G_c = \sigma_0 f R \chi \qquad (1)$$

where σ_0 is the uniaxial yield strength, f is the area fraction of reinforcements, $2R$ is the reinforcement thickness and χ is a work of rupture parameter that can vary between ~1/2 and ~6, depending upon the extent of interface debonding and the reinforcement constitutive behavior [1–3, 8]. Furthermore, the magnitude of χ is reflected in the non-dimensional stress–stretch relationship

$$\chi = \int_0^{\alpha^*} (\sigma/\sigma_0) \, d\alpha \qquad (2)$$

where, $\alpha = u/R$, with u being the crack opening displacement and α^* is the value of α at the rupture displacement, u^*. The principal intent of the present study is to examine the specific, yet coupled, effects of debonding and work hardening on χ, including the role of the interface/coating properties.

The systems selected for investigation consist of γ-TiAl reinforced with Nb and Ti–Nb alloys. These systems have been demonstrated to exhibit appreciable toughening in composite form [4, 9] and also are susceptible to interface debonding when a brittle reaction product (e.g. σ phase) forms between the reinforcement and the matrix [3]. Furthermore, extremes of work hardening behavior, as well as a substantial range of flow strength, are accessible in this system [3].

Tests that reflect toughening characteristics may be conducted using either composite cylinders [2, 3] [Fig. 1(a)] or laminates [9] [Fig. 1(b)]. Test specimens
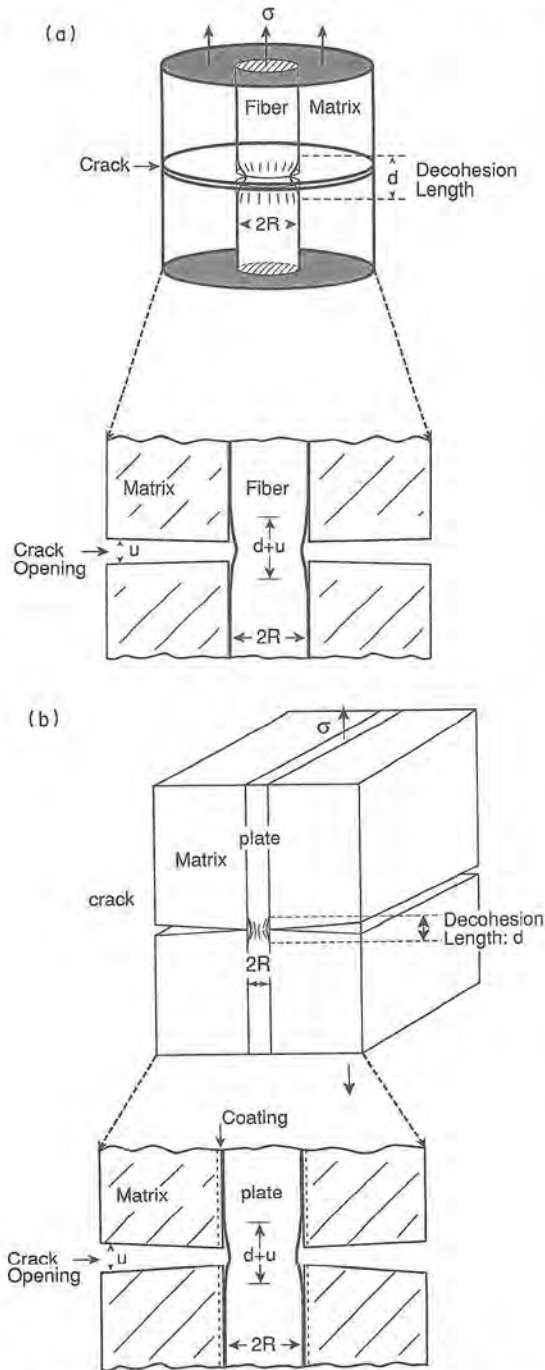
Fig. 1. (a) Schematic of a composite cylinder test specimen.
(b) Schematic of a composite laminate test specimen.

the matrix and the reinforcement. For this purpose, the potential for thin oxide coatings is given explicit consideration, with the extent of debonding assessed in terms of the fracture properties of the oxide material.

2. MATERIALS

Matrix plates (1.5 mm thickness) of TiAl (Ti–50.5 at.% Al) have been prepared from HIPed and forged billets by electro-discharge machining (EDM), followed by a homogenization heat treatment at 1000°C for 20 h. The resultant microstructure consists of predominantly equiaxed grains of γ-TiAl (grain size 100 μm) with small amounts of α_2 in a $(\alpha_2 + \gamma)$-lath structure. Thin reinforcement plates (from 0.12 to 0.17 mm thickness) of either pure Nb or Ti–33 at.% Nb produced by hot rolling have been annealed in vacuum at 1066°C for 4 h. This material consists of single phase β with equiaxed grains.

Some of the reinforcement plates were coated on both sides with ~2 μm of either Al_2O_3 or Y_2O_3. Coatings are deposited by radio-frequency reactive sputtering of 99.9% pure aluminum or yttrium metal targets using a 50%–50% mixture of research grade argon and oxygen. Substrates were rotated at ~1 rpm during sputtering to ensure uniform coverage, and were not externally cooled, heated or biased. As deposited coatings were examined by SEM and found to correspond to a zone 1 or zone T microstructure, as determined by Thornton [11].

Laminates suitable for testing [Fig. 1(b)] are produced by diffusion bonding. To achieve representative microstructures, the TiAl plates are carefully polished to provide good planarity and inserted into a bonding fixture depicted in Fig. 2. The diffusion bonding is carried in vacuum under a 10 MPa pressure at 1066°C for times varying between 1 h for the Ti–Nb alloys to 4 h for the pure Nb. In some cases, split plates of TiAl are used to facilitate matrix precracking, as indicated on Fig. 2.

3. MICROSTRUCTURES

The bonded laminates have been investigated by both scanning (SEM) and transmission (TEM) electron microscopy on sections normal to the interface. Analytical electron microscopy has indicated the following general features. In the absence of oxide

are more readily produced for the latter geometry, by direct diffusion bonding. Furthermore, this geometry is typical of that used for ductile phase reinforced intermetallics [4]. Consequently, a test procedure based on a plane strain laminate geometry [Fig. 1(b)] is devised and used to evaluate the toughening potential, based on equation (2).

The degree of debonding can be independently varied by introducing a non-reactive coating between

Fig. 2. The split plate geometry used for a convenient precrack specimen by diffusion bonding.

coatings, both SEM and TEM investigation [Fig. 3(a, b)], showed that the Nb reacts with the TiAl to form T_2 and σ intermediate phases [3]; whereas Ti–33%Nb produces α_2, and a duplex α/β layer[3] [Fig. 3(c, d)]. Coatings of Y_2O_3 are found to be essentially inert and also prevent the formation of reaction products between the reinforcements and the matrix [Fig. 4(a)].

The Al_2O_3 coating was subject to extensive reaction with the Ti–Nb reinforcement and fully reacted during diffusion bonding to form a complex multiphase reaction product zone [Fig. 4(b)]. These specimens were not subjected to mechanical testing. Conversely, little reaction occurred upon bonding with the Nb reinforcement [Fig. 4(b)]. The incidence of reactions in the presence of Al_2O_3 is consistent with previous studies, which have revealed that high purity Nb bonds to Al_2O_3 without reaction product formation

[12] whereas Ti reacts with Al_2O_3 to form a multiphase Ti aluminide layer [13].

4. MECHANICAL CHARACTERISTICS

4.1. Tensile properties

The mechanical properties of the laminates were evaluated by conducting uniaxial tensile tests, using the geometry indicated on Fig. 1(b). Symmetric pre-cracking of the TiAl outer layers prior to tensile testing was an essential feature of the experiment. This was most systematically achieved when the split plate bonds were used, followed by tensile loading. Some tests were conducted in a servohydraulic machine with displacements monitored from an axial extensometer. Other tests were conducted *in situ* in the scanning electron microscope. Tests were also conducted on the reinforcements, without bonding to
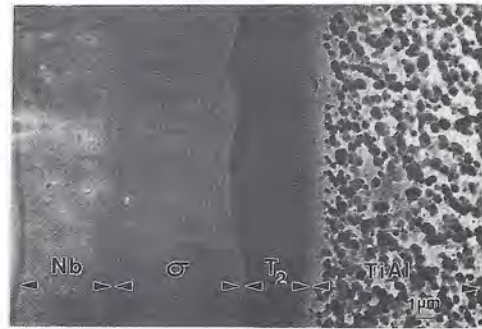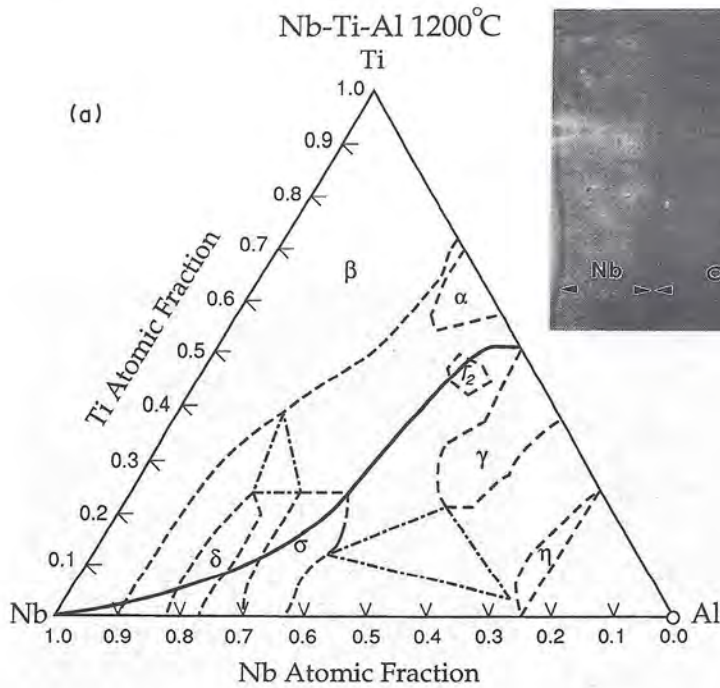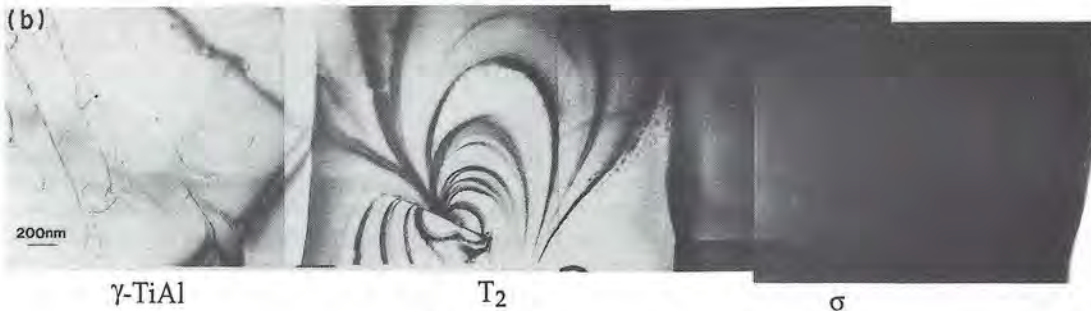
Fig. 3.(a,b) *Caption overleaf.*
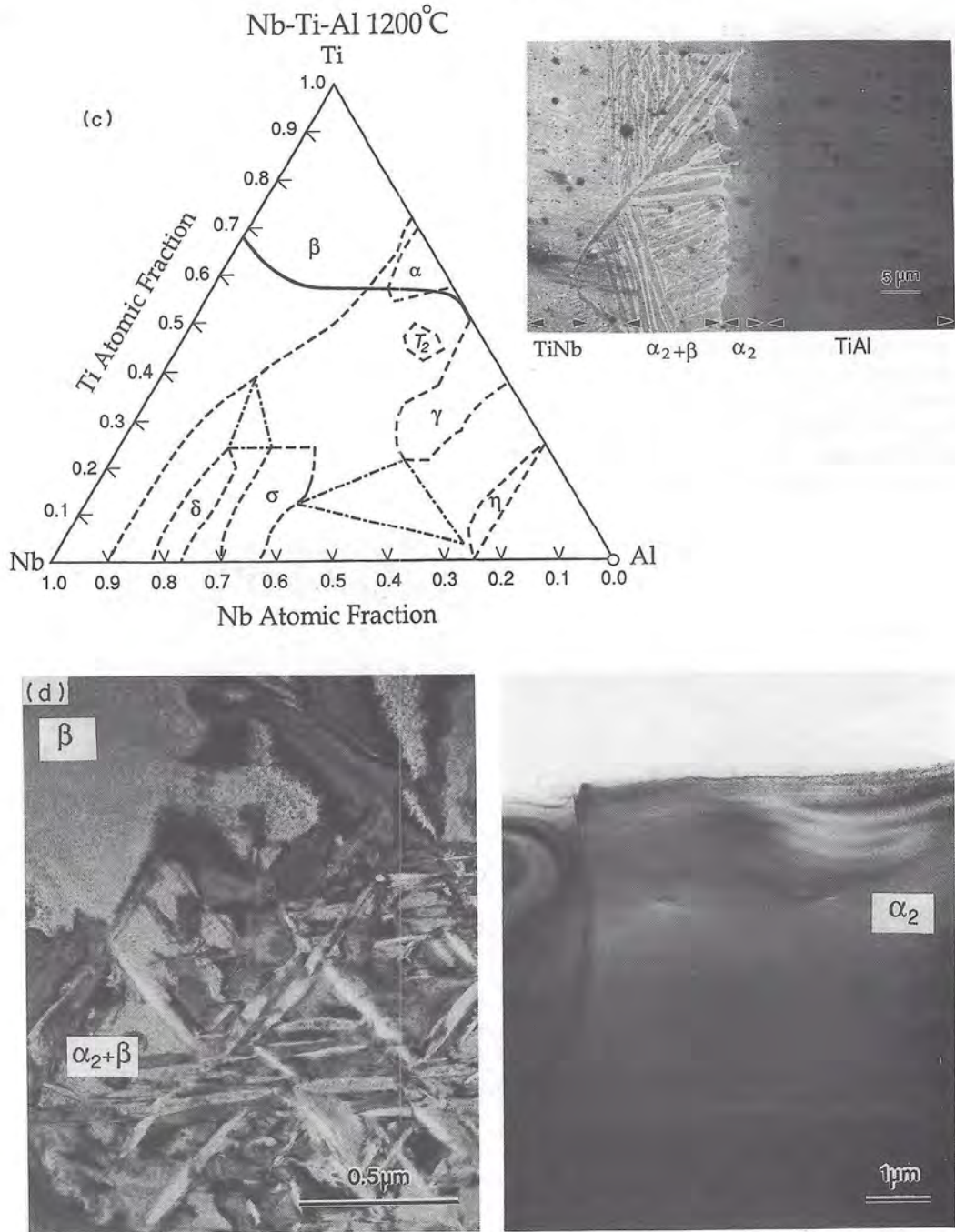
Fig. 3. A summary of reactions that occurred upon diffusion bonding. (a) The Nb/TiAl interfaces showing an SEM micrograph of the σ phase and T_2 reaction layer and the associated phase diagram [18] with the reaction paths indicated. (b) TEM micrograph of T_2 and σ phase reaction product layers shown in (a). (c) The TiNb/TiAl interface showing an SEM micrograph of the α_2 and α_2 & β matrix product layers, and the associated phase diagram [18]. (d) TEM micrograph of the α_2 and α_2 & β layer for (c).

the TiAl. Tensile stress/strain characteristic obtained on the unbonded Nb and Ti–Nb reinforcements [Fig. 5(a)] confirm previous studies [3] which revealed that appreciable work hardening occurs in the Nb, but that Ti–Nb exhibits early unstable plastic flow due to a low work hardening rate. It must be pointed out that since Ti–Nb undergoes localized plastic deformation, the nominal strain plotted in Fig. 5(a) is *dependent* on the initial gauge length. Tests on laminates indicate marked differences in behavior between the Nb and Ti–33 at.% Nb reinforcements and between specimens with and without oxide coatings, as summarized in Table 1 and Fig. 5.
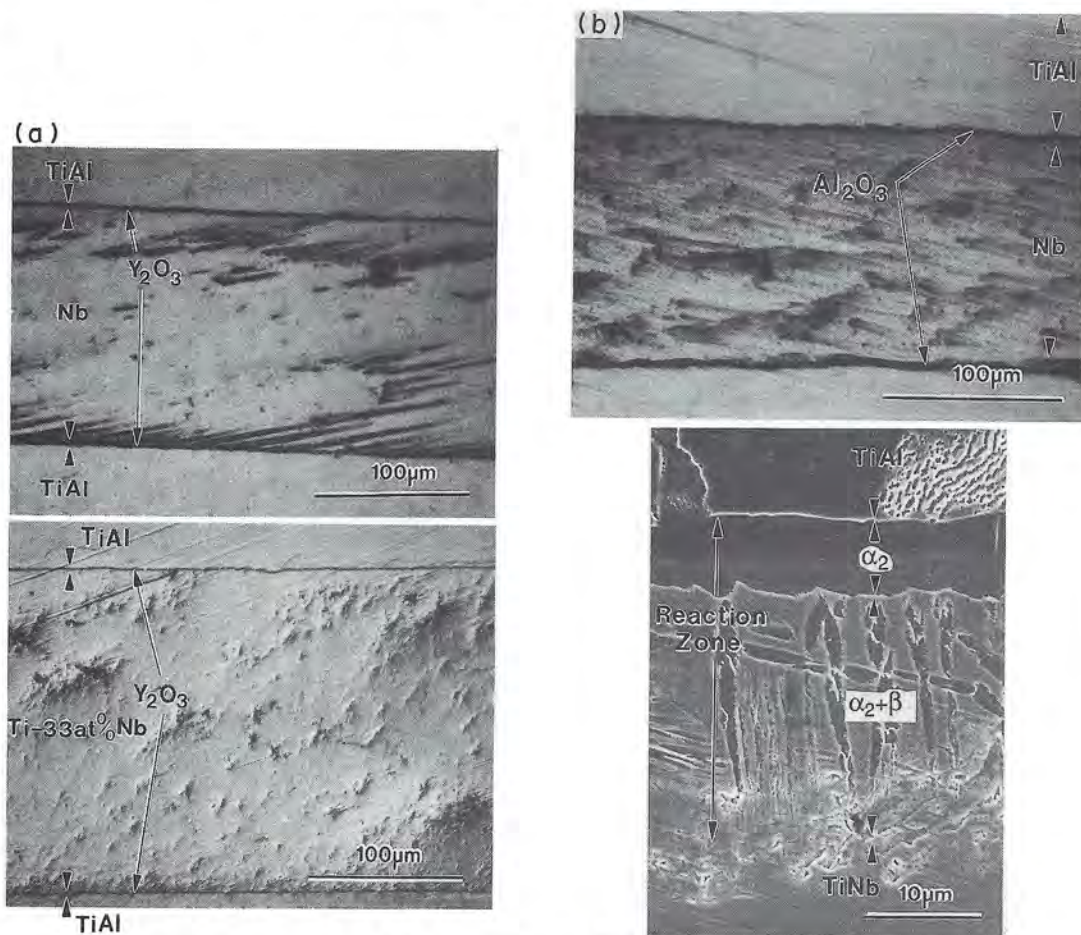
Fig. 4. (a) Optical micrograph of Y_2O_3 coating between TiAl and both Nb and TiNb after diffusion bonding showing the absence of reaction products. (b) Micrograph of Al_2O_3 coatings between TiAl and Both Nb and TiNb after diffusion bonding.

The presence of *oxide coatings* encouraged extensive debonding, which initiated with minimal plastic deformation of the reinforcement (Fig. 6) at stresses of the order of the uniaxial yield strength σ_0. The debonding occurred primarily between the oxide and the reinforcement. Detailed investigation revealed that the debond lengths, d, for the Nb reinforcements coated with either Y_2O_3 or Al_2O_3 [Fig. 6(b, c)] were substantially larger than those for uncoated reinforcements. The largest debonds occurred for Y_2O_3, $d \approx 24R$, while the Al_2O_3 coating gave, $d \approx 7$–$10R$, and the uncoated reinforcements gave, $d \approx 5R$ [Fig. 6(d)]. Furthermore, for oxide coated Nb reinforcements, the rupture stretch, u^*, is found to be proportional to the debond length, d (Fig. 7). Accordingly, the work of rupture χ is largest with Y_2O_3 coatings ($\chi \approx 8$) and of intermediate magnitude for Al_2O_3 coatings ($\chi \approx 4$), such that χ exhibits a linear dependence on either d/R (Fig. 8) or u^*/R.

The behavior of the composite can be most effectively understood by comparing the above stress/stretch characteristics of the laminates with the corresponding curves for the unbonded reinforcements, configured such that the gauge length co-

incides with the final debond length observed in the laminates. Then, the plastic stretch, u, and the nominal strain, ϵ, are related by: $u = \epsilon d$. The results are plotted on Fig. 9. A comparison of the normalized stress/nominal strain curves for the Nb laminates with those for unbonded reinforcements (Fig. 9) indicates that the peak stresses σ^{max}/σ_0 are similar, but that this peak occurs at a lower value of the nominal strain for the laminates, whereas the nominal strain *at failure* is similar for both laminated and unbonded reinforcements. Frictional sliding and ligament bridging along the debond surface [Fig. 6(b–d)], could also contribute to the constraint and modify the deformation and strain hardening (Fig. 9). For the Ti–Nb reinforcements [Fig. 5(c)], somewhat different behavior is obtained. Notably, this material does not exhibit a stage of uniform plastic deformation. Consequently, the strain to failure in a tensile test is dependent on the initial gauge length. Accordingly, an equivalent measure of the plastic stretch, u, for unbonded Ti–Nb, [Fig. 5(c)], is simply the difference between the current and the initial gauge length. Based on this choice, it is evident [Fig. 5(c)] that the stress/stretch behavior is essentially the same for both
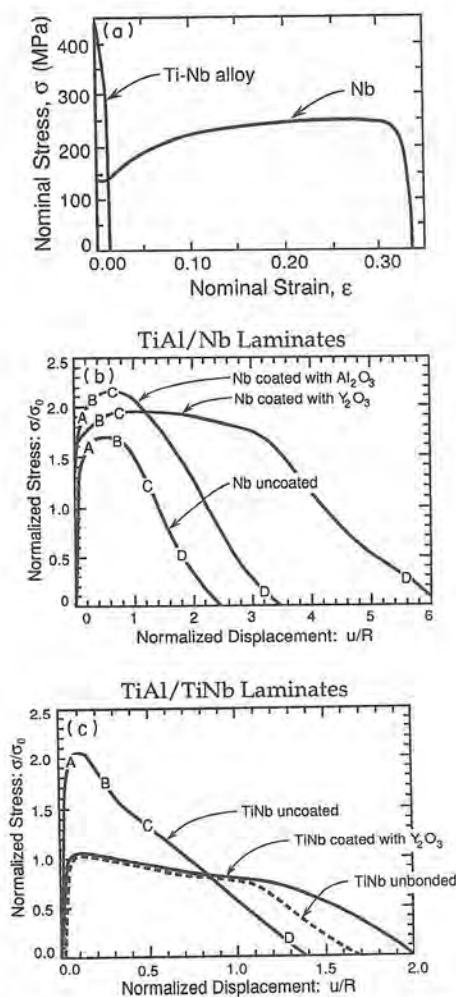
Fig. 5. (a) Tensile stress/strain curve for the unbonded reinforcements (the specimen gauge length was 10 mm). (b) Tensile stress/stretch curves for the TiAl/Nb laminates. The letters refer to the points on the curve that correspond with the *in situ* SEM pictures shown in Fig. 6. (c) Same as (b) but for the TiAl/TiNb laminates.

the coated Ti–Nb laminate and the unbonded reinforcement.

In the *absence of oxide coatings*, the behavior has similar features to that noted in previous studies on composite cylinders [3] and on actual composites [4, 9, 9]. Notably, the σ phase that forms with the Nb

Table 1. Summary of parameters obtained from composite laminate tests

Reinforcement	σ_y/σ_o [a]	u^*/R	d/R	χ
Nb	~1.4	~2	~5	~2.5
Nb: Y$_2$O$_3$ coating	~1.7	~6	~24	~8
Nb: Al$_2$O$_3$ coating	~1.7	~3	~7 to 10	~4
Ti/Nb	~2	~1.4	~1.5 [b]	~1.5
Ti/Nb: Y$_2$O$_3$ coating	1	~2	~25	~1.4

[a] σ_y is the 'yield stress' of the reinforcement.
[b] Within the laminate matrix crack length.

behaves as a debond layer [Fig. 6(d)], and debonding extends primarily within the σ phase. Necking then initiates and rupture occurs at a stretch $u \approx 2R$, such that the work of rupture is of intermediate magnitude, $\chi \approx 2.5$. Consequently, it is apparent that the σ phase is not as effective a debond medium as either the Y$_2$O$_3$ or Al$_2$O$_3$ coatings. The Ti–33 at.% Nb reinforcement does not form a brittle reaction product [3]. However, the present observations [Fig. 6(e)] indicate that the TiAl matrix can crack parallel to the interface. Such cracks inhibit the development of full constraint and apparently encourage the formation of shear bands that lead to reinforcement rupture. The work of rupture $\chi \approx 1.5$ is comparable than that apparent when the Y$_2$O$_3$ coating is used, although some constraint ($\sigma \approx 2\sigma_0$) develops before the matrix cracks nucleate. Nevertheless, the complete avoidance of matrix debonding might be desirable, since it would lead to high crack growth resistance while maintaining similar values of toughness [9].

4.2. Debond fracture energies

The fracture energies of some of the interfacial layers have been measured using the UCSB flexural test [14] (Fig. 10). For this test, sandwich specimens are notched in the TiAl layer on the tensile side and loaded in three-point flexure to introduce a precrack along the interface. Subsequently, the specimen is loaded in four-point flexure to cause further crack extension along the interface. The crack extension load and the specimen dimensions may then be used to give the fracture energy Γ_i [14]. Tests conducted on specimens with Y$_2$O$_3$ coatings gave $\Gamma_i \approx 25 \, \text{Jm}^{-2}$, with crack propagation occurring primarily between the Y$_2$O$_3$ and the reinforcement. This value is typical of the fracture energy found for polycrystalline oxides. Tests conducted on the TiAl/Nb specimens with a σ reaction product phase gave $\Gamma_i \approx 45 \, \text{Jm}^{-2}$, with crack growth occurring primarily within the σ phase.

5. IMPLICATIONS

5.1. Debonding

Debonding in ductile reinforcement toughened intermetallics is strongly influenced by the fracture properties of the phases that exist between the reinforcement and the matrix. *Oxide coatings* that have a small fracture energy ($\Gamma_i \approx 25 \, \text{Jm}^{-2}$ for Y$_2$O$_3$) debond extensively prior to significant plastic deformation of the reinforcement. Simple elastic calculations would suggest steady-state energy release rates [14] and predict unlimited symmetric debonding at a critical stress. In practice, the debond is found to arrest. The actual extent of debonding is thus influenced by other factors, such as frictional sliding and bridging ligaments along the debond surface [Fig. 6(b–d)]. Additionally, the somewhat larger debond resistance of the σ-phase ($\Gamma \approx 45 \, \text{Jm}^{-2}$) is
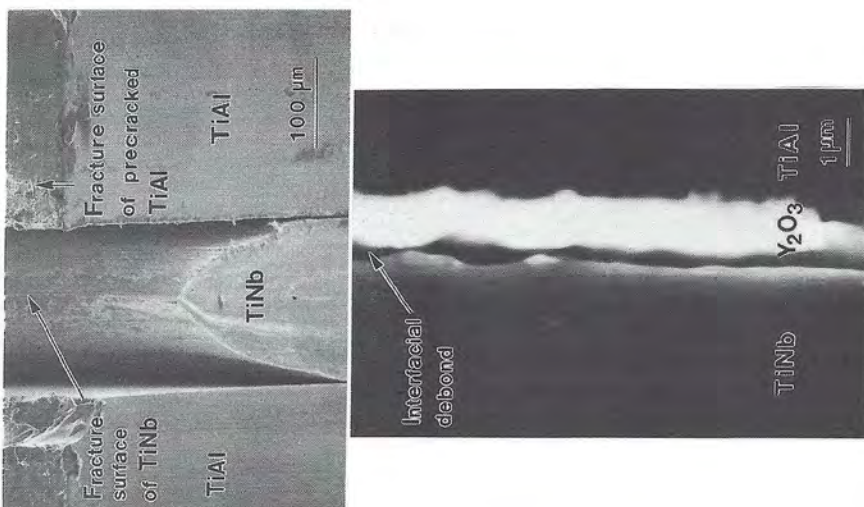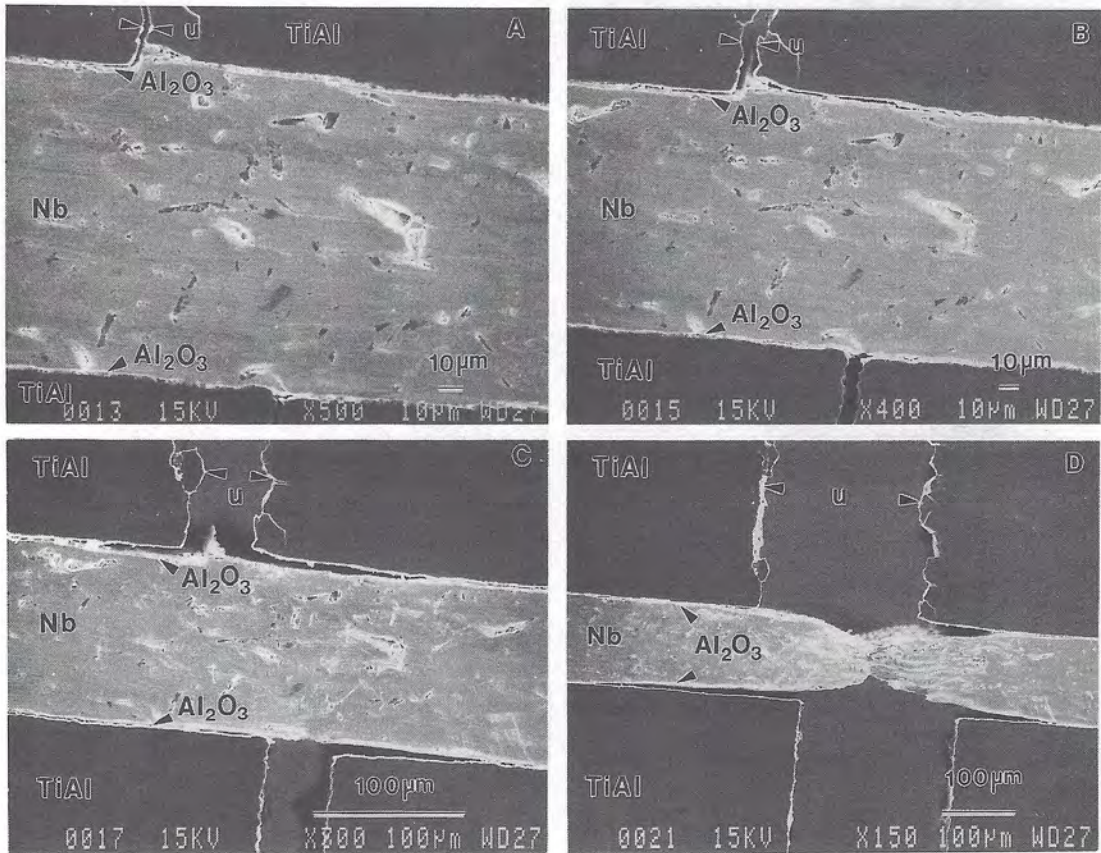
Fig. 6(b)

Fig. 6. Caption on p. 1500.

Fig. 6(a)

TiAl / Nb Coated with Al$_2$O$_3$

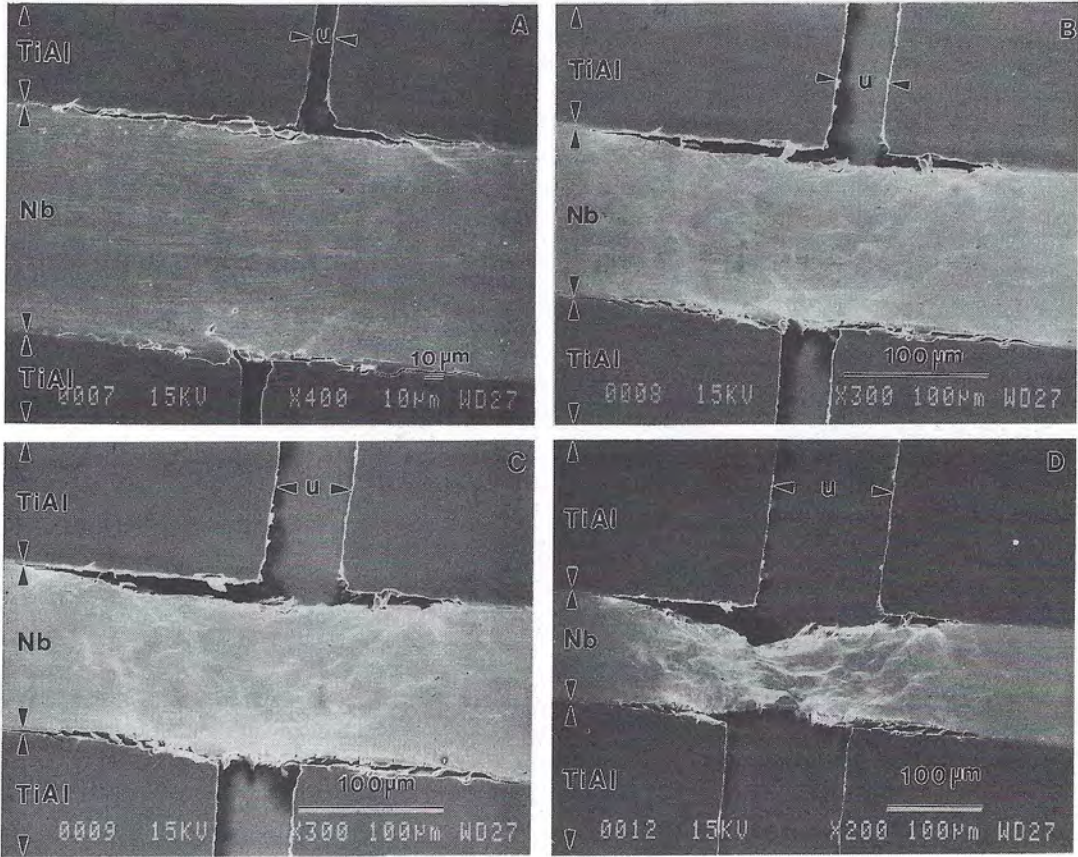

Fig. 6.(c) *Caption on p. 1500.*
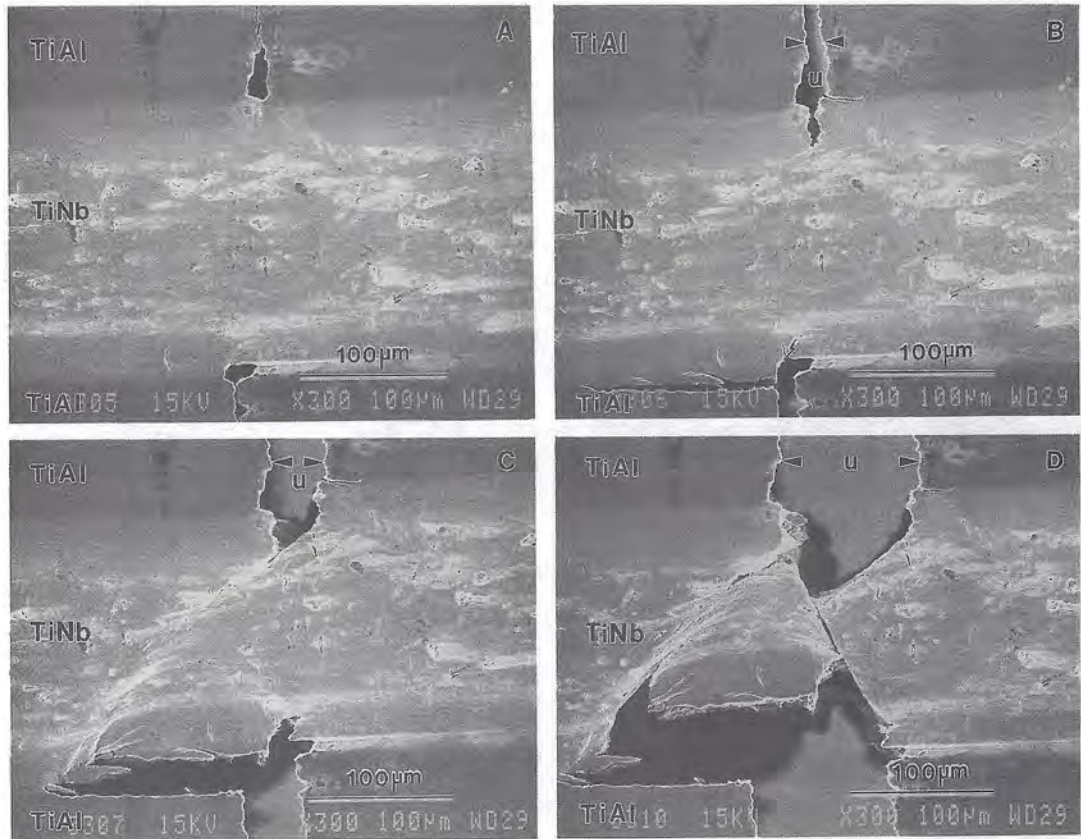
TiAl/Nb

Fig. 6.(d) *Caption on p. 1500.*

Fig. 6(e)

Fig. 6. *In situ* SEM views of the laminate specimens used to generate the stress/stretch curves shown in Fig. 5: (a) TiNb and Y_2O_3 coating; (b) Nb coated with Y_2O_3; (c) Nb coated with Al_2O_3; (d) uncoated Nb: note bridging ligament along the debond with σ phase; (e) uncoated TiNb.

apparently sufficient to substantially stabilize the debonding. Finally, it is noted that matrix debond cracking is possible with high strength Ti–Nb reinforcements. This occurs, albeit erratically, subject to a fracture energy [4], $\Gamma \approx 200 \, Jm^{-2}$.

5.2. Toughening

The present experiments provide a definite rationale for the attainment of an optimum steady-state toughness, as manifest in the work of rupture,

χ. The largest values of $\chi(\sim 8)$ occur for reinforcements that work harden substantially and for interfaces that debond readily. *The work hardening coefficient applicable to Nb (n = 0.3) coupled with an interface fracture energy typical of that for oxides, ($\Gamma_i \approx 25 \, Jm^{-2}$) satisfies these requirements.* Conversely, a fracture energy applicable to the σ-phase reaction product $(\Gamma_i \approx 45 \, Jm^{-2})$ is apparently too large to allow the requisite debonding. To further relate χ to debonding, the behavior of the
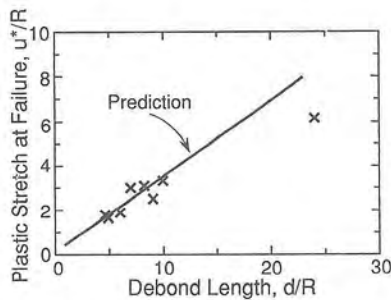
Fig. 7. Trend in the critical plastic stretch u^*/R with debonded length d/R for Nb reinforcements. The line is the prediction from equation (5).
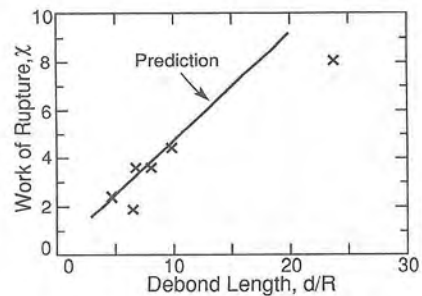
Fig. 8. Trend in the work of rupture χ with the debond length, d/R, for Nb reinforcements. The line is the prediction from equation (8).
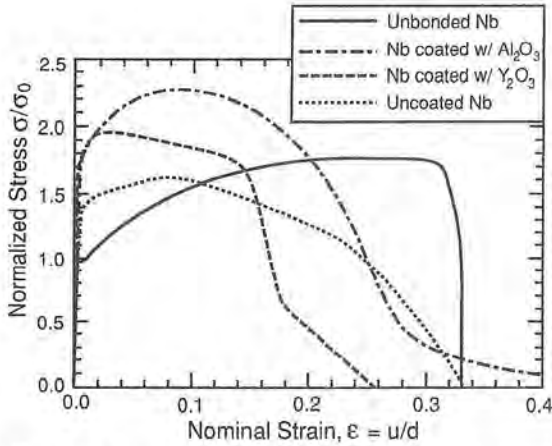
Fig. 9. A comparison of the normalized stress/nominal strain curves for bonded Nb laminates and unbonded Nb reinforcements.

reinforcement over the debond length is addressed. For fixed d, the engineering strain in this region, ϵ, is related to u and d, such that

$$\epsilon = u/d \qquad (3a)$$

or, at rupture

$$\epsilon^* = u^*/d. \qquad (3b)$$

The engineering plastic strain at rupture is governed by the work hardening coefficient n, viz

$$\epsilon^* \approx e^n - 1. \qquad (4)$$

Consequently (for fixed d) u^* and d are expected to be related by

$$u^* \approx d(e^n - 1). \qquad (5)$$

This result is indeed consistent with the measured trend, summarized in Fig. 7. Based on the same simplification that d remains constant, χ can also be estimated by re-expressing equation (1) as

$$\chi = \frac{d}{\sigma_0 R} \int_0^{\epsilon^*} \sigma \, d\epsilon \qquad (6)$$

Then, based on a power law hardening representation

$$\sigma_t = \sigma_0 (\epsilon_t/\epsilon_0)^n \qquad (7)$$

where σ_t and ϵ_t are the true stress and true strain, and by assuming that the true strain at failure is $\epsilon_t^* \approx n$, integration of equation (6) gives

$$\chi \approx [n^{n+1}/\epsilon_0^n(n+1)](d/R). \qquad (8)$$

The trend in χ predicted by equation (8), plotted on Fig. 8, conforms quite well with the present experimental results, and rationalizes the influence of debonding.

The behavior typified by the Ti–Nb reinforcement provides an important contrast. This reinforcement gives a desirably large work of rupture without debonding. Seemingly, in this case, when cracking of the matrix is suppressed, moderate constraint accompanied by appreciable plastic dissipation within shear bands is possible.

To further comprehend the significance of the above results, an important duality in behavior is noted, based on related research [16]. The work of rupture provided by the Nb reinforcements can only be *partially utilized* to give *composite toughness*. This limitation arises because of resistance curve and large scale bridging issues, which become accentuated as the debond length increases [15, 16]. Consequently, strictly on the basis of initiation toughness, the Ti–Nb reinforcements, which do not debond and have a high yield stress, are superior to the coated Nb reinforcements. However, the full plastic dissipation allowed by debonding of the reinforcement *can be utilized* in loading situations that sample the complete range of material resistance, such as *Charpy tests* [16]. Therefore, when the criterion used for material selection is based on the Charpy energy, oxide debond coatings, and reinforcements with high work hardening are preferred. The duality in behavior associated with debonding suggests that, in some cases, when both high Charpy energy and high initiation toughness are needed, a dual reinforcement scheme may be required: one reinforcement debonds and contributes to the Charpy energy, whereas the other bonds well and has the strength needed to provide a large toughness.

6. CONCLUDING REMARKS

The present set of experiments clarify the influence of debonding on the work of rupture, χ, of
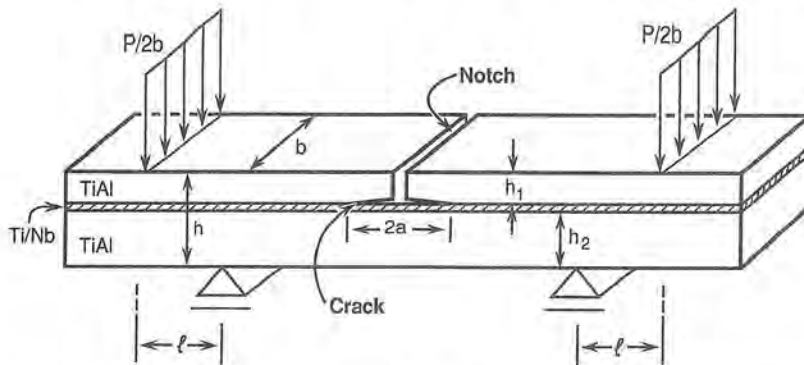

Fig. 10. A schematic of the test specimen used to measure the interface fracture energy.

intermetallics toughness with *highly ductile reinforce-ments*, such as Nb. In particular, for such reinforcements, it has been established that χ exhibits a linear dependence on the debond length, d. It is also apparent that inert oxide coatings emplaced between the reinforcement and the matrix have a sufficiently low fracture energy that extensive debonding is induced, leading to enhanced values of χ. However, it remains to explicitly relate the debond length to the specific fracture energy of the coatings. Furthermore, it has been demonstrated that debonding is undesirable when the reinforcements have limited intrinsic ductility, caused by an absence of work hardening, as exemplified by Ti–Nb reinforcements.

REFERENCES

1. L. S. Sigl, A. G. Evans, P. Mataga, R. M. McMeeking and B. J. Dalgleish, *Acta metall.* **36**, 946 (1988).
2. M. F. Ashby, F. J. Blunt and M. Bannister, *Acta metall.* **37**, 1847 (1989).
3. H. C. Cao, B. J. Dalgleish, H. E. Dève, C. Elliott, A. G. Evans, R. Mehrabian and G. R. Odette, *Acta metall.* **37**, 2969 (1989).
4. C. K. Elliott, G. R. Odette, G. E. Lucas and J. W. Sheckard, *MRS Proc.* **120**, 95 (1988).
5. V. D. Krstic, *Phil Mag. A* **48**, 695 (1983).
6. B. Budiansky, J. C. Amazigo and A. G. Evans, *J. Mech. Phys. Solids* **36**, 167 (1988).
7. A. G. Evans and R. M. McMeeking, *Acta metall.* **34**, 2435 (1986).
8. P. Mataga, *Acta metall.* **37**, 3349 (1989).
9. G. R. Odette, H. E. Dève, C. K. Elliott, A. Harigowa and G. E. Lucas, *Proc. TMS Symp on Interfaces in Ceram. metal. Composites* (edited by R. Y. Lin *et al.*), p. 443, TMS (1990).
10. B. J. Dalgleish, K. Trumble and A. G. Evans, *Acta metall.* **37**, 1923 (1989).
11. J. A. Thornton, *Ann. Rev. Mater. Sci.* **7**, 239 (1977).
12. W. Mader and M. Rühle, *Acta metall.* **37**, 853 (1989).
13. R. E. Tressler, T. L. Moore and R. L. Crane. *J. Mater. Sci.*, 151 (1973).
14. P. G. Charalambides, J. Lund, A. G. Evans and R. M. McMeeking, *J. appl. Mech.* **56**, 77 (1989).
15. F. Zok and C. Hom. *Acta metall. mater.* In press.
16. F. Zok, S. Jansson, A. G. Evans and V. Nardonne, *Metall. Trans.* In press.
17. T. J. Jewett, J. C. Lin, N. R. Ronda, L. Seitzmon, K. C. Hsieh, Y. A. Chang and J. H. Perepezko, *Proc. MRS Fall Meeting* (1988).

Diffusion of Sputtered INCONEL 617 Coatings in Titanium

MARIO EMILIANI, MARC RICHMAN, and RICHARD BROWN

INCONEL 617 coatings 10- to 13-μm thick were radio frequency (RF) magnetron sputtered onto commercially pure α-titanium substrates and heat-treated at 800 °C for 2 hours. The resulting structures were examined in cross section by scanning electron microscopy (SEM) and analytical transmission electron microscopy (TEM). Scanning electron microscopy of polished and etched cross sections showed that the coating remained continuous, and as a result of interdiffusion, a layer 66-μm thick had formed below the coating. Examination of the coating near the free surface by TEM showed it contained both $M_{23}C_6$ and M_6C carbide precipitates, while several micron-thick layers containing intermetallic phases such as σ, γ', and Ti_2Ni were found near the substrate. Kirkendall voids 75 to 300 Å in diameter were present near the original INCONEL 617/α-titanium interface. The microstructure further below that interface contained a thin layer of titanium martensite and Widmanstätten $\alpha + Ti_2Ni$. No TiNi or $TiNi_3$ was found. The diffusivity of nickel and titanium was reduced several orders of magnitude and is attributed primarily to the formation of intermetallic compounds in the coating and substrate.

I. INTRODUCTION

INCONEL* 617 (UNS N00617) is a nickel-base superalloy used in high-temperature environments ($\sim$1000 °C) due to its excellent mechanical stability and oxidation and corrosion resistance. This alloy is a face-centered cubic (fcc) solid solution containing nickel (52 pct), chromium (22 pct), cobalt (12 pct), and molybdenum (9 pct), with small amounts (<1.5 pct each) of Fe, Si, Ti, and Al,** and has a lattice parameter of 3.62 Å.[1,2]

---
*INCONEL is a trademark of Inco Alloys International, Huntington, WV.

**All compositions are in weight percent unless otherwise noted.

The nominal chemical composition of this alloy is given in Table I. Studies of the microstructure and phase stability of bulk INCONEL 617 have been reported previously.[2,3]

Because both nickel and titanium are the primary elemental constituents in this study, it would not be unexpected that a series of Ti_xNi_y phases would form as a result of heat treatment. The binary Ti-Ni phase diagram[4] as well as metallurgy of Ti-Ni alloys[5–12] are therefore briefly reviewed. Figure 1 shows that α-titanium has very limited solid solubility for nickel under equilibrium conditions ($\sim$0.2 pct at 27 °C and $\sim$0.5 pct at 765 °C). A eutectoid reaction ($\beta \rightarrow \alpha + Ti_2Ni$) occurs at about 6 pct Ni and 765 °C and has been an area of interest for producing high-strength titanium alloys.[5] At about 38 and 55 pct nickel, the intermetallic phases Ti_2Ni and TiNi, respectively, are formed and have narrow ranges of compositional variation. Another eutectoid reaction,

$TiNi \rightarrow Ti_2Ni + TiNi_3$, occurs at about 55 pct nickel and 630 °C. The next phase to form is the intermetallic $TiNi_3$ at 78.5 pct nickel and is a line compound with exact stoichiometry.

Near-equiatomic TiNi alloys have been studied extensively due to their commercial significance as shape-memory materials.[6,7] Rapidly quenched TiNi alloys form a heavily twinned martensitic structure with monoclinic crystal structure and lattice parameters of $a = 2.89$ Å, $b = 4.12$ Å, $c = 4.62$ Å, and $\beta = 96.8$ deg.[8,9] The shape-memory effect occurs upon heating plastically deformed TiNi martensite to 50 °C to 100 °C, resulting in the eutectoid reaction $TiNi \rightarrow Ti_2Ni + TiNi_3$.[6,10] The Ti_2Ni structure is fcc and has a lattice parameter of 11.30 Å, while $TiNi_3$ is hexagonal close-packed (hcp) with lattice parameters of $a = 5.10$ Å and $c = 8.30$ Å.[11,12] The morphology of Ti_2Ni is reported to be equiaxed,[11] while $TiNi_3$ contains stacking faults on basal planes.[10]

Beta-eutectoid decomposition of Ti-Ni alloys at near-equilibrium rates results in microstructures containing large α grains and segregation of coarse precipitates. In contrast, rapid solidification processing permits greater control of decomposition products, resulting in alloys with increased strength.[5] The microstructures of near-eutectoid Ti-Ni alloys rapidly solidified by splat quenching, pendant drop melt extraction, and chill-block melt spinning were investigated.[12] Examination of 5.9 to 7.9 pct Ni flakes and ribbons in cross section by SEM showed microstructures ranging from Widmanstätten to martensite, depending upon the composition and cooling rate. Examination of the former microstructure by TEM showed it consisted of proeutectoid α plates 0.3- to 0.5-μm thick and finely divided $\alpha + Ti_2Ni$ with an interlamellar spacing of about 0.1 μm.

Electroplated nickel coatings 25-μm thick applied to $\alpha + \beta$ and β titanium alloy substrates have been studied to determine their applicability in oxidizing or hot corrosion environments.[13] Coated samples were heat-treated at 593 °C for 100 hours. The resulting interfacial reactions were characterized by light microscopy, electron microprobe, and X-ray diffraction. Coatings on $\alpha + \beta$ titanium alloys contained a layer of $TiNi_3$ adjacent to the nickel coating and a layer of TiNi next to the substrate.

MARIO EMILIANI, Senior Materials Engineer, is with Pratt & Whitney, West Palm Beach, FL 33410. MARC RICHMAN, Professor of Engineering, is with the Division of Engineering, Brown University, Providence, RI 02912. RICHARD BROWN, Associate Professor, is with the Materials Laboratory, Department of Chemical Engineering, University of Rhode Island, Kingston, RI 02881.

Nickel	52.0
Chromium	22.0
Cobalt	12.5
Molybdenum	9.0
Iron	1.5
Aluminum	1.2
Manganese	0.5
Silicon	0.5
Titanium	0.3
Copper	0.2
Carbon	0.07
Sulfur	0.008

Both layers were continuous and about 4-μm in thickness. Growth of TiNi was concluded to be the result of inward diffusion of nickel and outward diffusion of titanium. Kirkendall voids were found between TiNi$_3$ and TiNi layers after exposure to 650 °C for 50 hours, resulting in spallation of the TiNi$_3$ layer. Ti$_2$Ni was not found until samples were heat-treated at temperatures $\geq$760 °C. No other phases such as γ' were found in the two $\alpha + \beta$ alloys investigated.

The present study is part of an investigation of the microstructure and phase stability of sputtered INCONEL 617 coating to determine its potential as an oxidation resistant coating.[14] Interdiffusion between the coating and substrate is examined to provide baseline characterization of reaction products in α-titanium.

II. EXPERIMENTAL PROCEDURE

A. Sputtering

INCONEL 617 coatings were deposited onto commercially pure (99.5 pct) α-titanium sheet (ASTM B265079 Grade 1) which contains equiaxed grains 10 to 20 μm in diameter, twins, and fine titanium hydride needles.[14,16] Metallographically polished titanium wafers 2.5-mm-wide by 1.3-mm-thick by 12.5-mm-long

were ultrasonically cleaned for 5 minutes each in trichloroethane, acetone, and ethanol, then immediately inserted into the sputtering unit. A vacuum of better than 3×10^{-6} torr was achieved. Sputtering was performed in a Materials Research Corporation (Orangeburg, NY) model 8667+2M 1.5 kW radio frequency (RF) (13.56 MHz) sputtering unit. The vacuum chamber was silicone oil diffusion pumped and equipped with a liquid nitrogen cold trap. Cold-rolled and solution-annealed INCONEL 617 plate 0.64-cm thick was machined into a circular disc 14.6 cm in diameter and bonded to a water-cooled oxygen-free high-conductivity (OFHC) copper magnetron backing plate using conducting silver-filled epoxy cement. Ultrahigh-purity (UHP) argon (99.999 pct) was used for sputter cleaning, target presputtering, and deposition of INCONEL 617 coatings.

The samples and vacuum chamber walls were sputter cleaned for 10 minutes in argon using a forward RF of 1000 W and a working gas pressure of 15 mtorr at a volumetric flow rate of 19.20 sccm. Substrates were shielded from the target, which was then sputter cleaned for 10 minutes at 1000 W forward RF and 2 mtorr Ar at 19.20 sccm. The optimum sputtering conditions were found to be a forward RF of 1000 W and an argon gas pressure of 2 mtorr at 19.20 sccm, resulting in a deposition rate of 1800 Å/min (0.18 μm/min) as determined by step profilometry. These conditions produced an average power density of 6 W/cm^2, 440 V across the electrodes, 2.27 amp discharge current, and 13.5 mA/cm^2 discharge current density. Coatings 10- to 13-μm thick were deposited in 75 minutes.

Substrates were not externally biased during deposition and are therefore assumed to have been at ground potential during sputtering. Samples were placed upon a water-cooled platform and were not externally heated. A thermocouple in contact with the water-cooled platform and located adjacent to the substrates during sputtering recorded a maximum temperature of 320 °C, resulting in a homologous temperature of $T/T_m = 0.36$. The microstructure produced under these conditions should therefore be Zone T and contain densely packed fibrous grains, as depicted in the Thornton Structural Zone Model.[15] Substrates were allowed to cool under vacuum for a minimum of 2 hours after sputtering. Microstructural analyses of coatings deposited in numerous runs showed that the above parameters resulted in reproducible and high-quality adherent coatings up to 34-μm thick.

B. Sample Preparation and Electron Microscopy

Coated samples were sealed in evacuated quartz tubes and placed in a furnace maintained at 800 °C $\pm$ 4 °C, heat-treated for 2 hours, then quenched in still room-temperature air. Heat-treated wafers were prepared for analysis in cross section by TEM using methods similar to those previously reported.[17,18] Identically sized uncoated α-titanium, glass, or sapphire wafers were used as backing material to make a two-ply sandwich in which the coating lay midway between the wafers. Coated and uncoated wafers were ultrasonically cleaned in acetone, dried on a hot plate, and LOCTITE* Speedbonder 326
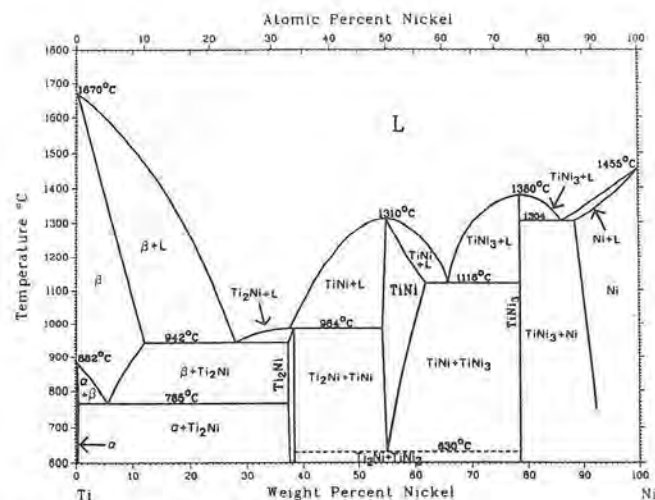
---

*LOCTITE is a trademark of Loctite Corporation, Newington, CT.

Fig. 1—Binary Ti-Ni phase diagram.[4]

brand structural acrylic adhesive was applied to both surfaces. The wafers were placed in a precision vise and inserted into a preheated vacuum oven to cure the adhesive. The sandwich was then attached to a glass microscope slide parallel to the bond line using a cyanoacrylate adhesive and sectioned into 300- to 500-μm thick samples using a low-speed diamond cutoff wheel.

Samples were mounted on flat sapphire windows and ground to a thickness of about 100 μm using SiC or diamond grinding media, then polished to 0.05 μm Al$_2$O$_3$ on one side only to reduce the amount of handling. Titanium rings 3 mm in diameter and about 150-μm thick were attached to the polished side using cyanoacrylate adhesive to provide support for the thinned samples. Samples were removed from the windows, washed in acetone, and dimpled opposite the polished side using a series of alumina slurries to produce a small hole slightly below the coating. Samples were ion milled for 2 to 5 hours at a gun voltage of 5 kV, 10 deg gun angle, 0.75 mA gun current, and 30 to 40 μA specimen current to produce electron transparent areas.

Scanning electron microscopy was performed using an AMR 1000A scanning electron microscope at 20 KeV equipped with an EDAX* energy dispersive spectrometer. Analytical electron microscopy was performed using a PHILIPS** 420T scanning transmission electron

---

---

microscope at 120 KeV equipped with a LaB$_6$ electron gun and EDAX System 9100/60 energy dispersive X-ray spectrometer (Be window). The microscope was operated in TEM mode and aligned prior to each use to ensure reproducible conditions for magnification, diffraction camera length, and energy dispersive microanalysis. Phase compositions were determined by quantitative energy dispersive spectroscopy (EDS) of K_α lines using the EDAX LIST halographic background stripping program and EDAX THIN software package employing the ratio method of analysis.[19] A minimum of 5000 counts, full-scale at a count rate of <2500 counts/s, was used for all energy dispersive spectra analyzed quantitatively. The elements of interest were "windowed" with an integrated intensity equal to 1.2 FWHM, and machine-generated k-values were used. Lattice parameters were determined by averaging the d-spacings of rings and spots from selected area or convergent beam electron diffraction patterns.

III. EXPERIMENTAL RESULTS

A. Scanning Electron Microscopy of Heat-Treated INCONEL 617 Coatings

Examination of polished and etched cross sections by SEM showed the coating was discrete and continuous, with a rapidly etching heat-affected zone about 66-μm thick parallel to the coating (Figure 2(a)). The microstructure of the substrate adjacent to the coating was extremely fine and could not be clearly characterized by SEM (Figure 2(b)). Qualitative analysis of the remaining
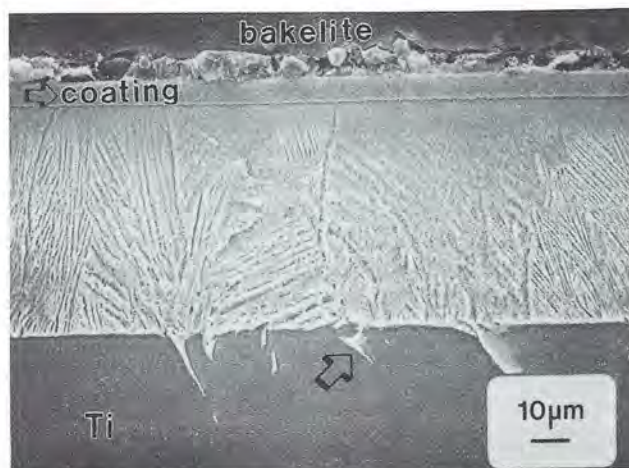
(a)

(b)
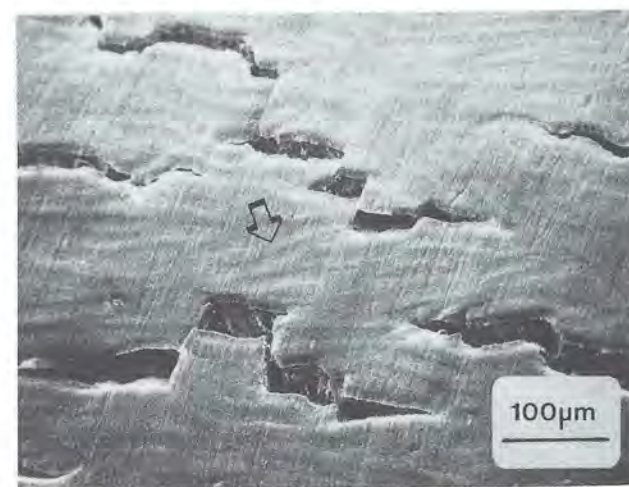
(c)

Fig. 2—(a) SEM micrograph of the INCONEL 617 coating (arrow) and subsurface microstructure after heat treatment at 800 °C for 2 h. Note the penetration of the intermetallic into α-titanium grain boundaries (arrow). (b) Micrograph showing the nondescript region found immediately below the coating (arrows). (c) SEM micrograph of the tortuous fracture morphology of heat-treated INCONEL 617 coatings on α-titanium. Note the ductile deformation and presence of broad wavy slip lines (arrow).

structure indicated the presence of a Widmanstätten α + intermetallic (*e.g.*, Ti$_2$Ni) microstructure (Figure 2(a)). The interface between the rapidly etching region and pure α-titanium was sharp and well defined, as shown in Figure 2(a). However, some α-titanium grain boundaries were penetrated by the intermetallic phase (Figure 2(a)). The microstructure hundreds of microns below the coatings consisted of large equiaxed α-titanium grains 50 to 100 μm in diameter, an increase in grain size of 5 times due to heat treatment, and thickened twins. Coatings were ductile and remained adherent to the substrate after heat treatment, as determined by 180 deg bend tests of coatings applied to 0.5-mm-thick α-titanium sheet (Figure 2(c)).

B. *Transmission Electron Microscopy of Heat-Treated INCONEL 617 Coatings*

Through transmission electron microscopy, the heat-treated coatings and the subsurface microstructure were found to consist of a minimum of eight layers containing over eight different phases (Figure 3). Because of the complex microstructure, ion milling rates were uneven, and numerous samples had to be examined to obtain a complete understanding of the coating and subsurface microstructures. Figure 4 is a schematic diagram showing more clearly the microstructure and phases found and depicts layers 2 through 7 shown in Figure 3.

The near-surface microstructure of the top layer, INCONEL 617 (layer 1), contained equiaxed grains 0.5 to 2 μm in diameter and annealing twins (Figure 5(a)).
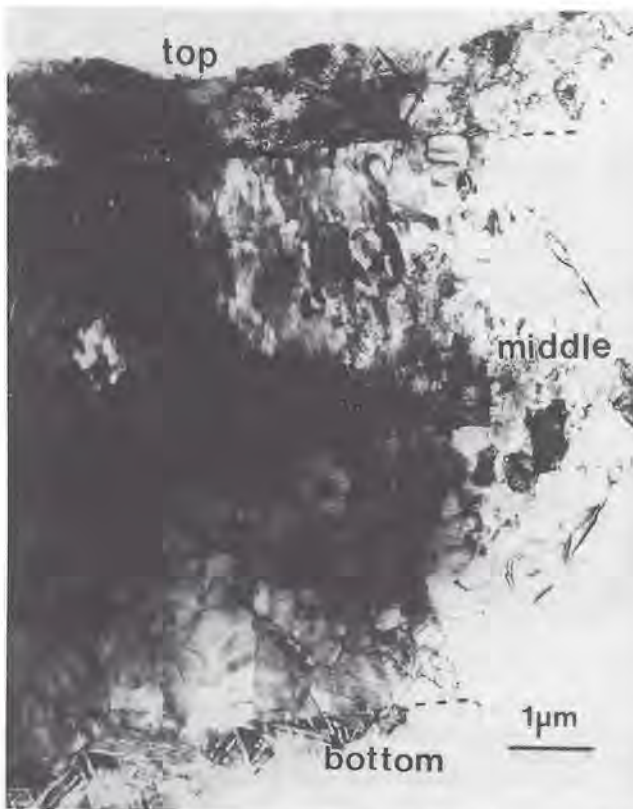
Fig. 3—Cross-sectional TEM micrograph of sputtered INCONEL 617 (top), intermediate phases (middle), and titanium martensite (bottom).
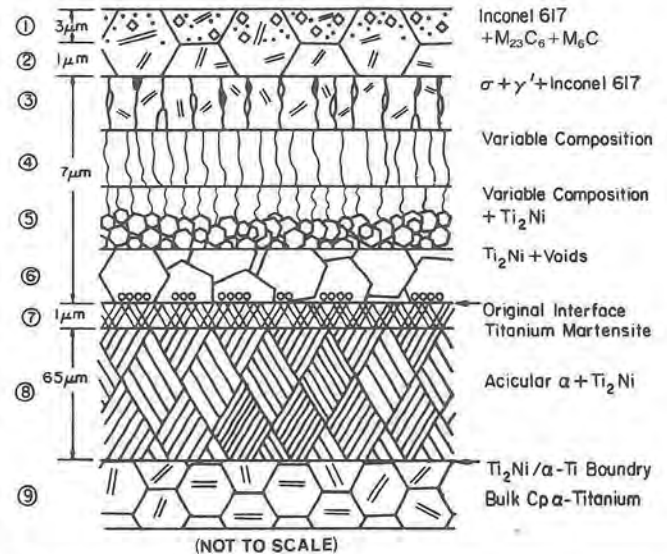
Fig. 4—Schematic diagram showing all phases and layers present in the coating and substrate after heat treatment at 800 °C for 2 h. Layers 2 through 7 are shown in Fig. 3.

The average lattice parameter of the γ phase was 3.67 Å (Figure 5(b)), as opposed to 3.66 Å for as-sputtered INCONEL 617 or 3.62 Å for bulk solution-annealed INCONEL 617.[2,16] The composition of the γ phase was 54.5 pct Ni, 25.4 pct Cr, 12.8 pct Co, and 7.3 pct Mo, with small amounts of Al, Si, Ti, and Fe (Figure 5(c)), and is in agreement with compositions found in other studies.[1,2,16] In addition, two phases were found near the free surface of heat-treated INCONEL 617 coatings. These precipitates were identified as M$_{23}$C$_6$ (M = Cr, Mo) with an average lattice parameter of 10.80 Å, and M$_2$M$_3'$SiC (*i.e.*, M$_6$C, eta carbide, where M = Ni + Co, M' = Mo + Cr) with an average lattice parameter of 11.14 Å (Figure 5(a)). A more complete discussion of the microstructure and phase stability of sputtered INCONEL 617 coatings will be presented in a separate publication.[20] The microstructure of INCONEL 617 immediately below layer 1 contained equiaxed γ grains but no M$_{23}$C$_6$ or M$_6$C precipitates. The composition of the coating in this region contained increased amounts of titanium and silicon, as shown in Figure 5(d).

A well-defined phase 1.75-μm thick was found below the coating (layer 3) and contained both globular and twinned columnar morphologies (Figure 6(a)). The composition of the columnar phase was approximately 48 pct Cr, 34 pct Ni and Co, 14 pct Mo, with a few percent Ti, Fe, and Si (Figure 6(b)). This phase was identified as sigma (σ), with tetragonal crystal structure (Figure 6(c)) and lattice parameters of approximately $a = 9.12$ Å and $c = 4.56$ Å.[21] Included within the σ phase (layer 3) was a globular fcc phase similar in composition to INCONEL 617 and a platelike nickel-titanium-aluminum phase (Figure 6(d)). The latter contained approximately 80 pct Ni, 14.5 pct Ti, and 5.5 pct Al (Figure 6(e)) with fcc crystal structure and an average lattice parameter of 3.66 Å (Figure 6(f)). This phase was therefore identified as fcc γ', Ni$_3$(Ti, Al).[21] The morphology of γ' is normally spherical or cubic when the γ/γ' mismatch is small
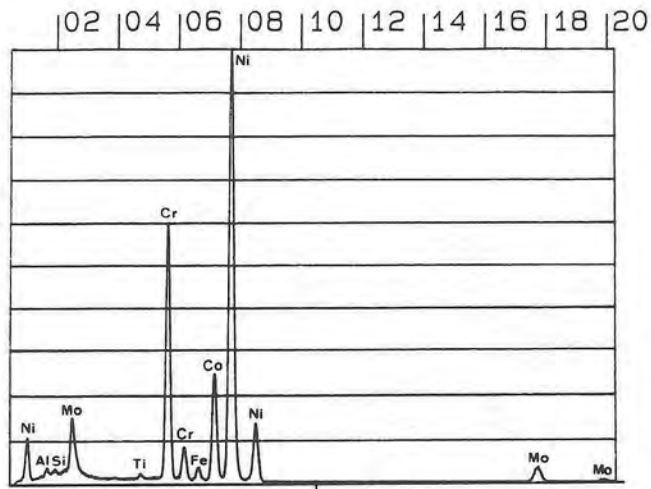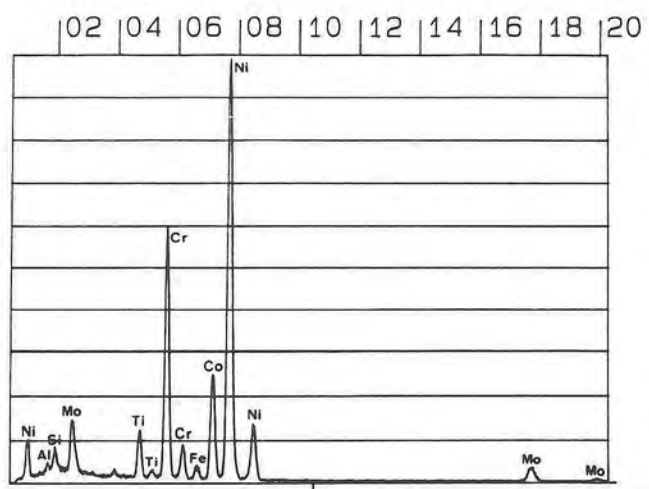
(a)
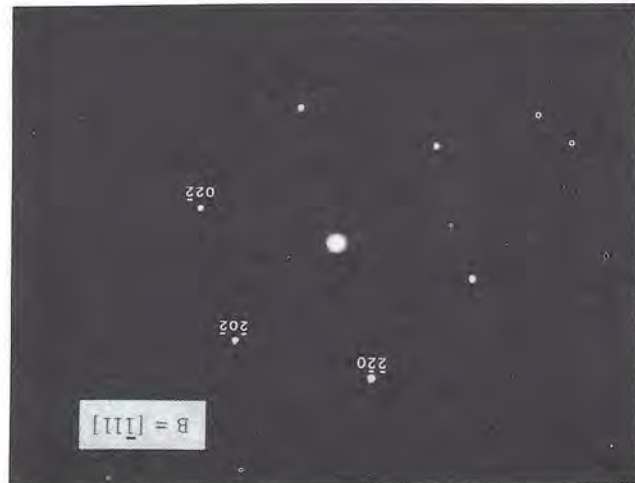
(b)

```
17-AUG-87 01:24:15
RATE:          CPS TIME      361LSEC
00-20KEV: 10EV/CH PRST:          OFF
A: T6P1 800/2 MTXB:
FS=  20071  MEM:   A    FS=  20071
 |02 |04 |06 |08 |10 |12 |14 |16 |18 |20
```

(c)

```
28-OCT-87 16:17:25
RATE:          CPS TIME      221LSEC
00-20KEV: 10EV/CH PRST:          OFF
A: PHASE:  1 - 617B:
FS=   5091  MEM:   A    FS=      200
 |02 |04 |06 |08 |10 |12 |14 |16 |18 |20
```

(d)

CURSOR (KEV) =10.240   EDAX

CURSOR (KEV) =10.240   EDAX

Fig. 5—(a) SEM micrograph of the near-surface microstructure of the INCONEL 617 coating showing twins and carbides. (b) 1-μm selected area diffraction pattern of the γ phase. (c) EDAX spectrum of the γ phase in a region free of precipitates near the free surface. (d) EDAX spectrum of the γ phase near the interface with σ phase (layer 3). Note the increased concentration of titanium and silicon in the coating.

($\sim$0.05 pct) and platelike when the mismatch is large (>1.25 pct).[22] In this study, the parent phase was σ, so the large lattice mismatch resulted in a platelike morphology.

Below the layer containing σ phase, a region about 1.75-μm thick with varying Cr, Ti, Ni, and Mo compositions was found (layer 4). Energy dispersive spectroscopy showed it contained primarily Cr (39.3 pct), Ni (25 pct), Ti (24 pct), and Mo (11.7 pct), with lesser amounts of Al, Si, Fe, and Co (Figure 7(a)). In other grains, however, the principal constituents were only Cr,

Ti, and Mo (Figure 7(b)). Due to the difference in composition from grain to grain, this region is apparently a nonequilibrium microstructure and therefore termed a layer of "variable composition" (Figure 4).

The next layer is about 1.25-μm thick and contained both an equiaxed titanium-nickel phase and columnar grains (layer 5, Figures 3 and 4). The columnar grains had a variable composition similar to that found in layer 4, while the equiaxed phase contained 63 pct Ti, 33.8 pct Ni, and 3.2 pct Cr, with small amounts (<1 pct each) of Si, Mo, Fe, and Co (Figure 8(a)). The layer beneath

(a)

28-OCT-87 16: 28: 10
RATE: CPS TIME   110LSEC
00-20KEV: 10EV/CH PRST: OFF
A: PHASE: 2   B:
FS=   5230   MEM: A   FS=   200
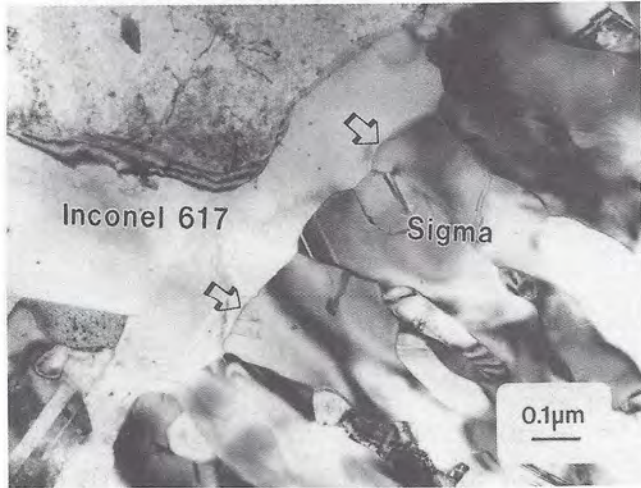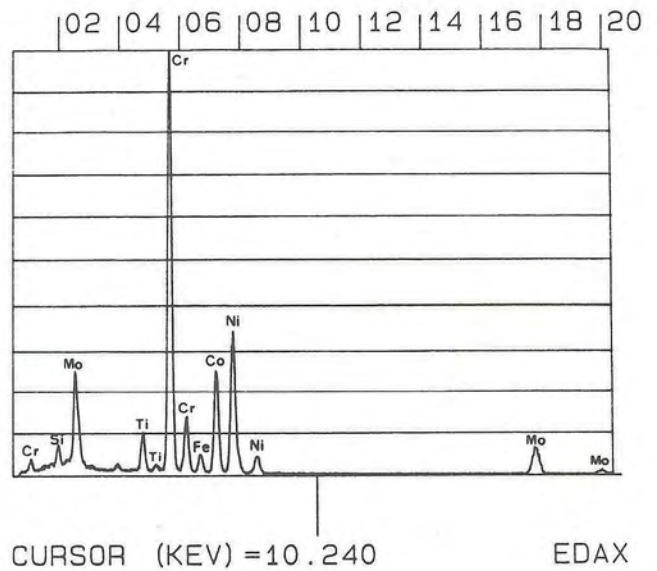
(b)


(c)
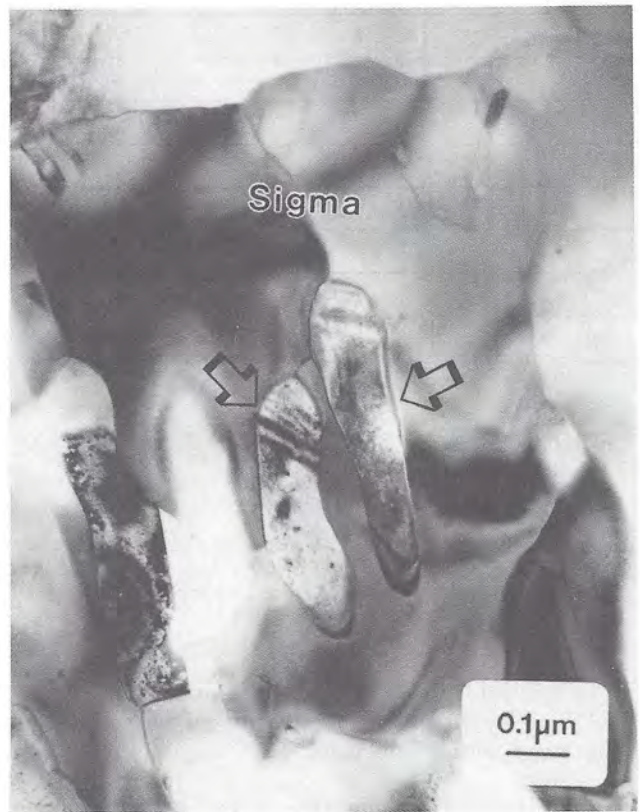
(d)

Fig. 6—(a) TEM micrograph of INCONEL 617 and σ. Note the sharp interface (arrows). (b) EDAX spectrum of the σ phase. (c) Convergent beam electron diffraction pattern of tetragonal σ phase. (d) TEM micrograph of γ' embedded in the σ phase (arrows). (e) EDAX spectrum γ'. (f) Fcc [011] convergent beam electron diffraction pattern of γ'.

28-OCT-87 16: 45: 57
RATE: CPS   TIME   1LSEC
00-20KEV: 10EV/CH PRST: OFF
A: PHASE: 3   B:
FS=   5152   MEM: A   FS=   200

|02 |04 |06 |08 |10 |12 |14 |16 |18 |20

CURSOR (KEV) =10.240   EDAX

(e)

B = [011]
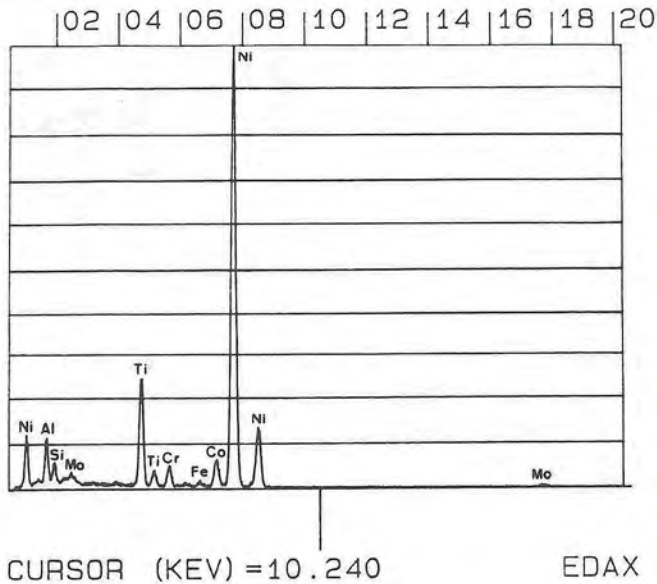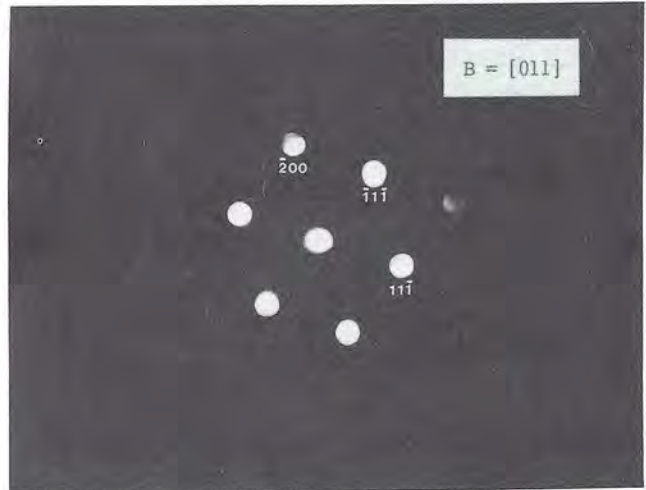
(f)

Fig. 6 Cont. —(a) TEM micrograph of INCONEL 617 and σ. Note the sharp interface (arrows). (b) EDAX spectrum of the σ phase. (c) Convergent beam electron diffraction pattern of tetragonal σ phase. (d) TEM micrograph of γ′ embedded in the σ phase (arrows). (e) EDAX spectrum γ′. (f) Fcc [011] convergent beam electron diffraction pattern of γ′.

28-OCT-87 17: 07: 23
RATE: CPS   TIME   226LSEC
00-20KEV: 10EV/CH PRST: OFF
A: PHASE: 5   B:
FS=   5135   MEM: A   FS=   200

|02 |04 |06 |08 |10 |12 |14 |16 |18 |20

CURSOR (KEV) =10.240   EDAX
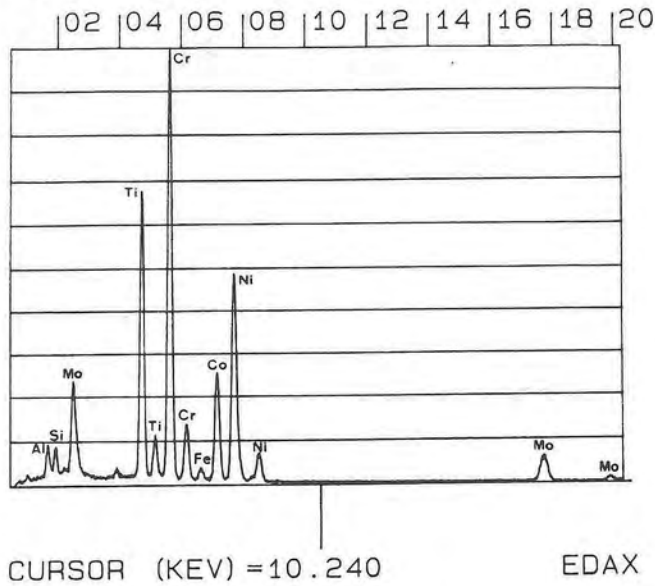
(a)

29-OCT-87 07: 55: 57
RATE: CPS   TIME   129LSEC
00-20KEV: 10EV/CH PRST: OFF
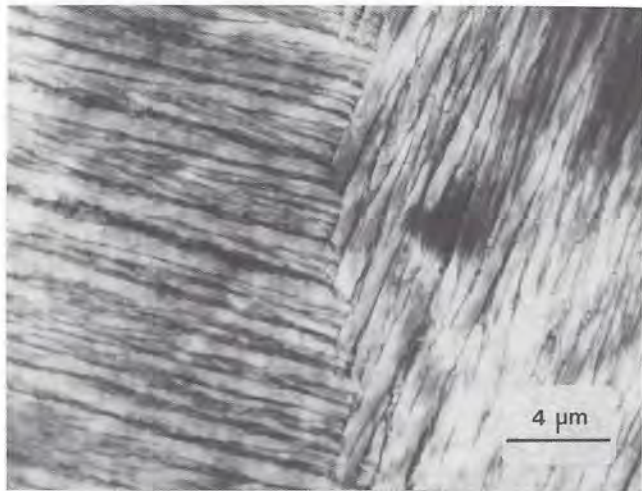A: PHASE: 6   B:
FS=   5135   MEM: A   FS=   200

|02 |04 |06 |08 |10 |12 |14 |16 |18 |20

CURSOR (KEV) =10.240   EDAX
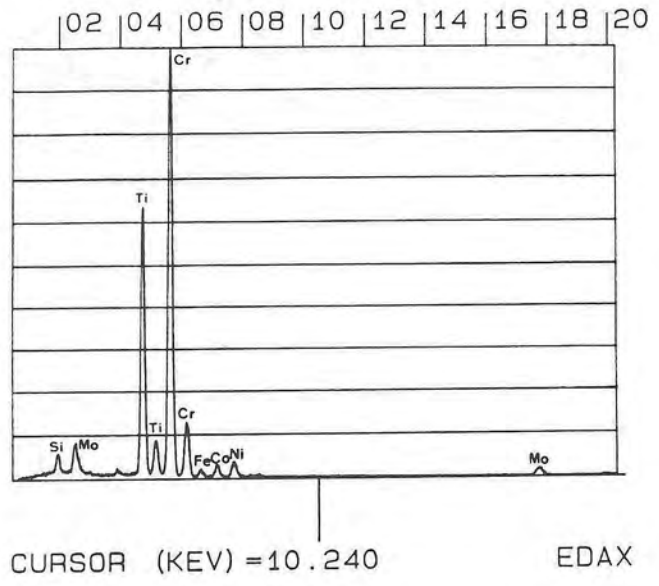
(b)

Fig. 7—(a) and (b) EDAX spectra of the region containing grains of variable composition.

29-OCT-87 08: 06: 37
RATE: CPS TIME   139LSEC
00-20KEV: 10EV/CH PRST: OFF
A: PHASE: 7   B:
FS=   5182   MEM: A   FS=   200

|02 |04 |06 |08 |10 |12 |14 |16 |18 |20
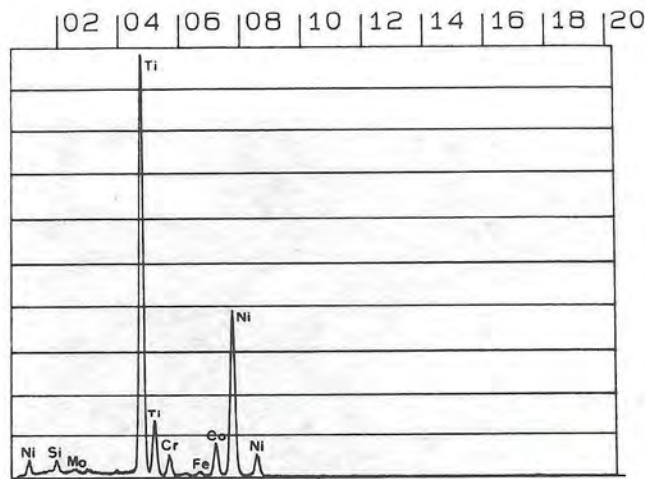
CURSOR (KEV) =10.240   EDAX

(a)
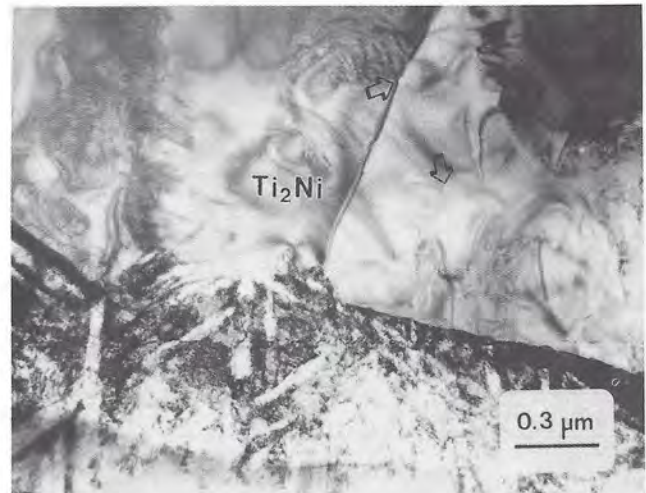
(b)
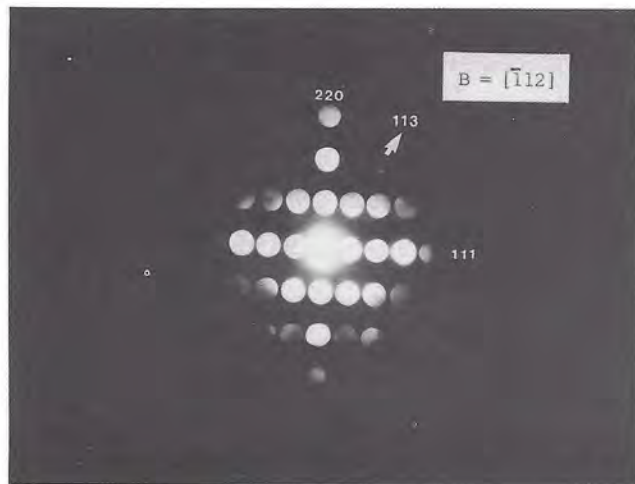
(c)
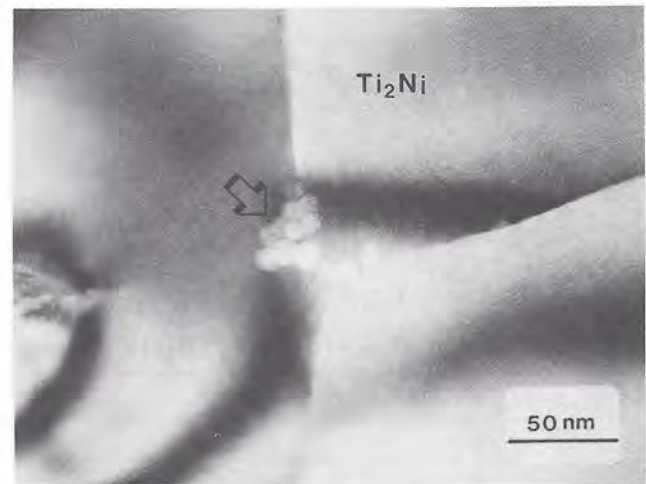
(d)

Fig. 8 — (a) EDAX spectrum of the Ti₂Ni phase. (b) TEM micrograph showing Ti₂Ni and titanium martensite below it. Kirkendall voids are arrowed. (c) Fcc [$\bar{1}$12] electron diffraction pattern of Ti₂Ni. (d) TEM micrograph of Kirkendall voids at a triple point in Ti₂Ni (arrow).

this (layer 6) was about 2.25-μm thick and contained larger equiaxed grains (Figures 4 and 8(b)) and had the same energy dispersive X-ray spectrum as the equiaxed grains in layer 4 (Figure 8(a)). Convergent beam electron diffraction showed that the crystal structure was fcc, with an average lattice parameter of 11.70 Å (Figure 8(c)), and was therefore identified as Ti₂Ni.[23] Kirkendall voids 75 to 300 Å in diameter were found in Ti₂Ni grains near the original INCONEL 617/α-titanium interface due to more rapid diffusion of INCONEL 617 into the α-titanium

substrate (Figure 8(d)). A layer of rutile (TiO₂) about 60-Å thick was found between as-sputtered INCONEL 617 coatings and the α-titanium substrate[24] but is no longer present due to reduction of the oxide by titanium atoms during heat treatment (Figure 8(b)).

The microstructures found thus far (layers 1 through 6) exist only in the INCONEL 617 coating. The region below the equiaxed Ti₂Ni region (layer 6) was also investigated and found to consist of three distinct layers (layers 7 through 9). The layer nearest to the original

(a)

29-OCT-87 08: 18: 53
RATE: CPS TIME   74LSEC
00-20KEV: 10EV/CH PRST: OFF
A: PHASE: 8   B:
FS=   5278   MEM: A   FS=   200
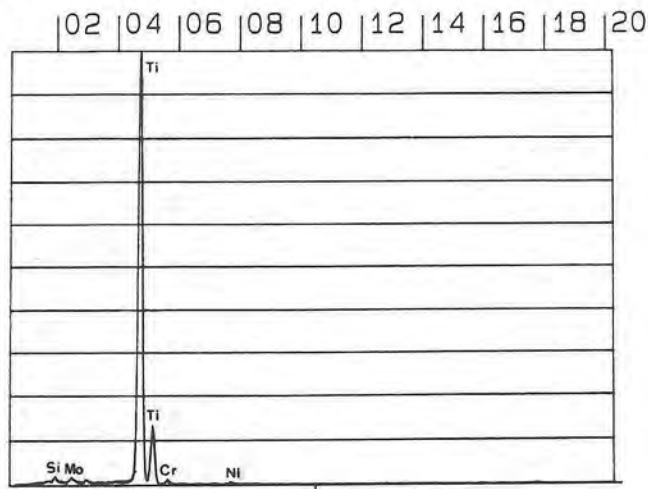
CURSOR (KEV) =10.240   EDAX

(b)

29-OCT-87 08: 31: 01
RATE: CPS TIME   107LSEC
00-20KEV: 10EV/CH PRST: OFF
A: PHASE: 9   B:
FS=   5138   MEM: A   FS=   200
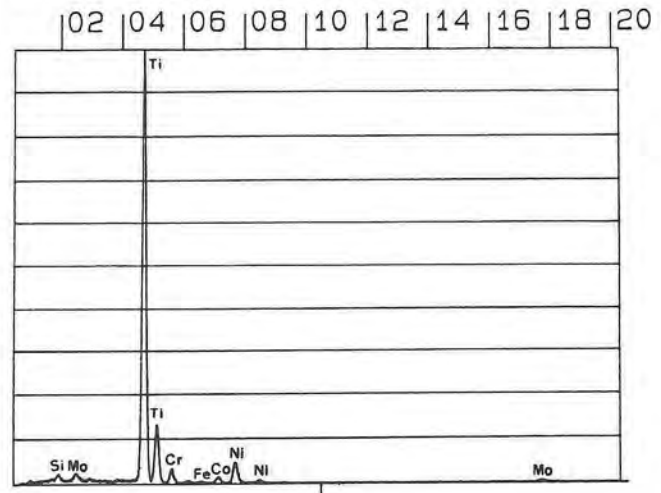
CURSOR (KEV) =10.240   EDAX

(c)

Fig. 9—(a) TEM micrograph of titanium martensite adjacent to Ti₂Ni. (b) EDAX spectrum of α-titanium platelets. (c) EDAX spectrum of the β phase in titanium martensite. Note the presence of nickel and chromium.

interface (layer 7, Figure 9(a)) was about 1-μm thick and contained almost pure α-titanium platelets (Figure 9(b)) in a bcc β-titanium matrix (Figure 9(c)). This phase was thus identified as titanium martensite which formed as a result of nonequilibrium cooling after heat treatment.[12]

The microstructure below layer 7 was identified as α + intermetallic distributed in a Widmanstätten morphology (Figure 2(b)) with an interlamellar spacing of 0.3 to 0.5 μm (layer 8, Figures 10(a) and (b)). Energy dispersive spectroscopy (Figure 10(c)) and convergent beam

electron diffraction (Figure 10(d)) show that interlamellar regions consist of pure α-titanium. Electron diffraction and EDS showed the intermetallic phase had similar chemical composition and the same crystal structure as Ti₂Ni found in layer 6. The morphology of Ti₂Ni in layer 8 contains a high density of stacking faults (Figure 10(e)) and differs in morphology from that reported in the literature.[11] Figure 10(f) shows the sharp planar interface between layer 8 and the pure α-titanium substrate (layer 9). The microstructure below layer 8 was
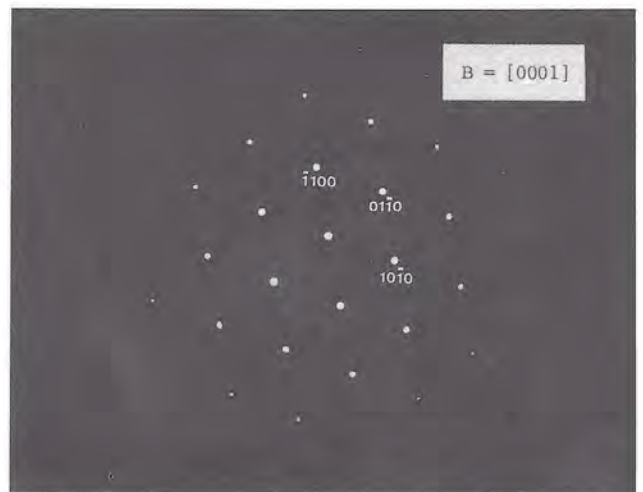
(a)
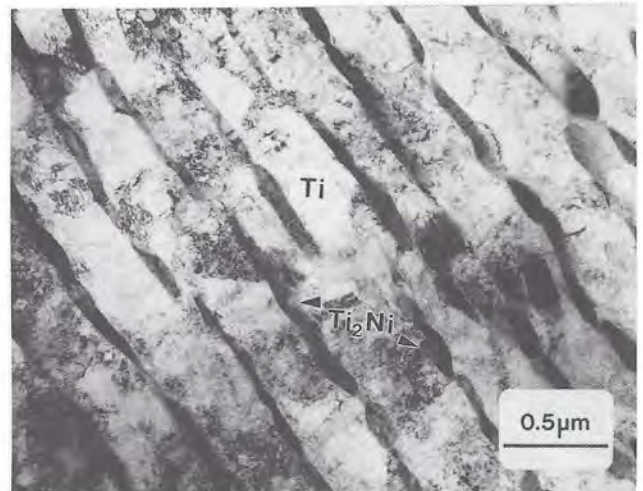
(b)

29-OCT-87 10: 18: 34
RATE: CPS TIME   118LSEC
00-20KEV: 10EV/CH PRST: OFF
A: PHASE: 11-CPTI B:
FS=   5137   MEM: A   FS=   5278

|02 |04 |06 |08 |10 |12 |14 |16 |18 |20

CURSOR (KEV) =10.240   EDAX

(c)

B = [0001]
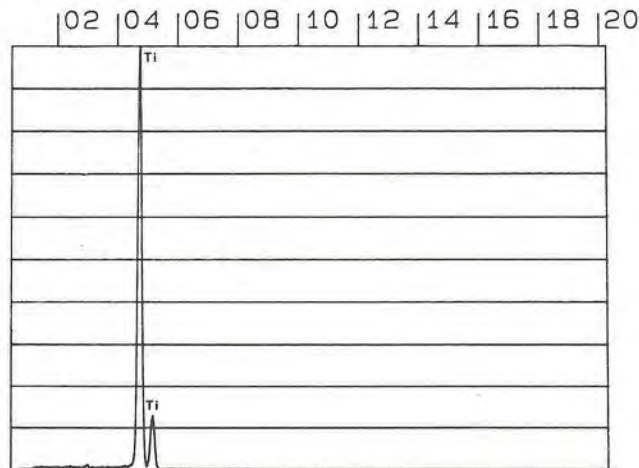
(d)

Fig. 10—(a) TEM micrograph of the Widmanstätten microstructure below titanium martensite. (b) TEM micrograph of lamellar α + Ti$_2$Ni (arrows). (c) EDAX spectrum of titanium lamellae in the Widmanstätten microstructure. (d) Hcp [0001] electron diffraction pattern of interlamellar α-titanium. (e) TEM micrograph of lamellar Ti$_2$Ni with a high density of stacking faults (arrow). (f) TEM micrograph showing the sharp interface between Ti$_2$Ni (arrows) and α-titanium.

equiaxed α-titanium grains with thickened twins, as shown in Figure 2(a)).

IV. DISCUSSION

A. Microstructure and Phase Stability

Heat-treated coatings were found to be highly adherent to α-titanium substrates, even after samples were bent 180 deg. Ductile deformation of the coating was evident due to the presence of slip lines (Figure 2(c)). Exami-

nation of polished and etched cross sections by SEM revealed that the INCONEL 617 coating was discrete and continuous (Figure 2(a)). The thick layer of Widmanstätten α + intermetallic microstructure formed below it is indicative of a considerable amount of diffusion for 2 hours' heat treatment. Only three phases, α, γ, and Ti$_2$Ni, could be identified by analytical SEM, albeit not completely unambiguously. It is worthwhile noting that the remaining phases were not resolvable by SEM but are, in fact, present and on a scale much finer than that normally investigated in studies of coating/substrate interactions at elevated temperatures.[13,25–27]
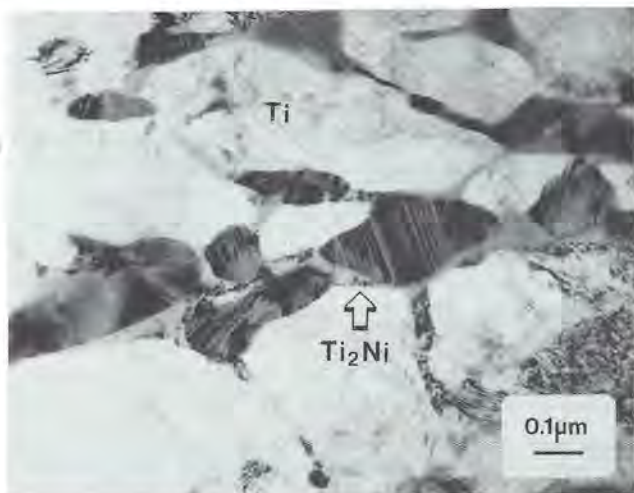
(e)
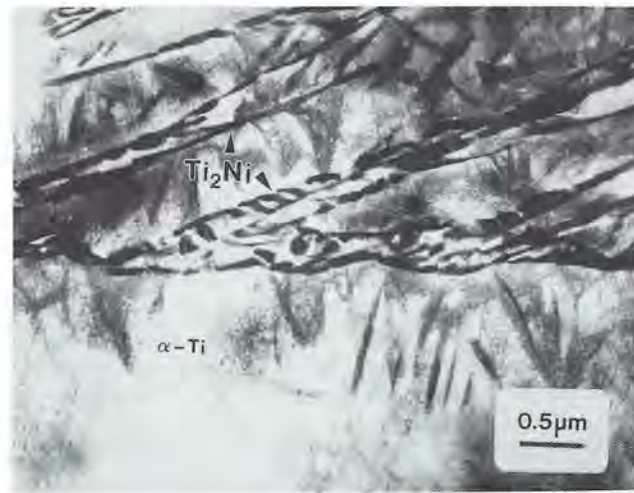
(f)

Fig. 10 Cont. — (a) TEM micrograph of the Widmanstätten microstructure below titanium martensite. (b) TEM micrograph of lamellar α + Ti$_2$Ni (arrows). (c) EDAX spectrum of titanium lamellae in the Widmanstätten microstructure. (d) Hcp [0001] electron diffraction pattern of interlamellar α-titanium. (e) TEM micrograph of lamellar Ti$_2$Ni with a high density of stacking faults (arrow). (f) TEM micrograph showing the sharp interface between Ti$_2$Ni (arrows) and α-titanium.

Transmission electron microscopy revealed the presence of additional phases within both the coating and the substrate. They include $M_{23}C_6$, M_6C, σ, β, and γ', which were present in a wide variety of morphologies. Energy dispersive spectroscopy showed that there was diffusion of all principal alloying elements in INCONEL 617 into the α-titanium substrate at 800 °C. Since diffusion was most pronounced between nickel and titanium, in terms of solute concentration away from the interface, INCONEL 617 coatings applied to α-titanium substrates can be modeled as a pseudobinary Ti-Ni diffusion couple. The phase diagram in Figure 1 shows that a Ti-Ni diffusion couple heated to >630 °C and rapidly quenched to retain the high-temperature equilibrium structure should contain three intermetallic phases: a nickel-rich phase near the nickel coating (i.e., TiNi$_3$), a titanium-rich phase near the titanium substrate (i.e., Ti$_2$Ni), and an equiatomic intermetallic between the two (i.e., TiNi). In the present study, however, neither TiNi$_3$ nor TiNi was found.

The absence of certain phases in diffusion couples is common. The use of equilibrium phase diagrams for predicting the phases present in studies of diffusion between thin film layered structures in microelectronic devices and in titanium-SiC fiber composites has been unsuccessful.[28-34] Heat treatment of nickel-silicon thin films at 500 °C and 750 °C results in the formation of a series of nickel silicides.[29] However, the product phases formed depend upon the mobility of Ni, which is a function of heat-treatment temperature. Studies of interdiffusion in Ni-Al couples have shown that at 600 °C, aluminum determines the reaction products (i.e., NiAl$_3$ and Ni$_2$Al$_3$), while at higher temperatures, the increased diffusivity of nickel determines product phases (i.e., NiAl, Ni$_2$Al$_3$, and Ni$_3$Al).[28,30] A TEM study of Ti-6Al-4V-2Ni containing 10.5 vol pct continuous SiC fibers (SCS-6) and pressed at 817 °C and 871 °C for about 4 hours contained only one silicide phase.[31] Submicron-sized Ti$_5$Si$_3$ was present as a layer of precipitates adjacent to the titanium matrix and as smaller crystallites mixed with TiC adjacent to the SiC fiber.

These observations have been attributed to both thermodynamic and kinetic considerations.[32,33] In thermodynamic treatments, the phase sequence can be determined by calculating an effective heat of formation ($\Delta H'$) based upon the concentration of reacting species.[32] This method has been shown to be useful for predicting the phase sequence in numerous transition metal silicides. The heat of formation alone, however, has been cited as insufficient to determine the product phases formed, especially in the presence of impurities.[33] Instead, kinetic considerations provide more rigorous explanation of observed effects.[33,34] Reactions between Co and Si can result in the formation of silicides with free energy higher than equiatomic intermetallic, depending upon the structure of the diffusion couple.[33]

The present investigation supports the finding that compound formation cannot be readily deduced from equilibrium phase diagrams.[34] Thus, partitioning of diffusive species may result in missing or reduced quantities of phases depending upon temperature, local composition, local diffusivities, stress, impurities, and heat-treatment time.[28,32-34] The microstructure and stability of phases found in the present study are further complicated by the alloy system investigated, in which diffusion occurs simultaneously among at least 11 elemental components in an environment containing a variety of metals, carbides, and intermetallic phases.

A previous study of interfacial reactions between electroplated nickel coatings and α + β titanium alloys heat-treated at 593 °C, 650 °C, and 705 °C did not find any Ti$_2$Ni adjacent to the substrate,[13] even though the latter two temperatures were above the TiNi → Ti$_2$Ni + TiNi$_3$ eutectoid reaction (Figure 1). However, Ti$_2$Ni was found in samples heat-treated at or above 760 °C, although no direct evidence was presented, and no explanation was given for its absence in samples heat-treated

at lower temperatures. Ti$_2$Ni may have been missing after heat treatment below 760 °C due to partitioning caused by alloy composition, local solute concentration, or other effects. It is possible, however, that Ti$_2$Ni was present in samples heat-treated at 650 °C and 705 °C but could not be detected due to the poor spatial resolution of the techniques employed compared to that obtainable by analytical TEM. Further, Ti$_2$Ni may have been discontinuous due to the presence of β at the grain boundaries.[13]

Unlike the present study, no evidence of β-eutectoid decomposition ($\beta \rightarrow \alpha + $ Ti$_2$Ni) was found below the coating/substrate interface.[13] The Widmanstätten microstructure shown in Figure 2(a) indicates that the cooling rate of air-quenched samples was similar to some of the slower cooling rates employed in a study of rapidly solidified Ti-Ni alloys.[12] Kirkendall voids were reported in samples after extended heat treatment at 650 °C, indicative of the temperature at which diffusion of nickel begins to dominate the product phases formed. Voids were cited as the cause of cracks in the TiNi$_3$/NiTi interface, causing spallation of the nickel plate plus TiNi$_3$ layer. While Kirkendall voids were found in the present study, they were small and mostly unconnected and not found to affect adhesion (Figures 2(a) and (c) and 8(b)).

B. Interdiffusion between INCONEL 617 and α-Titanium

Direct imaging of phase boundaries by TEM, coupled with quantitative EDS, permits calculation of the diffusivities of various elements. The reactions found between titanium and nickel are of interest in the present study due to the large body of literature available on the physical and mechanical metallurgy of Ti-Ni alloys[5-12] and its effect on the properties of candidate coating-substrate systems.[13]

A study of diffusion in the binary Ti-Ni system performed by joining nickel-5 pct titanium alloy diffusion couples and heat treating at 1100 °C to 1300 °C showed that diffusion obeyed an exponential dependence:[35]

$$D_{\text{Ti-Ni}} = 0.86 \exp \left(-61{,}400/RT \right) \qquad [1]$$

where R is the gas constant (J/mole K) and T is the temperature (K). The self-diffusion of nickel is

$$D_{\text{Ni}} = 1.27 \exp \left(-66{,}800/RT \right) \qquad [2]$$

Both equations have similar pre-exponential factors and activation energies. For the heat treatment temperature used in the present study, $T = 1073$ K and $D_{\text{Ti-Ni}} \approx 8.8 \times 10^{-4}$ cm^2/s. Ti-Ni alloys containing 2 to 21 pct titanium and heat-treated at 930 °C to 1200 °C generally showed an increase in activation energy with solute content.[36] Large increases in activation energy were attributed to the formation of Ti-Ni compounds (i.e., TiNi$_3$), which retarded the diffusion rate of titanium in nickel.

Quantitative EDS of heat-treated samples in cross section showed that titanium from the substrate diffused at a rate of about 4 μm per hour into the INCONEL 617 coating (Figure 5(d)). The concentration 8 μm from the original interface was about 5 pct titanium. The diffusivity of a Ti-INCONEL 617 system was determined using Grube's solution[37] to qualitatively assess the observed results assuming a binary Ti-Ni system. The diffusivity

of titanium in INCONEL 617 coatings was calculated to be $D_{\text{Ti-Ni}} \approx 1.21 \times 10^{-11}$ cm^2/s, which is seven orders of magnitude less than that determined in a previous study.[35]

The diffusivity of nickel into α-titanium has been shown to be rapid, about $D_{\text{Ni-Ti}} = 5 \times 10^{-8}$ cm^2/s at 800 °C, resulting in diffusion across 60 μm after 15 minutes of solution heat treatment.[38] In the present study, the diffusion rate of nickel in titanium was approximately 8 times greater than that of titanium into nickel, resulting in a diffusion rate of about 33 μm per hour into the substrate (Figure 2(a)). For a system containing Ti-52 pct nickel, $D_{\text{Ni-Ti}} \approx 1.5 \times 10^{-9}$ cm^2/s and is one order of magnitude lower than that found in Ni-Ti diffusion couples heat-treated at 786 °C to 868 °C.[38] This value of $D_{\text{Ni-Ti}}$ corresponds to an activation energy of about 180 kJ/mole, which is about 3 times greater than that given in Eq. [1] but is in reasonable agreement with another study.[36]

The decrease in diffusivity of titanium and nickel is attributed primarily to the formation of various intermetallic phases between the coating and substrate (Figure 4, layers 3 through 8) and lower heat-treatment temperatures. While the calculated diffusivities are certainly affected by the presence of numerous other alloying elements, they are in general agreement with previous results. It is also apparent that multicomponent diffusion is a complicated process which is markedly affected by factors such as temperature, local composition, local diffusivities, and heat-treatment time. The phases resulting from heat treatment, therefore, could not be easily predicted.

V. SUMMARY

INCONEL 617 coatings 10- to 13-μm thick were RF magnetron sputtered in argon onto commercially pure α-titanium substrates and heat-treated at 800 °C for 2 hours. Coatings were both ductile and adherent, as demonstrated by bend tests. Transmission electron microscopy showed that several micron-thick layers had formed within the coating and contained such intermetallic phases as σ, γ', and Ti$_2$Ni. Kirkendall voids 75 to 300 Å in diameter were present near the original INCONEL 617/α-titanium interface but did not affect coating adhesion. The microstructure below the interface contained titanium martensite and $\alpha + $ Ti$_2$Ni distributed in a Widmanstätten morphology. Kinetic factors were determined to be responsible for the observed phases. Calculations based upon a model Ti-Ni system showed that the diffusivity of both nickel and titanium was reduced several orders of magnitude due primarily to the formation of intermetallic compounds.

REFERENCES

1. *Inconel Alloy 617*, Huntington Alloys, Inc., Huntington, WV, 1979, pp. 1-6.
2. M. Emiliani, M. Richman, and R. Brown: Brown University, Providence, RI, unpublished research, 1987.
3. W.L. Mankins, J.C. Hosier, and T.H. Bassford: *Metall. Trans.*, 1974, vol. 5, pp. 2579-90.
4. *Binary Alloy Phase Diagrams*, T.B. Massalski, ed., ASM, Metals Park, OH, 1986, vol. 2, p. 1768.
5. S.M.L. Sastry, T.C. Peng, P.J. Meschter, and J.E. O'Neal: *J. Met.*, 1983, vol. 35 (9), pp. 21-28.
6. M. Nishida, C.M. Wayman, and T. Honma: *Metall. Trans. A*, 1986, vol. 17A, pp. 1505-15.
7. R. Kainuma and M. Matsumoto: *Scripta Metall.*, 1988, vol. 22, pp. 475-78.
8. K.M. Knowles and D.A. Smith: *Acta Metall.*, 1981, vol. 29, pp. 101-10.
9. M. Marcinkowski, A.S. Sastri, and D. Koskimaki: *Phil. Mag.*, 1968, vol. 18, pp. 945-58.
10. M. Nishida and C.M. Wayman: *Mater. Sci. Eng.*, 1987, vol. 93, pp. 191-203.
11. S.P. Gupta, K. Mukherjee, and A.A. Johnson: *Mater. Sci. Eng.*, 1973, vol. 11, pp. 283-97.
12. S. Krishnamurthy, A.G. Jackson, H. Jones, and F.H. Froes: *Metall. Trans. A*, 1988, vol. 19A, pp. 23-33.
13. J.K. Tien, J.C. Chesnutt, D.H. Boone, and G.W. Goward: *Titanium Science and Technology*, R.I. Jaffee and H.M. Burte, eds., Plenum Press, New York, NY, 1973, vol. 4, pp. 2517-25.
14. Mario L. Emiliani: Ph.D. Thesis, Brown University, Providence, RI, 1988.
15. J.A. Thornton: *Annu. Rev. Mater. Sci.*, Annual Reviews, Inc., Palo Alto, CA, 1977, vol. 7, pp. 239-60.
16. M. Emiliani, M. Richman, and R. Brown: *J. Mater. Sci.*, in press.
17. J.C. Bravman and S.C. Sinclair: *J. Electron Microsc. Tech.*, 1984, vol. 1, pp. 53-61.
18. A.K. Rai, M.H. Rashid, P.P. Pronko, A. Ezis, and D.W. Langer: *J. Electron Microsc. Tech.*, 1987, vol. 5, pp. 45-50.
19. *EDAX PV9100/60 Quantitative Thin Section User's Manual, Version 2.3*, EDAX International, Inc., Prairie View, IL, 1983.
20. M. Emiliani, M. Richman, and R. Brown: Brown University, Providence, RI, unpublished research, 1987.
21. *Convergent Beam Electron Diffraction of Alloy Phases*, J. Mansfield, ed., Adam Hilger Ltd., Bristol, U.K., 1984.
22. *Metals Handbook*, 9th ed., ASM, Metals Park, OH, 1985, vol. 9, pp. 305-13.
23. D. Koskimaki, M.J. Marcinkowski, and A.S. Sastri: *Trans. TMS-AIME*, 1969, vol. 245, pp. 1883-90.
24. M. Emiliani, M. Richman, and R. Brown: *J. Mater. Sci.*, in press.
25. R. Mévrel, C. Duret, and R. Pichoir: *Mater. Sci. Technol.*, 1986, vol. 2, pp. 201-06.
26. R. Bürgel: *Mater. Sci. Technol.*, 1986, vol. 2, pp. 302-08.
27. I.M. de J. Estrada-Plata and C.W. Haworth: *Mater. Sci. Eng.*, 1986, vol. 2, pp. 322-23.
28. S.R. Shatynski, J.P. Hirth, and R.A. Rapp: *Acta Metall.*, 1976, vol. 24, pp. 1071-78.
29. S.H. Chen, L.R. Zheng, C.B. Carter, and J.W. Mayer: *J. Appl. Phys.*, 1985, vol. 57, pp. 258-63.
30. M.M.P. Janssen and G.K. Rieck: *Trans. TMS-AIME*, 1967, vol. 239, pp. 1372-85.
31. C.G. Rhodes, A.K. Ghosh, and R.A. Spurling: *Metall. Trans. A*, 1987, vol. 18A, pp. 2151-56.
32. R. Pretorius: in *Thin Films and Interfaces II*, J.E.E. Baglin, D.R. Campbell and W.K. Chu, eds., Elsevier Science Publishers, New York, NY, 1984, pp. 15-20.
33. G. Ottaviani: in *Thin Films and Interfaces II*, J.E.E. Baglin, D.R. Campbell and W.K. Chu, eds., Elsevier Science Publishers, New York, NY, 1984, pp. 21-31.
34. M. Ruhle and A.G. Evans: *Mater. Sci. Eng.*, 1989, vol. A107, pp. 187-97.
35. P. Swalin and A. Martin: *J. Met.*, 1956, vol. 206, pp. 567-72.
36. A.Y. Shinyaev: *Phys. Met. Metallogr.*, 1966, vol. 5, pp. 76-80.
37. P.G. Shewmon: *Diffusion in Solids*, J. Williams Book Co., Jenks, OK, 1983, pp. 1-37.
38. G.M. Hood and R.J. Schultz: *Phil. Mag.*, 1972, vol. 26, pp. 329-36.

Characterization of sputtered Inconel 617

Part 1 *Coatings in plan section*

MARIO EMILIANI
Pratt and Whitney, P.O. Box 109600, MS 707-28, West Palm Beach, Florida 33410, USA

MARC RICHMAN
Division of Engineering, Brown University, Box D, Providence, Rhode Island 02912, USA

RICHARD BROWN
Department of Chemical Engineering, University of Rhode Island, Kingston, Rhode Island 02881, USA

Inconel 617 coatings 10 to 13 μm thick were r.f. magnetron sputtered on to commercially pure α-titanium substrates without external bias or heat and examined in the as-deposited condition by scanning electron microscopy (SEM), analytical transmission electron microscopy (TEM) and X-ray diffraction (XRD). The surface finish of coatings was smooth with few nodular growth defects, while bend tests showed the coatings failed in a ductile manner. TEM showed that Inconel 617 coatings consisted of an fcc solid solution with an average lattice parameter of 0.366 nm. The through-thickness microstructure contained equiaxed grains with an average diameter of 50 nm, while XRD showed the coatings had a (1 1 1) orientation with respect to the substrate. Coatings contained a large amount of interfacial area, and had an average Knoop microhardness of 503 kg mm^{-2}.

1. Introduction

Inconel 617 (UNS N00617) is a nickel-based superalloy used in high-temperature environments ($\sim 1000^\circ$C) due to its excellent mechanical stability and oxidation and corrosion resistance. Primary industrial applications are in the aerospace and chemical industries, and fossil and nuclear power generation [1]. This alloy is a face-centred cubic (fcc) solid solution of nickel (52 wt %), chromium (22 wt %), cobalt (12 wt %), and molybdenum (9 wt %), with small amounts (< 1.5 wt % each) of iron, silicon, titanium and aluminium. The nominal chemical composition is given in Table I.

Studies of the microstructure and phase stability of bulk Inconel 617 have been reported previously [2, 3], but are summarized here to provide a background for the discussion of sputtered Inconel 617 coatings. The as-received microstructure of solution-annealed Inconel 617 consists of large equiaxed γ grains, ASTM 5 (65 μm average diameter) or coarser, with grain boundary $M_{23}C_6$ (M = Cr, Mo) and intragranular MC carbides (M = Ti). Bulk Inconel 617 is not γ' strengthened in the solution-annealed condition, but will undergo slight strengthening after lengthy exposure to temperatures above 650°C, primarily due to extensive precipitation of intragranular $M_{23}C_6$ (M = Cr + Mo) [2]. A more recent study has shown that eta-carbide, M_6C (M = Mo, Ni, Si), is precipitated primarily upon pre-existing $M_{23}C_6$ after heat treatment at 800°C [3]. No topologically close packed (tcp) phases such as σ, χ, or μ have been identified [2, 3]. Photomicrographs representative of the micro-

structure of this alloy before and after heat treatment are shown in Figs 1a to d.

The present study is part of an investigation of the microstructure and phase stability of both as-received bulk and sputtered Inconel 617, in which the latter was characterized for potential use as an oxidation, corrosion, or erosion resistant coating [4]. The reader is referred to the literature for examples of the application of coatings in gas turbine engines [5]. The phase stability of sputtered Inconel 617 coatings will be published separately [6].

2. Experimental procedure

2.1. Substrate material and preparation

Inconel 617 coatings were deposited on to commercially pure α-titanium sheet (ASTM B265079 Grade 1). This substrate material contains equiaxed grains 10 to 20 μm in diameter and fine titanium hydride needles, as shown in Figs 2a and b, respectively. Its chemical composition is listed in Table II. Inconel 617 was

TABLE I Nominal chemical composition (wt %) of Inconel 617 [1]

Ni	Cr	Co	Mo	Fe	Al	Mn	Si	Ti	Cu	C	S
52.0	22.0	12.5	9.0	1.5	1.2	0.5	0.5	0.3	0.2	0.07	0.008

TABLE II Nominal chemical composition wt % of α-titanium [4]

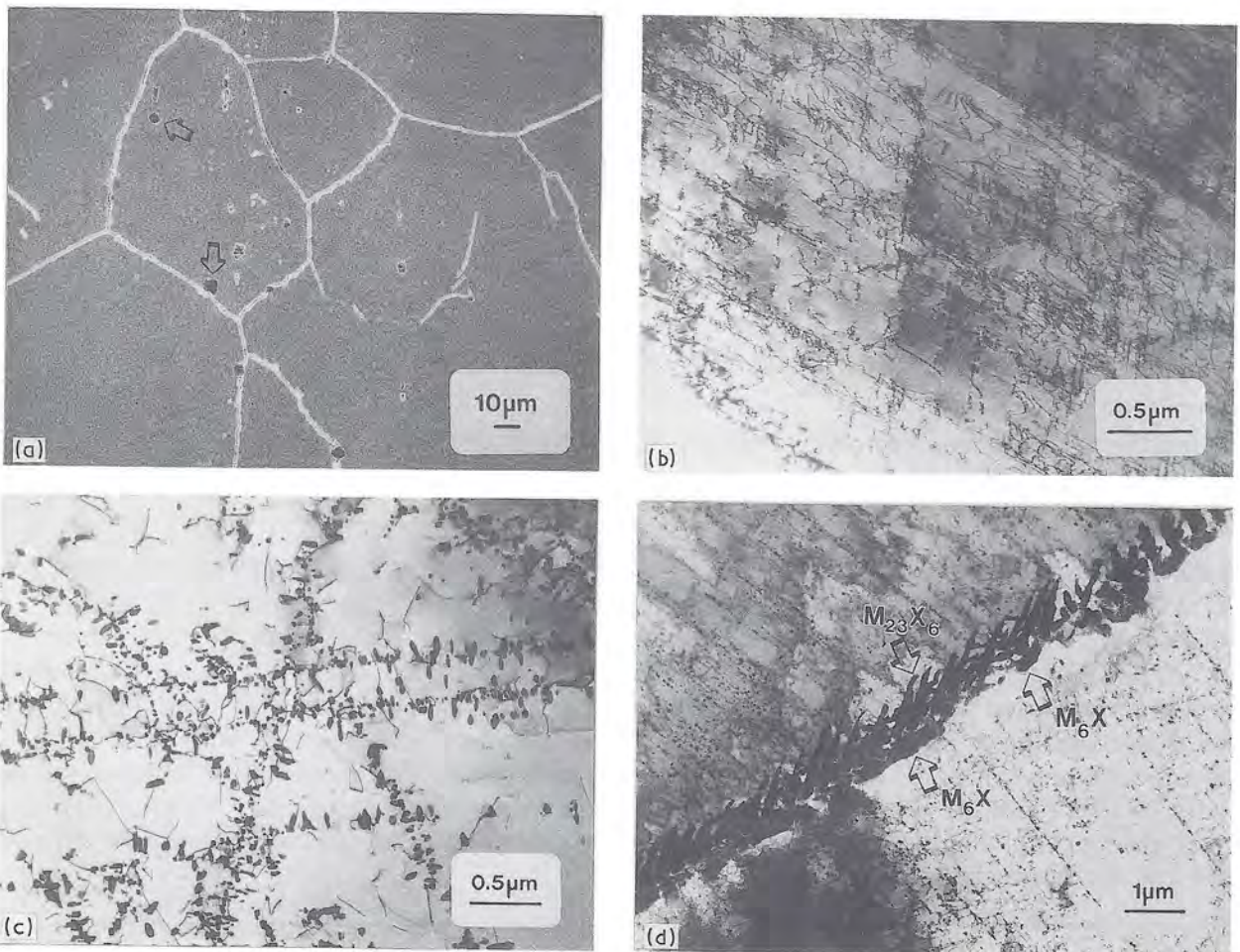| Ti	Fe	O	C	N	H
99.50	0.20	0.18	0.08	0.03	0.015

137

Figure 1 (a) Scanning electron micrograph of cold-rolled and solution-annealed Inconel 617 in the as-received condition showing grain boundary and intragranular carbide (arrows). Etched in glyceregia. (b) Dislocations in the γ phase of as-received Inconel 617. (c) Intragranular $M_{23}C_6$ nucleated upon slip lines and dislocations after heat treatment at 800° C for 200 h. (d) M_6C nucleated on grain boundary $M_{23}C_6$ (arrows). Note the extensive precipitation of intragranular $M_{23}C_6$.

deposited on to ground (30 μm SiC) titanium sheet 0.5 mm thick for evaluation of coating defects, adherence, and ductility by SEM. Coatings were also deposited on to metallographically polished titanium discs, 3 mm in diameter and about 100 μm thick, for TEM studies. All substrates were ultrasonically cleaned for 5 min each in trichloroethane, acetone, and ethanol, immediately inserted into the sputtering unit, and a vacuum of better than 3×10^{-6} torr was achieved.

2.2. Sputtering

Sputtering was performed in a Materials Research Corporation model 8667 + 2M 1.5 kW radio frequency (13.56 MHz) sputtering unit. The vacuum chamber was silicone oil diffusion pumped and equipped with a liquid nitrogen cold trap. Cold-rolled and solution-annealed Inconel 617 plate 0.64 cm thick was machined into a circular disc 14.6 cm diameter and bonded to a water-cooled OFHC copper magnetron backing plate using conducting silver-filled
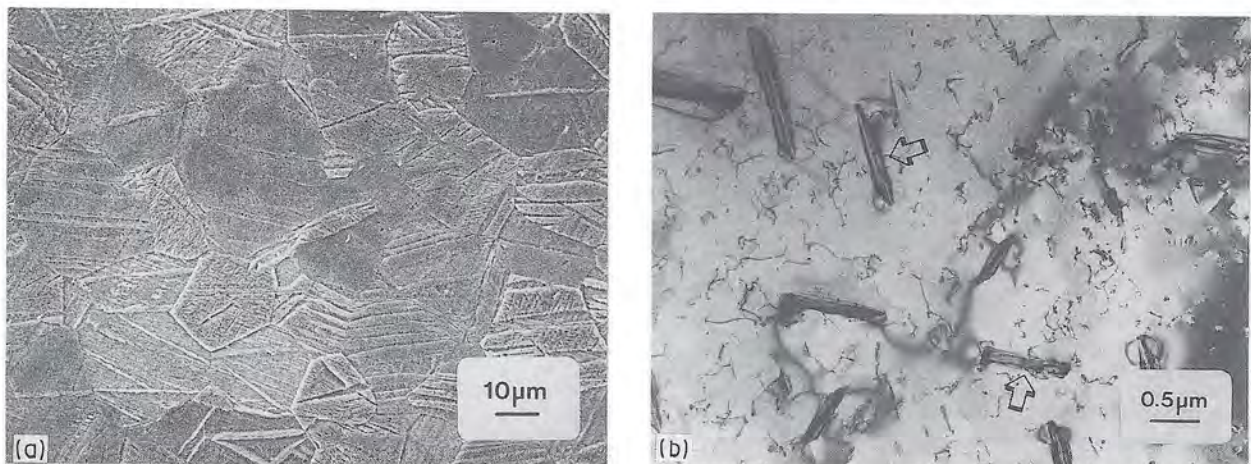
Figure 2 (a) Scanning electron micrograph of commercially pure α-titanium showing small equiaxed grains, twins, and titanium hydride precipitates (Etched in Kroll's solution). (b) Transmission electron micrograph of titanium hydride needles (arrows).

138

epoxy cement. Ultra-high purity (UHP) argon (99.999%) was used for sputter-cleaning, target pre-sputtering, and deposition of Inconel 617 coatings. The substrates and vacuum chamber walls were sputter-cleaned for 10 min in argon using a forward r.f. of 1000 W and a working gas pressure of 15 mtorr at a volumetric flow rate of 19.20 cm^3 sec^{-1}. Substrates were shielded from the target which was then sputter-cleaned for 10 min at 1000 W forward r.f. and 2 mtorr argon at 19.20 cm^3 sec^{-1}. The optimum sputtering conditions were found to be a forward r.f. of 1000 W and an argon gas pressure of 2 mtorr at 19.20 cm^3 sec^{-1}, resulting in an average deposition rate of 180 nm min^{-1} (0.18 μm min^{-1}) as determined by step profilometry. These conditions produced an average power density of 6 W cm^{-2}, 440 V across the electrodes, 2.27 A discharge current, and 13.5 mA cm^{-2} discharge current density. Coatings 10 to 13 μm thick (depending upon location below the target) were deposited in 75 min.

The substrates were not externally biased during deposition, and are therefore assumed to have been at ground potential during sputtering. Samples were placed upon a water-cooled platform and were not externally heated. A thermocouple in contact with the water-cooled platform and placed adjacent to the substrates during sputtering recorded a maximum temperature of 320° C, resulting in a homologous temperature of $T/T_m = 0.36$. Substrates were cooled under vacuum for a minimum of 2 h after sputtering. Numerous depositions and subsequent microstructural analyses showed that the above parameters resulted in reproducible and high-quality adherent coatings up to 34 μm thick.

2.3. Electron microscopy
Scanning electron microscopy was performed in an AMR 1000A SEM at 20 keV. Analytical electron microscopy was performed using a Philips 420T scanning transmission electron microscope (STEM) at 120 keV, and equipped with a LaB$_6$ electron gun, EDAX System 9100/60 energy dispersive X-ray spectrometer (beryllium window), and a Gatan Model 607 electron energy loss spectrometer (EELS). The microscope was operated in TEM mode and aligned prior to each use to ensure reproducible conditions for magnification, diffraction camera length, and energy dispersive microanalysis.

The lattice parameter of sputtered coatings was determined by averaging the d-spacings of rings and spots from selected-area and convergent-beam electron diffraction patterns, respectively. Phase compositions were determined by quantitative energy dispersive spectroscopy (EDS) of $K\alpha$ lines using EDAX LIST halographic background stripping program and EDAX THIN software package employing the ratio method of analysis [7]. A minimum of 5000 counts full-scale at a count rate of < 2500 counts/sec was used for all energy dispersive spectra analysed quantitively. The elements of interest were "windowed" with an integrated intensity equal to 1.2 FWHM, and machine-generated k-values were used.

The microstructure of Inconel 617 coatings was examined through-thickness by dimpling the uncoated side of 3 mm titanium discs with a series of alumina slurries using a VCR Group Model D500 dimpler. Dimpling was stopped at the onset of perforation, at which time a hole about 0.5 mm diameter was produced in the coating. Samples were then argon ion milled without external cooling in a Gatan Model 600 twin gun ion mill to produce electron-transparent regions. The ion-milling conditions employed were a 10° gun angle, 5 kV gun voltage, 0.75 mA gun current, and 30 to 40 μA specimen current for 30 to 60 min. This method reveals a microstructure representative of that about 1 μm below the surface of the coating.

EELS was used to determine the presence of argon, carbon, nitrogen and oxygen in sputtered coatings. However, samples were prepared by methods different from that given above (i.e. jet polishing) in order to eliminate artefacts such as argon from ion milling. Coatings 10 to 13 μm thick were peeled from 23 μm thick molybdenum foil substrates, mechanically punched into 3 mm discs, and jet polished using a Struers Tenupol-2 twin jet electropolishing unit. A solution of 25% nitric acid (HNO$_3$) in methanol was used as the electrolyte and maintained at $-30°$ C using Klein-Kryomat refrigeration system. Typical electropolishing conditions were 6 V and a current of 80 mA for 20 to 30 sec. These coatings were found to contain the same microstructure as that deposited on to titanium substrates.

3. Results and discussion
3.1. SEM of as-sputtered Inconel 617 coatings
Coatings on ground substrates were smoother than the surface finish of the initial substrate as determined by step profilometry. This is in contrast to most studies where the coating was found to faithfully replicate or even amplify surface irregularities in the absence of external bias and at low T/T_m [8, 9]. Nodular growth defects were occasionally observed on both ground and polished substrates, Figs 3a and b, but were generally rare in both cases. This is in contrast to studies showing that the formation of nodular growth defects is strongly dependent on surface finish [9]. Most growth nodules found in this study are attributed to embedded SiC and Al$_2$O$_3$ grinding and polishing abrasives, respectively, and other foreign debris on the substrate. The low number of defects and smooth surface finish are evidence of high adatom mobility, indicating the microstructure may be more indicative of a Zone 2 structure due to higher-than-measured substrate surface temperature and increased substrate bombardment [8, 9]. The density of coatings applied to polished titanium substrates was found to be the same as that of bulk Inconel 617 (8.36 g cm^{-3}).

The fracture morphology of coatings applied to 0.5 mm thick ground titanium substrates as determined by 180° bend tests showed that fracture did not initiate until samples were bent to an angle greater than 45°, and that coatings failed in a tortuous manner (Fig. 4a). Small dimples 0.2 to 0.5 μm diameter were indicative of ductile failure (Fig. 4b). Coatings
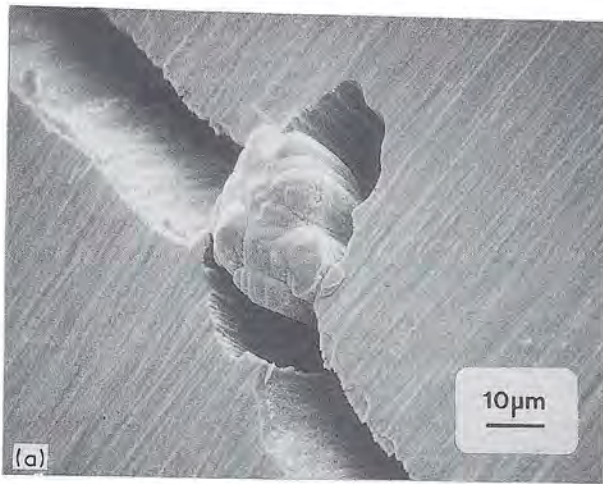
Figure 3 (a) Scanning electron micrograph of a nodular growth defect in sputtered Inconel 617 deposited on to ground α-titanium. Note that the coating has fractured around the growth defect in this bend test sample. (b) Scanning electron micrograph of a nodular growth defect in sputtered Inconel 617 deposited on to polished α-titanium. Note the smooth surface finish around the nodule.

were therefore strongly adherent to titanium substrates. However, fracture morphology is substrate-dependent. Much of the previous work determining the coating morphology has been on coatings applied to brittle substrates, which tend to show features more characteristic of microstructures as depicted in the Thornton Structural Zone Model [10]. Inconel 617 coatings deposited on glass and sapphire substrates showed a similar dependence; i.e. the coatings exhibited a columnar fracture morphology corresponding to both low T/T_m and working gas pressure.

The average Knoop microhardness of coatings deposited on to polished α-titanium substrates was $503\,kg\,mm^{-2}$ (100 g load). This corresponds to a Rockwell C hardness of approximately R_C 40 [11], as opposed to an average Rockwell B hardness of the as-received Inconel 617 sputtering target of R_B 88, and is indicative of a fine grain size in the coating. X-ray diffraction of the coating showed only one peak at $2\theta = 43.9°$ (Fig. 5), which corresponds to a d-spacing of 0.205 nm and indicates only (1 1 1) planes lying parallel to the substrate. This is consistent with other studies of copper and nickel coatings, in which the most dense crystal planes lie parallel to the substrate surface [12–14].

3.2. TEM of as-sputtered Inconel 617 coatings

TEM of the near-surface microstructure showed that the coatings were a solid solution with equiaxed γ grains ranging in size from 20 to 50 nm diameter (Fig. 6a). Grain boundaries are not clearly distinguishable due to high strain contrast and overlapping grains. A few grains as large as 150 nm in diameter were also found. In addition, the coating contained clusters of fine twins and stacking faults perpendicular to the substrate, Fig. 6b. Through-focus imaging did not reveal the presence of voids in the coating. This microstructure is similar to both sputtered nickel and copper [12, 13].

Quantitative stereological analysis of the microstructure using both area and intercept methods showed that there was an average of about 320 grains/μm^2 (3.2×10^8 grains/mm^2) with diameters of 40 to 60 nm. The grain-boundary density was calculated using the relationship:

$$S_v = 2P_L M \tag{1}$$

where S_v is the average grain boundary area per unit volume (cm^2 cm^{-3}), P_L is the average number of grain boundaries intercepted by a randomly placed straight line of known length, and M is the magnification of
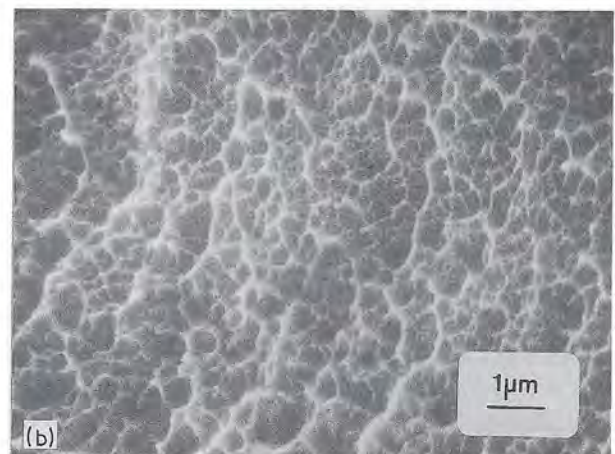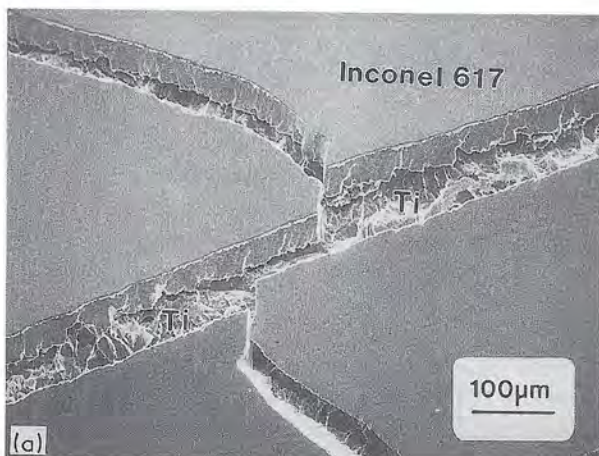
Figure 4 (a) Scanning electron micrograph showing the fracture morphology of as-sputtered Inconel 617 on ground α-titanium. (b) Scanning electron micrograph of ductile dimples in a bend test sample.
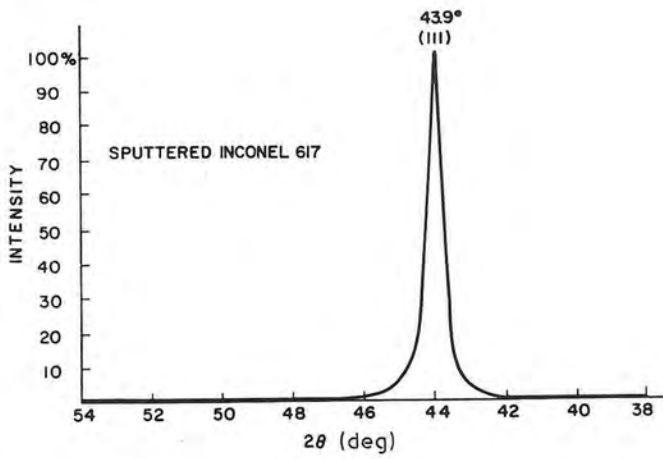
140

the micrograph [15]. The total average interfacial area was found to be $3.6 \times 10^6 \, \text{cm}^2 \, \text{cm}^{-3}$. If the width of the interfacial region is about 2 nm and the average grain size is 50 nm, then the volume fraction of grain-boundary material is about 15%. This is in contrast to conventional single-phase polycrystalline metals in which the volume fraction of interfacial material is only about 0.05% [16]. The significance of this with regards to the phase stability of this coating will be discussed in a separate publication [6].

A preliminary study indicated that the crystal structure of sputtered Inconel 617 was body-centred cubic [17]. The present, more detailed TEM investigation, however, shows that the structure is instead face-centred cubic with an average lattice parameter of 0.366 nm. Typical selected-area (SADP) and convergent-beam electron diffraction (CBED) patterns of the coating are shown in Figs 6c and d. The average lattice parameter of bulk solution annealed Inconel 617 is 0.362 nm; a difference of about 1% [3]. The continuous
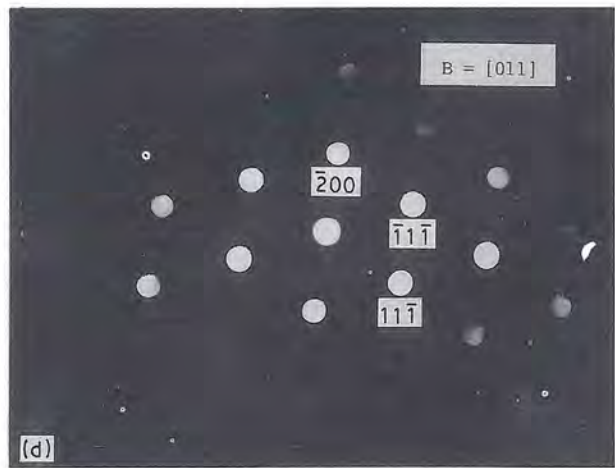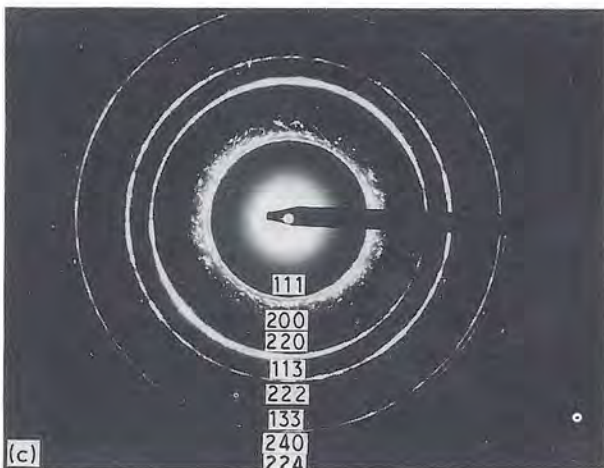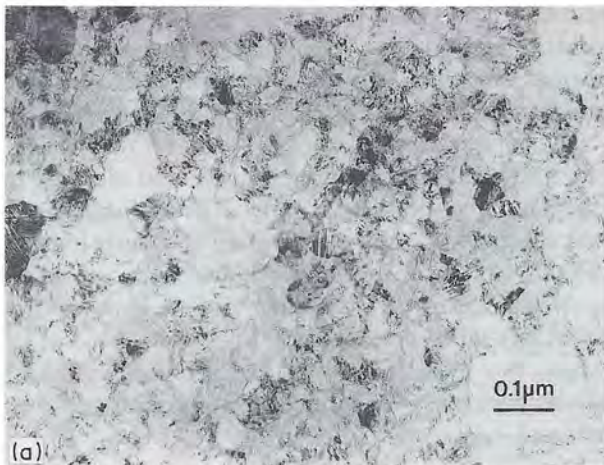
Figure 6 (a) Through-thickness transmission electron micrograph of as-sputtered Inconel 617 deposited on to polished α-titanium. Grains and grain boundaries are difficult to resolve due to the large amount of strain contrast. (b) Through thickness transmission electron micrograph showing clusters of twins and stacking faults perpendicular to the substrate (arrowed). (c) 2 μm SADP of as-sputtered Inconel 617. Note the diffuse f c c [1 1 1] and [2 0 0] rings, and [2 2 0] preferred orientation. (d) CBED of as-sputtered Inconel 617 showing the f c c [0 1 1] zone axis. (e) [1 1 1] + [2 0 0] dark-field transmission electron micrograph of as-sputtered Inconel 617. (f) [2 2 0] dark-field TEM of as-sputtered Inconel 617. A [2 2 0] preferred orientation is apparent compared to (e).

141
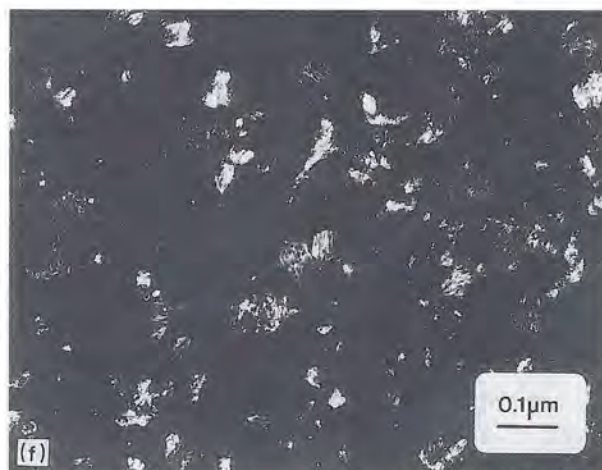
Figure 6 Continued

rings in Fig. 6c are indicative of a large number of grains contributing to the 2 μm selected-area diffraction pattern. A (2 2 0) preferred orientation is apparent in the SADP (Fig. 6c). Further, the (1 1 1) and (2 0 0) reflections are thickened and poorly defined due to the lack of (2 0 0) crystal orientations and the large amount of strain on (1 1 1) extrinsic stacking faults and twin planes, apparently resulting in inconsistent *d*-spacings. Higher order reflections (i.e. (4 0 0), (3 3 3), etc.) appear to be missing, but instead are

Figure 7 EDAX spectrum of as-sputtered Inconel 617.
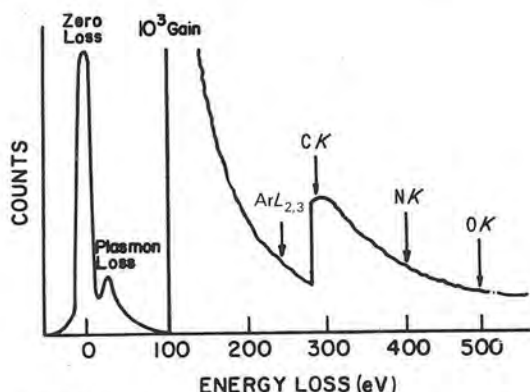
Figure 8 EELS spectrum showing the zero and plasmon electron loss features, and the location of Ar$L_{2,3}$, CK, NK, and OK edges. The carbon signal is commensurate with that expected from sputtering carbides in the target.

simply faint. Dark-field imaging of (1 1 1) + (2 0 0) reflections (combined) and (2 2 0) reflections (alone) provided further evidence of (2 2 0) texture (Figs 6e, f).

Quantitative EDS showed the four primary alloying elements in the γ-phase to be 54.8 wt % Ni, 24.5 wt % Cr, 12.9 wt % Co, and 7.8 wt % Mo. A small amount (~ 1 wt % each) of iron, aluminium, silicon and titanium was also detected (Fig. 7). This composition differs slightly from that given by the supplier of the sputtering target used in this study (Table I), and is probably the result of overlapping $K\beta$ lines, non-quantitative analysis of minor alloying elements, normal variations in alloy composition, and perhaps uncorrected ZAF.

Inconel 617 coatings were analysed for the presence of entrapped argon, carbon, oxygen, and nitrogen by EELS using jet-polished samples. The resultant energy loss spectrum is shown in Fig. 8. The magnitude of the CK edge is consistent with that expected in as-sputtered Inconel 617 coatings due to sputtering of refractory metal carbides (i.e. $M_{23}C_6$ and MC) in the target. No electron energy loss features indicative of the presence of argon, oxygen or nitrogen were detected.

4. Conclusion

Inconel 617 coatings 10 to 13 μm thick were r.f. magnetron sputtered in argon on to commercially pure α-titanium substrates without external bias or heat. Coatings were adherent, smooth, and mostly free of nodular growth defects. Bend tests produced dimples on coating fracture surfaces and are indicative of ductile failure. Coatings were an f c c solid solution with an average lattice parameter of 0.366 nm, compared to 0.362 nm for bulk solution-annealed Inconel 617. The through-thickness microstructure consisted of equiaxed γ grains an average of 50 nm diameter, resulting in a grain-boundary density of approximately 3.6×10^6 cm^2 cm^{-3}.

References

1. "Inconel Alloy 617" (Huntington Alloys Inc., Huntington, West Virginia, 1979).
2. W. L. MANKINS, J. C. HOSIER and T. H. BASSFORD, *Metall. Trans.* **5** (1974) 2579.
3. M. EMILIANI, PhD thesis, Brown University, 1988.
4. MARIO L. EMILIANI, *ibid.* (1988).
5. Special issue: "Protective Coating Systems for High Temperature Gas Turbine Components", *Mater. Sci. Tech.* **3** (1986) 193.
6. M. EMILIANI, M. RICHMAN and R. BROWN, 'The Microstructure and Phase Stability of Sputtered Inconel 617' in preparation.
7. "EDAX PV9100/60 Quantitative Thin Section User's Manual", Version 2.3 (EDAX International Inc., Prairie View, Illinois, 1983).
8. J. A. THORNTON, *J. Vac. Sci. Technol.* **A4** (1986) 3059.
9. T. SPALVINS and W. A. BRAINARD, *ibid.* **11** (1974) 1186.
10. J. A. THORNTON, *ibid.* **11** (1974) 666.
11. G. F. VANDER VOORT, "Metallography" (McGraw-Hill, New York, 1984) Ch. 5.
12. S. D. DAHLGREN, *J. Vac. Sci. Technol.* **11** (1974) 832.
13. S. D. DAHLGREN, W. L. NICHOLSON, M. D. MERZ, W. BOLLMANN, J. F. DEVLIN and R. WANG, *Thin Solid Films* **40** (1977) 345.
14. R. W. VOOK and F. WITT, *J. Vac. Sci. Technol.* **2** (1965) 49.
15. R. T. DEHOFF and F. N. RHINES, "Quantitative Metallography" (McGraw-Hill, New York, 1968) Ch. 4.
16. P. M. FABIS, *J. Vac. Sci. Technol.* **A5** (1987) 75.
17. M. EMILIANI, M. RICHMAN, R. BROWN and O. GREGORY, *Surf. Coat. Tech.* **33** (1987) 267.

Characterization of sputtered Inconel 617

Part 2 *Coatings in cross-section*

MARIO EMILIANI
Pratt and Whitney, PO Box 109 600, MS 707-28, West Palm Beach, Florida 33410, USA

MARC RICHMAN
Division of Engineering, Brown University, Box D, Providence, Rhode Island 02913, USA

RICHARD BROWN
Department of Chemical Engineering, University of Rhode Island, Kingston, Rhode Island 02881, USA

Inconel 617 coatings, 10 to 13 µm thick, were r.f. magnetron sputtered on to commercially pure α-titanium substrates without external bias or heat and examined in the as-deposited condition by analytical transmission electron microscopy (TEM). Coatings were an f c c solid solution with an average lattice parameter of 0.366 nm and had a (1 1 1) preferred orientation. Examination of the microstructure in cross-section showed it consisted of columnar grains on average 60 nm wide, and contained a high density of twins and stacking faults parallel to the substrate. Comparison with sputtered copper and nickel coatings indicate that the stacking fault energy of sputtered Inconel 617 is similar to that of pure copper.

1. Introduction

Inconel 617 (UNS N00617) is a nickel-based superalloy used in high-temperature environments ($\sim 1000°$ C) due to its excellent mechanical stability, oxidation, and corrosion resistance. This alloy is a face-centred cubic solid solution of nickel (52%), chromium (22 wt %), cobalt (12 wt %), and molybdenum (9 wt %), with small amounts (< 1.5 wt % each) of iron, silicon, titanium and aluminium [1]. The microstructure of solution annealed in Inconel 617 consists of equiaxed γ grains 65 µm average diameter or coarser, with grain boundary $M_{23}C_6$ (M = Cr, Mo) and intragranular MC carbides (M = Ti). Bulk Inconel 617 is not γ' strengthened in the solution-annealed condition, but will undergo slight strengthening after lengthy exposure to temperatures above 650° C primarily due to precipitation of intragranular $M_{23}C_6$ (M = Cr + Mo) [2]. No topologically close packed (t c p) phases such as σ, χ, or μ have been identified [2, 3].

The as-sputtered microstructure of Inconel 617 found in this study is similar to other sputtered transition metals, particularly copper and nickel [4–6, 8, 10]. Thick (0.1 to 1.0 mm) copper coatings d.c. sputtered at approximately 600 nm min^{-1} on to copper and aluminium substrates maintained at -196 to 13° C with biases of -20 to -75 V, respectively, were examined in both plan (through thickness) and cross-section by transmission electron microscopy (TEM) [4]. The gain size (or equivalently, column width) was found to depend upon substrate temperature and bias. For example, coatings in plan section deposited at 6° C and -75 V bias had a bimodal distribution of equiaxed grains ranging in diameter from 250 to 1000 nm, with some randomly oriented twins and

stacking faults perpendicular to the substrate. Cross-sections showed long columnar grains perpendicular to the substrate which contained a high density of twins and stacking faults parallel to the substrate. Columnar grains were f c c with a (1 1 1) orientation, indicating that the most densely packed atom planes are parallel to the substrate.

In contrast, coatings deposited on to substrates maintained at temperatures up to 13° C recrystallized at or below room temperature resulting in a (1 0 0) orientation parallel to the substrate. This behaviour has been found in other studies of vacuum-deposited copper coatings [5, 6], and is attributed to intrinsic coating stress and a high, non-equilibrium, concentration of vacancies formed during sputter deposition at a low homologous temperature (T/T_M). These provide the driving force for dislocation climb, and were found to be sensitive to substrate bias and impurities in the coating [6].

The high density of twins and stacking faults in columnar grains of vacuum-deposited f c c coatings are generated as follows [4]. Atoms impinging upon the substrate compete for favourable close-packed positions on densely packed (1 1 1) planes, but not all are incorporated into the (1 1 1) orientation. Atoms that cannot be accommodated will still deposit as close-packed planes and produce planar defects (stacking faults) which may form the mirror plane required for twins. Subsequent addition of sputtered atoms on to new orientations produces twins of measureable thickness. Stacking faults may also be formed by shear stresses across (1 1 1) planes due to impingement of columnar grains during growth of the coating.
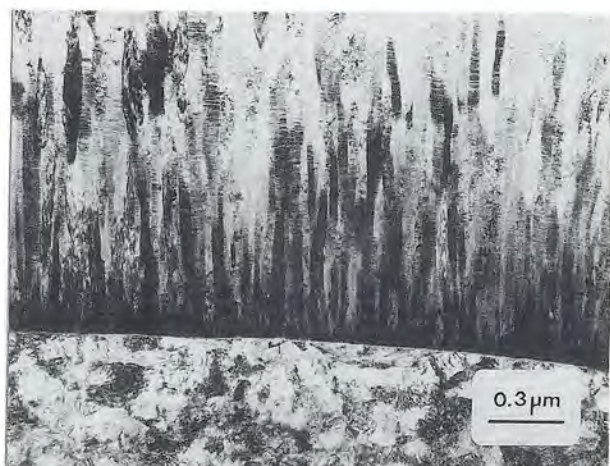
Figure 1 Transmission electron micrograph of as-sputtered Inconel 617 in cross-section deposited on to commercially pure α-titanium showing columnar grain morphology. Note the large number of planar defects parallel to the substrate in each column.
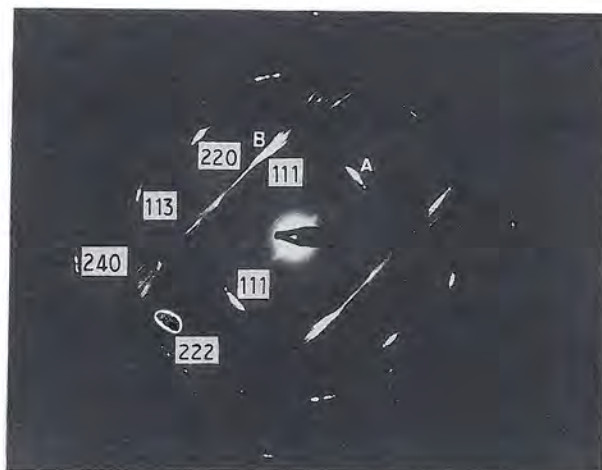

Figure 3 2 μm selected-area diffraction pattern of Inconel 617 in cross-section. The streaks are due to twins and stacking faults on {1 1 1} planes.

In situ X-ray diffraction of peak shifts and line asymmetries in evaporated copper coatings showed that they contain mostly extrinsic stacking faults [5]. The resulting fault has a finite thickness, and hence can be considered a very thin twin visible at high magnification in the TEM. Deformation twins may also be produced if the local strain caused by impingement of columnar grains is high enough. However, the probability of this happening in f c c metals is low, due to the presence of numerous slip systems which are activated at lower energies. Therefore, slip normally occurs in preference to twinning [7].

TEM of pure nickel and copper coatings sputter deposited at high rates (750 nm min^{-1}) under identical conditions and at low T/T_M showed similar microstructures: i.e. columnar grains, stacking faults, and twins [8]. Columns in nickel and copper coatings were found to have about the same diameter, while twins were approximately six times thicker in the nickel deposits. This was attributed to a lower probability of twin-boundary formation due to the high twin-boundary energy of nickel (400 erg cm^{-2}) compared to copper (73 erg cm^{-2}) [8, 9]. Statistical analysis of twin

spacings in columnar copper grains sputtered on to substrates maintained at 100 and 140° C showed that they were randomly spaced [10].

2. Experimental procedure
2.1. Sputtering
Sputtering was performed in a Materials Research Corportion model 8667 + 2M 1.5 kW radio frequency (13.56 MHz) sputtering unit. The vacuum chamber was silicone oil diffusion pumped and equipped with a liquid nitrogen cold trap. Cold-rolled and solution-annealed Inconel 617 plate 0.64 cm thick was machined into a circular disc, 14.6 cm diameter, and bonded to a water-cooled OFHC copper magnetron backing plate using conducting silver-filled epoxy cement. Ultra-high purity (UHP) argon (99.999%) was used for sputter-cleaning, target presputtering, and deposition of Inconel 617 coatings.

The substrates and vacuum chamber walls were sputter-cleaned for 10 min in argon using a forward r.f. of 1000 W and a working gas pressure of 15 m torr at a volumetric flow rate of 19.20 cm^3 sec^{-1}. Substrates were shielded from the target which was then
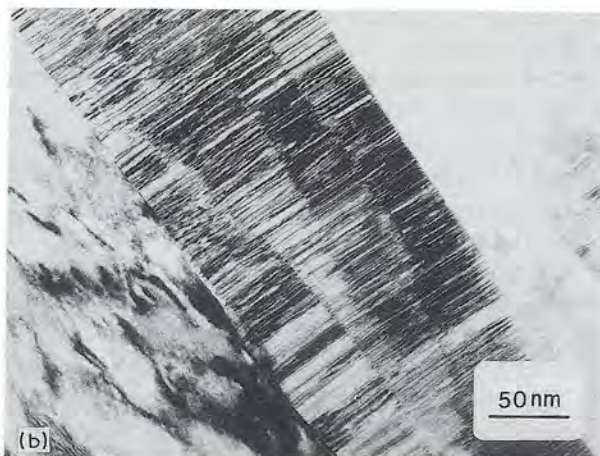

Figure 2 (a) Transmission electron micrograpn showing the morphology of columns, twins, and stacking faults in as-sputtered Inconel 617. (b) Higher magnification transmission micrograph illustrating the high density and fineness of planar defects.
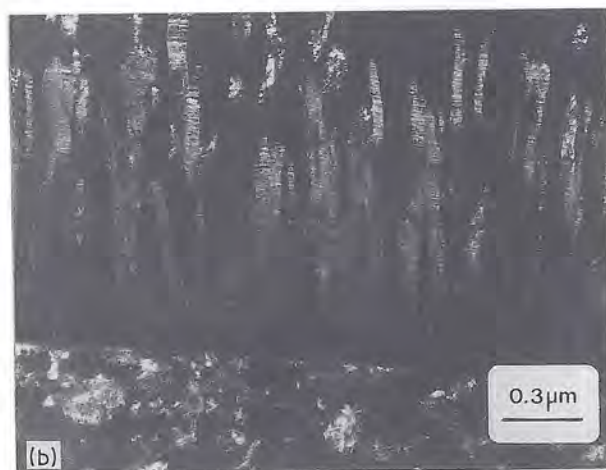
145

Figure 4 (a) Dark-field transmission electron micrograph of the diffusion spot labelled "A" in Fig. 3. (b) Dark field transmission electron micrograph of the diffraction spot labelled "B" in Fig. 3, showing that streaking is due to {1 1 1} planar defects.

sputter-cleaned for 10 min at 1000 W forward r.f. and 2 m torr argon at 19.20 cm^3 sec^{-1}. The optimum sputtering conditions were found to be a forward r.f. of 1000 W and an argon agas pressure of 2 m torr at 19.20 cm^3 sec^{-1}, resulting in an average deposition rate of 180 nm min^{-1} (0.18 μm min^{-1}) as determined by step profilometry. These conditions produced an average power density of 6 W cm^{-2} and 440 V across the electrodes. Coatings 10 to 13 μm thick, depending upon location below the target, were deposited in 75 min.

The substrates were not externally biased during deposition and are therefore assumed to have been at ground potential during sputtering. Samples were placed upon a water-cooled platform and were not externally heated. A thermocouple in contact with the water-cooled platform and placed adjacent to the substrates during sputtering recorded a maximum temperature of 320° C, resulting in a homologous temperature of $T/T_m = 0.36$, indicative of a Zone T microstructure according to the Thornton Structural Zone Model [11]. Substrates were allowed to cool under vacuum for a minimum of 2 h after sputtering.

2.2. Sample preparation and electron microscopy

Inconel 617 coatings were deposited on to metallographically polished α-titanium (ASTM B265079 Grade 1) wafers 2.5 mm wide by 1.3 mm thick by 12.5 mm long and prepared for examination in cross-section using methods similar to that previously reported [12, 13]. Uncoated α-titanium, glass, or sapphire wafers were used as backing material to make a two-ply sandwich in which the coating lay midway between the wafers.

Coated and uncoated wafers were ultrasonically cleaned in acetone and dried on a hot plate immediately prior to application of the adhesive. Loctite Speedbonder 326 brand structural acrylic adhesive was used to bond the wafers together. The wafers were placed in a precision vice and inserted into a preheated vacuum oven to cure the adhesive. The sandwich was then attached to a glass microscope slide parallel to the bond line using a cyanoacrylate adhesive and sec-

tioned into 300 to 500 μm thick samples using a low-speed diamond cut-off wheel.

Samples were mounted on flat sapphire windows and ground to a thickness of about 100 μm using SiC or diamond grinding media, then polished to 0.05 μm Al$_2$O$_3$ on one side only to reduce the amount of handling. Titanium rings 3 mm in diameter and about 150 μm thick were bonded to the polished side using a Sicomet 50 brand cyanoacrylate adhesive to provide support for the thinned samples. Samples were removed from the windows, washed in acetone, and dimpled opposite the polished side using alumina slurries to produce a small hole slightly below the coating. Samples were ion milled for 2 to 5 h at a gun voltage of 5 kV, 10° gun angle, 0.75 mA gun current, 30 to 40 μA specimen current to produce electron-transparent areas.

Analytical electron microscopy was performed using a Philips 420T scanning transmission electron microscope (STEM) at 120 keV, and equipped with a LaB$_6$ electron gun, EDAX System 9100/60 energy dispersive X-ray spectrometer (Beryllium window), and a Gatan Model 607 electron energy loss spectrometer (EELS). The microscope was operated in
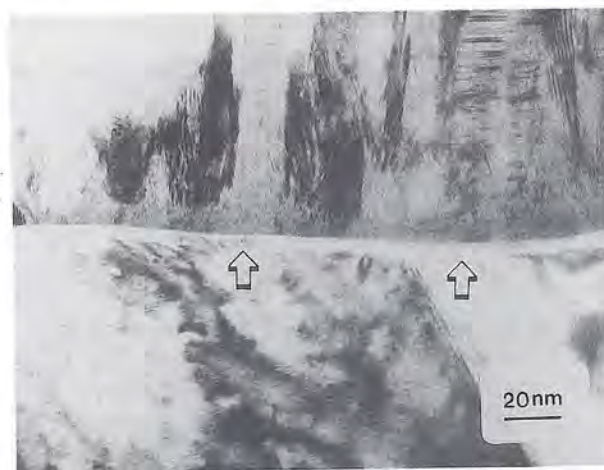

Figure 5 Transmission electron micrograph showing the Inconel 617/TiO$_2$/α-titanium interface. Note the oxide layer (arrowed) and the fine grain size of Inconel 617 above it.

146

TEM mode and aligned prior to each use to ensure reproducible conditions for magnification, diffraction camera length, and energy dispersive microanalysis.

3. Results and discussion
3.1. TEM of as-sputtered Inconel 617 coatings

The microstructure of sputtered Inconel 617 in cross-section was found to consist of long columnar γ grains 20 to 150 nm wide perpendicular to the substrate, as shown in Fig. 1. Some grains appear to have nucleated from within the coating, but are instead likely to have not fully intersected the plane of the micrograph. Therefore, most columnar grains grew continuously from the substrate. No $M_{23}C_6$ nor TiC precipitates were found in as-sputtered coatings. The column width remained relatively constant and was generally not found to increase with distance from the substrate. While the experimentally determined homologous temperature indicates the structure is Zone T, direct imaging by TEM shows the as-deposited microstructure is, in fact, better characterized as Zone 2 due to the absence of shadowing effects [11].

A high density of twins and stacking faults parallel to the substrate were also found, and they ranged in thickness from about 1.5 to 50 nm (Figs 2a and b). Selected-area diffraction (Fig. 3) showed that the coatings are highly textured and contain streaks. Dark-field imaging of streaked and unstreaked f c c (1 1 1) reflections confirmed that streaking was due to (1 1 1) twins and stacking faults (Figs 4a and b). Stereological analysis showed that there were 16 to 18 columns per micrometre parallel to the substrate, and their average diameter was about 60 nm. This is consistent with the average grain size found in plan sections [14]. In contrast, computer modelling of Zone 2 columnar growth in vapour-deposited coatings has shown that the average grain size (or column width) increases with distance from the substrate [15].

The high density of twins and stacking faults parallel to the substrate (Fig. 2b), coupled with overlapping grains and strain contrast, made it difficult to perform accurate stereological analysis. Most twins and stacking faults had thicknesses ranging from 1 to 15 nm, with the majority less than 30 nm thick, and 30 to 100 nm wide. The average linear density of planar defects is then about 500 per micrometer. Because plan sections represent parallel slices through twins and stacking faults which each appear as a single grain, the total interfacial area is approximately 1000 times greater than the grain-boundary area, resulting in a total of about $3.2 \times 10^9 \, cm^2 \, cm^{-3}$ [14].

The morphology of as-sputtered Inconel 617 and the mechanism of columnar growth appear to be in good agreement with previous studies [4, 8, 10]. However, TEM studies of the morphology of twins and stacking faults in sputtered copper and nickel coatings showed that the density of planar defects is greater in copper coatings, whereas twins were about six times thicker in nickel coatings [8, 10]. Inconel 617 coatings, which contain about 52% nickel, had a high density of planar defects, and therefore, stacking fault energy more like that found in sputtered copper coatings [8, 9]. The low interfacial energy in Inconel 617 is believed to be related to deposition parameters specific to the present study and the presence of alloying elements.
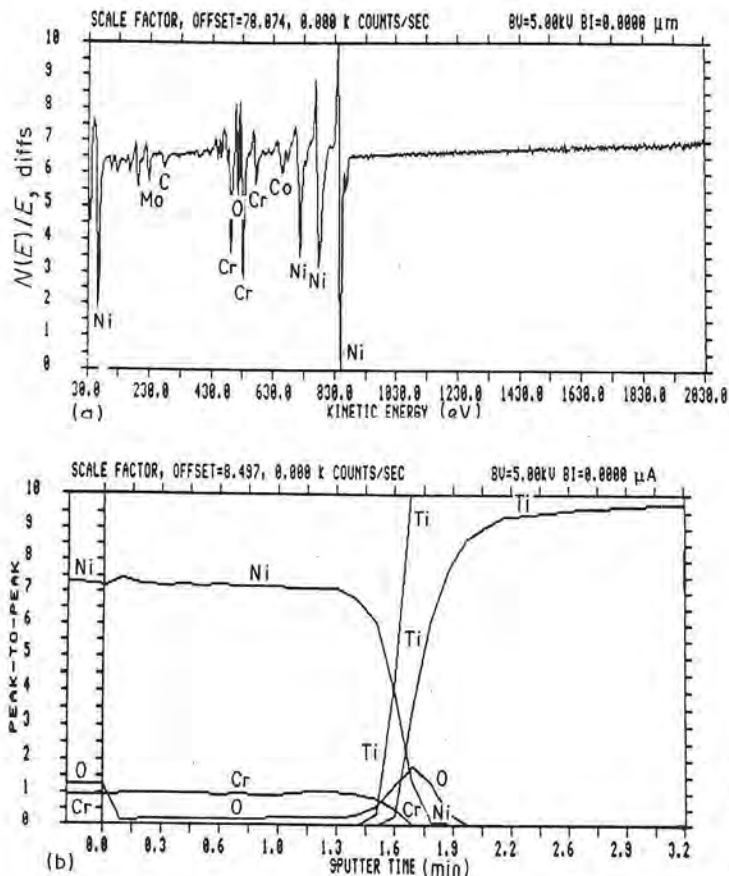

Figure 6 (a) Auger electron spectrum of as-sputtered Inconel 617. The carbon content is commensurate with that expected from sputtering refractory metal carbides in the Inconel 617 target. (b) Auger electron depth profile showing nickel, chromium, titanium and oxygen signals. A sharp Inconel 617/titanium interface is apparent.

147

3.2. Inconel 617/titanium interface

The Inconel 617/titanium interface was also examined by TEM and found to contain Inconel 617 nuclei on a thin layer of TiO_2 (anatase) (Fig. 5). The oxide thickness varied from sample-to-sample, and was 4 to 7 nm thick as determined from transmission electron micrographs. The quality of as-sputtered Inconel 617 coatings and the oxide layer thickness was also examined by scanning Auger microscopy (SAM). In this analysis, metallographically polished titanium substrates were sputter-etched prior to deposition and coated with approximately 200 nm of Inconel 617 to retard further growth of the oxide layer. The multichannel analyser was programmed to record titanium, nickel, chromium, cobalt, molybdenum, carbon and oxygen. A portion of the coating was briefly sputter-etched by argon ions to remove gross contaminants. An Auger spectrum of this area showed elements characteristic of Inconel 617 (Fig. 6a). The carbon signal is consistent with that expected in sputtered coatings due to the presence of carbides in the sputtering target, while the oxygen level is indicative of the formation of a near-surface oxide layer due to exposure of the sample to air.

Sputter depth profiling through the remainder of the coating showed a decreasing oxygen signal until the Inconel 617/TiO_2 interface was reached (Fig. 6b). The oxide layer thickness was calculated using the known parameters of Inconel 617 coating thickness and sputtering time through the oxide layer, and an estimation of the oxide sputtering rate [16]. This analysis showed the oxide layer was 5.1 nm thick, and corresponds to that determined by direct imaging of the Inconel 617/titanium interface. In addition, no nickel was detected in either the TiO_2 layer or below in the pure α-titanium substrate.

4. Conclusion

Inconel 617 coatings 10 to 13 μm thick were r.f. magnetron sputtered in argon on to commercially pure α-titanium substrates without external bias or heat. Coatings were an f c c solid solution with an average lattice parameter of 0.366 nm, compared to 0.362 nm for bulk solution-annealed Inconel 617, and had a

(1 1 1) preferred orientation. Coatings examined in cross-section by TEM contained columnar grains, on average 60 nm wide, with a linear density of planar defects calculated to be about 500 per micrometre perpendicular to the substrate, resulting in a total interfacial area of approximately 3.6×10^9 cm^2 cm^{-3}.

References

1. "Inconel Alloy 617" (Huntington Alloys Inc., Huntington, West Virginia, 1979).
2. W. L. MANKINS, J. C. HOSIER and T. H. BASSFORD, *Metal. Trans.* 5 (1974) 2579.
3. M. EMILIANI, PhD thesis, Brown University (1988).
4. S. D. DAHLGREN, *J. Vac. Sci. Technol.* 11 (1974) 832.
5. R. W. VOOK and F. WITT, *ibid.* 2 (1965) 49.
6. J. W. PATTEN, E. D. McCLANAHAN and J. W. JOHNSTON, *J. Appl. Phys.* 42 (1971) 4371.
7. R. W. HERTZBERG, "Deformation and Fracture Mechanics of Engineering Materials" (Wiley, New York, 1976) Ch. 4.
8. R. WANG and S. D. DAHLGREN, *J. Mater. Sci. Lett.* 10 (1975) 1456.
9. R. E. REED-HILL, "Physical Metallurgy Principles", 2nd Edn (Van Nostrand, New York, 1973) p. 893.
10. S. D. DAHLGREN, W. L. NICHOLSON, M. D. MERZ, W. BOLLMANN, J. F. DEVLIN and R. WANG, *Thin Solid Films* 40 (1977) 345.
11. J. A. THORNTON, *Ann. Rev. Mater. Sci.* 7 (1977) 239.
12. J. C. BRAVMAN and S. C. SINCLAIR, *J. Electron Micros. Tech.* 1 (1984) 53.
13. A. K. RAI, M. H. RASHID, P. P. PRONKO, A. EZIS and D. W. LANGER, *ibid.* 5 (1987) 45.
14. M. EMILIANI, M. RICHMAN and R. BROWN, *J. Mater. Sci.* 24 (1989).
15. D. J. SROLOVITZ, A. MAZOR and B. G. BUKIET, *J. Vac. Sci. Technol.* A6 (1988) 2371.
16. B. CHAPMAN, "Glow Discharge Processes" (Wiley, New York, 1980) pp. 385–96.

jOurnal

Assessment of Oxide Debond Coatings for Metal-Toughened Intermetallics

Mario L. Emiliani*

Materials Engineering, Pratt and Whitney, West Palm Beach, Florida 33410

Hervé E. Dève*

Metal Matrix Composites Program, 3M, St. Paul, Minnesota 55144–1000

The interfacial debond characteristics of sputtered Al_2O_3 and Y_2O_3 coatings were assessed in a γ-TiAl/Nb composite. The preferred debond coating identified for this composite system was Y_2O_3, which also protected the ductile reinforcing phase from reaction with the matrix. Tension tests on a model laminate specimen were performed to characterize the toughening behavior and showed that interfacial debonding promoted extensive plastic deformation of the ductile phase over a large volume. The coatings were characterized to understand the debonding behavior. Comparison is made with other metal/oxide systems. [Key words: debonding, interfaces, toughening, metal oxide, coatings.]

I. Introduction

PROTECTIVE and debond coatings are required on reinforcements used to improve the fracture toughness of brittle-matrix composite systems.[1-3] This study is part of an effort to determine the general requirement for debond coatings and to guide the selection of coating candidates. The substantial toughening of intermetallics and ceramics achieved by ductile phase reinforcements[4,10] is caused by plastic dissipation in the reinforcements bridging the crack faces. The steady-state toughening, ΔG_{ss}, is given by[11,12]

$$\Delta G_{ss} = f \sigma_0 R \chi \tag{1}$$

where σ_0 is the uniaxial yield strength, f is the area fraction of reinforcement intercepted by the crack, $2R$ is the reinforcement thickness, and χ is a nondimensional work-of-rupture term that varies depending upon the properties of the interface, as well as the constitutive behavior of the reinforcement.[7-9,13] For weakly bonded interfaces* the work of rupture is related to the interface properties by[14,15]

$$\chi = (\ell/R)\xi \tag{2}$$

where ℓ is the gauge length of the deforming reinforcement and is a function of interfacial properties. ξ is a nondimensional term[†] proportional to the *ductility* of the reinforcement.[14,15] To

*An interface is defined as "weak" in this context if the debond length, d, is sufficiently long to suppress constraint effects (Ref. 15), i.e., $d/R \gtrsim 1$.
[†]In the absence of constraint, ξ is independent of ℓ_e.
[‡]Philips 400T at 120 kV, equipped with a Kevex, "Quantum" ultrathin window energy dispersive X-ray spectrometer.
[§]It is assumed that the thickness of the reinforcement is small compared with the matrix.

a first approximation, ℓ/R is governed by interface friction[14,15]

$$\frac{\ell}{R} = \frac{\sigma_{max} - \sigma_0}{2\tau} \tag{3}$$

where τ is the frictional sliding stress and σ_{max} is the maximum stress in the reinforcement. It is clear from Eqs. (1) to (3) that a low interfacial shear stress is beneficial for high toughening. The material selected for the present investigation is γ-TiAl reinforced with niobium. This composite system has been shown to exhibit appreciable toughness.[4,5] It is also susceptible to interfacial debonding when a brittle σ-phase reaction product forms between the reinforcement and the matrix.[6] The amount of debonding could be varied by introducing a nonreactive coating at the interface. The potential role of oxide coatings is addressed in this article.

Some background is provided by prior research on the interfaces between Al_2O_3/Nb and Al_2O_3/Ti.[16-19] The consensus concerning the Nb/Al_2O_3 interface, whether prepared by diffusion bonding, internal oxidation, or thermal evaporation, is that there is no reaction product.[16,17] Furthermore, mechanical measurements have shown that the interface is susceptible to fracture, with a fracture energy, Γ_i, that exhibits a strong dependence on the relative orientations of the Nb and Al_2O_3.[16] Bonds formed between Al_2O_3 and Ti alloys are more complex.[18,19] Reaction layers form that comprise γ-TiAl and α_2-Ti_3Al, as well as the σ-phase, when refractory alloy additions are present. The oxygen released in the formation of these layers appears to diffuse into the Ti when a γ-TiAl reaction product forms. Crack propagation studies[19] have illustrated that fracture occurs at the interface between the Al_2O_3 and the γ-TiAl reaction product, with a fracture energy $\Gamma_i \approx 20$ J·m^{-2}. Furthermore, these studies suggest that the Al_2O_3/TiAl interface should exhibit good stability. Further aspects of γ-TiAl/Al_2O_3 interfaces are explored in the present article.

II. Experimental Procedure

(1) Coating Deposition

Yttrium oxide and aluminum oxide *coatings* were deposited onto polycrystalline niobium, single-crystal Al_2O_3 (0001), and NaCl substrates by reactive sputtering, using a 50%–50% mixture of research-grade argon and oxygen at a total working gas pressure of ≈ 6 mtorr. Before coating, Nb and Al_2O_3 substrates were ultrasonically cleaned in soapy water, rinsed in ethyl alcohol, and dried by forced hot air. Sputtering was performed in a Plasma-Therm Model AMNS-1000E 1000-W radio frequency diode sputtering unit equipped with dual opposed 6-in.-diameter targets. The coatings were deposited from yttrium and aluminum metal targets with a purity of >99.5%. The top and bottom targets were maintained at 3000 and 500 V, respectively. Deposition of Y_2O_3 for ~10 h

resulted in coatings 0.8 to 1.4 μm thick. Coatings were deposited at a substrate temperature ~1/10 the oxide melting temperature.

The as-deposited Y_2O_3 coatings were characterized by a variety of analytical methods, including analytical transmission electron microscopy (TEM),[‡] and by nanoindentor measurements. TEM was performed by depositing a thin coating onto rock salt. Then dissolving the rock salt in water and collecting the film on a copper grid.

(2) Interfaces

Sandwich specimens between basal plane sapphire and γ-TiAl have been made and characterized. The specimens were fabricated by diffusion bonding thin layers between two sapphire plates. For this purpose, TiAl thin sheets were spark cut from hot isostatically pressed and forged billets, with composition Ti–50.5 at.% Al and homogenized at 1000°C for 20 h. The microstructure consisted of equiaxed grains of γ-TiAl approximately 100 μm in diameter, with an intermittent phase consisting of small grains containing α_2 (Ti_3Al) laths alternating with γ laths.[5,7] The plates were metallographically polished to ensure planarity and vacuum diffusion bonded to sapphire at 1200°C for 4 h subject to a pressure of ~1 MPa.

Laminated specimens between Nb and γ-TiAl were also made. Niobium plates, 125 μm thick, were coated with either Y_2O_3 or Al_2O_3, inserted between polished γ-TiAl plates and diffusion bonded under a pressure of 10 MPa at 1066°C for 4 h. A polished cross section (Fig. 1) illustrates the structure of the laminate. Subsequently, the TiAl matrix was symmetrically precracked from a notch on each side of the sample using a three-point bend fixture. Tension tests of the precracked laminates[7] were then conducted either in situ in a scanning electron microscope or in a stiff servohydraulic frame, to evaluate relationships between the imposed stress, the crack opening, and the debonding. Finally, information concerning the fracture energies of the interfaces was obtained using flexural tests.[20]

III. Results

(1) Coatings and Interfaces

X-ray diffraction patterns of as-sputtered yttria-coated sapphire (Fig. 2), obtained using a thin film goniometer, revealed that the coating is BCC Y_2O_3. *X-ray photoelectron spectroscopy* showed that the surface contained physisorbed hydrocarbons, carbon, and OH. Argon sputtering decreased the C and increased the O signals, such that sputtering to a depth of 10 nm revealed only stoichiometric Y_2O_3. *Secondary ion mass spectroscopy* was used to determine the type and amount of trace elements in the coating ~10 nm below the free surface. A variety of elements were found (including B, C, Na, Al, Si, K, Ca, Ti, Fe, Nn, and Nd) all at levels of <0.1 at.%. These impurities are typical of those found in the yttrium sputtering targets.

Conventional TEM of the coating revealed a homogeneous distribution of fine grains, 10 to 30 nm in diameter (Fig. 3(A)). Energy dispersive spectroscopy (EDS) in the TEM showed yttrium and oxygen, with a small amount of aluminum and silicon in some areas (Fig. 3(B)). However, there was no diffraction evidence for the existence of crystalline compounds containing either aluminum or silicon.

The hardness of the Y_2O_3 coatings on sapphire, determined by nanoindentation (Fig. 4(a)), showed a variation with indentation depth. However, at indentation depths of $\geq$0.4 μm, the hardness was nearly constant at ~7.5 GPa, in good agreement with results for bulk Y_2O_3.[21] An estimate of the elastic modulus of the coatings was inferred using nanoindentor measurements, by considering the elastic recovery, the stiffness of the indentor, and the depth of the plastic indentation.[22] Measured values ranged between 150 and 270 GPa (Fig. 4(b)), which encompasses the elastic modulus of bulk Y_2O_3 (134 GPa).[23]
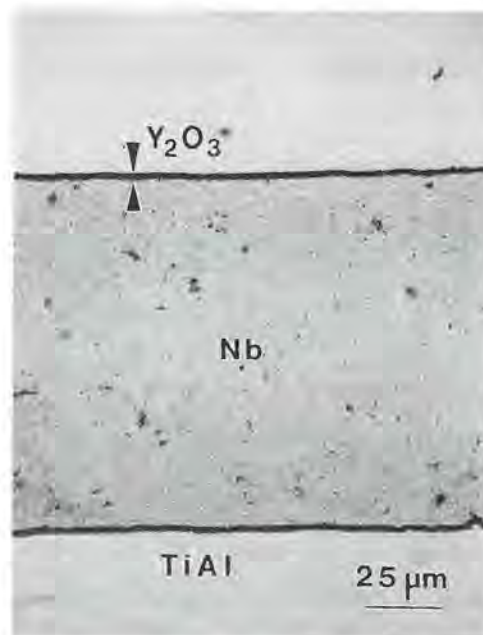
Fig. 1. Optical micrograph of composite laminate test specimen after diffusion bonding at 1066°C for 4 h and 10 MPa pressure. Note the absence of reaction products due to the Y_2O_3 coating, which remains discrete.

While it is important to investigate the properties of the as-deposited coatings, it is also imperative to realize that microstructural changes accompany composite fabrication and such changes can drastically alter the in situ coating properties. The properties of bonded interfaces processed under conditions similar to those used to produce composites have thus been investigated. Specifically, the interface fracture energy, Γ_i, measured using a flexure specimen[7] on γ-TiAl/Nb *laminates* containing Y_2O_3 interfacial coatings gave $\Gamma_i \approx 25$ J·m^{-2}, with crack propagation occurring primarily along the Nb/Y_2O_3 interface. This value is at the lower end of the range measured for Al_2O_3 bonded to Nb.[17] Conversely, flexural tests performed on laminates containing uncoated niobium reinforcements resulted in $\Gamma_i \approx 45$ J·m^{-2}, with crack growth occurring primarily within the (σ-phase) reaction product.

A corresponding study of the γ-TiAl/Al_2O_3 interface conducted, using the flexure specimen,[20] revealed that cracks that were extended stably through the Al_2O_3, up to the interface, propagated into the lower γ-TiAl layer without debonding (Fig. 5). Similar characteristics were obtained using indentation tests.[21] Debonding criteria for the interface[24] would thus indicate that this interface has a fracture energy at least 4 times that for sapphire, i.e., $\Gamma_i > 50$ J·m^{-2}. A similar interface formed by reaction between Ti and Al_2O_3 gave a much lower value, $\Gamma_i \approx 20$ J·m^{-2}.[19] A basic understanding of the thermochemical and microstructural origin of these values of toughness has yet to emerge.

(2) Toughness Measurement

Stress-stretch characteristics of TiAl reinforced with Nb was measured on precracked tensile specimens. The results are reflected in a plot of trends in the normalized stress (σ/σ_0) with the normalized crack opening (u/R) (Fig. 6). In specimens with uncoated niobium, necking initiated after a small amount of debonding within the σ-phase reaction product (Fig. 7). Fracture of the reinforcement occurred at a displacement $u \approx 2R$ with a debond length $d \approx 5R$, resulting in a work of rupture $\chi \approx 2.5$. The oxide coatings encouraged more extensive debonding, which initiated following minimal
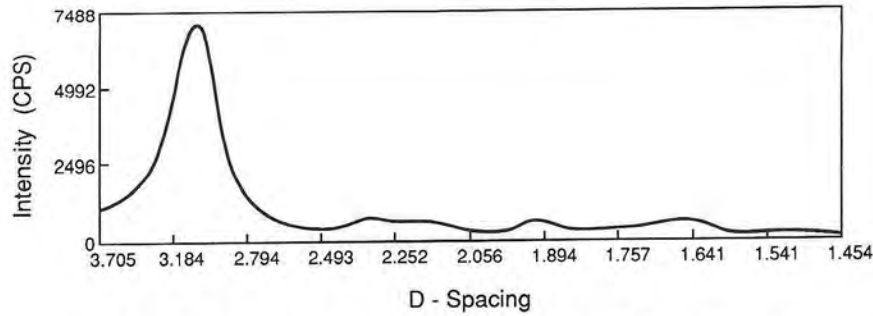
Fig. 2. X-ray diffraction pattern of reactively sputtered Y_2O_3 on sapphire.

plastic deformation of the reinforcement (Figs. 8 and 9) and resulted in $\chi \approx 4$ for Al_2O_3 and $\chi \approx 8$ for Y_2O_3 (Table I).

IV. Discussion

The role of the oxide coatings can be appreciated by investigating the loading that induces debonding (Fig. 10). Debonding before significant plastic stretch of the reinforcement is a dominantly mode II process. The mode II loading tends to deflect the debond toward the metal/coating interface, consistent with the observations that this interface dominates

debonding. Debond propagation in mode II is *resisted* both by the debond energy of the metal/oxide interface; as well as by frictional sliding at asperity contacts in the wake of the debond.[14] The *motivation* for such debonding is the strain energy release rate G. For the laminate geometry, G has a steady-state value G_{ss} given by[§,25,26]

$$G_{ss} \approx \frac{R}{2E}(\sigma_{appl} + \sigma_R)^2 \qquad (4)$$

where $2R$ is the reinforcement thickness, E is Young's modulus of the reinforcement, σ_{appl} is the applied stress, and σ_R is
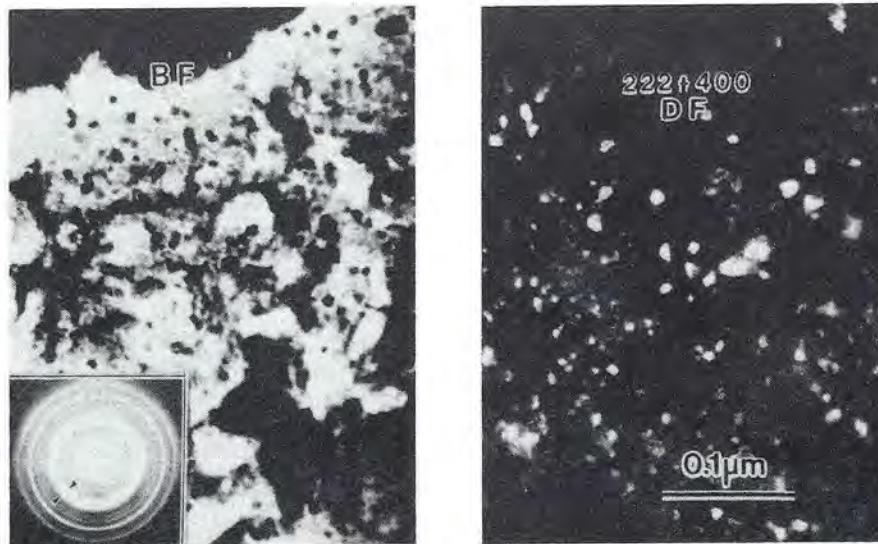
(A)
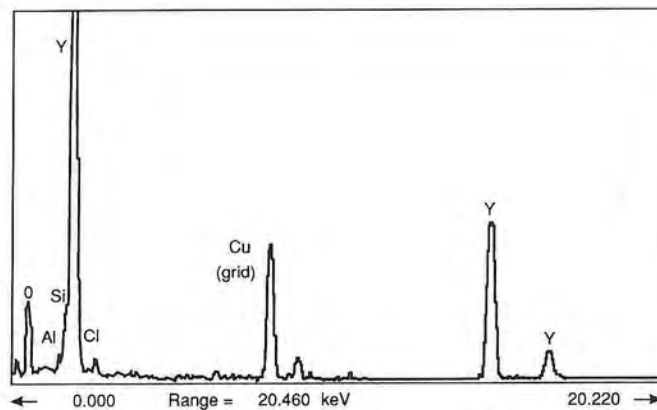
(B)

Fig. 3. (A) Bright-field (left) and dark-field (right) TEM micrographs and Y_2O_3 deposited on NaCl. Arrows on the selected area diffraction pattern (inset) bracket the two rings used to make the dark-field micrograph. The coating is BCC Y_2O_3 with $a_0 = 1.0602$ nm. (B) Energy dispersive X-ray spectrum of the Y_2O_3 coating. A small amount of Al and Si may be present at discrete locations in the coating.
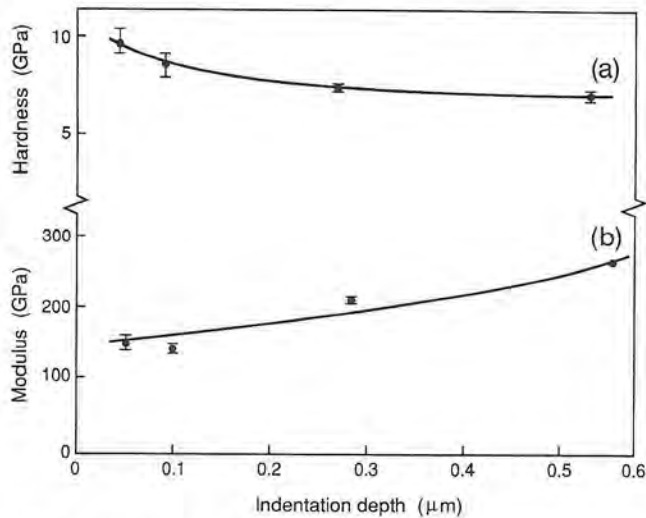
Fig. 4. (a) Hardness vs indentation depth as determined by the nanoindentation technique. The hardness for ~0.5 μm deep indentation is 7.5 GPa. Higher hardness at smaller indentation depths is due to the indentation size effect. (b) Elastic modulus of Y_2O_3 vs indentation depth. The modulus at small indentation depths (0.05 to 0.1 μm) is characteristic of bulk Y_2O_3.

Fig. 6. Normalized stress vs displacement curves for TiAl/Nb laminates. The area under each curve represents the work of rupture, χ. The letters on each curve correspond to the in situ SEM micrographs shown in Figs. 7 to 9.

the residual stress. TiAl has an appreciably larger thermal expansion coefficient than niobium, causing the reinforcement to be under compressive stress that is sufficient to cause yielding. Therefore, σ_R is approximately equal to the yield strength of niobium. The maximum nominal stress that develops in the reinforcement is controlled by strain hardening and experimentally is found to be $\sigma \approx 1.7\sigma_0$.[7] Consequently, for a reinforcement thickness, $R \approx 125$ μm and a flow stress $\sigma_0 \approx 140$ MPa,[7] the available energy release rate $G_{ss} \approx 90$ J·m^{-2}. Comparison with the debond energies ($\Gamma_i \approx 25$ J·m^{-2} for the oxide coatings and $\Gamma_i \approx 45$ J·m^{-2} for the σ-phase) validates that the available energy release rate is sufficient to cause the debonding. It is also noted that in the absence

of oxide coatings, the relatively large debond resistance $\Gamma \approx 45$ J·m^{-2}, as governed by the σ-phase reaction product layer, elevates the stress needed to initiate the debond stress. The observed arrest of the debond is dominated by frictional sliding that limits the G available to the debond, as found in fiber-reinforced composites.[26] Similarly, frictional sliding restricts the length of reinforcement that participates to plastic deformation. The information on the sliding stress, inferred from ℓ, rationalizes the larger debond lengths obtained with Y_2O_3 coatings compared to Al_2O_3. Similarly to results obtained on fiber-reinforced intermetallics,[14] the work of rupture is governed by frictional sliding of the interface. In this situation yttria seems to be the most efficient coating for promoting a relatively low interface friction (Table I).

V. Concluding Remarks

It is now well established that *debonding* and *low interfacial friction* are prerequisites for high toughness in brittle-matrix composites reinforced with ductile phases. In addition to the mechanical property requirements on the interfaces, the detrimental reactivity of intermetallic matrices with most reinforcing metal phases justifies the use of coatings such as Al_2O_3 and Y_2O_3 to act as a stable diffusion barrier. As a general guideline, debonding of bridging reinforcements is promoted by a combination of low interface fracture energy and large axial stress in the reinforcement. Once debonding is established, the toughness is governed by the interface frictional stress and is independent of the interface fracture energy.

The interfacial fracture energy of Al_2O_3 or Y_2O_3 coatings on some refractory metals, including niobium, has been experimentally determined to be sufficiently low to satisfy debonding. In the case of niobium reinforcements, Y_2O_3 coatings appear to provide a lower sliding stress than Al_2O_3. However, more studies are needed to validate this trend. Finally in closing, it should be noted that for short reinforcements, debonding is obviously detrimental if the debond crack goes around the reinforcement since in such case the bridging contributions would be lost.

Fig. 5. Crack extension occurring across the TiAl/Al_2O_3 interface without debonding.
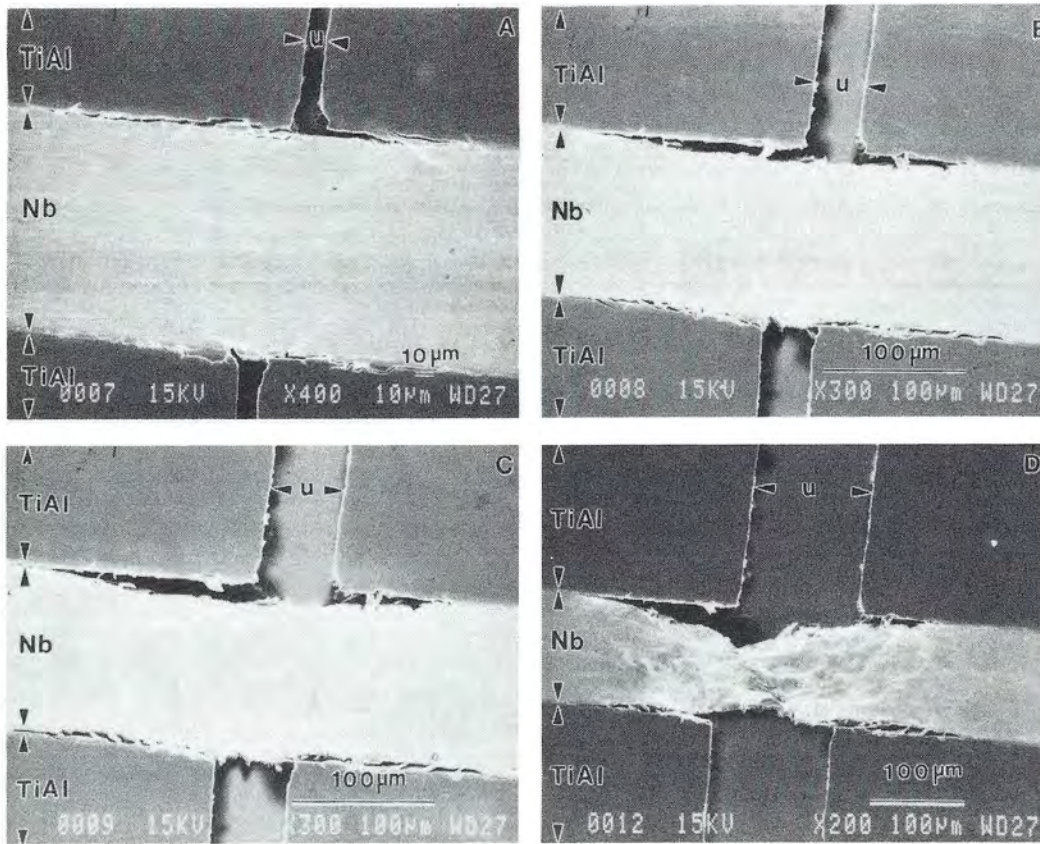
Fig. 7. In situ SEM micrographs of the TiAl-uncoated Nb test specimen. Debonding along the σ-phase is limited, resulting in necking of the niobium at small crack opening displacements. Compare the micrometer markers in Figs. 7 to 9.
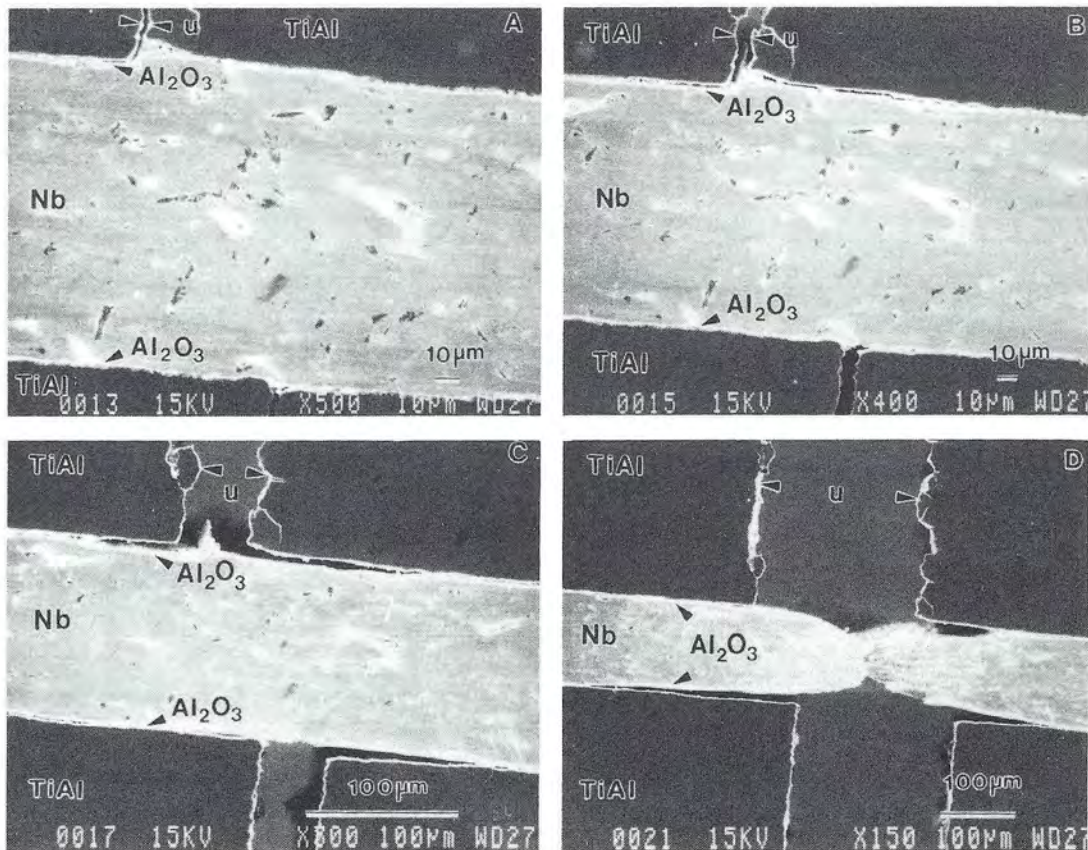

Fig. 8. In situ SEM micrographs of the TiAl–Al$_2$O$_3$ coated Nb test specimen. The debond length and crack opening displacement are larger than in Fig. 7.
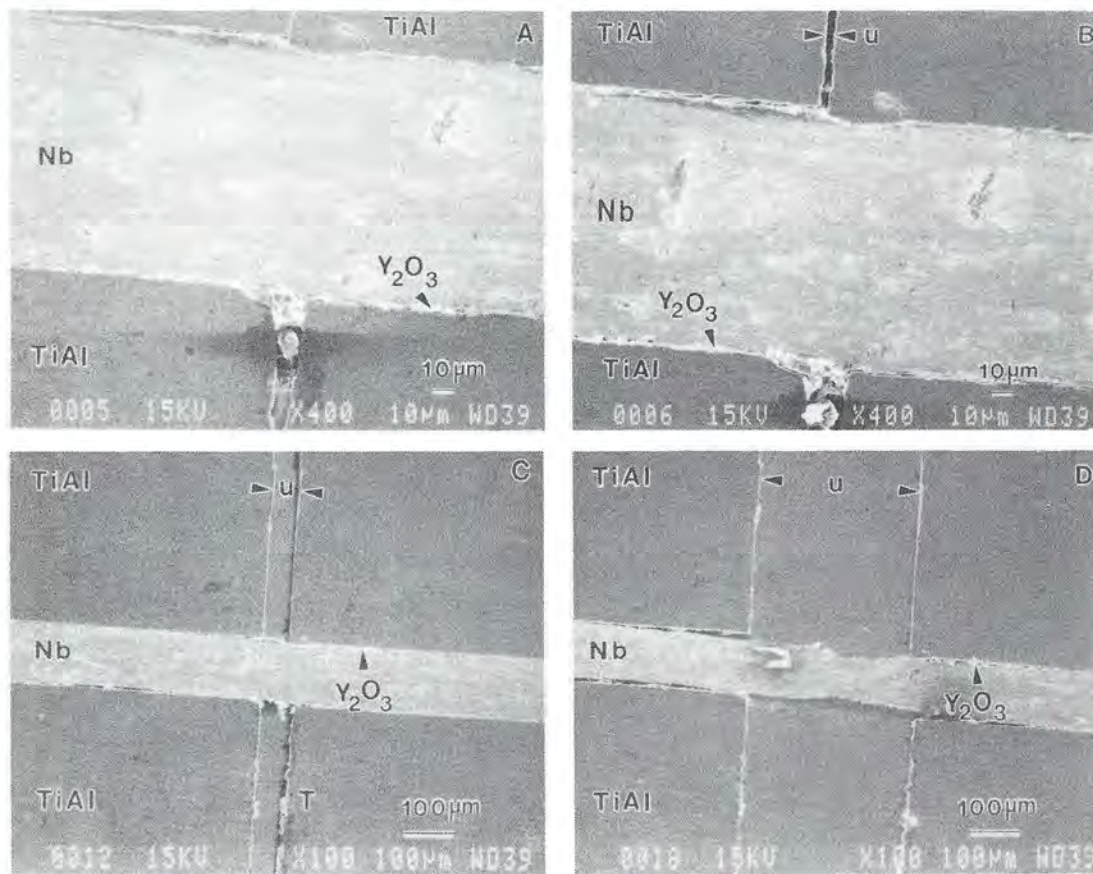
Fig. 9. In situ SEM micrographs of the TiAl–Y_2O_3 coated Nb test specimen. Extensive debonding has resulted in a large crack opening displacement.

Table I. Experimental Results on γ-TiAl/Nb

	Interface fracture energy, Γ_i (J·m^{-2})	Debond length, d/R	Gauge length, ℓ/R	Interface shear stress, τ (MPa)*	Work of rupture, χ	Normalized work, $\xi^\dagger$
TiAl/Nb (uncoated)	45	2.5	2	35	2.5	1.2
TiAl/Nb (Al_2O_3 coating)	25	5	3.5	20	4	1.1
TiAl/Nb (Y_2O_3 coating)	25	12	7	10	8	1.1

*Inferred from Eq. (3). †Inferred from Eq. (2).
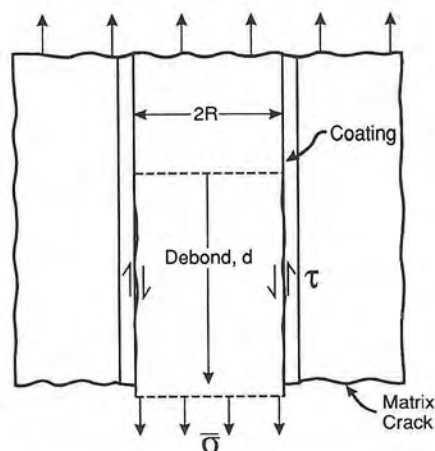
Fig. 10. Schematic of the debonding process, illustrating the mode II nature of the debond with debonding induced at the coating/reinforcement interface, followed by frictional sliding in the debond wake.

References

[1] A. G. Evans, "Perspective on the Development of High-Toughness Ceramics," *J. Am. Ceram. Soc.*, **73**, 187–205 (1990).

[2] C.-H. Hseuh, "Analytical Evaluation of Interfacial Shear Strength for Fiber-Reinforced Composites," *J. Am. Ceram. Soc.*, **71**, 490–93 (1988).

[3] V. Gupta, A. S. Argon, and J. A. Cornie, *J. Mater. Sci.*, **24**, 2031 (1989).

[4] C. K. Elliott, G. R. Odette, G. E. Lucas, and J. W. Sheckherd, "Toughening Mechanisms in Intermetallics γ-TiAl Alloys Containing Ductile Phases," *Mater. Res. Soc. Symp. Proc.*, **120**, 95–102 (1988).

[5] G. R. Odette, H. E. Dève, C. K. Elliott, A. Hasegawa, and G. E. Lucas, "The Influence of the Reaction Layer Structure and Properties on Ductile Phase Toughening in Titanium Aluminide–Niobium Composites"; p. 443 in *Interfaces in Ceramic and Metal Composites*. Edited by R. Y. Lin *et al.* The Metallurgical Society, Warrendale, PA, 1990.

[6] H. C. Cao, B. J. Dalgleish, H. E. Dève, C. Elliott, A. G. Evans, R. Mehrabian, and G. R. Odette, "A Test Procedure for Characterizing the Toughening of Brittle Intermetallics by Ductile Reinforcements," *Acta Metall.*, **37**, 2969–77 (1989).

[7] H. E. Dève, A. G. Evans, G. R. Odette, R. Mehrabian, M. L. Emiliani, and R. J. Hecht, "Ductile Reinforcement Toughening of γ-TiAl: Effects of Debonding and Ductility," *Acta Metall.*, **38**, 1491–502 (1990).

[8] M. F. Ashby, F. J. Blunt, and M. Bannister, "Flow Characteristics of Highly Constrained Metal Wires," *Acta Metall.*, **37**, 1847–57 (1989).

[9] L. S. Sigl, A. G. Evans, P. A. Mataga, R. M. McMeeking, and B. J. Dalgleish, "On the Toughness of Brittle Materials Reinforced with a Ductile Phase," *Acta Metall.*, **36**, 946 (1988).

[10] V. D. Krstic, "On the Fracture of Brittle Matrix/Ductile-Particle Composites," *Philos. Mag.*, **A48**, 695–708 (1983).

[11] B. Budiansky, J. C. Amazigo, and A. G. Evans, "Small Scale Bridging and the Fracture Toughness of Particulate-Reinforced Ceramics," *J. Mech. Phys. Solids*, **36**, 167–87 (1988).

[12] A. G. Evans and R. M. McMeeking, "On the Toughening of Ceramics by Strong Reinforcements," *Acta Metall.*, **34**, 2435 (1986).

[13] P. A. Mataga, "Deformation of Crack-Bridging Ductile Reinforcements in Toughened Brittle Materials," *Acta Metall.*, **37**, 3349 (1989).

[14] H. E. Dève and M. Maloney, "On the Toughening of Intermetallics with Ductile Fibers: Role of Interfaces," *Acta Metall.*, **39**, 2275 (1991).

[15] H. E. Dève and S. Schmauder, "Role of Interface Properties on the Toughness of Brittle Matrix Composites Reinforced with Ductile Phases"; unpublished work.

[16] W. Mader and M. Rühle, "Electron Microscopy Studies of Defects at Diffusion-Bonded Nb/Al$_2$O$_3$ Interfaces," *Acta Metall.*, **37**, 853–66 (1989).

[17] M. Kuwabara, J. C. H. Spence, and M. Rühle, "On the Atomic Structure of the Nb/Al$_2$O$_3$ Interface and the Growth of Al$_2$O$_3$ Particles," *J. Mater. Res.*, **4**, 972–77 (1989).

[18] J. Kennedy and G. Geschwind in *Titanium Science and Technology*, Vol. 4; p. 2299. Edited by R. I. Jaffee and H. M. Burte. Plenum Press, New York, 1973.

[19] A. Bartlett, M. Rühle, and A. G. Evans; unpublished work.

[20] M. Abouelleil, L. Conopask, W. Nighan, W. Roman, and D. Price, "Nano-indentation Hardness of Thin Films"; pp. 457–75 in Ceramic Transactions, Vol. 15, *Materials and Processes for Microelectronic Systems*. Edited by K. M. Nair, R. Pohanka, and R. C. Buchanan. American Ceramic Society, Westerville, OH, 1990.

[21] P. G. Charalambides, J. Lund, A. G. Evans, and R. M. McMeeking, "A Test Specimen for Determining the Fracture Resistance of Bimaterial Interfaces," *J. Appl. Mech.*, **56**, 77–82 (1989).

[22] G. Fantoi, G. Orange, K. Liang, and E. Gillet, "Effect of Nonstoichiometry of Fracture Toughness and Hardness of Yttrium Oxide Ceramics," *J. Am. Ceram. Soc.*, **72**, 1562 (1989).

[23] J. Haggerty, "Production of Fibers by a Floating Zone Fiber Drawing Technique," Final Report, NASA Report No. CR-120984, May 1972, p. 52.

[24] M. Y. He and J. W. Hutchinson, "Crack Deflection at an Interface Between Dissimilar Elastic Materials," *Int. J. Solids Struct.*, **25**, 1337 (1989).

[25] J. W. Hutchinson and H. Jensen, "Models of Fiber Debonding and Pullout in Brittle Composite with Friction," *Mech. Mater.*, **9**, 139 (1990).

[26] P. Charalambides, H. C. Cao, J. Lund, and A. G. Evans, "Development of a Test Method of Measuring the Mixed Mode Fracture Resistance of Bimaterial Interfaces," *Mech. Mater.*, **8**, 269–83 (1990).   □

Debond coating requirements for brittle matrix composites

M.L. EMILIANI
Pratt and Whitney, Materials Engineering, P.O. Box 109600, Mail Stop 706-06, West Palm Beach, FL 33410, USA

The cause of improved fracture toughness in Y_2O_3-coated niobium-toughened TiAl relative to either uncoated niobium or Al_2O_3-coated niobium was examined. Reactively sputtered Y_2O_3 coatings, 1–2 μm thick, were deposited on to rock salt (NaCl), polished single-crystal (0001) Al_2O_3, and polished polycrystalline niobium. Sputtered niobium coatings, 1–2 μm thick, were also deposited on to polished single-crystal Y_2O_3 substrates for comparison. The oxide coating was characterized and consisted of stoichiometric b c c Y_2O_3 with $a_0 = 1.0602$ nm. Indentation tests were performed to correlate the fracture toughness and debond characteristics of as-deposited Y_2O_3 coatings on Al_2O_3 and polycrystalline niobium, and niobium coatings on single-crystal Y_2O_3, to that found in TiAl/Nb and Al_2O_3/Al_2O_3 laminates. The calculated fracture toughness of sputtered Y_2O_3 on sapphire was similar to reported values for bulk Y_2O_3. However, a wide variation in interfacial fracture toughness was obtained by indentation methods, and is attributed to the microstructure of as-deposited coatings and to weak bonding between as-deposited yttria and the sapphire substrate. These results are related to factors that affect debonding and fracture toughness of brittle matrix composites. Reactive and non-reactive metal/ceramic systems were reviewed in an effort to understand why Y_2O_3 coatings perform well. It is postulated that yttrium oxide coatings applied to niobium have an atomically sharp interface that has a lower fracture energy compared to Nb/Al_2O_3, resulting in improved interfacial debonding and composite fracture toughness.

1. Introduction

Fibre coatings will probably be required for brittle matrix composites in order to improve composite fracture toughness or reduce fibre/matrix interaction at elevated temperatures [1–4]. Coatings have been successfully used to improve the thermochemical compatibility or fracture behaviour of a few ductile and brittle matrix systems including boron- [4] or SiC- [5] reinforced titanium or aluminium alloys and SiC-reinforced lithium aluminosilicate (AS) glass [2]. The purpose of this research was to identify protective and debond coatings that improve the toughness of intermetallic and ceramic matrix composites, and contribute to a generalized understanding of the requirements for successful debond coatings. The latter may allow the development of predictive guidelines for future coating selections in other composite systems.

Two composite systems, niobium-reinforced TiAl and Al_2O_3-reinforced Al_2O_3, have exhibited improved fracture toughness through the use of chemically compatible interfacial coatings [6, 7]. An elastic indentation technique, Hertzian cone cracking, has been used to assess the specific fracture energy, Γ_i, of Al_2O_3 laminate composites containing various interfacial coatings [7]. Yttria interfacial coatings, applied by sputtering or sol–gel, exhibit a specific fracture energy of 25 J m^{-2}. This is approximately five times

greater than that achieved with sputtered molybdenum coatings [8], and results in incomplete debonding. Reaction between the Al_2O_3 substrate and Y_2O_3 to form YAG ($Y_3Al_5O_{12}$) was found to be responsible for the high fracture energy.

The debonding characteristics of a model niobium-reinforced TiAl composite have been evaluated using uncoated niobium, Al_2O_3-coated niobium, and Y_2O_3-coated niobium [6]. Uniaxial tension tests of pre-cracked TiAl/Nb laminates were performed *in situ* in the scanning electron microscope. The Y_2O_3 coating produced the lowest specific fracture energy, thus allowing extensive debonding which permitted plastic deformation of the niobium over a large volume and resulting in a high work of rupture. The measured fracture toughness is thought to be due to the presence of an atomically sharp Y_2O_3/Nb interface similar to that found in Al_2O_3/Nb couples [9].

The present study examines as-sputtered Y_2O_3 coatings deposited on to rock salt (NaCl), single-crystal (0001) Al_2O_3, and polycrystalline niobium to understand better why this coating improves the toughness of niobium-reinforced TiAl. As-deposited yttria coatings were characterized by scanning electron microscopy (SEM), energy dispersive spectroscopy (EDS), transmission electron microscopy (TEM), X-ray photoelectron spectroscopy (XPS),

secondary ion mass spectroscopy (SIMS), X-ray diffraction (XRD), and indentation techniques. Nanoindenter® and Vickers indentation tests [10] were used to determine the fracture toughness, K_c, interfacial fracture toughness $K_{c,i}$, and specific fracture energy, Γ_i, of as-sputtered coatings. The results were compared to that found for diffusion-bonded Al_2O_3/Al_2O_3 and TiAl/Nb laminates [6, 7]. In addition, niobium coatings, 1–2 µm thick, were deposited on to polished single-crystal Y_2O_3 wafers by sputtering to compare debonding behaviour. A TEM study was also performed on Y_2O_3-coated niobium-reinforced TiAl laminate.

2. Experimental procedure
2.1. Sputtered coatings
Yttrium oxide coatings were deposited on to polished single-crystal Al_2O_3 4 mm thick, commercial purity polycrystalline niobium foil 125 µm thick, and rock salt substrates. Prior to coating, Al_2O_3 and niobium substrates were ultrasonically cleaned in soapy water, rinsed in water, rinsed in ethyl alcohol, and dried by forced hot air. Sputtering was performed in a Plasma-Therm Model AMNS-1000E 1000 W radio frequency diode sputtering unit equipped with dual-opposed 6 in (~ 15.24 cm) diameter yttrium metal targets (99.9 wt % purity). A 142 µm monofilament SiC fibre (Textron SCS-6) was also coated to determine coating thickness and microstructure by fractography. Yttrium oxide coatings were deposited by reactive sputtering using a 50%–50% mixture of research grade argon and oxygen at a total working gas pressure of $P_T = 6$ m torr. The substrates were not externally cooled, heated, or biased during sputtering. The top and bottom targets were maintained at 3000 and 500 V, respectively. Deposition of Y_2O_3 for ~ 10 h resulted in coatings 1–2 µm thick. The only equilibrium oxide phase formed according to the Y–O phase diagram is Y_2O_3 [11].

Niobium coatings were sputter deposited on to polished Y_2O_3 wafers ~ 0.5 mm thick using research-grade argon at $P_T = 6$ m torr and 99.5 wt % purity niobium metal targets maintained at 5000 and 500 V. The resultant coatings were 3–4 µm thick.

2.2. Indentation tests to determine coating hardness and elastic modulus
The hardness and elastic modulus of as-sputtered coatings were determined using a Nano Instruments Inc. Nanoindenter® [12]. This instrument is a sub-micrometre indentation tester that uses a triangular diamond indentor with the same projected area-to-depth ratio as the Vickers square pyramid indentor. The maximum load that can be applied by this technique is 0.1 N. Coating hardness and modulus were determined by taking five or more indentations at depths ranging from 0.04–0.7 µm.

2.3. Indentation tests to determine coating fracture properties
Nanoindenter® and Vickers indentation tests were used to initiate coating fracture or interfacial debonding in Y_2O_3-coated Al_2O_3, Y_2O_3-coated niobium and niobium coated Y_2O_3. All coatings were evaluated in the as-sputtered condition. Loads greater than 0.1 N and up to 10 N were applied using a Vickers diamond indentor. Six measurements are typically made at each indentation depth. While there are numerous relationships for obtaining quantitative values of fracture toughness [13], only selected equations are applied in the present study. The equations used to determine coating fracture toughness, K_c, interfacial fracture toughness, $K_{c,i}$, and specific fracture energy, Γ_i are briefly reviewed.

The fracture toughness of thin coatings can be determined by measuring radial crack lengths and the dimensions of indentations made by indentation tests [13, 14]. Equations to determine fracture toughness have been empirically determined assuming the crack shape is radial–median (i.e. "halfpenny") or Palmqvist
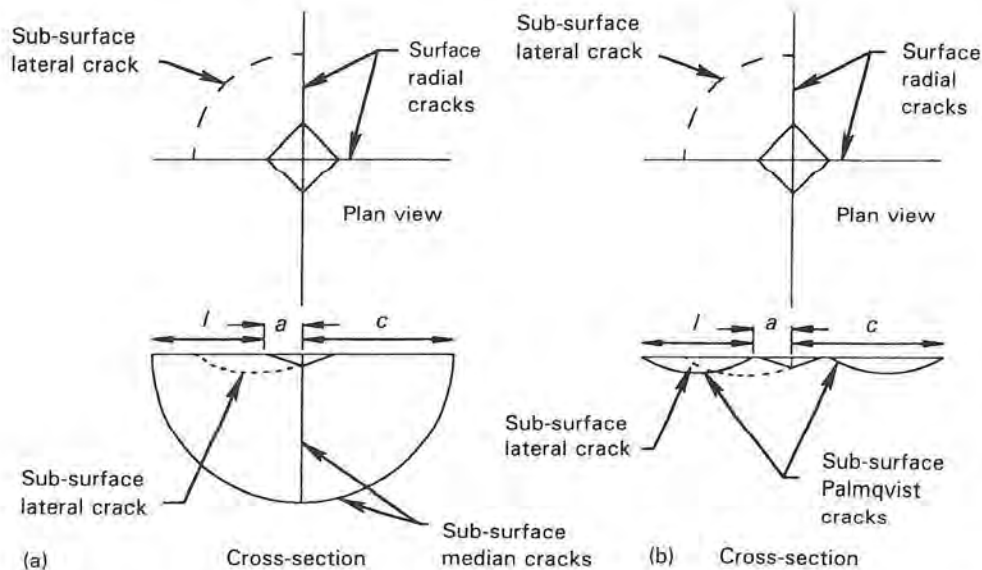

Figure 1 Schematic diagrams of Vickers indentations resulting in the formation of (a) radial–median and (b) Palmqvist cracks [14].

[14]. The critical indentation and crack-related dimensions are the indentation half-diagonal length, a, radial surface crack length, C, and the Palmqvist surface crack length, l (Fig. 1). Equations to determine fracture toughness take the following general form for halfpenny (Equation 1) and Palmqvist (Equation 2) shaped cracks [14]

$$K_c = k\frac{P}{aC^{1/2}} \quad (1)$$

$$K_c = k\,(E/H_v)^{2/5}\frac{P}{al^{1/2}} \quad (2)$$

where k is a constant typically between 0.001 and 0.5, P is the applied indentor load (N), H_v is the Vickers microhardness (GPa), E is the elastic modulus (GPa), and a, C, l are the indentation and crack related-dimensions (m), as shown in Fig. 1. Values of K_c for selected glass and oxide ceramics have been compared to K_{Ic} fracture toughness of the same materials by traditional mechanical testing techniques [13]. The average results for both types of test were reported to be within $\pm$ 30%. Thus, the values of fracture toughness obtained by indentation methods are comparable to that obtained by more elaborate mechanical tests. In general, averaged values of fracture toughness calculated using either halfpenny or Palmqvist-based equations yield similar results.

The interfacial fracture toughness, $K_{c,i}$, of thin coatings can also be determined from indentation tests [15]. This information also provides a measure of coating adhesion to the substrate, and is required to determine the specific fracture energy, Γ_i, of the interface. The interfacial fracture toughness can be represented by

$$K_{c,i} = k\,t^{3/2}\,H_v^{1/2}\frac{(1 - P_0/P)P^{1/2}}{C^2} \quad (3)$$

where k is a constant determined to be 0.16 in the present study, t is the coating thickness (m), H_v is the Vickers hardness of the coating (GPa), P_0 is the threshold load for crack formation (MN), P is the maximum indentor load (MN), and C is the lateral crack length (m). Knowledge of the fracture toughness allows calculation of the specific fracture energy, Γ_i, and provides a basis for understanding the contribution of coatings to interfacial debonding. The fracture toughness for a Mode I (tensile) crack is [16]

$$K_{Ic} = Y\,\sigma\,(\pi a^{1/2}) \quad (4)$$

where Y is the geometric crack factor (typically $= \pi^{1/2}$ for a halfpenny-shaped crack), σ is the applied stress (N), and a is the half-crack length (m). The Griffith relationship for plane (biaxial) stress ($\sigma_z = 0$) is

$$\sigma = (2\,E\,\gamma_s/\pi\,a)^{1/2} \quad (5)$$

Combining Equations 4 and 5 yields the specific fracture energy

$$\gamma_s = \frac{K_{Ic}^2}{2\,Y\,E} = \Gamma_i \quad (6)$$

Thus, the specific fracture energy (in $J\,m^{-2}$), depends only upon the fracture toughness (where $K_{Ic} = K_c$ or $K_{c,i}$), geometric crack factor, and elastic modulus of the coating. The latter may vary depending upon thickness.

3. Results
3.1. Characterization of sputtered Y_2O_3 coatings

X-ray diffraction of yttria-coated sapphire wafer was performed using a Huber Model 651 Guinier thin-film goniometer. The resulting spectrum corresponds to b c c Y_2O_3 (JCPDS pattern 25-1200), Fig. 2. X-ray
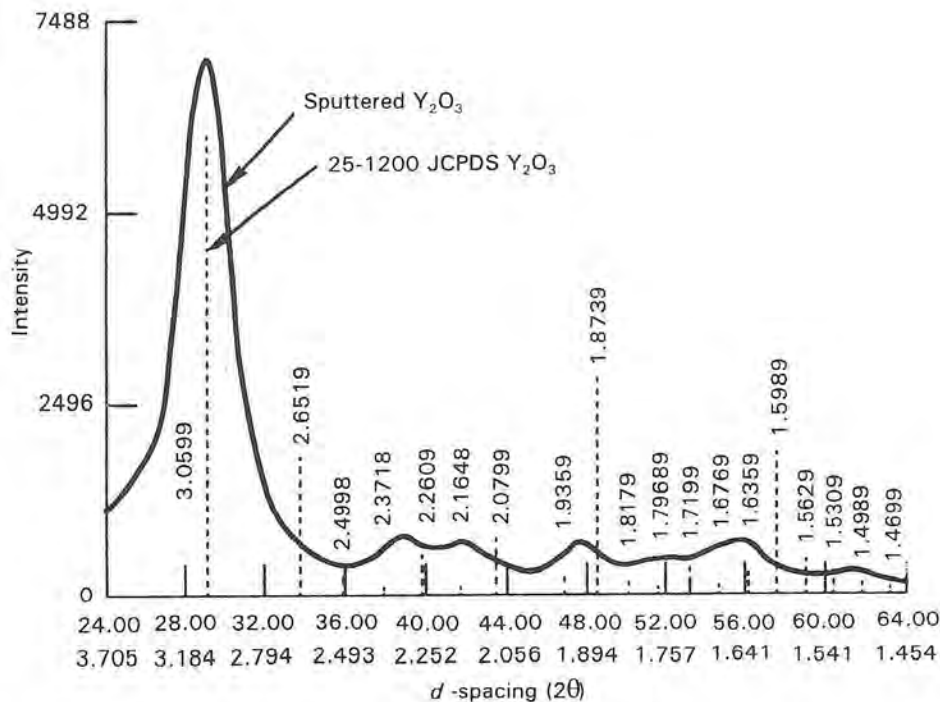

Figure 2 X-ray diffraction pattern of reactively sputtered Y_2O_3 showing good correlation with the JCPDS reference pattern (vertical lines).

5282

photoelectron spectroscopy was performed using a PHI Model 5400 multiprobe. The surface contained excess physisorbed hydrocarbon or carbon and oxygen or oxide due to exposure to the ambient. Oxygen in the form of OH or H_2O was detected. Argon sputtering to a depth of ~ 5 nm removed gross contaminants, resulting in decreased carbon and increased oxygen signals. Additional sputtering to a depth of 10 nm showed only yttrium and oxygen (Fig. 3). Secondary ion mass spectroscopy (SIMS) data were obtained using a Kratos Ion Microprobe. SIMS showed that boron, carbon, aluminium, silicon, potassium, titanium, iron, niobium and neodymium were present in the coating ~ 10 nm below the free surface, all at levels of < 0.1 at %.

The surface finish of Y_2O_3 coatings on SiC fibres was examined by SEM and found faithfully to replicate the surface finish of the substrate which consists of nodules characteristic of coatings deposited by chemical vapour deposition (Fig. 4). Coating microstructure was characterized by SEM of fractured SiC fibres and found to consist of columnar grains which extend through the thickness of the coating. This is typical of that found in sputtered coatings deposited at low homologous temperature (T/T_M, where T is the substrate temperature and T_M the melting temperature of Y_2O_3) [17, 18]. For $T_M(Y_2O_3) = 2400\,°C$ and assuming $T_{substrate} \approx 300\,°C$, $T/T_M \approx 0.12$. These coatings were found to correspond well to the Zone 1 microstructure as described by Thornton [18].

Electron-transparent Y_2O_3 samples for TEM were produced by depositing a thin coating on to rock salt, dissolving the substrate in water, then collecting the oxide film on a copper grid. Y_2O_3 samples were
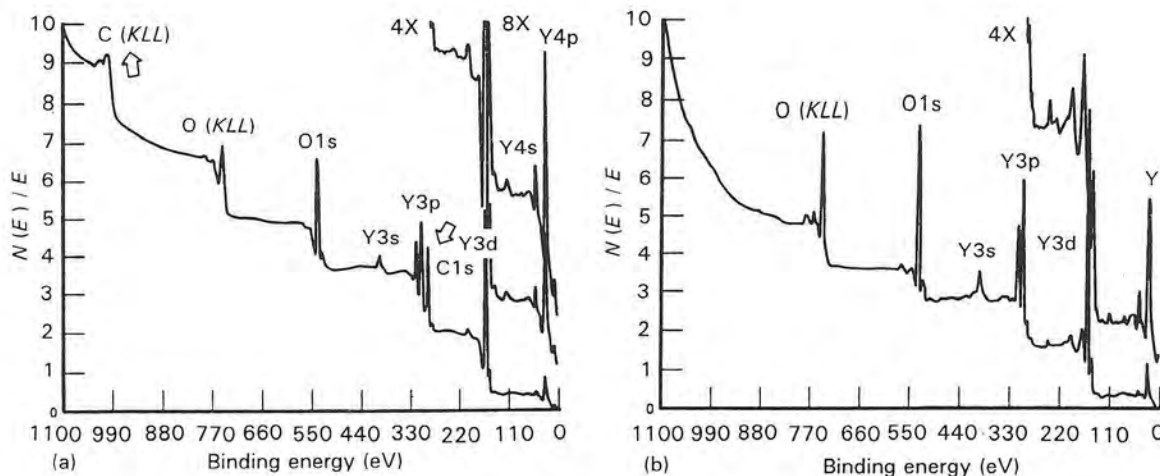
Figure 3 XPS spectra of Y_2O_3 coating, (a) as-received, and (b) 10 nm below the free surface. The carbon signal is prominent in as-received samples (arrowed), while only yttrium and oxygen are present 10 nm below the free surface.
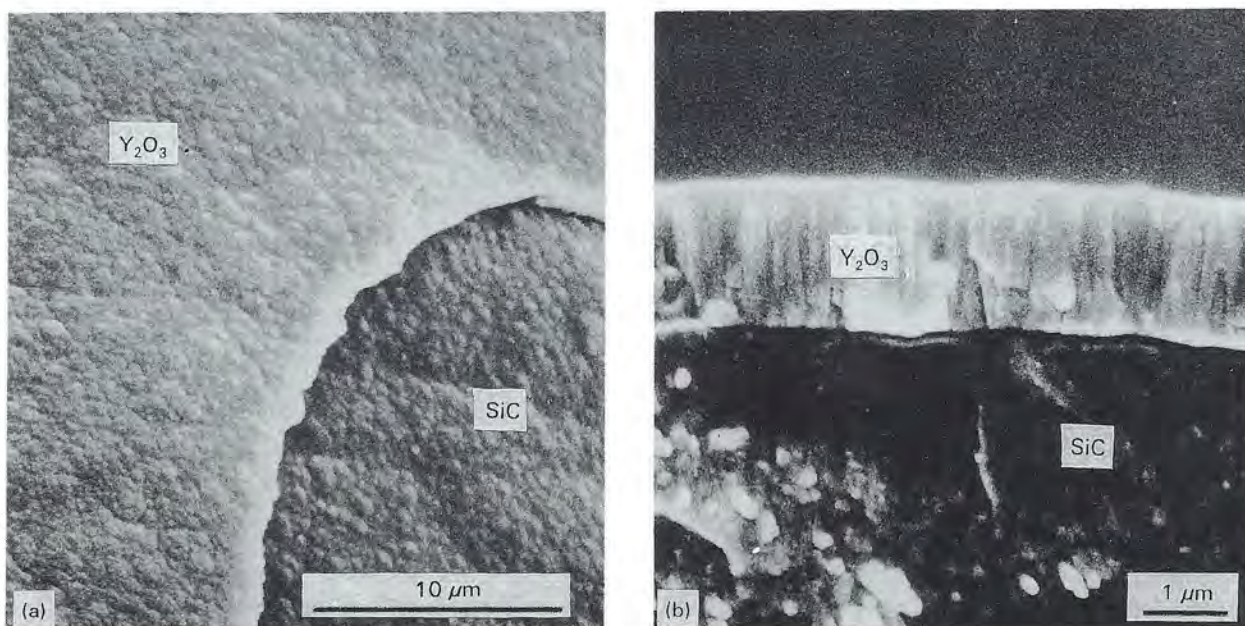
Figure 4 (a) Scanning electron micrograph showing the surface finish of as-deposited Y_2O_3 coating which has replicated the surface finish of the SiC fibre. (b) Scanning electron micrograph showing the thickness and structure of as-deposited Y_2O_3 coating. The columnar morphology of the coating is evident.
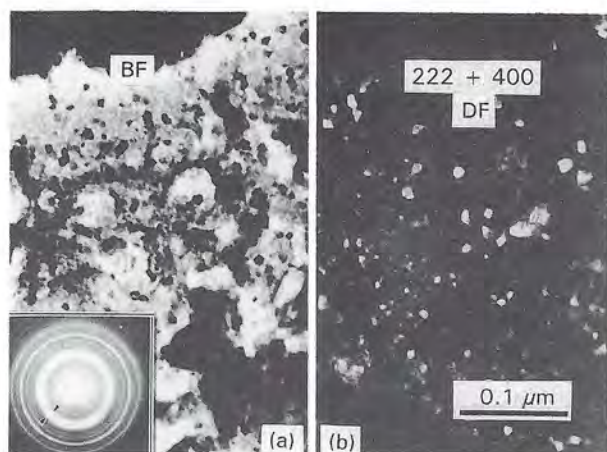
Figure 5 (a) Bright-field (BF) and (b) dark-field (DF) transmission electron micrographs of as-sputtered Y_2O_3. Arrows on the selected-area diffraction pattern (inset) bracket the two rings used to make the dark-field micrograph. The coating consists of b c c Y_2O_3 with $a_0 = 1.0602$ nm.
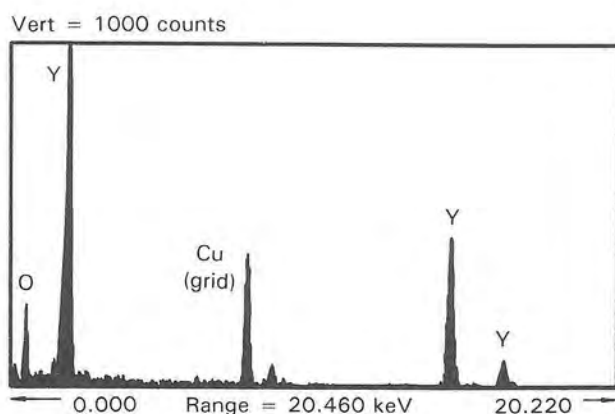

Figure 6 Energy-dispersive X-ray spectrum of the Y_2O_3 coating.

Figure 7 Light micrograph of a TiAl/Nb laminate test specimen after diffusion bonding at 1066 °C for 4 h and 10 MPa pressure. Note the absence of interfacial reaction products.

Figure 8 Transmission electron micrograph of a portion of the Y_2O_3 coating and selected-area electron diffraction pattern (inset) from a TiAl/Nb laminate. Note the grains remain columnar after hot-pressing at 1066 °C for 4 h.

examined using a Philips 400T at 120 kV and equipped with a Kevex Quantum energy-dispersive X-ray spectrometer. Direct imaging of the coating microstructure through-thickness by transmission electron microscopy showed it contained a homogeneous distribution of fine grains 10–30 nm diameter (Fig. 5). Energy dispersive spectroscopy of the coating showed yttrium and oxygen (Fig. 6). Selected-area electron diffraction patterns (Fig. 5, inset) contained well-defined continuous rings with spacings characteristic of body-centred cubic Y_2O_3 (Pearson Symbol cI80, Mn_2O_3 prototype structure), with a lattice parameter of $a_0 = 1.0602$ nm.

Yttrium oxide-coated niobium foils were diffusion bonded between two TiAl plates in vacuum at 1066 °C under a pressure of 10 MPa for 4 h (Fig. 7) [6]. The resulting laminate was prepared for TEM by sectioning small wafers perpendicular to the TiAl/Y_2O_3/Nb interface using a low-speed diamond saw. Most of the samples fractured during sectioning, grinding to final thickness, or ion milling due to the low specific fracture energy of the Y_2O_3/Nb interface.

The interface between Y_2O_3 and niobium is of interest because it is the location where debonding

occurs. Unfortunately, it could not be observed due to decohesion of the interface. The Y_2O_3/TiAl interface is more strongly bonded and therefore could be examined by TEM. The most interesting aspect of this interface is the morphology of Y_2O_3 coating (Fig. 8), which has been exposed to 1066 °C for 4 h. The Y_2O_3 coating retains a columnar morphology, with columns ~0.15 μm wide and extending through the entire thickness of the coating. Reflections from selected-area diffraction patterns contained intense arcs. This, coupled with the shape of individual grains, suggests that the columnar Y_2O_3 grains contain a dense substructure of low-angle grain boundaries that have begun to coalesce. Thus, diffusion bonding resulted in
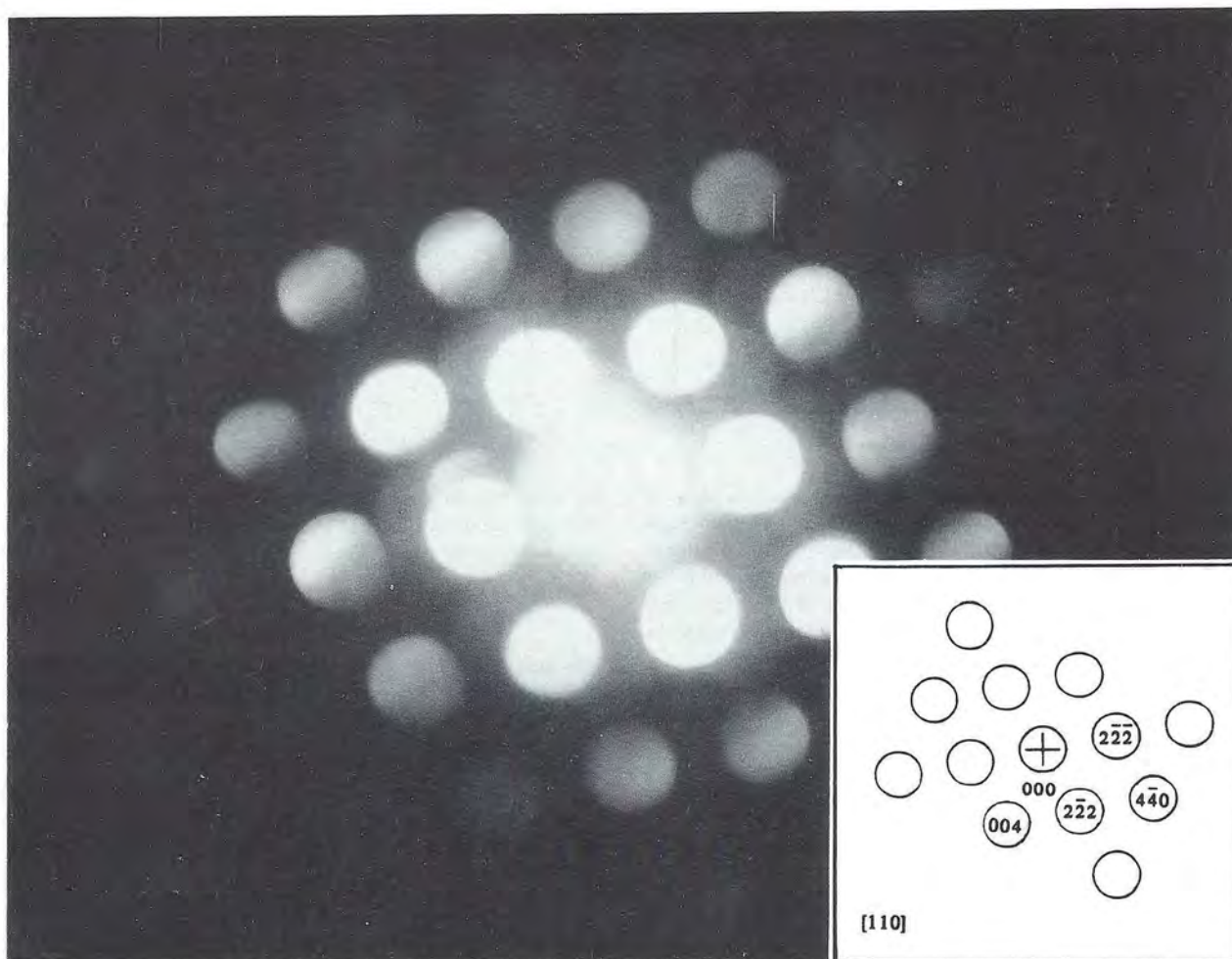
Figure 9 Convergent-beam electron diffraction pattern of Y_2O_3 and corresponding computer-generated [1 1 0] zone axis pattern.

little or no grain growth of the oxide coating. Selected-area (Fig. 8, inset) and convergent beam electron diffraction (Fig. 9) of the coating shows it consists of cubic Y_2O_3 with lattice parameter of $a_0 = 1.0602$ nm, and is in agreement with the results for as-deposited Y_2O_3. Direct imaging and EDS did not reveal extensive chemical reaction between Y_2O_3 and TiAl.

3.2. Indentation-derived coating hardness and elastic modulus

The hardness of as-sputtered yttria coatings on polished sapphire substrates was determined using the Nanoindenter® by taking five or more indentations at depths ranging from 0.05–0.5 μm. Fig. 10 shows the variation in coating hardness as a function of indentation depth. The rapid increase in hardness with decreasing indentation depth is due to the well-known indentation size effect [19]. However, at indentation depths ≥ 0.4 μm the hardness remains nearly constant at ~ 750 kg mm^{-2} (7.5 GPa). This is in good agreement with previous results for bulk Y_2O_3 [20].

The hardness of as-sputtered Y_2O_3 coating on commercially pure polycrystalline niobium was also determined using the Nanoindenter® (Fig. 11). There is a dramatic decrease at ~ 0.6 μm depth due to plastic deformation of the soft niobium substrate (film–substrate effect, FSE) [21]. Conversely, a rapid increase in hardness was found at indentation depths
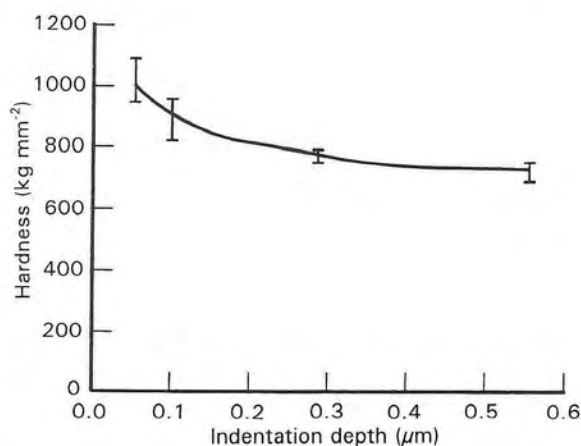
Figure 10 Hardness versus indentation depth as determined by the nanoindentation technique. The hardness of Y_2O_3 at ~ 0.5 μm deep indentations is ~ 750 kg mm^{-2} (7.5 GPa). Higher hardness at smaller indentation depths are due to the indentation size effect [19].

< 0.1 μm due to the indentation size effect (ISE) [19]. The hardness of the Y_2O_3 coating measured at indentation depths between 0.1 μm $< d < 0.5$ μm is 800–850 kg mm^{-2} (8–8.5 GPa). This is approximately the same hardness as that measured for as-sputtered Y_2O_3 on single-crystal Al_2O_3, and agrees with that reported for bulk Y_2O_3 [20, 22]. Thus, accurate values of Y_2O_3 coating hardness independent of the sub-
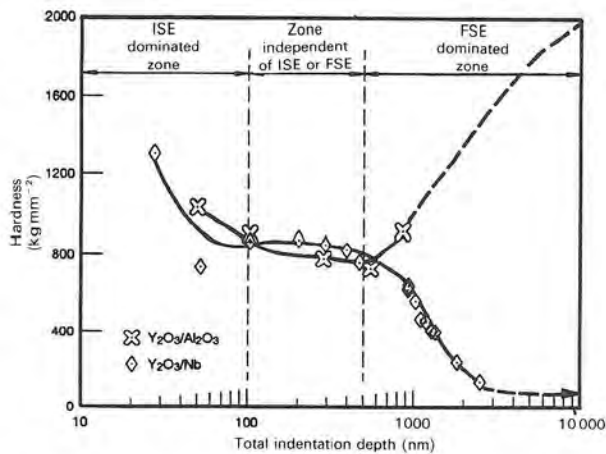
5285

Figure 11 Plot of Nanoindenter® hardness versus indentation depth for as-sputtered Y_2O_3 coating on Al_2O_3 and niobium. High hardness values are obtained at indentation depths < 0.1 μm due to the indentation size effect (ISE) [14], while the coating hardness is dominated by interaction with the substrate for $d \gtrsim 0.8$ μm (film substrate effect, FSE) [21]. Note the good correlation in coating hardness for indentations depths between 0.1 and 0.5 μm.
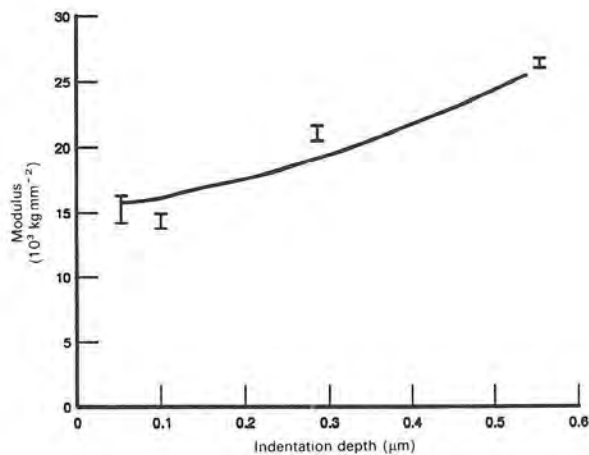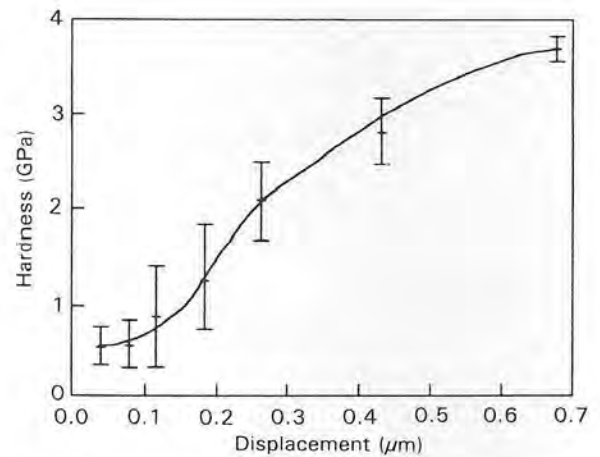

Figure 13 Hardness versus indentation depth as determined by the nanoindentation technique. The hardness of niobium at ~0.4 μm deep indentations is 2.8 GPa.

Figure 12 Elastic modulus of Y_2O_3 versus indentation depth. The modulus at small indentation depths (0.05–0.1 μm) is characteristic of bulk Y_2O_3.
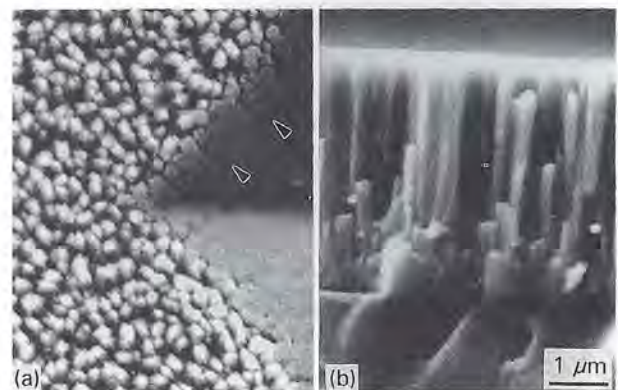

Figure 14 (a) Scanning electron micrograph showing the surface finish of as-deposited niobium coating which consists of domed tops ~0.2 μm in diameter. Note the Vickers indentation which made only partial contact with the coating at the edged (arrowed). (b) Scanning electron micrograph showing the thickness and columnar structure of as-deposited niobium.

strate material were determined using the Nanoindenter® at indentation depths between 0.1 and 0.3 μm.

The elastic modulus of Y_2O_3 coatings was also determined using the Nanoindenter® (Fig. 12), assuming Poisson's ratio = 0.33. The modulus increases almost linearly from 15×10^3–27×10^3 kg mm^{-2} (150–270 GPa) throughout the range of indentation depths. The elastic modulus of Y_2O_3 at ~0.5 μm indentation depths approaches that of bulk Al_2O_3 (~350 GPa), indicating that the coating modulus is very sensitive to substrate modulus. The elastic modulus of bulk Y_2O_3 is reported as ~13.4×10^3 kg mm^{-2} (134 GPa) [23], and is in agreement with data generated at indentation depths of 0.05–0.1 μm.

The hardness and elastic modulus of niobium coatings on Y_2O_3 were determined from indentations ranging in depth from 0.04–0.7 μm. The hardness increased with increasing indentation depth due to the film–substrate effect (Fig. 13). To minimize this effect, the ratio of indentation depth to coating thickness

should be $d/t < 0.1$ (Fig. 14a). However, indentations less than 0.4 μm may be influenced by surface roughness (Fig. 14b). Because of these factors, the hardness at a depth of ~0.4 μm, $H_v \approx 2.8$ GPa, is expected to be representative of the actual hardness of the niobium film. In contrast, the hardness of bulk wrought niobium is ~1.6 GPa [24]. A plot of the elastic modulus of the niobium film versus indentation depth shows less dependence upon substrate effects (Fig. 15), and $E = 88$ GPa at an indentation depth of 0.4 μm. This value is in reasonable agreement with the literature [25].

3.3. Y_2O_3 coating on sapphire
3.3.1 Coating fracture toughness, K_c

The Nanoindenter® could not be used to determine the coating fracture toughness K_c, because the maximum load was insufficient to initiate radial cracks. Vickers indentation tests were therefore used to obtain the desired crack morphology. The yttrium oxide coating spalled from alumina substrates at loads as
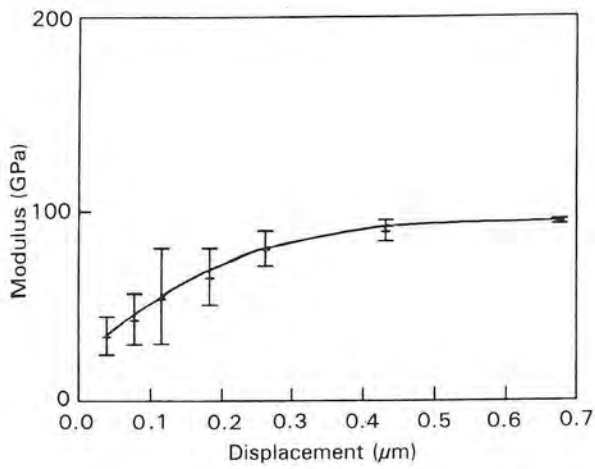
Figure 15 Elastic modulus of niobium versus indentation depth. The modulus at an indentation depth of 0.4 μm is ~88 GPa.
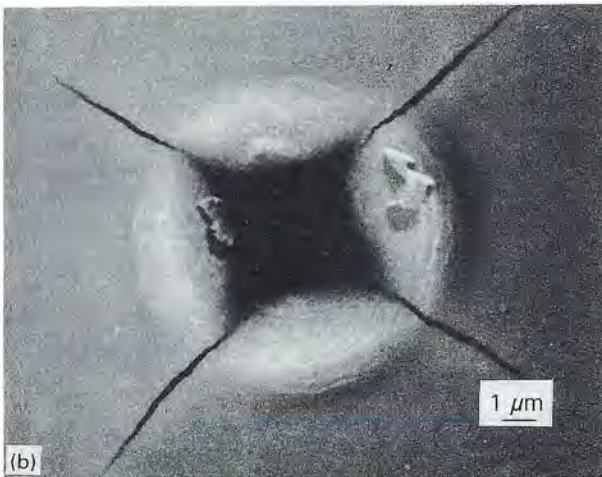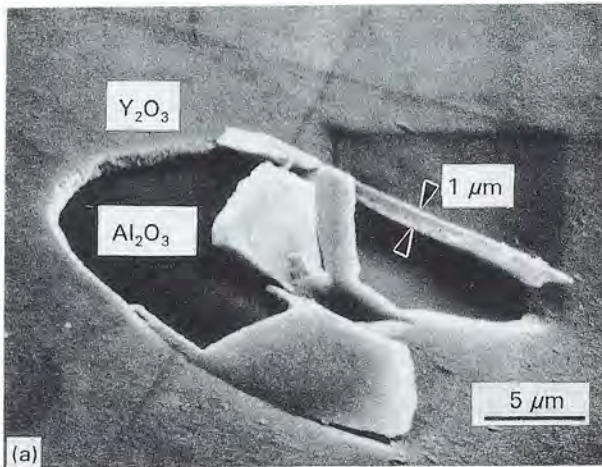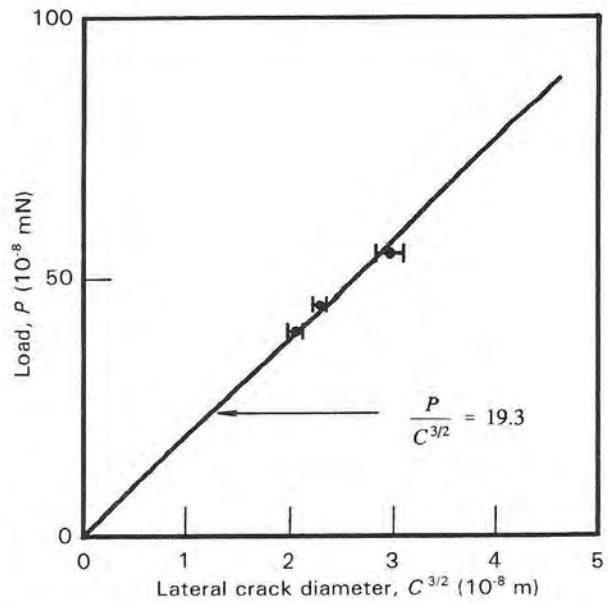

Figure 17 Plot of Vickers indentation load versus radial crack length used to determine the fracture toughness of sputtered Y_2O_3 coatings on sapphire.

Figure 16 (a) Scanning electron micrograph of Y_2O_3 coating spalled from (0 0 0 1) sapphire substrate by a 0.196 N Vickers indentation. The coating thickness is ~1 μm. (b) Backscattered scanning electron micrograph of a Vickers indentation in Y_2O_3 coating at 0.49 N load. Note the radial cracks at the corners of the indentation.

low as 0.147 N (Fig. 16a). Approximately 0.02 μm gold was sputtered on to the Y_2O_3 to prevent coating spallation and post-indentation slow crack growth. This should not effect the fracture toughness results because the gold film is < 2% of the Y_2O_3 coating thickness. Further, the hardness of the Y_2O_3 coating,

as measured using the Nanoindenter®, was unaffected by the gold film.

Vickers indentation tests of gold-coated Y_2O_3 did not produce radial cracks at loads less than 0.391 N, while loads > 0.538 N caused coating spallation which prevented measurement of radial cracks. Fig. 16b shows radial cracks introduced in Y_2O_3 by Vickers indentation at 0.49 N load. Five indentations were made at various loads to obtain average values of radial crack length. The indentor load is plotted versus the radial crack length according to the relation [26].

$$K_c = 0.019 \, [E/H_v]^{1/2} \frac{P}{C^{3/2}} \qquad (7)$$

where E is the elastic modulus of the coating (GPa), H_v is the Vickers hardness (GPa), P the applied load (N), and C the radial crack length (m). The results of the indentation tests are plotted in Fig. 17. The slope of the curve is $P/C^{3/2} = 19.3$ MN m$^{-3/2}$. The hardness and elastic modulus of Y_2O_3 coatings on sapphire were previously found to be 8 and 150 GPa, respectively. The coating fracture toughness is calculated to be $K_c = 1.58$ MN m$^{-3/2}$. This value is approximately one-half that of bulk Y_2O_3 [20].

3.3.2. Interfacial fracture toughness, $K_{c,i}$

The Nanoindenter® was used to assess adhesion of Y_2O_3 coatings on sapphire. Six indentations were performed at depths ranging from 0.3–0.7 μm. However, the coating did not delaminate at indentation depths < 0.4 μm. Fig. 18a shows a typical load–displacement curve for a 0.67 μm indentation, in which the delamination event is characterized by an abrupt change in slope near zero load. The maximum indentor load, P, is plotted against crack length, C (Fig. 18b). The interfacial fracture toughness is
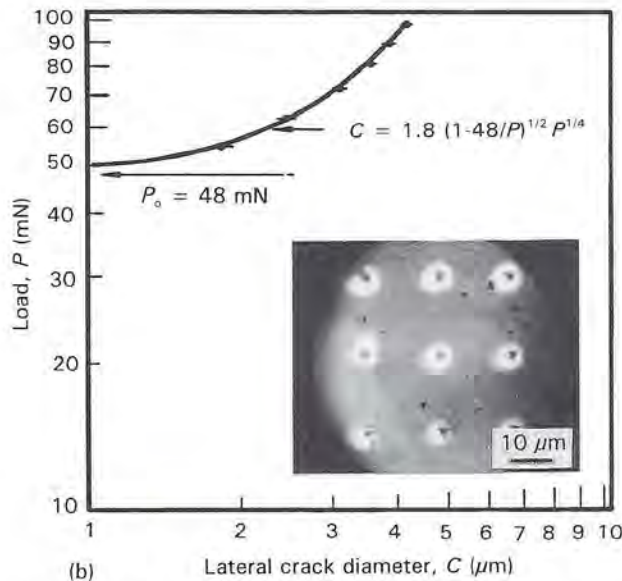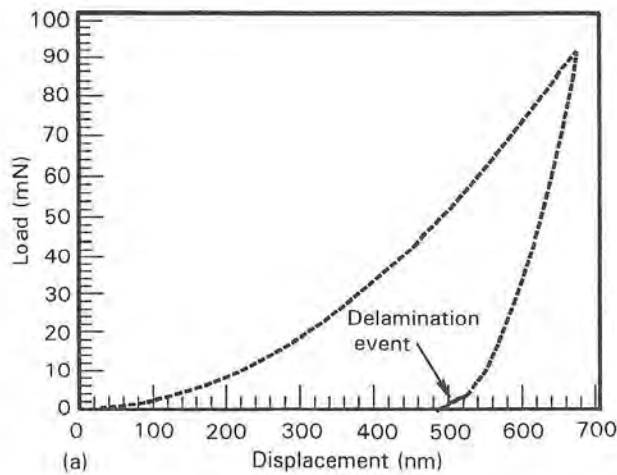
(a)

(b)

Figure 18 (a) Typical load–displacement curve produced using the Nanoindenter®. The coating delamination event is characterized by the change in slope near zero load. (b) Plot of Nanoindenter® load versus crack length use to determine Y_2O_3/Al_2O_3 interfacial toughness and light micrograph of several indentations (inset). Bright areas around indentations are indicative of debonding.

obtained from Equation 3, where $k = 0.16$, $t = 1 \times 10^{-6}$ m, $H_v = 8$ GPa, $P_0 = 48$ mN, $P = 75 \times 10^{-9}$ MN, and $C = 3 \times 10^{-6}$ m, and calculated to be $K_{c,i} = 0.15$ MN m$^{-3/2}$. This indicates that the Y_2O_3/Al_2O_3 interface is very weak.

3.3.3. Specific fracture energy, Γ_i

The specific fracture energy of the Y_2O_3 coating on sapphire is calculated using Equation 6, where the geometric crack factor $Y = \pi^{1/2}$ and the elastic modulus of the coating is $E = 150$ GPa. The specific fracture energy of the Y_2O_3 coating is $\Gamma_i = 4.7$ J m^{-2}. For $K_{c,i} = 0.15$ MN m$^{-3/2}$, the specific fracture energy of the Y_2O_3/Al_2O_3 interface is $\Gamma_i = 0.046$ J m^{-2}.

3.4. Y_2O_3 coating on polycrystalline niobium
3.4.1. Coating fracture toughness K_c

The fracture toughness of as-sputtered Y_2O_3 on

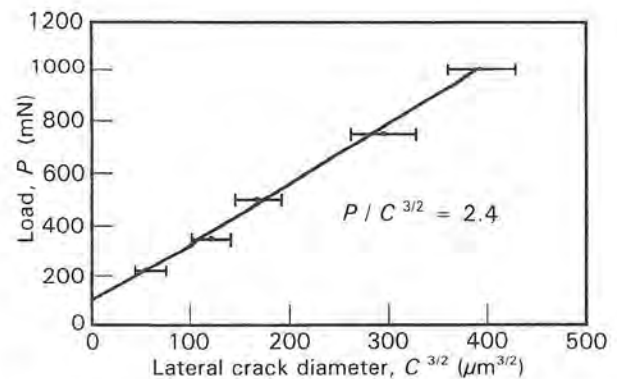*Figure 19* Plot of Vickers indentation load versus radial crack length used to determine the fracture toughness of sputtered Y_2O_3 coatings on niobium.

niobium was determined using Vickers indentation tests at loads ranging from 0.1–1 N. Y_2O_3 coatings on niobium did not exhibit a tendency to spall, unlike that found for Y_2O_3 coatings on Al_2O_3, and were thus not coated with gold. The indentor load, P, is plotted against crack length, $C^{3/2}$, and is shown in Fig. 19. The coating fracture toughness is calculated using Equation 7, where $P/C^{3/2} = 2.4$ MN m$^{-3/2}$, Vickers microhardness of Y_2O_3 is $H_v = 8$ GPa, coating elastic modulus $E = 150$ GPa, and found to be $K_c = 0.20$ MN m$^{-3/2}$. This value is approximately one-tenth of that found for Y_2O_3-coated Al_2O_3. The differences in fracture toughness are likely due to extensive deformation of the niobium substrate (Fig. 20) [10].

3.4.2 Interfacial fracture toughness, $K_{c,i}$

As-deposited Y_2O_3 coatings were not observed to debond from the niobium substrate at loads up to 0.078 N using the Nanoindenter® and 9.8 N using the Vickers indentor. However, lateral cracks formed in the Y_2O_3 coating at loads > 0.078 N (Fig. 20a and b). In contrast, as-sputtered Y_2O_3 coatings (with no gold overcoat) were observed to debond from Al_2O_3 at loads as low as 0.147 N. This result implies that the fracture toughness of the Y_2O_3/Nb interface is greater than the Y_2O_3/Al_2O_3 interface, but is not consistent with previous results where the Y_2O_3/Nb interface was found to be weaker than Al_2O_3/Nb [1] or Y_2O_3/Al_2O_3 [2].

Examination of the indentations showed that the Y_2O_3 coating did not buckle or spall at loads up to 9.8 N (Fig. 20b). Instead, the cracked coating appears to be well-bonded to the niobium substrate. A plot of indentor load versus lateral crack diameter (Fig. 21) does not reveal an asymptotic load at which lateral cracks vanish (Fig. 18b). This suggests that cracks caused by indentation tests propagate towards the surface rather than initiate delamination at the interface.

3.4.3. Specific fracture energy, Γ_i

The specific fracture energy of as-sputtered Y_2O_3 coating on niobium is calculated using Equation 6,

(a)

Figure 21 Plot showing the variation load versus lateral crack diameter for both Vickers ($P > 120$ mN) and Nanoindenter® ($P \lesssim 125$ mN) tests.
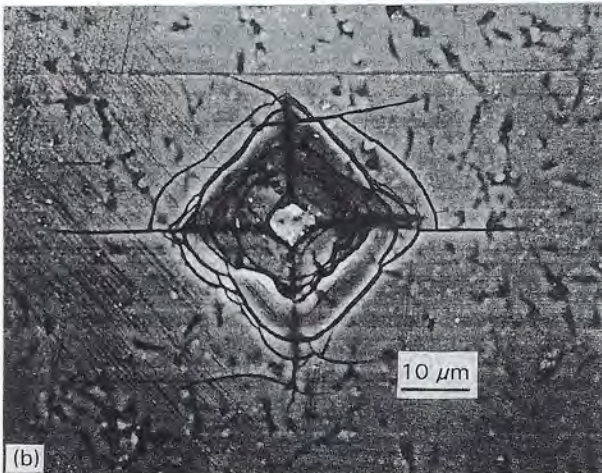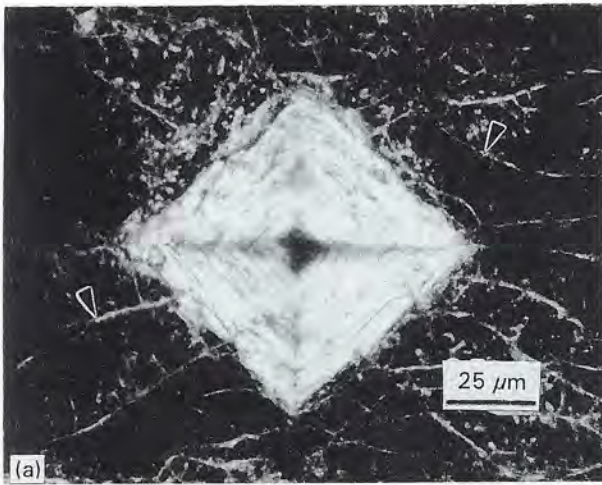

(b)

Figure 20 (a) Dark-field optical micrograph of a 9.8 N indentation for Y$_2$O$_3$-coated niobium. Note the numerous cracks emanating from the indentation. (b) Backscattered scanning electron micrograph of a 0.98 N indentation for Y$_2$O$_3$ coated niobium. Note the radial and lateral cracks, as well as adherence of the coating to the niobium substrate.
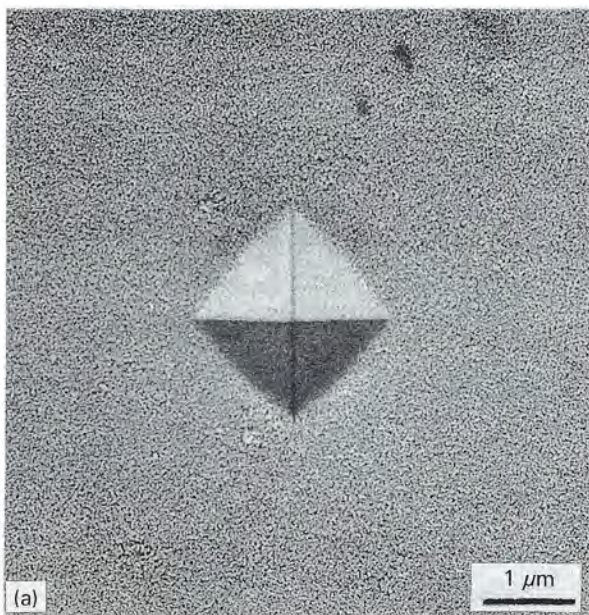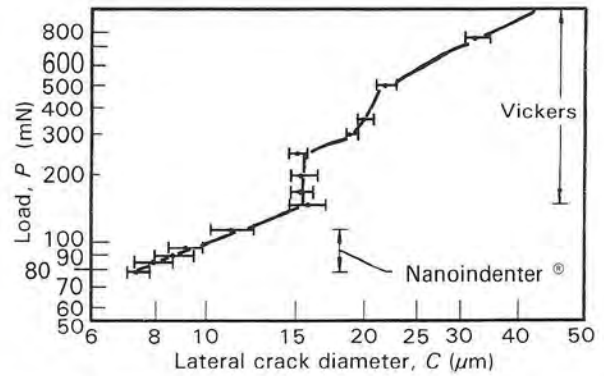
where $K_c = 0.2$ MN m$^{-3/2}$, $Y = \pi^{1/2}$, and $E = 150$ GPa. The specific fracture energy of the Y$_2$O$_3$ coating is $\Gamma_i = 0.074$ J m^{-2}.

3.5. Niobium coating on single-crystal Y$_2$O$_3$
3.5.1. Coating fracture toughness, K_c

The fracture toughness of as-sputtered niobium on Y$_2$O$_3$ was determined using Vickers indentation tests at loads ranging from 2–10 N. Niobium coatings did not exhibit a tendency to crack or spall at 2 N, while radial cracks were produced at 3, 5, and 10 N (Fig. 22). A plot of the indentor load, P, versus crack length, $C^{3/2}$, as measured from the niobium coating and transparent rearside of the Y$_2$O$_3$ wafer is shown in Fig. 23. The coating fracture toughness is calculated using Equation 7, where the average of the two curves is $P/C^{3/2} = 11.5$ MN m$^{-3/2}$, the Vickers microhardness of Y$_2$O$_3$ is $H_v = 2.8$ GPa, coating elastic modulus $E = 88$ GPa, and found to be $K_c = 1.22$ MN m$^{-3/2}$. This value is much lower than the room-temperature

(a)

(b)

Figure 22 Scanning electron micrographs of indentations produced by loads of (a) 2 N and (b) 10 N showing radial cracks.
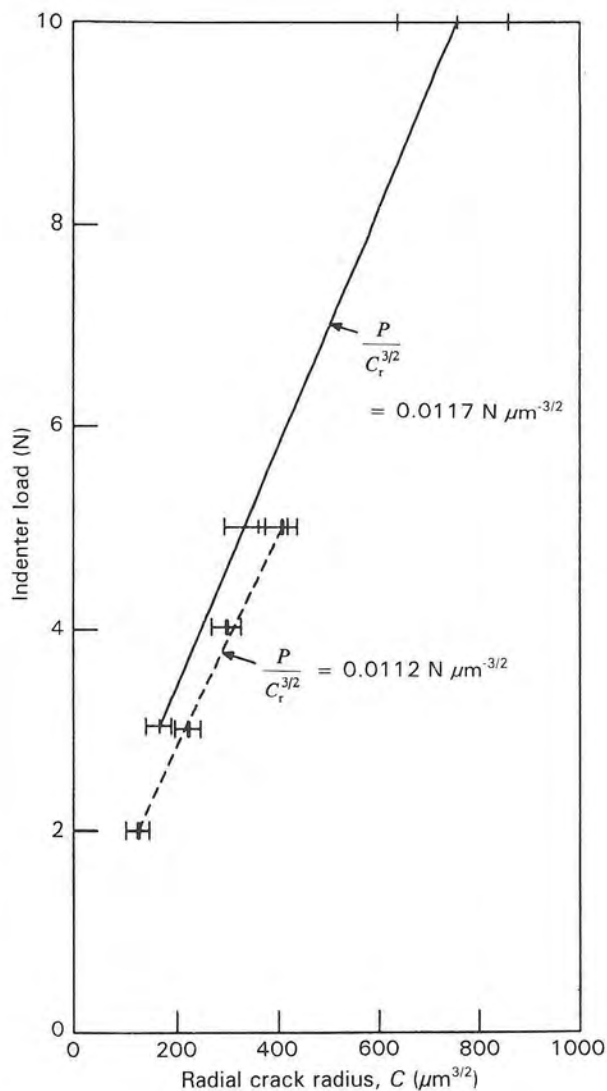
5289

Figure 23 Plots of Vickers indentor load versus radial crack length for the niobium coating. Crack lengths were measured from the top (solid line, Fig. 22) and from the back through the transparent Y_2O_3 wafer, and show good correlation.

Figure 24 Light micrographs showing debonding of the niobium coating at loads of (a) 1.5 N and (b) 3 N, as viewed from the transparent rearside of the Y_2O_3 wafer. Radial cracks produced by the 3 N load are apparent.

fracture toughness of bulk niobium ([16] p. 363). The difference in fracture toughness is most likely due to coating thickness, columnar microstructure, and the presence of a residual stress in as-deposited niobium.

3.5.2. Interfacial fracture toughness, $K_{c,i}$

As-deposited niobium coatings were observed to debond from the Y_2O_3 substrate at loads as low as 0.25 N using the Vickers indentor. The delamination event was observed from the backside of the transparent Y_2O_3 substrate through the formation of interference rings (Fig. 24). A plot of indentor load, P, versus lateral crack length, C, is shown in Fig. 25. The interfacial fracture toughness is obtained from Equation 3, where $k = 0.16$, $t = 4 \times 10^{-6}$ m, $H_v = 2.8$ GPa, $P_0 = 135$ mN, $P = 1500$ mN, and $C = 20 \times 10^{-6}$ m, and calculated to be $K_{c,i} = 0.18$ MN m$^{-3/2}$. This value is two orders of magnitude lower than that measured in uniaxial tension tests of niobium-reinforced TiAl laminates with Y_2O_3 interfacial coating [6].
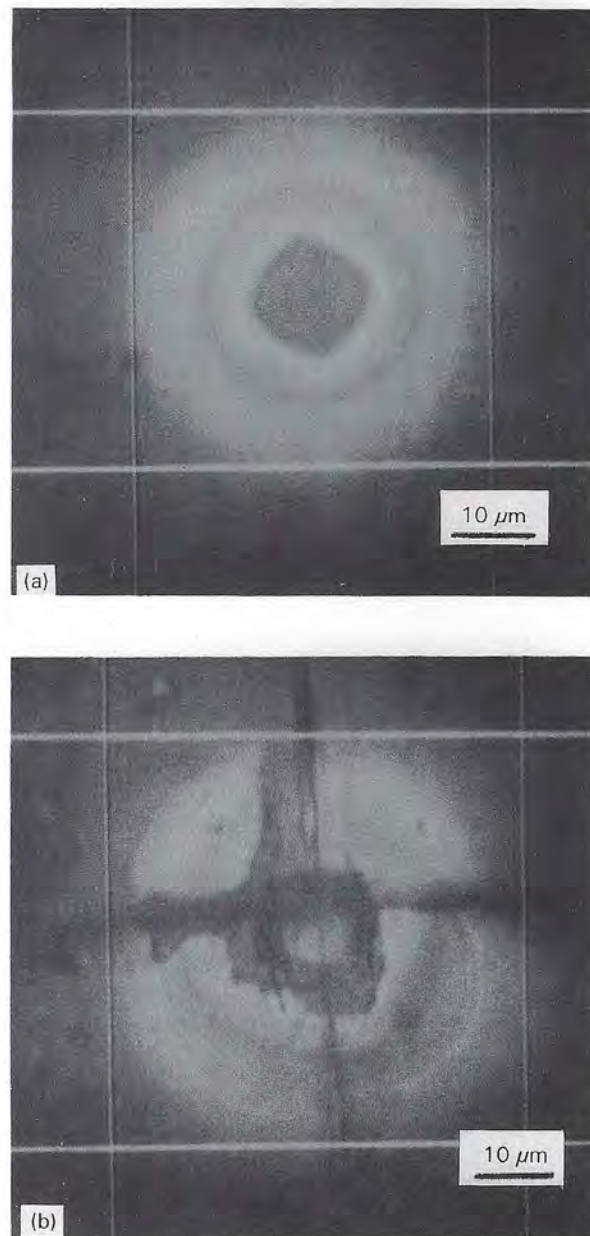
3.5.3. Specific fracture energy, Γ_i

The specific fracture energy of as-sputtered niobium on Y_2O_3 is calculated using Equation 6, where $K_c = 1.22$ MN m$^{-3/2}$, $Y = \pi^{1/2}$, and $E(Nb) = 88$ GPa. The specific fracture energy of the coating is $\Gamma_i = 4.78$ J m^{-2}. For $K_{c,i} = 0.18$ MN m$^{-3/2}$, the specific fracture energy of the Nb/Y_2O_3 interface is $\Gamma_i = 0.104$ J m^{-2}. The coating fracture toughness, interfacial fracture toughness, and specific fracture energy results presented in Sections 3.3–3.5 are summarized in Table I.

4. Discussion
4.1. Characterization of as-deposited Y_2O_3
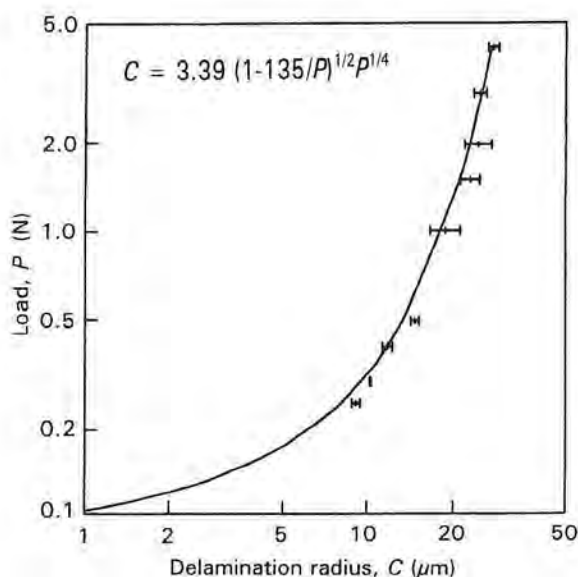Evaluation of reactively sputtered Y_2O_3 coatings

$$C = 3.39 \, (1\text{-}135/P)^{1/2} P^{1/4}$$

Figure 25 Plot of load versus crack length used to determine Nb/Y$_2$O$_3$ interfacial fracture toughness.

shows they are stoichiometric and contain low levels of impurities. The coating microstructure is typical of that found in thin vapour-deposited coatings examined through-thickness. A feature unique to vapour deposition is the range of microstructures, and hence physical and mechanical properties, that can be obtained in as-deposited coatings. An experimentally determined model of the structure of metal and ceramic coatings deposited by d.c. and r.f. sputtering as a function of working gas pressure and homologous temperature T/T_M, shows a trend from high aspect ratio columnar (Zone 1) to equiaxed (Zone 3) grains [18]. The Zone 1 microstructure consists of tapered crystallites with a fibrous internal structure, continuous voids at grain boundaries, and domed tops whose diameter increases with increasing substrate temperature. The formation of an intergranular network of voids is further enhanced by shadowing due to substrate surface roughness or preferential growth of crystallites and low adatom surface mobility. The mechanism by which grain boundaries coalesce to produce dense columnar microstructures is attributed to increased adatom mobility caused by higher T/T_M as well as increased desorption of inert gas atoms.

Coating microstructures produced at low T/T_M are found in most vapour-deposited coatings. Fig. 4 shows that sputtered Y$_2$O$_3$ coatings consist of columnar grains whose length extends through the entire coating thickness. These microstructures may be the least desirable because pipe diffusion can occur easily along porous grain boundaries and result in increased interaction with the substrate during hot pressing. In addition, sputtered coatings often contain a large amount of interfacial area which should affect the thermochemical stability and mechanical properties of the matrix/reinforcement interface [27–31]. The microstructure normally found in coatings deposited at low T/T_M may contain 50–400 grains/μm^2, resulting in 15%–25% grain-boundary area [27, 28, 30, 31] compared to 0.05% for bulk polycrystalline materials [27]. Coatings may contain additional interfacial area in the form of twins and stacking faults [29]. However, diffusion bonding niobium-reinforced TiAl results in a coating with better defined columnar grains, minimal reaction with the matrix or reinforcement, and composites with improved interfacial debonding and fracture toughness. This is due to the intrinsic thermochemical stability of Y$_2$O$_3$ in contact with niobium and TiAl, and thermodynamic preference to reduce interfacial area at the temperature and time used to bond the laminates together.

4.2. Nb/Al$_2$O$_3$ and Ti/Al$_2$O$_3$ interfaces

Uniaxial tension tests of precracked TiAl/Nb laminates fractured *in situ* in the scanning electron microscope showed that debonding occurs along the Nb/Y$_2$O$_3$ interface, which permits plastic deformation of the ductile phase over long lengths [6]. The yttria coating results in a 200% increase in work of fracture compared to Al$_2$O$_3$-coated niobium. The Nb/Y$_2$O$_3$ system has not been previously studied. However, both the Nb/Al$_2$O$_3$ [9, 32, 33] and Ti/Al$_2$O$_3$ [34–36] interfaces are well-characterized, and represent examples of non-reactive and reactive metal/ceramic systems, respectively. Understanding each provides a basis for determining the cause of a high work of rupture in Y$_2$O$_3$-coated niobium-reinforced TiAl.

The Nb/Al$_2$O$_3$ interface has been characterized by direct imaging using high-resolution TEM [9]. Pol-

TABLE I Summary of coating fracture data

Coating/substrate	Test method	K_c (MN m$^{-3/2}$)	$K_{c,i}$ (MN m$^{-3/2}$)	Γ_i (J m^{-2})
Y$_2$O$_3$/Al$_2$O$_3$	Indentation	1.58	–	4.70
Y$_2$O$_3$/Al$_2$O$_3$ interface	Indentation	–	0.15	0.046
Y$_2$O$_3$/Al$_2$O$_3$ interface [7]	Cone crack	–	3.65[a]	25
Y$_2$O$_3$/Nb	Indentation	0.20	–	0.074
Y$_2$O$_3$/Nb interface	Indentation	–	–	–
Y$_2$O$_3$/Nb interface [6]	Tensile	–	3.65[a]	25
Nb/Y$_2$O$_3$	Indentation	1.22	–	4.78
Nb/Y$_2$O$_3$ interface	Indentation	–	0.180	0.104
Y$_2$O$_3$/Nb interface [6]	Tensile	–	3.65[a]	25
Bulk Y$_2$O$_3$ [20]	Indentation	2.85	–	15

[a] $K_{c,i}$ obtained from Γ_i using Equation 6.

ished single crystals of niobium and Al_2O_3 were diffusion bonded at 1700 °C for 2 h in high vacuum ($\sim 10^{-3}$ Pa) and 10 MPa load. The couples were bonded in a $(110)_{Nb} \parallel (0001)_{Al_2O_3}$ and $[001]_{Nb} \parallel [2\overline{1}\overline{1}0]_{Al_2O_3}$ orientation relationship. Samples for high-resolution TEM were obtained from the bulk couple with foil planes normal to $[001]_{Nb}$ and $[1\overline{1}0]_{Nb}$. High-resolution TEM of the interface did not reveal the presence of a reaction layer. This is in contrast to other studies, where niobium oxides [37] or impurities present in polycrystalline Al_2O_3 or niobium segregated or catalysed reactions at the interface during hot pressing [38]. Non-equilibrium phases may form at the interface due to diffusion of impurities to accommodate misfit strain. While Al_2O_3 is dissolved by niobium at ~ 1700 °C, no metallic aluminium found in single-crystal couples bonded at 1700 °C for 2 h [9]. It is possible that a small amount of Al_2O_3 was dissolved and subsequently precipitated at the interface upon cooling. This should form defects at the interface due to the misfit strains developed at the interface, but none were observed. These results indicate that chemical interaction between high-purity single-crystal niobium and Al_2O_3 is minimal during diffusion bonding.

Another study examined the Nb/Al_2O_3 interface by internally oxidizing an Nb–3 at % Al alloy at 1450 °C [32]. No interfacial compounds were detected by high-resolution TEM, and the interface was observed to be atomically flat. The outer layer of Al_2O_3 was suggested to consist of a monolayer of oxygen atoms. The Nb/Al_2O_3 interface has also been examined by XPS and Auger electron spectroscopy (AES). Several monolayers of niobium were evaporated in situ on to (0001) sapphire substrates heated to 1000 °C [33]. High-resolution spectra of Nb (3d), O(1s), and Al(2p) versus niobium coating thickness indicate that the niobium donates electrons to surface oxygen atoms to form Nb–O bonds. Thus, a chemical reaction occurs between niobium and Al_2O_3, but it is limited to approximately one monolayer.

The former TEM study [9] did not discuss the presence of an oxide layer on polished niobium (1–2 nm thick) or physisorbed or chemisorbed species on niobium or sapphire. Physisorbed species such as H_2O will mostly desorb upon heating, while monolayer coverage of hydrocarbon should innocuously diffuse into an infinite sink of niobium. At temperatures typical of diffusion bonding, the oxide layer on niobium will likely be reduced by bulk niobium, which has ~ 0.1 wt % solubility for oxygen at 25 °C. Remarkably, efforts to determine the nature of the Nb/Al_2O_3 interface exhibit similar results while utilizing samples prepared by greatly different methods and with different levels of surface contamination [9, 32, 33].

The Ti/Al_2O_3 system, in contrast, is highly reactive, resulting in considerable degradation of the interface [34–36]. Single-crystal Al_2O_3 fibres, ~ 300 μm diameter, were hot pressed between commercially pure α-titanium sheets ~ 400 μm thick at 815 °C for 2 h and 110 MPa [34], then vacuum annealed at 600–1000 °C for times sufficient to produce measur-

able reaction zones and determine rate constants. The resulting reactions were characterized by XRD and electron microprobe. The reaction product after exposure to 1000 °C for 100 h was ~ 40 μm thick and found to consist of Ti_3Al and TiAl. Microhardness measurements were used to determine the extent of oxygen diffusion into the surrounding matrix.

Reactions between thin films of titanium on bulk alumina and on alumina-containing substrates have been extensively studied [35, 36]. Single-crystal alumina substrates maintained at 25 and 1000 °C were coated with titanium by evaporation, then examined by XPS [35]. At 25 °C, several monolayers of titanium were found to reduce the Al_2O_3 surface and produce Ti–O bonds. In contrast, coatings deposited on substrates held at 1000 °C produced both Ti–O and Ti–Al bonds. In the former, titanium bonds to a monolayer of oxygen atoms on the oxide surface, while in the latter reduction of the oxide is extensive and enables the formation of titanium–aluminium compounds.

Interfacial reactions between titanium and amorphous cordierite-based ($2MgO \cdot Al_2O_3 \cdot 5SiO_2$) ceramic films 200 nm thick on single-crystal silicon were characterized by XPS [36]. Si–O bonds were found to dissociate at room temperature with sub-monolayer coverages of titanium. Additional coverage by titanium began to reduce Al–O bonds. Vacuum annealing results in increased reaction kinetics between titanium and SiO_2 and Al_2O_3. However, titanium was not observed to reduce the Mg–O bond up to 800 °C. Magnesium oxide-based compounds may be debond coatings worth investigating in titanium matrix composites.

It is apparent that a reactive system such as Ti/Al_2O_3 produces intermetallic reaction products that thicken with extended exposure to elevated temperature, thereby forming a more complicated interface. If the fracture energy of the reaction products is sufficient to discourage extensive debonding, then the toughness of the composite is reduced. For example, uncoated niobium plates diffusion bonded to TiAl reacted to form σ and T_2 phases 4–6 μm thick [6]. Tensile testing showed debonding occurred in the σ phase, which had a measured fracture energy of $\Gamma_i = 45$ J m^{-2}. This is sufficient to retard debonding and reduce the work of rupture by 66%. These results suggest that there may be similarity between the Nb/Al_2O_3 and Nb/Y_2O_3 systems [6, 9, 32, 33]. The Nb/Y_2O_3 interface may be atomically sharp, similar to that found in Nb/Al_2O_3 [9]. This, coupled with a lower Y_2O_3 fracture energy, may cause the improved debonding and higher fracture toughness observed experimentally [6].

4.3. Relationships to debonding

The success of a particular material as a debond coating will depend on a combination of several factors, including coating thickness, surface and bulk impurities, local stress state, coating mechanical properties, bond strength between the coating and reinforcement or matrix, thermodynamic stability, and microstructure.

Coating thickness has not yet been quantified, but it is reasonable to assume that there are optimum thicknesses that may be defined by other variables in the composite system such as reinforcement size or diffusivity. Impurities in the bulk can accumulate at the interface [9], and are expected to be detrimental in most cases. The effect of surface impurities remains uncertain, but does not appear to cause difficulties in the case of Nb/Al_2O_3 [9, 32, 33]. However, the use of high surface area reinforcements such as multifilament fibre tows, whiskers, or particulates, may require preferential treatment to avoid the introduction of large amounts of physisorbed species. Interstitials or minor alloying elements may locally stabilize unwanted phases or precipitate new phases, thereby deleteriously affecting matrix properties.

Debonding has been observed in many fibre coating/matrix systems including $Nb/Y_2O_3/TiAl$ [6], $Al_2O_3/Mo/Al_2O_3$ [7], $Al_2O_3/porous$ ZrO_2/Al_2O_3 [8], $SiC/C/AS$ [2], $SiC/BN/SiC$ [39], and $W/Al_2O_3/TiTaAl_2$ [40]. The coefficient of thermal expansion (CTE) should be an important consideration in selecting debond coatings. In particular, the difference in relative CTE between the fibre/coating/matrix should be small ($\Delta\alpha = 1-3$ p.p.m. $^{\circ}C^{-1}$). In some case the interface is in compression, while in others the interface is in a small amount of tension. There seems to be no simple rule for determining which case is most desirable, other than that the magnitude of the tensile stress cannot be high.

Oxide coatings perform well in ductile phase-reinforced brittle-matrix systems because they fracture at low applied stress, enabling plastic deformation of the toughening phase [6]. The specific fracture energy, Γ_i, of oxide coatings is small, typically on the order of 25 J m^{-2}. The improved debonding obtained with Y_2O_3 versus Al_2O_3 coatings suggests the fracture energy of the former is lower. In addition, pores in the coating will affect coating fracture toughness and debonding behaviour of composites [8]. Thus, prior knowledge of thin-film fracture toughness, its dependence upon porosity, and control of porosity in the application of coatings can be useful in guiding future coating selection. Successful debond coatings must also be thermally stable and substantially non-reactive with respect to both the matrix and reinforcing phase. The Gibb's free energy of formation of α-Al_2O_3 and Y_2O_3 is -378.2 and -434.2 kcal mol^{-1}, respectively [41]. Yttria should, therefore, be more difficult to reduce by niobium and TiAl at typical diffusion-bonding temperatures and times, thus retaining a sharp interface. For similar reasons, Y_2O_3 also serves as a protective coating between the niobium reinforcement and the TiAl matrix.

The microstructure of sputtered Y_2O_3 was found to consist of tapered crystallites extending through the thickness of the coating, perhaps resulting in pipe diffusion and increased reaction with the matrix or reinforcement. Such interaction should affect debonding by altering the interfacial chemistry. While this may occur in some systems, it has not yet been observed in the composite system under investigation. Further, sputtered Y_2O_3 coatings evaluated in nio-

bium-reinforced TiAl matrices remain columnar after hot-pressing (Fig. 8). Conversely, molybdenum and ZrO_2 coatings in Al_2O_3/Al_2O_3 laminate specimens become equiaxed after hot-pressing [7, 8]. This will also probably affect the mechanical properties of the coating, interface, or crack path. For example, thermal exposure during composite processing or coating microstructure may determine the location of debonding, i.e. within the coating, at the coating/fibre interface, or at the coating/matrix interface, whichever has the lowest specific fracture energy. No rationale has yet been developed to guide selection of the preferred debonding site.

4.4 Analysis of indentation-derived coating fracture results
4.4.1. Y_2O_3 coatings on Al_2O_3
The specific fracture energy of interfaces modified with coatings was measured by Hertzian cone cracking experiments using a model single-crystal Al_2O_3/Al_2O_3 composite system [7, 8]. The coatings evaluated include molybdenum, yttria-stabilized ZrO_2 (tetragonal structure), TiAl, m-ZrO_2 (m = monoclinic), and Y_2O_3. All coatings were deposited by sputtering, while the latter two were also applied using sol–gels, at a nominal coating thickness of 1 µm. Single-ply laminate specimens were fabricated by diffusion-bonding coated Al_2O_3 wafers in vacuum at 1000–1400 °C under a pressure of 1 MPa. Cracks were introduced into the Al_2O_3 laminate by applying a point load using a 12.5 mm WC ball. The Hertzian crack reaches the interface and either passes through the coating or is deflected by fracture along the interfacial coating, resulting in improved toughness. Coatings which exhibited this behaviour had low specific fracture energies and include molybdenum ($\Gamma_i = 3-5$ J m^{-2}) and $\sim 50\%$ porous monoclinic ZrO_2 ($\Gamma_i = 4$ J m^{-2}). Conversely neither sputtered nor sol–gel Y_2O_3 coatings were suitable because they reacted partially with the Al_2O_3 substrate to form YAG at the interface, resulting in a high specific fracture energy ($\Gamma_i = 25$ J m^{-2}).

The fracture toughness and specific fracture energy of the Al_2O_3/Y_2O_3 interface measured in the present study by indentation tests are 0.15 MN m$^{-3/2}$ and 0.046 J m^{-2}, respectively (Table I). Both values are lower than expected. The difference is attributed to the evaluation of as-deposited coatings which did not react with the Al_2O_3 substrate to form YAG, due to the low substrate temperature during sputtering, and the columnar microstructure. The low specific fracture energy of the Y_2O_3/Al_2O_3 interface ($\Gamma_i = 0.046$ J m^{-2}) is indicative of weak bonding between as-deposited Y_2O_3 coating and the alumina substrate.

4.4.2. Y_2O_3 coatings on niobium
The interfacial debonding characteristics of sputtered Al_2O_3 and Y_2O_3 interface in a TiAl/Nb composite showed that the preferred debond coating is Y_2O_3. The specific fracture energy of the Y_2O_3/Nb interface

is $\sim 25\ \mathrm{J\,m^{-2}}$, and is sufficiently low in this composite system to promote extensive plastic deformation of the ductile phase over a large volume. Debonding, coupled with a ductile phase which easily work hardens, results in a composite with high toughness. Indentation test data (Table I) show that the calculated fracture toughness and fracture energy of as-deposited Y_2O_3 on niobium reflect failure of the Y_2O_3 coating and deformation of the niobium substrate as a single unit. Thus, measurements of $K_{c,i}$ could not be made because coating failure is not independent of the substrate.

4.4.3. Niobium coatings on Y_2O_3

Indentation tests to determine the fracture toughness and fracture energy of the Nb–Y_2O_3 interface could not only be assessed if the test specimen geometry were reversed, i.e. sputtered niobium coating on single-crystal Y_2O_3. The interfacial fracture toughness is an order of magnitude lower than that found in uniaxial tensile tests of niobium-reinforced TiAl laminates [6]. As a result, the specific fracture energy of the Nb–Y_2O_3 interface as determined by indentation tests did not correlate with that found in tensile tests using diffusion-bonded Nb–TiAl laminates.

4.4.4. Bulk Y_2O_3

The fracture toughness of bulk Y_2O_3 reportedly varies from 2.3–3.4 $\mathrm{MN\,m^{-3/2}}$ [20], resulting in $\Gamma_i = 9.95$–$21.7\ \mathrm{J\,m^{-2}}$. Conversely, the measured indentation-derived fractured toughness of as-deposited Y_2O_3 coating on sapphire is 1.58 $\mathrm{MN\,m^{-3/2}}$, resulting in $\Gamma_i = 4.7\ \mathrm{J\,m^{-2}}$ (Table I). The intrinsic fracture toughness of as-deposited Y_2O_3 coating is about half that of bulk Y_2O_3. The difference is due to the evaluation of dissimilar microstructures, i.e. sub-micrometre columnar Y_2O_3 grains for vapour-deposited Y_2O_3 versus equiaxed grains in bulk Y_2O_3. Regardless, reasonable correlation to bulk properties can be achieved via Vickers indentation testing, provided the coating is deposited on to a hard substrate.

4.5. Factors affecting fracture toughness results

There are several factors which can affect the response of the coating to indentation tests. These include thickness, residual stress, bond strength, microstructure, and elastic modulus. The hardness, elastic modulus, and fracture properties of micrometre-thick coatings can be evaluated using the Nanoindenter®. However, the loads required to initiate radial cracks at the corners of the indentation may exceed that load range of this instrument, as was the case for as-deposited Y_2O_3 coatings on sapphire (Section 3.3.1). Thus, it is reasonable to assume that there is minimum thickness that is required for testing. The present study indicates that coatings $\sim 1\ \mu\mathrm{m}$ thick are suitable for testing. This is also a useful coating thickness for applications requiring debond coatings on monofilament or multifilament fibres.

Residual tensile or compressive stresses are commonly found in as-deposited sputtered coatings, and may be caused by the sputtering equipment geometry or deposition conditions. These include target-to-substrate distance, working gas pressure, reactive gas partial pressure, substrate bias, or coating/substrate thermal expansion mismatch [42]. The residual stress in as-deposited films can affect indentation tests. For example, coatings with residual compressive stress may inhibit radial cracking and result in higher K_c. Conversely, $K_{c,i}$ may be reduced due to a propensity for the coating to buckle. Residual stress may not be a significant factor in the present study because the fracture toughness of as-deposited Y_2O_3 is in reasonable agreement with bulk Y_2O_3.

The bond between the coating and substrate must have sufficient strength to allow the coating to be probed at loads required to produce the desired coating fracture morphology. This will be most greatly influenced by post-deposition processing of the coating/substrate system such as hot-pressing. Laminate samples previously evaluated were hot-pressed at temperatures ranging from 1066–1450 °C [6, 7], which may result in the formation of interfacial compounds. For example, Y_2O_3 coatings on sapphire reacted to form a layer of YAG at the interface [7]. The interfacial fracture toughness of this system will be higher than as-sputtered Y_2O_3 on sapphire.

The microstructure of as-deposited Y_2O_3 coatings consists of tapered crystallites extending through the thickness of the coating and is produced by low adatom mobility due to low homologous temperature and preferential growth of crystallites [18]. This microstructure will affect the results of indentation tests because the load is applied parallel to columnar grains. The difference in fracture toughness between as-deposited Y_2O_3 and bulk Y_2O_3 is attributed to evaluation of dissimilar microstructures, i.e. sub-micrometre columnar Y_2O_3 grains for vapour-deposited Y_2O_3 versus 1–10 μm diameter equiaxed grains in bulk Y_2O_3 [20].

Calculations to determine Γ_i utilize the elastic modulus of Y_2O_3 as determined by the Nanoindenter®. This value, 150 GPa, agrees with that previously determined for bulk Y_2O_3 [23]. The elastic modulus is determined by a uniaxial tension test where stress is linearly proportional to strain. However, this condition is not satisfied by indentation tests nor for thin coatings attached to a substrate. In addition, the indentor does not load the coating in uniaxial tension, the condition under which Young's modulus is obtained. The elastic modulus is also a directional property [43], so the modulus of free-standing films deposited at low T/T_M will be anisotropic and vary depending upon orientation to the columnar grains. These factors cause uncertainty in the application of bulk elastic properties to the determination of K_c and Γ_i.

The modulus of elasticity is also a function of the type of chemical bonding in a crystal, i.e. ionic, covalent, metallic [43]. A thin free-standing film should, therefore, exhibit bulk elastic properties, provided the ratio of surface atoms to interior atoms is low. A 1 μm

thick film contains ~ 3000 atoms through-thickness, which should be sufficient to satisfy this criterion and exhibit bulk or near-bulk properties. A similar argument may also apply to other properties of coatings 1–2 μm thick.

The elastic modulus of supported and unsupported thin films has been determined by different techniques, and varies from 0.1–0.9 of bulk properties [45–46]. These results indicate that elastic properties are dependent upon many variables related to mechanical test conditions, coating deposition method, and perhaps even sputter-deposition parameters. The specific fracture energy of as-deposited Y_2O_3 on Al_2O_3 was found to be 4.7 J m^{-2} (Table I). Calculation of this parameter using 75 and 15 GPa (instead of 150 GPa) yields specific fracture toughnesses of 9.4 and 46.9 J m^{-2}, respectively. The specific fracture energy of as-deposited Y_2O_3 approaches that of bulk Y_2O_3 for $E = 75$ GPa. However, there are distinct differences in microstructure as previously noted. Thus, values of K_c and $K_{c,i}$ calculated for as-deposited Y_2O_3 on sapphire using Young's modulus for bulk Y_2O_3 may, indeed, be indicative of actual coating fracture properties and interfacial debonding behaviour.

The calculated values for fracture toughness and fracture energy derived by indentation tests must be used carefully because numerous test-related factors can affect the results [13, 14, 19, 47]. Many of the factors related to the coating, its deposition, or indentation test technique are difficult, if not impossible to control. However, the results presented in Table I show that indentation and tests can be used to determine coating fracture properties, K_c, with reasonable correlation to bulk properties. However, the interfacial fracture toughness, $K_{c,i}$, and specific fracture energy, Γ_i, could not be correlated to results obtained from laminates evaluated by tensile [6] or cone crack [7, 8] tests. This is attributed to differences in test methods and sample preparation. For example, tensile tests to determine Γ_i in niobium-reinforced TiAl measures decohesion along two interfaces, while indentation tests measure only one interface. Hertzian cone crack tests are an elastic indentation test method, while Nanoindenter® and Vickers indentation tests are plastic indentation test methods. Samples prepared by r.f. sputtering were not exposed to the same thermal history as diffusion-bonded samples.

5. Conclusion

The fracture toughness, interfacial fracture toughness, and specific fracture energy for as-sputtered Y_2O_3 coatings on sapphire and commercial purity polycrystalline niobium substrates, and niobium-coated Y_2O_3 were determined via micro- and nanoindentation techniques. The results were compared to fracture toughness studies of Al_2O_3/Al_2O_3 [7, 8] and niobium-reinforced TiAl laminate coupons containing Y_2O_3 interfacial coating [6]. The calculated fracture toughness of as-deposited Y_2O_3 on sapphire was similar to reported values for bulk Y_2O_3. However, the fracture toughness of the Y_2O_3-Nb interface is lower than that

previously reported. As a result, the specific fracture energy of the interface was also lower than expected, and is attributed to differences in coating microstructure and weak bonding between as-deposited coatings and the substrates.

These results were related to factors which may affect debonding and fracture toughness of brittle matrix composites. Reactive and non-reactive metal/ceramic systems were reviewed in an effort to understand why this coating performs well. It is postulated that Y_2O_3-coated niobium has an atomically sharp interface which has a lower fracture energy compared to Nb/Al_2O_3, resulting in improved debonding and fracture toughness in niobium-reinforced TiAl [6]. Additional studies must be performed to quantify better the attributes common to fibre/coating/matrix systems that exhibit desirable fracture behaviour, so that predictive guidelines can be used to select debond and protective coatings.

References

1. A. G. EVANS and D. B. MARSHALL, Acta Metall. 37 (1989) 2567.
2. H. C. CAO, E. BISCHOFF, O. SBAIZERO, M. RÜHLE, A. G. EVANS, D. B. MARSHALL and J. J. BRENNAN, J. Am. Ceram. Soc. 73 (1990) 1691.
3. V. GUPTA, A. S. ARGON and J. A. CORNIE, J. Mater. Sci. 24 (1989) 2031.
4. M. BASCHE, R. FANTI and F. GALASSO, Fiber Sci. Technol. 1 (1968) 19.
5. F. WAWNER, A. Y. TENG and S. R. NUTT, SAMPE Q. 14 (1983) 39.
6. H. DÈVE, A. G. EVANS, G. R. ODETTE, R. MEHRABIAN, M. L. EMILIANI and R. J. HECHT, Acta Metall. 38 (1990) 1491.
7. J. DAVIS, H. C. CAO, G. BAO and A. G. EVANS, ibid. 39 (1991) 1019.
8. A. G. EVANS, A. BARTLETT, J. B. DAVIS, B. D. FLINN, M. TURNER and I. E. REIMANIS, Scripta Metall. Mater. 25 (1991) 1003.
9. W. MADER and M. RÜHLE, Acta Metall. 37 (1989) 853.
10. L. G. ROSENFELD, J. E. RITTER and T. J. LARDNER, "Interfaces in Composites", Materials Research Society Symposium Proceedings, Vol. 170 (Materials Research Society, Pittsburgh, PA, 1990) p. 11–16.
11. T. B. MASSALSKI, (Ed.), "Binary Alloy Phase Diagrams", Vol. 2 (American Society for Metals, Metals Park, OH, 1986) p. 1799.
12. M. ABOUELLEIL, L. CONOPASK, W. NIGHAN, W. ROMAN and D. PRICE, Ceram. Trans. 15 (1990) 457.
13. C. B. PONTON and R. D. RAWLINGS, Mater. Sci. Technol. 5 (1989) 961.
14. Idem, ibid. 5 (1989) 865.

15. S. CHAING, D. MARSHALL and A. EVANS, in "Surfaces and Interface of Ceramics and Ceramic/Metal Systems", edited by J. Pask and A. Evans, (Plenum Press, New York, 1981) pp. 603–17.
16. R. W. HERTZBERG, "Deformation and Fracture Mechanics of Engineering Materials", (Wiley, New York, 1976) pp. 255–96.
17. B. A. MOVCHAN and A. V. DEMSHICHIN, *Phys. Met. Metall.* **28** (1969) 83.
18. J. A. THORNTON, *Ann. Rev. Mater. Sci.* **7** (1977) 239.
19. P. SARGENT, in "Microhardness Techniques in Materials Science and Engineering", edited by P. Blau and R. Lawn, ASTM STP 889 (American Society for Testing and Materials, Philadelphia, PA, 1986) pp. 160–74.
20. G. FANTOZZI, G. ORANGE, K. LIANG and E. GILLET, *J. Am. Ceram. Soc.* **72** (1989) 1562.
21. P. J. BURNETT and D. S. RICKERBY, *Thin Solid Films* **148** (1987) 51.
22. R. COOK, M. PASCUCCI, and H. RHODES, *J. Am. Ceram. Soc.* **73** (1990) 1873.
23. J. HAGGERTY, "Production of Fibers by a Floating Zone Fiber Drawing Technique", Final Report, NASA Report CR-120984, May 1972, p. 52.
24. H. BAKER (ed.), "Metals Handbook", Vol. 2, 9th Edn (ASM International, Metals Park, OH, 1979) p. 779.
25. *Idem*, Vol. 2, 10th Edn (ASM International, Metals Park, OH, 1990) pp. 567–68.
26. B. LAWN, A. EVANS and D. MARSHALL, *J. Am. Ceram. Soc.* **63** (1980) 574.
27. P. M. FABIS, *J. Vac. Sci. Technol.* **A5** (1987) 75.
28. M. EMILIANI, M. RICHMAN and R. BROWN, *J. Mater. Sci.* **25** (1990) 137.
29. *Idem, ibid.* **25** (1990) 144.
30. R. BIRRINGER, *Mater. Sci. Eng.* **A117** (1989) 33.
31. D. J. SROLOVITZ, *J. Vac. Sci. Technol.* A **6** (1986) 2925.
32. M. KUWABARA, J. C. H. SPENCE and M. RÜHLE, *J. Mater. Res.* **4** (1989) 972.
33. F. S. OHUCHI, *J. Mater. Sci. Lett.* **8** (1989) 1427.
34. J. KENNEDY and G. GESCHWIND, in "Titanium Science and Technology", Vol. 4, edited by R. I. Jaffee and H. M. Burte (Plenum Press, New York, 1973) p. 2299.
35. J. H. SELVERIAN, M. BORTZ, F. S. OHUCHI and M. R. NOTIS. in "Electronic Packaging Materials Science III", edited by R. Jaccodine, K. A. Jackson and R. C. Sundahl, Materials Research Society Symposium Proceedings, Vol, 108 (Materials Research Society, Pittsburgh, PA, 1988) p. 107.
36. M. BORTZ and F. S. OHUCHI, *J. Appl. Phys.* **64** (1988) 2054.
37. S. MOROZUMI, M. KIKUCHI and T. NISHINO, *J. Mater. Sci.* **16** (1981) 2137.
38. Y. ISHIDA, H. ICHINOSE, J. WANG and T. SUGA, in "Proceedings of the 46th Annual Meeting of EMSA", edited by G. W. Bailey (San Francisco Press Inc., San Francisco, CA, 1988) p. 728.
39. R. NASLAIN, O. DUGNE, A. GUETTE, J. SEVELY, C. R. BROSSE, J-P. ROCHER and J. COTTERET, *J. Am. Ceram. Soc.* **74** (1991) 2482.
40. H. E. DÈVE and M. J. MALONEY, *Acta Metall. Mater.* **39** (1991) 2275.
41. R. C. WEAST (Ed.), "CRC Handbook of Chemistry and Physics", 68th Edn (CRC, Boca Raton, FL, 1987) p. D-51 and D-92.
42. J. A. THORNTON, in "Deposition Technologies for Thin Films and Coatings", edited by R. F. Bunshah (Noyes, Park Ridge, NJ, 1982) pp. 170–243.
43. M. F. ASHBY and D. R. H. JONES, "Engineering Materials" (Pergamon Press, New York, 1980) Chs 3 and 4.
44. M. L. SCOTT, in "Laser-Induced Damage in Optical Materials", NBS Special Publication 688, November 1985.
45. R. W. HOFFMAN, in "Thin Films: Stresses and Mechanical Properties", Materials Research Society Symposium Proceedings, Vol. 130, edited by J. D. Bravman, W. D. Nix, D. M. Barnett and D. A. Smith (Materials Research Society, Pittsburgh, PA, 1989) p. 87–92.
46. T. P. WEIHS, S. HONG, J. C. BRAVMAN and W. D. NIX, *ibid.* p. 295–306.
47. J. D. HORNER, in "Testing of Metallic and Inorganic Coatings", edited by W. B. Harding and G. A. Bari, ASTM STP 947 (American Society for Testing and Materials, Philadelphia, PA, 1987) p. 96.

journal

Fiber Coating Concepts for Brittle-Matrix Composites

Janet B. Davis,* Jan P. A. Löfvander, and Anthony G. Evans*

Materials Department, College of Engineering, University of California, Santa Barbara, California 93106–5050

Ewald Bischoff

Max-Planck-Institut für Metallforschung, D-7000 Stuttgart 1, Germany

Mario L. Emiliani

Pratt and Whitney, Materials Engineering, West Palm Beach, Florida 33410

The current interest in tough, high-temperature materials has motivated fiber coating development for brittle-matrix composites with brittle reinforcements. Such coatings are needed for controlled interface debonding and frictional sliding. The system investigated in this study was sapphire fiber-reinforced alumina. This system is thermochemically stable for severe use conditions, exhibits little thermal expansion mismatch, and utilizes the excellent strength and creep resistance of sapphire reinforcements. Porous oxide and refractory metal coatings which satisfy requirements for toughness improvement in these composites were identified by employing a variety of newly developed mechanical testing techniques for determining the interfacial fracture energies and sliding resistances.

I. Introduction

THE mechanical requirements for fiber coatings in brittle-matrix composites are reflected in two properties:[1-3] debonding and sliding. These properties are manifest as an interface debond energy, Γ_i, and a stress to cause sliding along the debonded interface, τ. A prerequisite for good composite strength and toughness is that a debond criterion be satisfied, wherein the debond energy relative to the fiber fracture energy, Γ_f, satisfy $\Gamma_i/\Gamma_f < 1/4$.[4] Control of sliding is needed to ensure a notch-resistant material, such that $\tau \gtrsim 100$ MPa. Larger values result in high stress concentrations on fibers around notches and lead to notch-sensitive materials.[5] Coatings of C and BN meet these criteria, but both are susceptible to oxidation. Consequently, when SiC fibers are used, and when matrix cracks are present, oxidation embrittlement is encountered because the fiber oxidizes to form a silicate layer that violates debonding requirements.[6] Other coatings are thus desirable for high-temperature applications. The present study examines some alternative fiber coating concepts, with emphasis on coatings for *oxide fibers*, such as sapphire, which are not subject to the above oxidation problem.

Debonding of sapphire fibers* requires coatings with a debond energy $\Gamma_i \gtrsim 5$ J·m^{-2}. Few high-temperature materials have *intrinsic fracture energies* small enough to satisfy such a requirement. Potential options are oriented micas,[8,†] some amorphous oxides,[9] and fugitive coatings which are removed after composite consolidation.[10] However, the amorphous coatings have limitations governed by viscous flow at elevated temperatures, plus reaction with Al$_2$O$_3$. Two alternative concepts are explored in this article: (i) porous oxide coatings and (ii) coatings that form "weak" interfaces with Al$_2$O$_3$. The first concept recognizes that *porosity* generally decreases the fracture energy of brittle materials, such as oxides.[11] Consequently, certain porous oxide coatings may be able to satisfy debonding requirements for sapphire fibers, by allowing debonding *within the coating* itself. The second concept is based on the expectation that certain nonoxide coatings may allow *interface debonding*.[5] While most such interfaces have relatively high fracture energies ($\Gamma_i > 10$ J·m^{-2}),[5,12,13] larger than that required for the debonding of sapphire fibers, preliminary evidence has suggested that certain refractory metals provide suitably low values.[5]

An effective coating should have the attribute that it does not degrade the strength of the fibers. Consequently, coatings that either react with or dissolve the fibers are usually unacceptable. This thermochemical requirement further limits the potential set of coating materials. Various refractory materials that exhibit known thermochemical compatibility with Al$_2$O$_3$ at 1500°C have been evaluated (Table I), plus C, Y$_2$O$_3$, and the refractory metals, Mo, W, Cr, and Zr. The latter are still susceptible to oxidation, but in conjunction with oxide fibers, it is hoped that the composite system would have good durability in oxidizing atmospheres, superior to either C or BN coatings on SiC fibers.

II. Approach

The overall approach used to identify viable fiber coating concepts is illustrated in Fig. 1. Planar geometries readily amenable to processing and testing are used to screen candidate coating materials. The associated test procedures include a Hertzian indentation technique[14] and a mixed-mode flexure test[15] (Figs. 1(a) and (b)). For coatings that exhibit debonding,

---

R. J. Kerans—contributing editor

†This concept is being explored at Corning Incorporated, by K. Chyung.

Table I. Some Materials Thermochemically Stable with Al$_2$O$_3$ at 1500°C

Material	Ref.	Remarks
γ-TiAl	29	Al$_2$O$_3$ dissolves
Nb	30	Al$_2$O$_3$ dissolves
NiAl	31	
ZrO$_2$	32	

the fracture energy. Γ, may also be determined from these tests. The subset of coating materials that satisfy fiber debonding requirements is then used to address composite performance. For this purpose, sapphire fibers are coated and incorporated into a brittle matrix. Beam specimens are cut from the consolidated plate (Fig. 1(c)), with the fibers oriented along the beam axis. Tensile and/or flexural tests are then used to assess the interaction of a crack with the coated fibers and to obtain information about the sliding stress. τ. The magnitude of τ is ascertained from a measurement of the crack opening displacement as a function of the applied load.[16] Such tests also permit measurement of the fiber pull-out length, h, and the fiber fracture mirror radii.[17-19] The latter yield a direct estimate of the *in situ* strengths of fibers, S.[19] The magnitudes of S and h, in turn, give another estimate of τ, and thus provide a useful consistency check. In addition, τ can be obtained from fiber push-through tests (Fig. 1(d)).[20-22] In the present study, a combination of the above tests is used to assess coating concepts for sapphire fibers in polycrystalline Al_2O_3.

III. Experimental Procedure

(1) Processing

The coatings were deposited either by evaporation, sputtering, chemical vapor deposition, or sol-gel methods. For the *planar geometry*, coatings were deposited on two surfaces, each representing either the fiber or matrix component of the composite. Bonding was then conducted by hot pressing at homologous temperatures (for the coating material) in the range $0.4 < T/T_m < 0.7$. Consequently, the system experienced a thermal cycle analogous to that expected for composite processing. *Specimens containing fibers* were produced by sputter or evaporation coating sapphire fibers and incorporating them into powder matrices, using hot pressing to achieve consolidation.

(A) *Coating Deposition:* Oxide "sol-gel" coatings were produced from liquid precursor materials. A spin coating apparatus was used to deposit the coatings onto the planar substrates used for diffusion bonding. The coated substrates were then heat-treated in air to temperatures suitable for pyrolysis of the precursor, typically below 1000°C. During pyrolysis, the film is converted to an oxide. Subsequent iterations were used to increase the thickness of the coating.

Sputtered coatings were deposited onto sapphire *disks* and *fibers* (Saphikon single-crystal sapphire fibers) in an rf diode sputtering unit. The sputtering targets used in most cases were high purity ($\geq 99.9\%$): only the W target had a lower purity ($\sim 99.5\%$). Oxide coatings were deposited by reactive sputtering using a 50%–50% mixture of research-grade argon and oxygen at a total working gas pressure of 6 mtorr. The intermetallic compounds were produced from dual opposed targets of the pure elements. Both the refractory metal and intermetallic coatings were deposited in an atmosphere comprised of research-grade argon at 6 mtorr working gas pressure. The top and bottom target voltages were maintained at 3 and 0.5 kV, respectively. Fibers were rotated during coating at ~ 1 rpm.

Submicrometer-thick Mo coatings were deposited onto sapphire fibers using an electron beam evaporator and a high-purity target. A glow discharge cleaning procedure was used prior to coating the fibers. Deposition was carried out at relatively high vacuum ($< 10^{-6}$ torr), with the fibers rotated at ~ 10 rpm.

The carbon coatings were produced by a low-pressure chemical vapor deposition technique in which methane was mixed with research-grade argon carrier gas in a tube furnace. Flow rates of 10 cm³/min, for the methane, and 100 cm³/min. for the argon, were used. Throughout deposition, the furnace temperature was maintained at 1200° to 1300°C.

(B) *Bonding and Consolidation:* For experiments to be conducted with planar configurations, three different Al_2O_3 materials were used: (i) (0001) sapphire; (ii) a high-purity poly-

crystalline material; and (iii) a low-purity material (Coors AD-995 and Coors AD-96 substrates, respectively). The test specimens were produced by diffusion bonding, using a procedure described elsewhere.[14] Bonding at $T/T_m \approx 0.5$ allowed coatings to be produced with relative density levels in the range 0.65 to 1.

Tests on coated sapphire fibers were conducted after incorporating into a high-purity (99.9%) polycrystalline Al_2O_3 matrix. For this purpose, submicrometer Al_2O_3 powder (AKP-50 with a particle size of ~ 0.2 μm obtained from Sumitomo Chemical Co.. Ltd.) was isostatically cold-pressed into two thin disks ~ 5 cm in diameter. These disks were then sintered in air at 1500°C for 2 h. A row of coated fibers and loose powder were placed between the disks, the assembly inserted between dies and vacuum hot-pressed at 1500°C for 2 h subject to an axial pressure of ~ 2 MPa. These consolidation conditions resulted in an essentially fully dense matrix.

(2) Testing and Analysis

(A) *Mechanical Behavior:* The Hertzian indentation and mixed-mode flexure testing procedures used with planar specimens have been described elsewhere.[14,15] The flexural tests required precracking. This step was conducted in three-point flexure, using a row of Knoop indentations along the tensile surface to control the crack pop-in load and, hence, the extent of the precrack along the interface.

The tests used with the specimens containing fibers have been performed using a combination of fiber push-out and pull-out techniques. The fiber push-out technique has been described previously.[20] The fiber pull-out tests required that chevron notches be machined into beams containing single fibers (Fig. 1(c)). This notch geometry ensured stable crack growth through the beam upon flexural loading. The crack was grown until the crack front passed below the fiber. This occurred with a small crack opening, which induced some fiber debonding and sliding. After precracking, the beam was supported and the remaining matrix ligament mechanically removed. This procedure created a specimen consisting of two blocks of matrix material bridged by a single fiber, amenable to tensile testing. Tests were conducted *in situ* in a Hitachi 2100 scanning electron microscope (SEM) to permit measurement of the crack opening displacement and the corresponding tensile loads. These measurements may be used to evaluate the sliding resistance, τ.[16]

(B) *Analytical Techniques:* Specimens for scanning electron microscopy were prepared using standard metallographic techniques. Carbon-coated samples were examined in a JEOL SM 840 SEM in secondary mode. The microscope was equipped with a Tracor Northern TN 5500 system. Samples for transmission electron microscopy (TEM) were prepared by grinding wafers to a final thickness of approximately 100 μm before cutting 3-mm-diameter specimens. These were subsequently dimple-ground and ion milled to electron transparency with Ar at 5 kV and 1 mA at 14° incidence angle. The samples were examined at 200 kV in a JEOL 2000FX TEM equipped with a LINK eXL high take-off angle energy dispersive spectroscopy system. Computer simulations and indexing of selected area diffraction (SAD) patterns were facilitated by the Diffract software package (Microdev Software, Hillsboro, OR 97124).

IV. Coating Characterization

(1) Oxides

For the oxide coatings, a range of porosities was generated, as illustrated in Fig. 2. At the equivalent bonding cycle, the thinner, sol-gel coatings had lower *intercoating* porosity than the sputtered coatings, whereas the porosity at the interface was similar for both. In all cases, the grain size was about equal to the coating thickness. The most notable features found by TEM
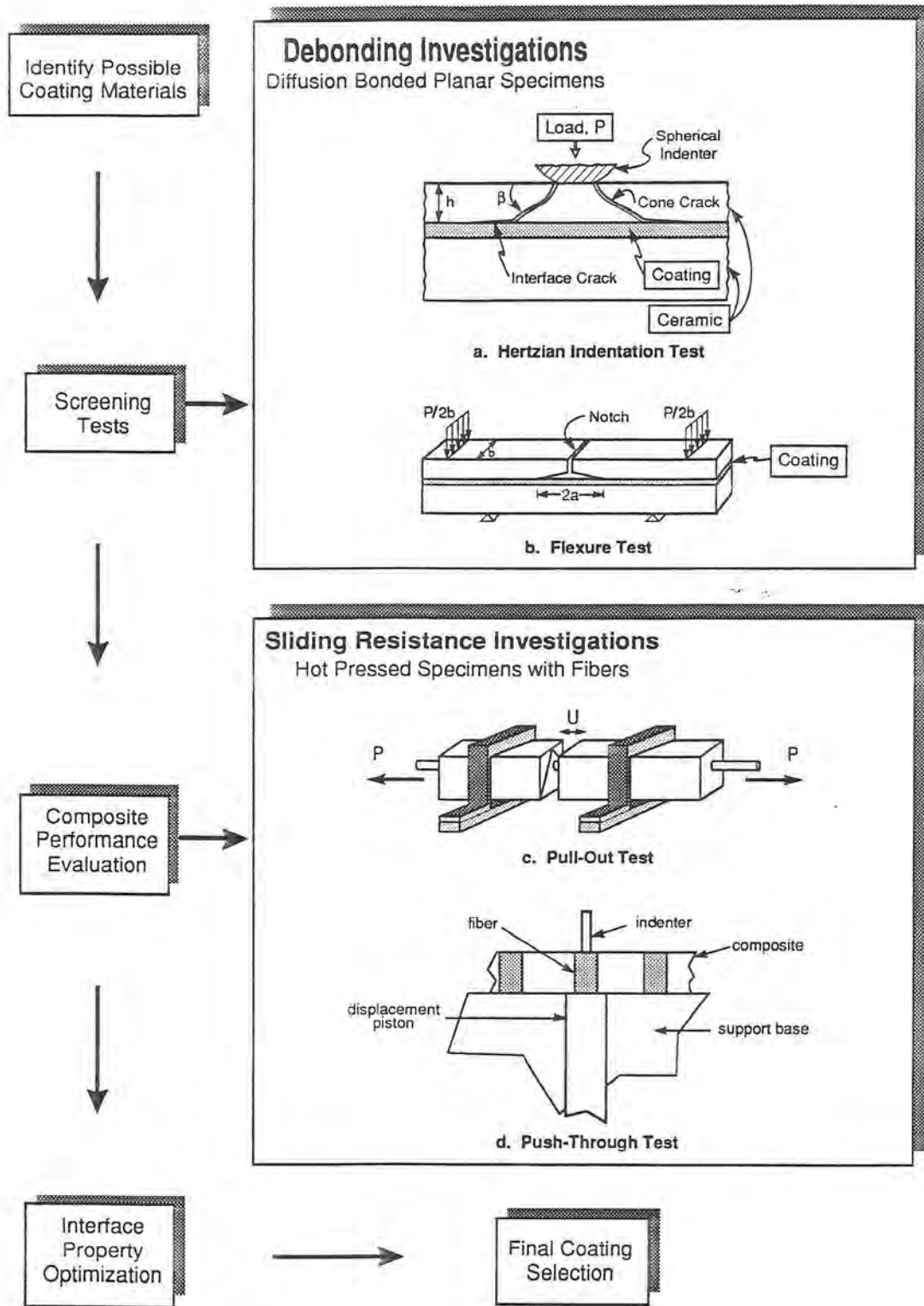
Debonding Investigations
Diffusion Bonded Planar Specimens

a. Hertzian Indentation Test

b. Flexure Test

Sliding Resistance Investigations
Hot Pressed Specimens with Fibers

c. Pull-Out Test

d. Push-Through Test

Identify Possible Coating Materials

Screening Tests

Composite Performance Evaluation

Interface Property Optimization

Final Coating Selection

Fig. 1. Approach adopted to identify viable fiber coating concepts for brittle-matrix composites, consisting of developing testing procedures to evaluate the debonding and sliding propensities of various coatings on sapphire.

were bend contours in the sapphire caused by residual strains[23] (Fig. 3). For unstabilized ZrO_2 coatings, extensive straining in the sapphire was apparent, as well as microcracks within the coating (Fig. 3(A)). This effect diminished with decreasing coating thickness (Fig. 3(B)). Selected area diffraction indicated that the ZrO_2 was monoclinic and the strains are attributed to the tetragonal-to-monoclinic phase transformation. For ZrO_2 coatings partially stabilized with 3 mol% Y_2O_3, the tetragonal phase was retained and the intensity of the strain contours diminished (Fig. 3(C)). However, some residual strain persisted, attributed to the thermal expansion mismatch between

ZrO_2 and Al_2O_3. Such strains appear to be an inherent problem with oxide coatings, potentially leading to fiber strength degradation (Appendix).

(2) Refractory Metals

For the refractory metal coatings, thin foil cross sections for TEM were difficult to produce, because of debonding. However, for Mo, results have been obtained in two cases: (a) a thin (0.7 μm) *evaporated* coating with the high-purity Al_2O_3 matrix and (b) a thicker (>3 μm) *sputtered* coating with the lower-purity Al_2O_3 matrix. For the former, the coating appeared to
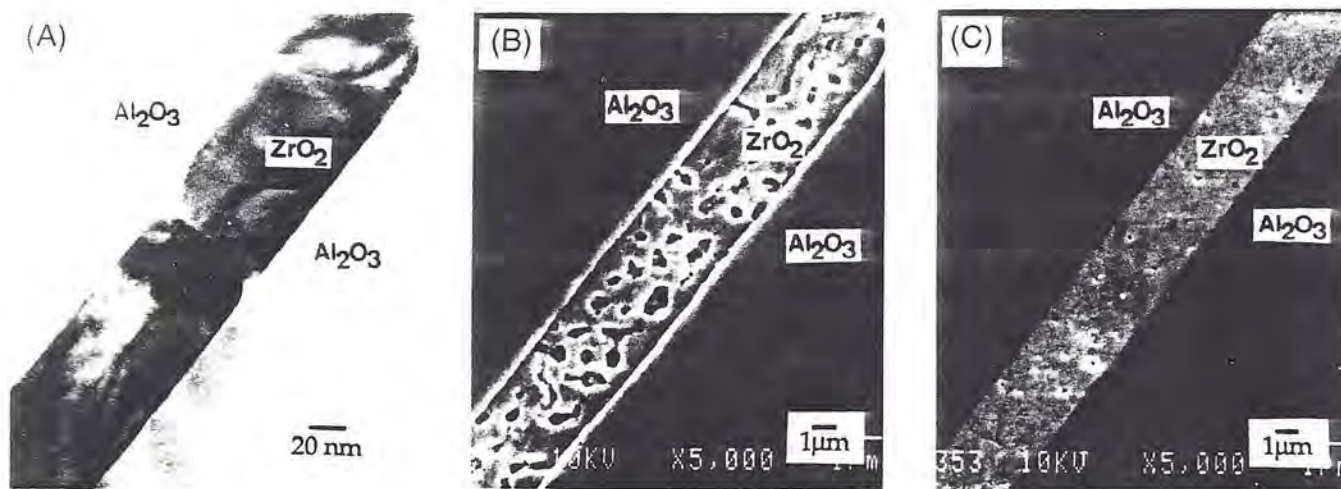
Fig. 2. ZrO_2 coating/sapphire interfaces produced by the following diffusion bonding schedules: (A) sol–gel coating diffusion bonded at 1300°C for 12 h with an applied load of ~1 MPa; (B) sputtered coating diffusion bonded at 1300°C for 12 h with an applied load of ~1 MPa; (C) sputtered coating diffusion bonded at 1300°C for 48 h with an applied load of ~3 MPa.

have some discontinuity (Fig. 4(A)), but otherwise survived the consolidation. These discontinuities, which are induced by diffusion, are typical for thin, polycrystalline films.[21] EDS analysis was unable to detect either Mo in the Al_2O_3 or Al in the Mo. For the latter, a relatively thick (~300 nm) dense polycrystalline MoO_2 phase was found at the sapphire interface (Fig. 4(B)). In addition, an amorphous silicate phase was observed at the MoO_2/Mo interface that presumably resulted from viscous flow of the silicate from the polycrystalline Al_2O_3 into porosity at this interface.

The Mo coatings were also investigated by SEM, *after debonding*. For *sputtered* coatings, oxide particles (identified as MoO_2) were found to be attached to the sapphire in regions where debonding occurred between the Mo and sapphire. X-ray diffraction of the debond surface confirmed the presence of MoO_2 on the sapphire. Shallow ridges were also apparent on the sapphire side of the debond surface, having spacings comparable to the grain size in the metal (Fig. 5(A)). These ridges are believed to form at grain boundaries, by diffusion during the bonding process, as equilibrium dihedral angles are established. Small impressions were evident on the Mo side of the debonded surface between Mo and the *higher-purity Al_2O_3* (Fig. 6), having dimensions which coincide with the Al_2O_3 grain size. These are believed to have formed by deformation of the Mo during diffusion bonding.

The *sputtered* Cr coatings exhibited similar features. A thin polycrystalline chromium oxide (~200 nm thick) was attached to the sapphire (Fig. 7), with the remainder of the coating being Cr. Analysis by EDS indicated no Cr in the Al_2O_3 and only trace amounts of Al in the chromium oxide. Selected area diffraction patterns established that the chromium oxide was Cr_2O_3, and significant porosity existed at the metal/oxide interface. Debonding was evident, occurring between the metal and its oxide layer.

The *sputtered* W coatings on sapphire exhibited pronounced ridges on the sapphire side of the debond surface (Fig. 5(B)). These have been associated with Fe- and Cr-rich grain boundary impurity phases, originating in the sputtering target. The resulting degradation of the sapphire, evident in Fig. 5(B), illustrates the importance of selecting chemically stable coatings. Similar features were observed at C/Al_2O_3 interfaces diffusion bonded at high temperatures (>1400°C) under high vacuum (>10^{-6} torr). For this system, the ridges are attributed to the formation of an Al_4C_3 reaction product.

Studies of the *as-sputtered* Mo and Cr films, using WDS and X-ray diffraction, revealed an oxide surface layer. In addition, there was an oxide layer adjacent to the sapphire, identified by peeling the coating from the substrate. These findings indicate
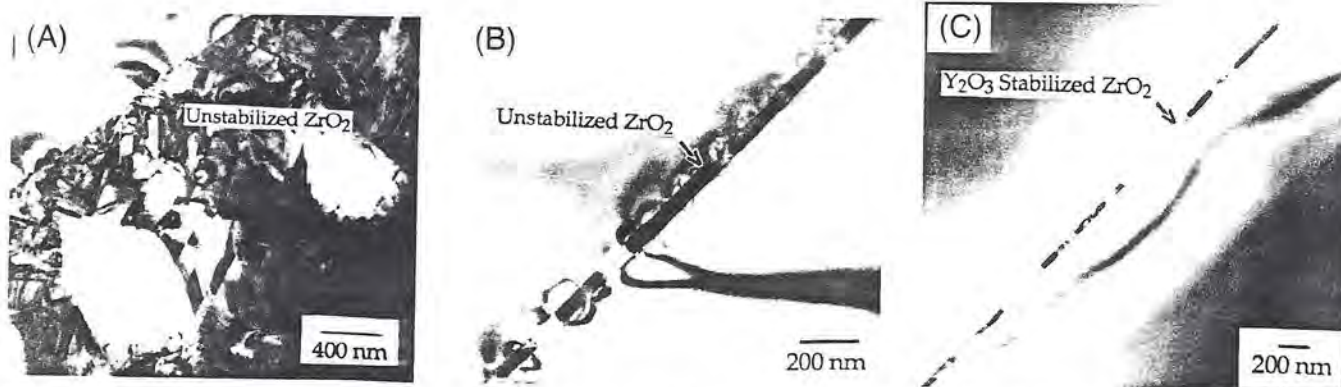
Fig. 3. (A) Extensive bend contours in the sapphire when unstabilized ZrO_2 sputtered coatings were used. It is believed that the contours result from strain in the fiber due to the $t \rightarrow m$-ZrO_2 phase transformation. (B) The bend contours in the sapphire decrease with coating thickness for the unstabilized sol–gel ZrO_2 coating. (C) The extent of bend contours was further reduced when thin stabilized sol–gel ZrO_2 coatings were used. The remaining stresses are believed to result from CTE mismatch across the well-bonded interface.
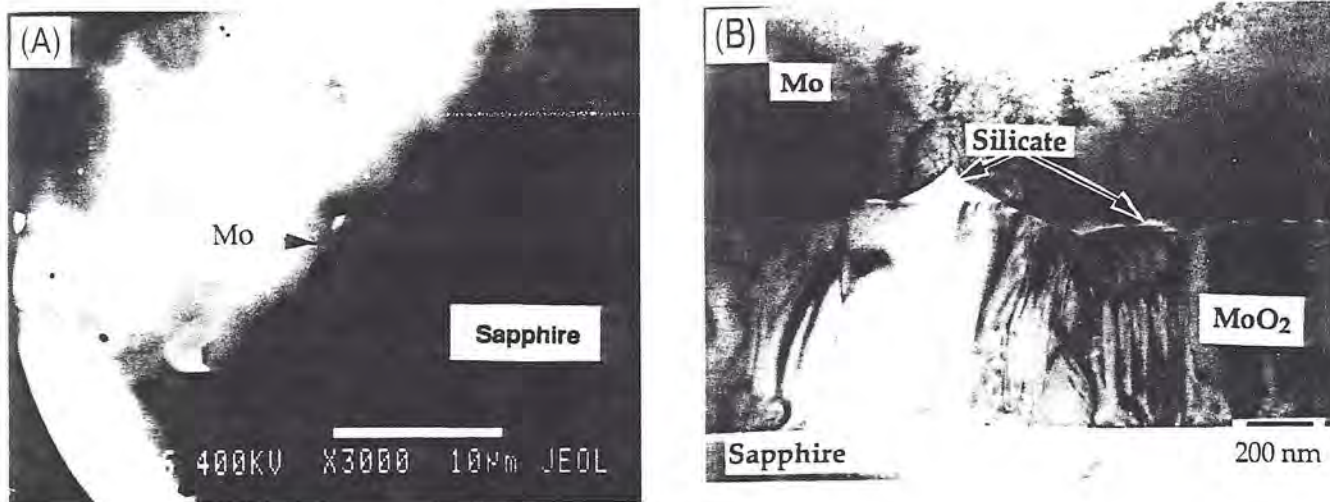
Fig. 4. (A) TEM micrograph showing the discontinuous submicrometer Mo coating on a sapphire fiber in the high-purity Al_2O_3 matrix. (B) TEM micrographs of a diffusion bonded Mo/sapphire interface with the lower-purity Al_2O_3. A continuous MoO_2 phase occurs adjacent to the sapphire and an amorphous silicate phase exists within the interfacial pores between Mo and the MoO_2 phase.

that the oxide phase is initially deposited on the sapphire substrate during sputtering and that a surface oxide forms subsequent to deposition, prior to diffusion bonding.

V. Mechanical Measurements

(1) Debonding

Preliminary experiments conducted on planar specimens with a spherical indenter provided information about the incidence of debonding at a 30° crack inclination to the interface. From such experiments, it was established that most diffusion-bonded coatings formed high fracture energy interfaces. Only the coatings consisting of Mo, W, Cr, Zr, and C debonded consistently. Coatings of ZrO_2 and $Y_3Al_5O_{12}$[‡] were found to exhibit variable debonding tendencies. Coatings of Nb, γ-TiAl, and NiAl did not debond. Furthermore, from the list of promising coating materials, several were observed to chemically react with the sapphire during diffusion bonding. The only coating materials from this set which were found to be *chemically stable* with sapphire above 1300°C and to *reliably debond* were

Mo, Cr, porous ZrO_2, and porous Al_2O_3. Further studies were confined to these materials. The refractory metals would obviously oxidize during service. The effects of oxide formation on coating performance would need to be further studied. In at least one instance, for Mo, coating oxidation can be beneficial, as discussed in Section V(2).

The debonding propensity of the *refractory metal* coatings was observed to vary with the purity of the Al_2O_3. When either sapphire or sapphire plus *high-purity* polycrystalline Al_2O_3 was used, debonding occurred consistently with $\Gamma_i \approx 4$ J·m^{-2} for Mo and 2–3 J·m^{-2} for Cr. Furthermore, as already noted, the debonding occurred at the interfaces between either Mo/Al_2O_3 or Mo/MoO_2 and Cr/Cr_2O_3. Conversely, when the *impure* Al_2O_3 was used, debonding was not observed in the Hertzian indentation test, implying a *lower bound* for Γ_i of ~16 J·m^{-2}.[§] This behavior is attributed to the silicate phase found at the Mo/MoO_2 interface, which seemingly forms a strong bond[25,26] and increases Γ_i for that interface. In addition, as already noted, MoO_2 appears to bond well with sapphire.

[‡]Formed by chemical reaction during bonding with Y_2O_3 coatings.

[§]This lower bound is $\Gamma_i = 0.8\Gamma_f$, corresponding to a crack/interface inclination of 30°, with $\Gamma_f \approx 20$ J·m^{-2}.
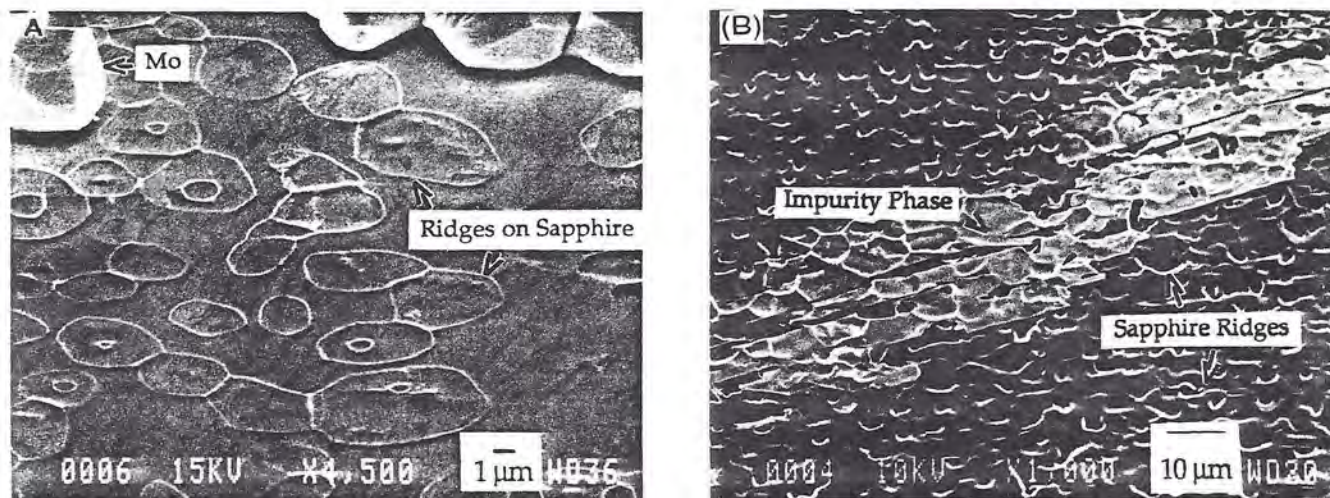

Fig. 5. (A) Shallow ridges observed on the sapphire surface of a Mo/sapphire diffusion couple upon debonding. (B) Pronounced ridges on the debonded sapphire surface when an impure W coating was used. The grain boundary impurity phase is composed of Fe and Cr.
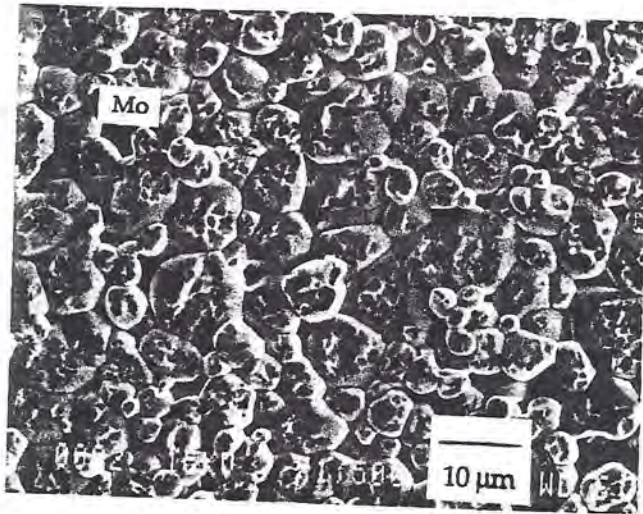
Fig. 6. Mo coating conforming to the surface features of a high-purity polycrystalline Al_2O_3 substrate during diffusion bonding.

The results for the *oxide coatings* were found to be sensitive to the coating porosity. The *dense* coatings, which have a relatively high interfacial fracture energy, debond along the *interface*. But debonding only occurred when the crack approached the interface at a shallow inclination. Conversely, the coatings having the *lowest relative density* ($\rho \approx 0.65$), exhibited a relatively low interfacial fracture energy, $\Gamma_i \approx 5$ J·m^{-2}, and debonded *within the coating, at all crack inclinations*. Such debonds exhibit fracture surface features typical of those for porous ceramics.[11] These debonding tendencies are rationalized by using the coating density, ρ, as a plotting variable against the ratio of the interfacial fracture energy to sapphire fracture energy Γ_i/Γ_f (Fig. 8(A)).

The debonding results obtained *for all of the above coatings* can be displayed on a debond diagram, relevant to sapphire fiber-reinforced brittle-matrix composites (Fig. 8(B)).

(A)

(B)

Fig. 8. (A) The relative density of oxide coatings plotted as a function of Γ_i/Γ_f clarifies the role of coating porosity in the debonding process. (B) A summary of the interfacial fracture energy measurements for various coatings on sapphire is presented on a "debond map." Coatings which fall within the fiber debonding regime of the map have some potential for sapphire fibers. However, coatings denoted by ★ were found to chemically react with sapphire: these were precluded from further consideration.

(2) Sliding Resistance

For *porous oxide coatings* on sapphire fibers in a polycrystalline Al_2O_3 matrix, single-fiber tests revealed small fiber pull-out (Fig. 9). Debonding resulted in a monolayer of the oxide particles attached to the fiber that remained throughout the sliding process (Fig. 9). These particles are believed to act as asperities that resist sliding, resulting in a relatively large sliding stress, τ. This stress was estimated from the pull-out length and the fracture[16-18] mirror radius to be ~140 MPa (Table II). A similar value was obtained from fiber push-out measurements. This value of τ is larger than that required for optimum composite strength and toughness.

The refractory metal coatings debond readily during single-fiber pull-out tests, but the coating is plastically deformed. This deformation occurs because the coating conforms to both the matrix and the fiber during consolidation and results in prohibitively high sliding resistances, such that little fiber pull-out
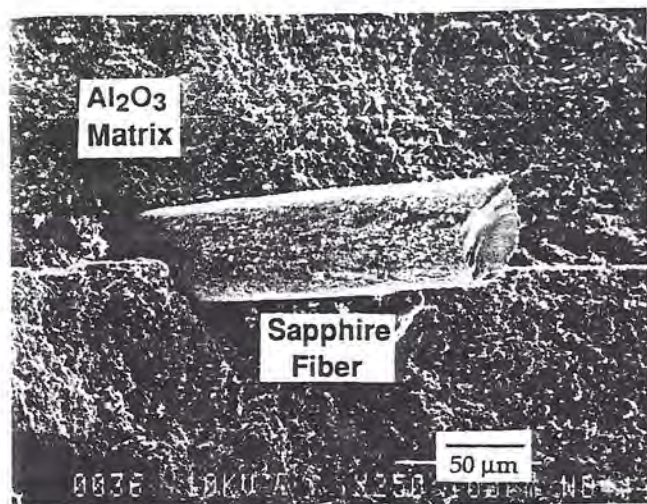

Fig. 7. Cr/sapphire diffusion bond containing a Cr_2O_3 phase adjacent to the interface.

Fig. 9. A porous oxide interface led to fiber pull-out of a few fiber diameters. Oxide particles were observed to sinter to the sapphire fiber and remained attached during pull-out. The fracture mirror on the fiber is also visible.

occurs (Fig. 10). Similar behavior is found during push-out tests (Fig. 11(A)), which also indicate a high sliding resistance, $\tau \approx 120$ MPa (Fig. 13).

A reduction in the sliding resistance for Mo-coated fibers has been achieved by *removing the coating*, after composite consolidation, to leave a gap between the fiber and the matrix. This has been accomplished by heating the composite in air* (1000°C for 2 h). The surface roughness of the fiber and the matrix then provide the sliding resistance. For coatings somewhat thicker than the asperity amplitude on the fiber (~ 1 μm), the sliding resistance obtained from crack opening displacement measurements in single-fiber pull-out tests is found to be small ($\tau < 1$ MPa), with large associated pull-out lengths (Fig. 12). This sliding resistance is too low for the requisite combination of strength and toughness in the composite. For thinner (~ 0.7 μm) coatings, push-out tests indicate a sliding resistance within the requisite range, $\tau \approx 20$ MPa (Fig. 13), with no evidence of wear mechanisms on the fiber surface (Fig. 11(B)).

VI. Concluding Remarks

The debonding and sliding properties of various coating materials on sapphire fibers have been evaluated. In general, most materials bonded well to sapphire. The notable exceptions were certain *refractory metals* (such as Mo, Cr, and W) which formed low fracture energy interfaces with sapphire. Several factors may be responsible for the low debond energies: porosity at the interfaces, oxygen dissolved in the metal (that suppresses plastic dissipation),[13] and the formation of a metal oxide

(MoO₂ or Cr₂O₃).[25-28] A systematic study would be needed to identify the critical factor(s).

Oxide coatings, which form strong interfaces with sapphire, can also be useful debond coatings, provided that they contain a significant amount of porosity subsequent to composite consolidation. The porosity in these coatings provides a low fracture energy path causing debonding within the coating. The practical problem of ensuring coating porosity may be approached by incorporating a second phase material, such as colloidal graphite, into the coating and removing it after the composite is consolidated.[33]

The sliding characteristics of the various interfaces were also investigated. The sliding resistance obtained on interfaces produced with refractory metal coatings is apparently too high for significant fiber pull-out, because the coating deforms during sliding. However, for coatings such as Mo, which form volatile oxides, the interfacial sliding resistance can be significantly reduced through coating removal by heat treatment in air. Fugitive carbon coatings also have this attribute,[10] but were not used in this study because the carbon reacted with the sapphire in the diffusion bonding experiments. It is recognized, however, that altering the processing conditions could eliminate this problem. Once the coating has been removed, the fiber surface and matrix roughness provide the sliding resistance needed for load transfer. The resultant system is also oxidatively stable. The coating thickness relative to the fiber and matrix roughness amplitude is now a key parameter.[22] An optimization study is in progress.

The *sliding resistances* of oxide coatings examined in this study were also unacceptably high, because of the undulating debond trajectory. It is believed that τ can be reduced if the grain size and porosity of the coating are carefully controlled. Further studies of the effect of debond surface irregularities on the sliding behavior are needed to address this issue.

Fiber strength degradation is another concern for oxide coatings. When reaction products with the fiber coating are avoided, potential sources of fiber strength degradation persist, including residual strain (Fig. 3) and undulations produced on the fiber surface by diffusion (Fig. 5). Some basic characteristics are amenable to analysis (Appendix). The predictions (Fig. 14) indicate that m-ZrO₂ coatings are unacceptable because, for typical coating thicknesses ($h \approx 0.1-1$ μm), the large mismatch stresses caused by the transformation lead to fiber strengths below the acceptable limit for high-performance applications ($S < 1$ GPa). Furthermore, coatings such as YAG with a mismatch governed by thermal expansion are also predicted to cause an unacceptably low fiber strength ($S < 2$ GPa), unless the coatings are thin ($h < 3$ μm). A general implication is that

---

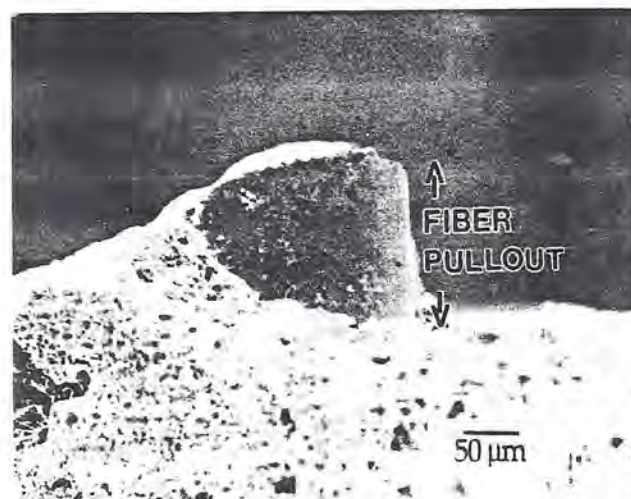*Because Mo forms volatile oxides.

Table II. Sliding Stress with Porous Alumina Interface

Fracture mirror radius, a_m (μm)	*In situ* fiber strength, S^* (GPa)	Pullout length, h (μm)	Sliding stress, τ (MPa)
27	1.68	193	142

*$S = 3.5 (K_c / \sqrt{a_m})$, where K_c is the fiber toughness (~ 2.5 MPa).[13] $\tau = S(r/2h)$, where r is the sapphire fiber radius.[13]

Fig. 10. Short fiber pull-out lengths were observed when Mo coatings were used.
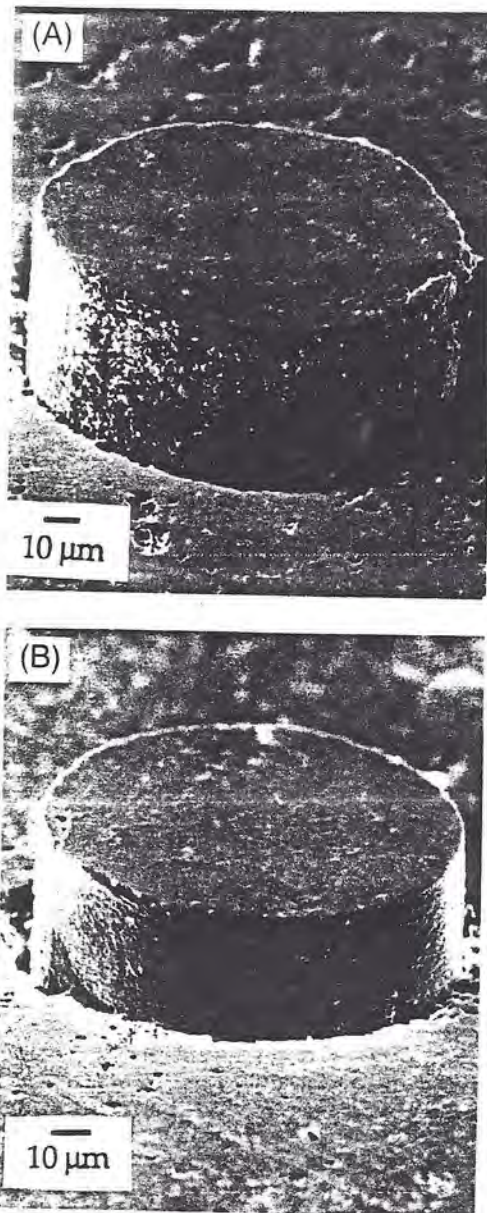
Fig. 11. The surface morphology of the pushed-out sapphire fibers was found to change when the Mo coating was removed by oxidation: (A) as-hot-pressed condition; (B) heat-treated condition.
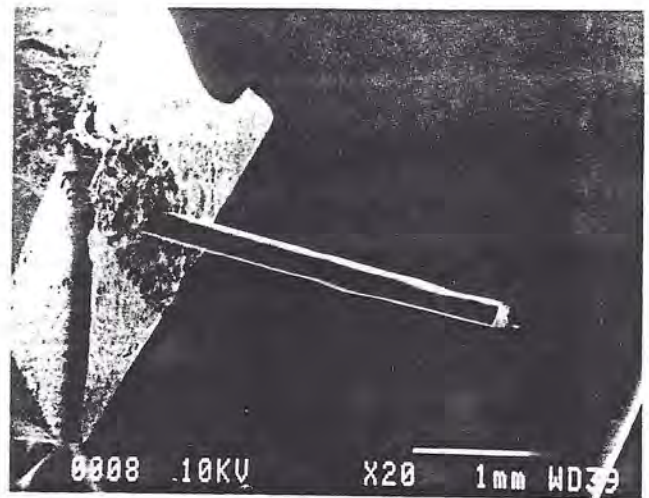

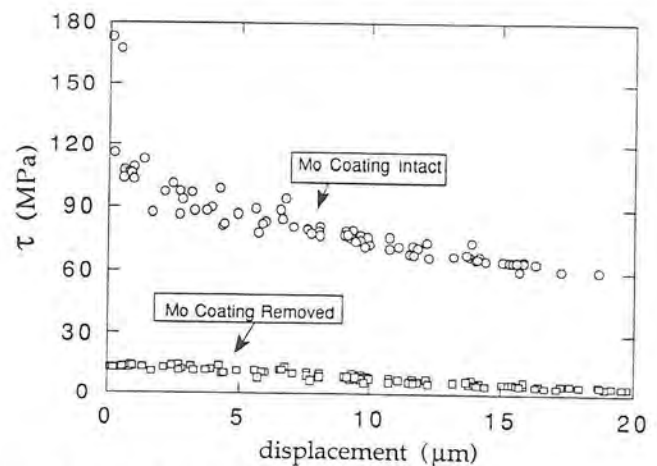**Fig. 12.** Long fiber pull-out can result when thick ($\sim$6 µm) Mo coatings are removed by oxidation.

Fig. 13. Fiber push-out curves reveal that the interfacial sliding resistance was decreased to an acceptable level by removing the submicrometer thick (0.7 µm) Mo coating from the interface.

oxide coatings, which typically bond well to sapphire, are a possible source of fiber strength degradation. The extent of degradation is diminished by thin coatings and small thermal expansion mismatch. Also, porosity in the coating tends to alleviate the degradation problem.

APPENDIX

Fiber Degradation

When the coating is in residual tension caused by thermal expansion misfit, the coating cracks before fiber failure and may cause a degradation in fiber strength. When this crack penetrates into the fiber, the stress intensity factor, K_R, for a crack of depth a associated with the residual field from the coating is[34]

$$K_R = 1.1 E_c \varepsilon_T h / \sqrt{\pi a}(1 - \nu)$$
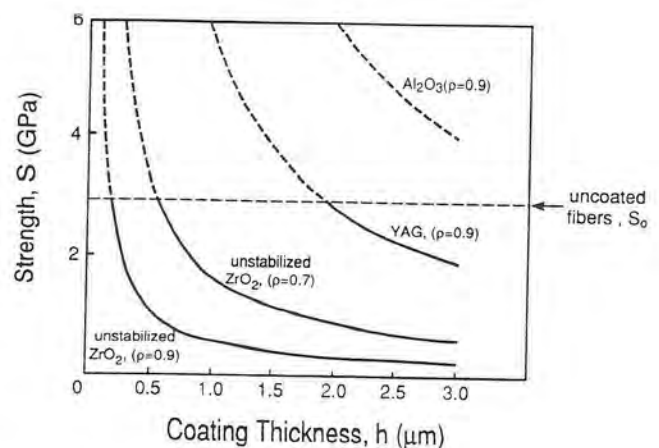$$\equiv 1.1 \sigma_0 h / \sqrt{\pi a} \tag{A-1}$$

Fig. 14. The predicted influence of oxide coatings on the strength of sapphire fiber: ρ is the coating density. It is assumed that the uncoated fibers have a strength $S_0 = 2.5$ GPa.

where ε_f is the misfit strain, h the coating thickness, E_c its Young's modulus, ν its Poisson's ratio, and σ_0 the misfit stress. The applied stress σ also induces a stress intensity[34]

$$K = 1.1\sigma\sqrt{\pi a} \qquad (A-2)$$

By adding the K's and equating to the fracture resistance of the fiber, the stress/crack length relation becomes

$$\sigma = 0.9\sqrt{\frac{E_f\Gamma_f}{\pi a}} - \frac{\sigma_0 h}{\pi a} \qquad (A-3)$$

Differentiating Eq. (A-3) and setting $d\sigma/da = 0$ for the maximum, σ_{max}, gives a fiber strength,

$$S \equiv \sigma_{max} = 0.2(E_f\Gamma_f/\sigma_0 h) \qquad (A-4)$$

This result applies when S is smaller than the strength S_0 of the uncoated fibers. Fiber strengths as a function of coating thickness for a range of dense and porous oxide coatings are plotted in Fig. 14.

References

[1]J. Aveston, G. A. Cooper, and A. Kelly, *Properties of Fibre Composites*. IPC Science and Technology Press, London, U.K., 1971.

[2]D. B. Marshall and A. G. Evans, Overview No. 85, "The Mechanical Behavior of Ceramic Matrix Composites," *Acta Metall. Mater.*, **37** [10] 2567–83 (1989).

[3]D. B. Marshall, B. N. Cox, and A. G. Evans, "The Mechanics of Matrix Cracking in Brittle-Matrix Fiber Composites," *Acta Metall. Mater.*, **33** [11] 2013–21 (1985).

[4]M. Y. He and J. W. Hutchinson, "Crack Deflection at an Interface Between Dissimilar Materials," *Int. J. Solids Struct.*, **25**, 1053–67 (1989).

[5]A. G. Evans, F. W. Zok, and J. B. Davis, "The Role of Interfaces in Fiber-Reinforced Brittle Matrix Composites," *Compos. Sci. Technol.*, **42**, 3–24 (1991).

[6]H. C. Cao, E. Bischoff, O. Sbaizero, M. Rühle, A. G. Evans, D. B. Marshall, and J. J. Brennan, "Effect of Interfaces on the Properties of Fiber-Reinforced Ceramics," *J. Am. Ceram. Soc.*, **73**, 1691 (1990).

[7]S. M. Weiderhorn, "Fracture of Sapphire," *J. Am. Ceram. Soc.*, **52**, 485 (1969).

[8]D. H. Roach, S. Lathabai, and B. R. Lawn, "Interfacial Layers in Brittle Cracks," *J. Am. Ceram. Soc.*, **71** [2] 97–105 (1988).

[9]S. M. Weiderhorn, *Fracture Mechanics of Ceramics*, Vol. 2; p. 20. Edited by R. C. Bradt *et al.* Plenum Press, New York, 1974.

[10]T. Mah, K. Keller, T. A. Parthasarathy, and J. Guth, "Fugitive Interface Coating in Oxide–Oxide Composites: A Viability Study," *Ceram. Eng. Sci. Proc.*, **12** [9–10] 1802–15 (1991).

[11]R. W. Rice, "Effects of Inhomogeneous Porosity on Elastic Properties of Ceramics," *J. Am. Ceram. Soc.*, **58** [9–10] 458–59 (1975).

[12]M. Rühle and A. G. Evans, "Structure and Chemistry of Metal/Ceramic Interfaces," *Mater. Res. Soc. Symp. Proc.*, **120**, 293–311 (1988).

[13]A. G. Evans and B. J. Dalgleish, "The Fracture Resistance of Metal–Ceramic Interfaces"; p. 295 in *Proceedings of the International Symposium of Metal–Ceramic Interfaces*. Pergamon Press, Oxford, U.K., 1992.

[14]J. B. Davis, H. C. Cao, G. Bao, and A. G. Evans, "The Fracture Energy of Interfaces: An Elastic Indentation Technique," *Acta Metall. Mater.*, **39** [5] 1019–24 (1991).

[15]P. G. Charalambides, H. C. Cao, J. Lund, and A. G. Evans, "Development of a Test Method for Measuring the Mixed Mode Fracture Resistance of Bimaterial Interfaces," *Mech. Mater.*, **8**, 269–83 (1990).

[16]D. B. Marshall, M. C. Shaw, and W. L. Morris, "Measurement of Interfacial Debonding and Sliding Resistance in Fiber Reinforced Intermetallics," *Acta Metall. Mater.*, **40** [3] 443–54 (1992).

[17]M. D. Thouless, O. Sbaizero, L. S. Sigl, and A. G. Evans, "Effect of Interface Mechanical Properties on Pullout in a SiC-Fiber-Reinforced Lithium Aluminum Silicate Glass Ceramic," *J. Am. Ceram. Soc.*, **72** [4] 525–32 (1989).

[18]F. E. Heredia, S. M. Spearing, A. G. Evans, P. Mosher, and W. A. Curtin, "Mechanical Properties of Continuous-Fiber-Reinforced Carbon Matrix Composites and Relationships to Constituent Properties," *J. Am. Ceram. Soc.*, **75** [11] 3017–25 (1992).

[19]W. A. Curtin, "Theory of Mechanical Properties of Ceramic-Matrix Composites," *J. Am. Ceram. Soc.*, **74** [11] 2837–45 (1991).

[20]D. B. Marshall and W. C. Oliver, "Measurement of Interfacial Mechanical Properties in Fiber-Reinforced Ceramic Composites," *J. Am. Ceram. Soc.*, **70** [8] 542–48 (1987).

[21]P. D. Jero and R. J. Kerans, "The Contribution of Interfacial Roughness to Sliding Friction of Ceramic Fibers in a Glass Matrix," *Scr. Metall. Mater.*, **24**, 2315–18 (1990).

[22]T. J. Mackin, P. D. Warren, and A. G. Evans, "The Effects of Fiber Roughness on Interface Sliding in Composites," *Acta Metall. Mater.*, **40** [6] 1251–57 (1992).

[23]J. B. Davis, E. Bischoff, and A. G. Evans, "Zirconia Coatings for Sapphire Fiber-Reinforced Composites"; pp. 631–38 in *Advanced Composite Materials*. Edited by M. D. Sacks. American Ceramic Society, Westerville, OH, 1991.

[24]K. T. Miller, F. F. Lange, and D. B. Marshall, "The Instability of Polycrystalline Thin Films: Experiment and Theory," *Mater. Res. Soc. Symp. Proc. Ultrastr. Proc.*, **121** [3] 823–30 (1988); *J. Mater. Res.*, **1** [5] 151–60 (1990).

[25]S. S. Cole, Jr., and G. Sommer, "Glass-Migration Mechanism of Ceramic-to-Metal Seal Adherence," *J. Am. Ceram. Soc.*, **44** [6] 265–71 (1961).

[26]E. Samuel and P. Hrma, "MoO₃ Diffusion in Aluminosilicate Glass," *J. Am. Ceram. Soc.*, **72** [6] 1091–92 (1989).

[27]*The Metal Molybdenum*. Proceedings of a Symposium sponsored by the Office of Naval Research. Edited by J. Harwood. American Society for Metals, Metals Park, OH, 1958.

[28]*Ductile Chromium and Its Alloys*, Proceedings of a Conference sponsored by the Office of Ordnance Research. American Society for Metals, Metals Park, OH, 1957.

[29]H. E. Dève, A. G. Evans, G. R. Odette, R. Mehrabian, M. L. Emiliani, and R. J. Hecht, "Ductile Reinforcement Toughening of γ-TiAl: Effect of Debonding and Ductility," *Acta Metall. Mater.*, **37**, 853–90 (1989).

[30]M. Rühle, K. Burger, W. Mader, and A. G. Evans, "Some Aspects of Structures and Mechanical Properties of Metal/Ceramic Bonded Systems"; pp. 43–70 in *Fundamentals of Diffusion Bonding*. Edited by Y. Ishida. Elsevier, New York, 1987.

[31]K. P. Trumble and M. Rühle, "The Thermodynamcis of Spinel Interphase Formation of Diffusion-Bonded Ni/Al₂O₃ Interfaces," *Acta Metall. Mater.*, **39** [8] 1915–24 (1991).

[32]M. Rühle, A. Strecker, D. Waidelich, and B. Kraus, "*In Situ* Observations of Stress-Induced Phase Transformations in ZrO₂-Containing Ceramics"; pp. 256–74 in Advances in Ceramics, Vol. 12, *Science and Technology of Zirconia II*. Edited by N. Claussen, M. Rühle and A. H. Heuer. American Ceramic Society, Columbus, OH, 1984.

[33]T. J. Mackin, J. Yang, C. G. Levi, and A. G. Evans, "Environmentally Compatible Double Coating Concepts for Sapphire Fiber-Reinforced γ-TiAl," *Mater. Sci. Eng. A*, in press.

[34]H. Tada, P. C. Paris, and C. R. Irwin, *The Stress Analysis of Cracks Handbook*. Del Research Corp., St. Louis, MO, 1973, 1985. □

Characterization and oxidation resistance of hot-pressed chromium diboride

M. L. Emiliani

Pratt & Whitney, Materials Engineering Laboratory, P.O. Box 109600, West Palm Beach, FL 33410 (USA)

Abstract

Hot-pressed chromium diboride was extensively characterized to evaluate the suitability of this material as a candidate reinforcing fiber produced by d.c. hollow cathode magnetron sputtering for NiAl intermetallic matrix composites. Bulk hot-pressed CrB_2 from which monofilament fibers would be produced was characterized and found to contain equiaxed grains 25–30 μm in diameter, approximately 12% porosity, and aluminosilicate inclusions. This starting material was also examined by Auger electron spectroscopy and found to be nominally stoichiometric. The average linear thermal expansion of hot-pressed CrB_2 from room temperature to 600 °C is 6–8 p.p.m, °C^{-1}, and approximately 10 p.p.m. °C^{-1} from 800 to 1400 °C. The room temperature bend strength of hot-pressed CrB_2 is 207 MPa. However, the room temperature elastic modulus is low (76.5 GPa), and will limit its utility as a reinforcing fiber. The thermal shock resistance of hot-pressed CrB_2 is poor, as samples quenched in water from 1100 °C contained extensive cracks. Static oxidation for up to 150 h showed that hot-pressed CrB_2 forms a thin granular oxidation product at 1000 °C, with little weight change. However, a massive chromium borate ($CrBO_3$) scale is formed at 1100 °C. In cyclic oxidation, CrB_2 exhibits a small weight loss at 1000 °C owing to evaporation of B_2O_3 and CrO_3, and much larger weight gain at 1100 °C owing to the formation of $CrBO_3$. Based on these results, the maximum use temperature for CrB_2 fibers exposed to ambient is approximately 1000 °C.

1. Introduction

Chromium diboride is a candidate monofilament fiber reinforcement selected for development owing to its high thermal expansion [1] and calculated thermodynamic stability in β'-NiAl alloys (40–50 at.% Al) at 1100–1400 °C [2]. A follow-up study to verify the accuracy of the thermodynamic calculations was performed using flat plate diffusion couples [3]. Hot-pressed CrB_2/Ni–50at.%Al couples diffusion bonded for 100 h at 1200 °C showed no visible reaction at the interface. However, CrB_2 reacted extensively with Ni–45at.%Al.

The desire for fibers 75–100 μm in diameter with complex structure of novel composition brings forth another fabrication route, d.c. hollow cathode magnetron sputtering. This method offers several potential advantages over other processing methods including control of well understood deposition parameters, energetic particle bombardment, the ability to deposit doped or multicomponent coatings by reactive sputtering or using multiple targets, fabrication of fibers with tailored microstructures [4], and more rapid screening of candidate materials owing to the availability of sputtering targets in a wide range of compositions.

The overall objective of this proof-of-concept effort is to produce continuous high strength polycrystalline CrB_2 fiber 75–100 μm in diameter by hollow cathode sputtering [5]. Hot-pressed CrB_2 was extensively characterized prior to static and cyclic oxidation testing to aid in determining the quality of as-received material compared with that previously reported in the literature. The static and cyclic oxidation resistance of bulk hot-pressed CrB_2 was evaluated to determine the potential oxidation resistance of CrB_2 monofilament fibers.

2. Characterization of chromium diboride

2.1. Hot-pressed chromium diboride
2.1.1. X-ray diffraction and light microscopy

Chromium diboride powder was made by Cerac Inc. (Milwaukee, WI) using a thermic reduction process, *i.e.*
$$MeO + B_2O_3 + Al(Mg,Si,Ca) \rightarrow MeB_2 + Al(Mg,Si,Ca)_xO_y$$
(where MeO is metal oxide). Spectrographic analysis of lot number 45121-C-1 [6] showed it contained a total of 0.298 wt.% metallic impurities: 0.1 wt.% Si, 0.1 wt.% Fe, 0.05 wt.% Al, 0.02 wt.% Ca, 0.01 wt.% Mg, 0.01 wt.% Ni and 0.08 wt.% Cu. Cu, Ni and Fe may

have been impurities in the Cr precursor, and Fe or an Fe salt may have been added as a sintering aid during the thermic reduction process [7]. The powder is − 325 mesh (less than or equal to 44 μm diameter) and reported to be 99.5% pure with respect to metallic impurities. A sample of powder was obtained from Cerac and found to be irregular with sharp edges characteristic of powder made by crushing monolithic material. Many large particles were found, some with aspect ratios of 2:1 or more, as is typical of sieved powder, while a considerable fraction of the powder was less than 5 μm in diameter.

X-ray diffraction (XRD) of the as-received powder and hot-pressed material shows it consists of CrB_2 (JCPDS diffraction file card no. 34-369). No elemental Cr and B, or their respective oxides, carbides and nitrides were found. In contrast, unreacted B_2O_3 was found to be a primary contaminant in a previous study [8]. The B content was determined by Cerac to be 29.40 wt.% (29.37 wt.% theoretical). The powder was hot pressed by Cerac using a proprietary method.

A sample of hot-pressed CrB_2 was sectioned using a diamond saw and polished with diamond pastes. Light microscopy of the as-polished material shows extensive pull-out due to sectioning and polishing (Fig. 1). It is difficult to distinguish between pull-out and porosity in this sample, which has a density of 84%–89% theoretical. CrB_2 is reportedly etched by a 1:1 mixture of $HNO_3 + HCl$ at room temperature in 1–2 s [9]. However, the microstructure was not revealed after etching with this solution for up to 11 min.

2.1.2. Scanning electron microscopy

Scanning electron microscopy (SEM) of as-polished CrB_2 shows that pull-out appears as acicular regions

(Fig. 2). Energy-dispersive spectroscopy (EDS) of an approximately 100 μm^2 area shows small amounts of Al, Si and Fe are present in the material (Fig. 3(a)). Dark circular areas less than 10 μm in diameter were initially thought to be porosity (Fig. 2, arrows). EDS showed these are rich in Al, with a small amount of Si (Fig. 3(b)). These inclusions are identified as $AlSi_xO_y$ (aluminosilicate), and are probably formed during the thermic reduction process and remain after sieving and hot-pressing. The trace of Fe detected in Fig. 3(a) is most probably in solution in the diboride. The porosity remains difficult to distinguish in polished sections by SEM.

Porosity and other microstructural features of interest were revealed more clearly when fractured samples of hot-pressed CrB_2 were examined by SEM (Fig. 4). Numerous pores, some of which probably contained $AlSi_xO_y$ inclusions, are evident. Most pores are less than 5 μm in diameter and are present both inter-granularly and at grain boundaries. However, they do not appear to be connected. The grains are equiaxed, with an average grain size of 20–30 μm. Fractured CrB_2 fails by cleavage, as shown in Fig. 4.

2.1.3. Interstitial analysis

The type and average level of interstitials in hot-pressed CrB_2 was determined by combustion analysis and found to be 0.019 wt.% C, 0.001 wt.% S, 0.0012 wt.% H, 0.0689 wt.% N, and 0.232 wt.% O. There is substantial O in hot-pressed CrB_2, a large proportion of which is probably from $Al(Si)_xO_y$ inclusions. The low level of C found in hot-pressed CrB_2 further supports the reasoning that the powder was made by the thermic reduction process [7]. These analyses show that the principal impurities in hot-pressed CrB_2 are
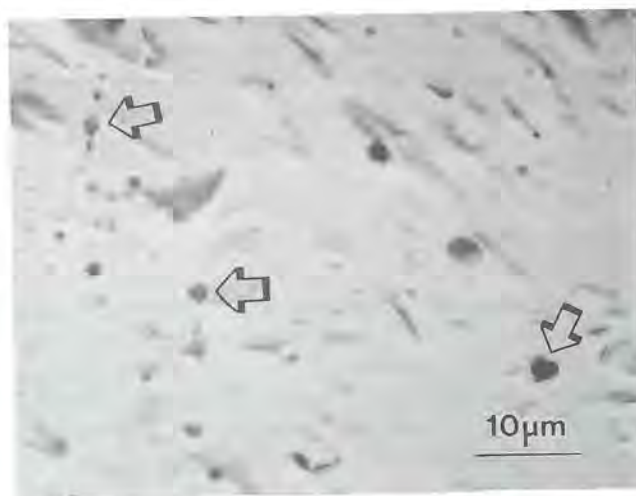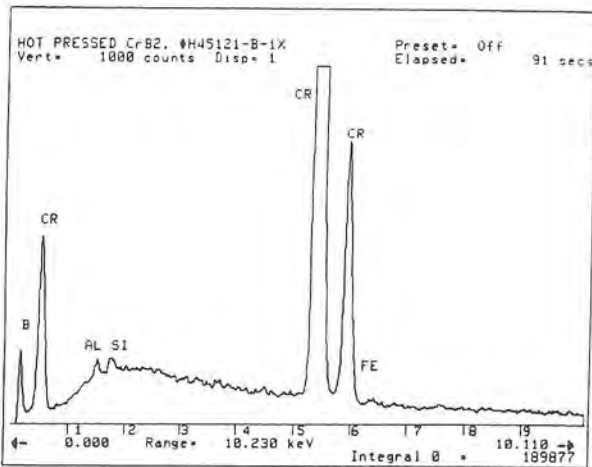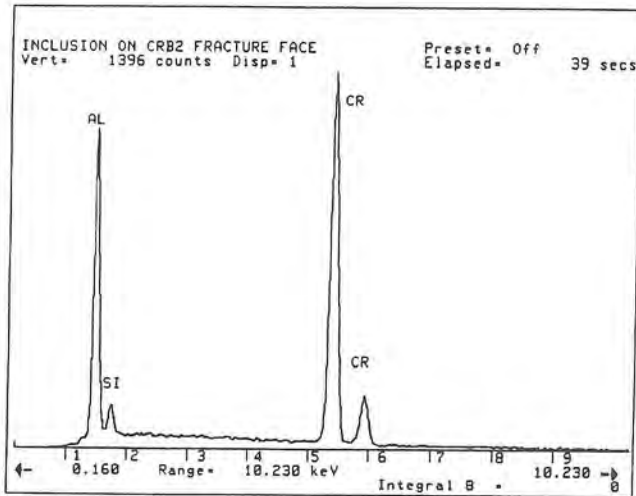

Fig. 1. Light micrograph of polished hot-pressed CrB_2. Pull-out appears as acicular regions. Porosity is not evident in this micrograph.

Fig. 2. SEM image of polished hot-pressed CrB_2. Dark areas (arrows) were identified by EDS as aluminosilicate inclusions.

(a)

(b)

Fig. 3. (a) Large-area EDS spectrum of hot-pressed CrB_2 showing Al, Si and Fe. (b) EDS spectrum of inclusions arrowed in Fig. 2. The inclusions are identified as $AlSi_xO_y$ produced during powder fabrication.

Fig. 4. Fractograph of CrB_2 showing failure by cleavage. Unconnected porosity and $AlSi_xO_y$ inclusions are apparent. The grain size is 20–30 μm. The density of hot-pressed CrB_2 is approximately 88% of theoretical.
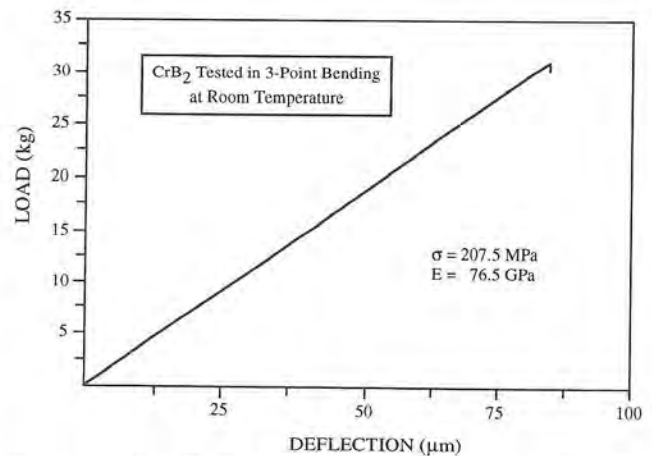

Fig. 5. Load–deflection curve for hot-pressed CrB_2 tested in three-point bending at room temperature.

Al, Si, Fe and O, and that they total approximately 0.5 wt.%. The amount of O is in agreement with a previous study [10], while the C content is low compared with that found in CrB_2 compacts fabricated by other methods [11, 12].

2.1.4. Vickers microhardness

Indentations were placed in regions free of gross pull-out and porosity. As Fig. 4 shows, however, porosity may be present in any plane below the indentation. The average microhardnesses at 25 and 200 g loads were found to be 2010 kg mm^{-2} and 2228 kg mm^{-2} respectively. This is in approximate agreement with the literature, which reports Vickers microhardnesses of 1800 kg mm^{-2} (100 g load) [13] and 2100 kg mm^{-2} (50 g load) [14]. The Knoop hardness is reported to be 1700 kg mm^{-2} [15]. In comparison, the Vickers hardness of Al_2O_3 is approximately 2100 kg mm^{-2}.

2.1.5. Bend tests

Monolithic CrB_2 was characterized by bend tests to determine the room temperature bend strength and elastic modulus. Hot-pressed CrB_2 test bars 0.25 cm $\times$ 0.25 cm $\times$ 2.54 cm long were evaluated in three-point bending. A typical load–deflection curve is shown in Fig. 5. The average bend strength was calculated to be 207.5 MPa, while the elastic modulus is 76.5 GPa. Both values are approximately 33% of that previously reported [13, 16].

2.1.6. Linear thermal expansion

The linear thermal expansion of hot-pressed CrB_2 was measured by dilatometry (Pt standard) and compared with previous data [17]. CrB_2 samples 0.25 cm $\times$ 0.25 cm $\times$ 2.54 cm long were spark cut from bulk

CrB_2 and tested to 1400 °C. Thermal expansion was measured in Ar, with data sampled at 10 °C intervals. The results, along with selected data from the literature, are plotted in Fig. 6.

The coefficient of thermal expansion (CTE) of CrB_2 is generally similar to that previously reported [17]. The average CTE from room temperature to 600 °C is 6–8 ppm °C^{-1} and approximately 10 ppm °C^{-1} from 800 to 1400 °C. The latter is about 10% lower than the average CTE previously reported from 20 to 1100 °C [18]. The shape of the curve may be caused by stress relief in hot-pressed compacts. Substantial residual stress has been found in various types of diboride compacts after hot-pressing, requiring a post-stress anneal at $T/T_M = 0.6-0.7$ ($T_M(CrB_2) = 2200$ °C) for several hours [19]. The targets were not stress relieved in a separate step after hot-pressing, but this may be incorporated as part of Cerac's proprietary hot-pressing procedures [20]. Porosity or aluminosilicate inclusions may also have had an effect in determining the shape of the curve at temperatures less than 600 °C. The CTE is 4–5 ppm °C^{-1} lower than that of equiatomic NiAl at 600–900 °C, and will result in a significant thermal mismatch.

Aluminosilicate inclusions present in hot-pressed CrB_2 may have contributed to the observed 10% decrease in CTE from 700 to 1400 °C (by rule of mixtures). For example, mullite ($3Al_2O_3 \cdot 2SiO_2$) has a linear thermal expansion of only 4 ppm °C^{-1}. The thermal expansion of CrB_2 reportedly depends on the amount of porosity [21]. The density of hot-pressed CrB_2 evaluated in the present study was calculated by measuring the sample weight and dimensions and found to be 4.92 g cm^{-3}, or 87.7% of theoretical. A previous study measured a CTE of 15.8 ppm °C^{-1} at 21–500 °C for CrB_2 containing 13.4% porosity [21].

This is, on average, double that determined experimentally in the present study over the same temperature range (Fig. 6). Thus, the material porosity may also have contributed to the observed low temperature thermal expansion behavior.

2.1.7. Surface spectroscopy, as-received

Hot-pressed CrB_2 was evaluated by X-ray photoelectron spectroscopy (XPS) and Auger electron spectroscopy (AES). The surface of hot-pressed CrB_2 was prepared by grinding with 120 grit SiC prior to examination to remove gross contaminants. XPS showed elements typically introduced during handling and exposure to atmosphere including Na, Ca, Si, Al, N, C and O. The B and Cr signals are low, while the C and O peaks dominate the spectrum. It is likely that both Cr_2O_3 (binding energy 576 eV [8]) and B_2O_3 (binding energy 191.5 eV [8]) are present on the surface of as-received CrB_2.

Sputtering the diboride surface to a depth of approximately 10 nm revealed stronger B and Cr signals and reduced O signals (Fig. 7). The stoichiometry of the sample increases rapidly with additional sputtering (the binding energy of CrB_2 is 573.6 and 187.6 eV [8]). This is in contrast to a previous study where extensive sputtering was required to remove a thick surface layer of B_2O_3 from hot-pressed CrB_2 [8].

2.1.8. Surface spectroscopy, fracture surface

Hot-pressed CrB_2 was fractured in air and then analyzed by XPS. The resulting spectrum exhibits a significant O signal due to brief exposure to atmosphere while the B signal is prominent, in contrast to that found in as-received CrB_2. The sample was then sputtered to a depth of approximately 5 nm, revealing strong Cr and B signals (Fig. 8). Note that O and C remain detectable at this depth below the fracture surface.

AES was performed on the as-fractured surface of CrB_2 in a region free of oxide inclusions (Fig. 9(a)), and reveals significant levels of C and O. Sputtering to a
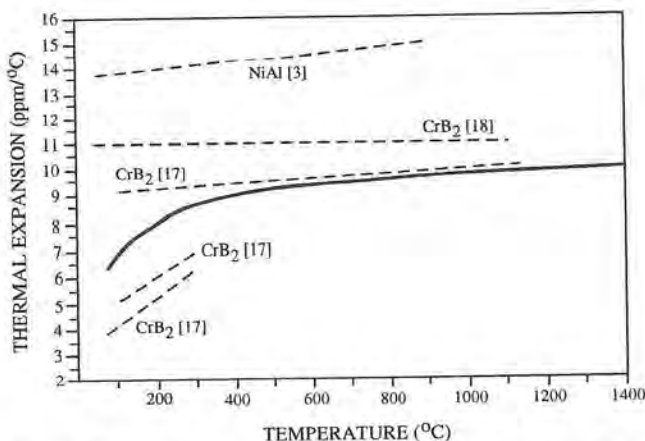

Fig. 6. Plot of linear thermal expansion for hot-pressed CrB_2. The thermal expansion of NiAl is shown for comparison. The experimentally determined expansion is approximately 10 ppm °C^{-1} from 800 to 1400 °C.
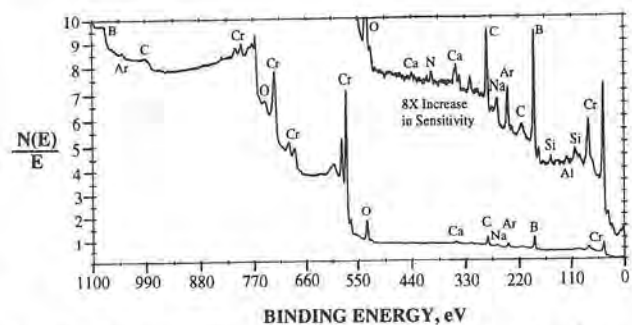

Fig. 7. XPS spectrum of the surface of as-received hot-pressed CrB_2 after sputtering to approximately 10 nm below the free surface.

depth of 300 nm revealed strong Cr and B signals, a small C signal, and no O (Fig. 9(b)). C was detected at levels of approximately 2 at.% (0.7 wt.%) at depths greater than 5 nm. The stoichiometry of freshly fractured CrB_2 *vs.* depth below the free surface was determined by quantitative AES using peak heights and
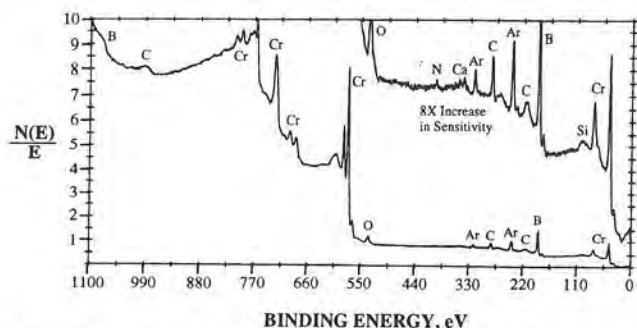

Fig. 8. XPS spectrum of a hot-pressed CrB_2 fracture surface after sputtering to approximately 5 nm below the free surface.
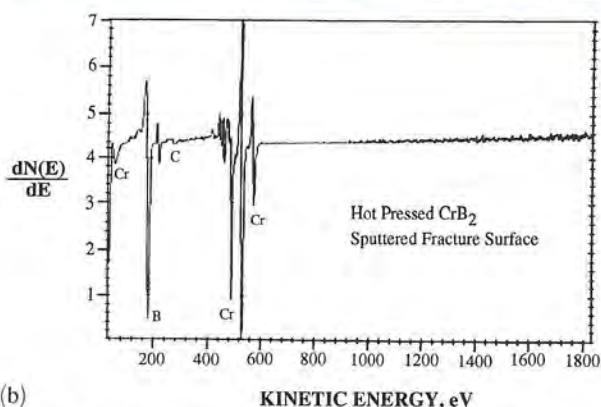

(a)

(b)

Fig. 9. (a) SEM image of the fracture surface of hot-pressed CrB_2. The location of the Auger analysis is labeled X. Note the aluminosilicate inclusion (arrow). (b) Auger spectrum of a fracture surface of hot-pressed CrB_2 after sputtering to approximately 300 nm below the free surface. Only Cr, B and C are detected.

instrument sensitivity factors (Table 1). The average B-to-Cr ratio indicates that the as-received material is stoichiometric within the limits of experimental error.

2.2. Oxidation of hot-pressed chromium diboride
2.2.1. Thermal shock

The thermal shock resistance of hot-pressed CrB_2 was assessed by heating coupons in static furnace air to 1100 °C for 30 min and quenching in water at 25 °C. The samples contained extensive cracks (Fig. 10(a), arrows), but did not fracture into smaller pieces. Secondary and backscattered electron images of cracks are shown in Figs. 10(b) and 10(c). The backscattered image (Fig. 10(c)) shows variations in chemical composition of the surface oxide scale, with darker areas containing higher concentrations of low atomic weight elements such as O or B.

2.2.2. Static oxidation

Hot-pressed CrB_2 was oxidized at 1100 °C in static furnace air for 100 h to assess its oxidation resistance. Coupons placed in 99.8% pure alumina crucibles were bonded to the bottom of the crucible after heat treatment (Fig. 11(a), arrows). The oxidation product is generally massive, colored various shades of green, and is non-adherent in some areas (Figs. 11(b) and 11(c)). Large regions free of thick oxide scale are present near the bottom of the sample, suggesting that it may have been starved of O in the crucible.

Oxidized CrB_2 was examined in cross-section by light microscopy and found to contain a thick, porous, largely adherent and non-protective oxide with a $CrB_2 \rightarrow$ oxide transition zone approximately 100 μm thick (Fig. 12(a)). The oxidation product also contains uniform dispersion of fine particles. A corresponding scanning electron micrograph (Fig. 12(b)) shows fracture of the oxide scale at the transition region. Secondary and backscattered electron images of the CrB_2 transition zone are shown in Figs. 13(a) and 13(b). The contrast in Fig. 13(b) is indicative of local variations in

TABLE 1. Composition of CrB_2 fracture surface, in atomic per cent

Depth below surface (nm)	B	Cr	C	B to Cr ratio
2.5	65.3	30.9	3.8	2.11
5	66.0	31.7	2.4	2.08
20	64.7	33.1	2.1	1.95
100	65.0	33.6	1.4	1.93
300	64.8	33.5	1.7	1.93

The sputtering rate of CrB_2 is assumed to be the same as that of tantalum pentoxide.
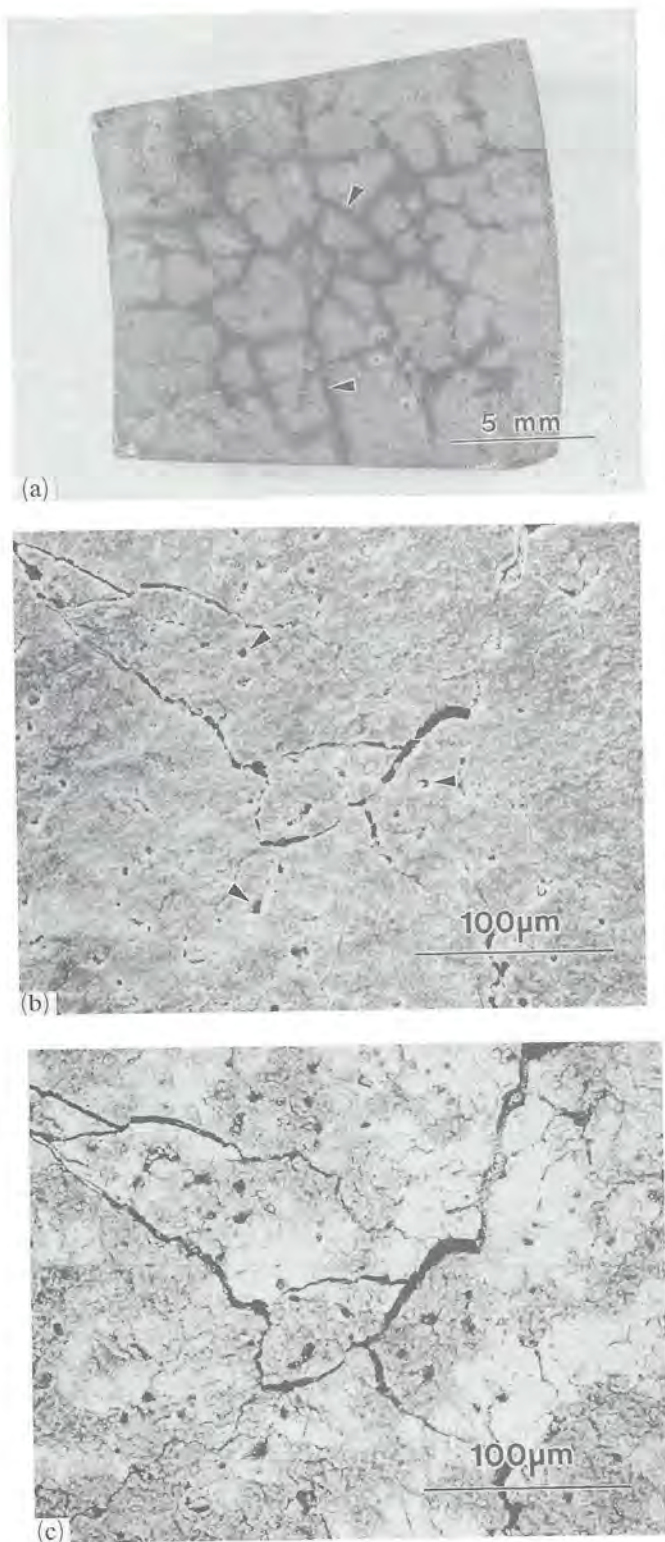Sensitivity factors used to determine the composition by the instrument manufacturer.

(a)

(b)

(c)

Fig. 10. (a) Photomacrograph of hot-pressed CrB_2 water quenched from 1100 °C. The coupon remained in a single piece despite containing extensive cracks (arrows). (b) Secondary electron micrograph of cracks in hot-pressed CrB_2 water quenched from 1100 °C. Note the pores in the surface characteristic of those found in hot-pressed CrB_2 (arrows). (c) Backscattered electron micrograph of cracks in hot-pressed CrB_2 water quenched from 1100 °C. The dark areas are rich in O or B.

atomic weight. The transition zone (labeled T) contains a phase with brighter contrast compared with bulk CrB_2. In addition, there is a continuous layer between the transition zone and bulk CrB_2 (labeled X) with similar contrast. Both contain higher Cr contents than bulk CrB_2, indicating that B oxidizes selectively.

The results of electron microprobe studies of the oxide and transition region are shown in Figs. 14 and 15. Metal-rich particles were found randomly distributed in the oxidation product (Fig. 14(a)). Cr and O X-ray maps of the oxidation product indicate it is rich in these two elements (Figs. 14(b) and 14(c)). Conversely, the B X-ray map (Fig. 14(d)) indicates that the oxide scale (and bulk CrB_2) is deficient in B. The actual B content is greater than it appears in Fig. 14(d) because the microprobe used to analyze this sample was not optimized for B detection by wavelength-dispersive spectroscopy (WDS). EDS of metal-rich particles in the oxide show they contain primarily Cr. A WDS search for low Z elements shows B is present in these particles (Fig. 15, inset). The solubility of B in Cr is less than 1 at.% below 1500 °C, indicating the particles may be a metal-rich boride phase such as Cr_2B or Cr_5B_3 [22]. The range of composition over which these phases are stable is not known.

The surface of the oxidation product was examined by SEM (Fig. 16(a)) and contained small faceted particles less than 5 μm in diameter (arrows) and a discontinuous phase with a glass-like appearance (labeled G). EDS showed the primary constituent is Cr, with small amounts (less than or equal to 1 wt.% each) of Si and Fe (Fig. 16(b)). A WDS search for low Z elements detected both O and B (Fig. 16(b), insets). The poor signal-to-noise ratio of the B peak is due to limitations in detection capability by WDS. B is probably concentrated on the surface as an oxide. B_2O_3 melts at 450 °C [23], and begins to vaporize at 1100 °C [24].

A portion of the oxidation product was removed and examined by XRD. The pattern corresponds to chromium borate, $CrBO_3$ (JCPDS diffraction file card no. 15-663), with hexagonal crystal structure and lattice parameter $a_0 = 0.4578$ nm and $c_0 = 1.4258$ nm. An unidentified phase with d-spacings of 0.3196 nm, 0.1669 nm, and 0.1487 nm was also present at lower values of 2Θ, but could not be matched to reference patterns for Cr_2O_3 or crystalline B_2O_3. In addition, ternary oxide phases may be amorphous and not identifiable by XRD. The unidentified peaks may also be from the Cr-rich particles found in the oxidation product (Fig. 14(a)). Evaluation of JCPDS diffraction file cards for Cr_2B and Cr_5B_3 (nos, 38-1399 and 32-278 respectively) indicate a possible match with Cr_5B_3.

Additional oxidation tests were performed at 1000 °C in static air for 150 h to measure the weight change per unit area. The samples experienced a small
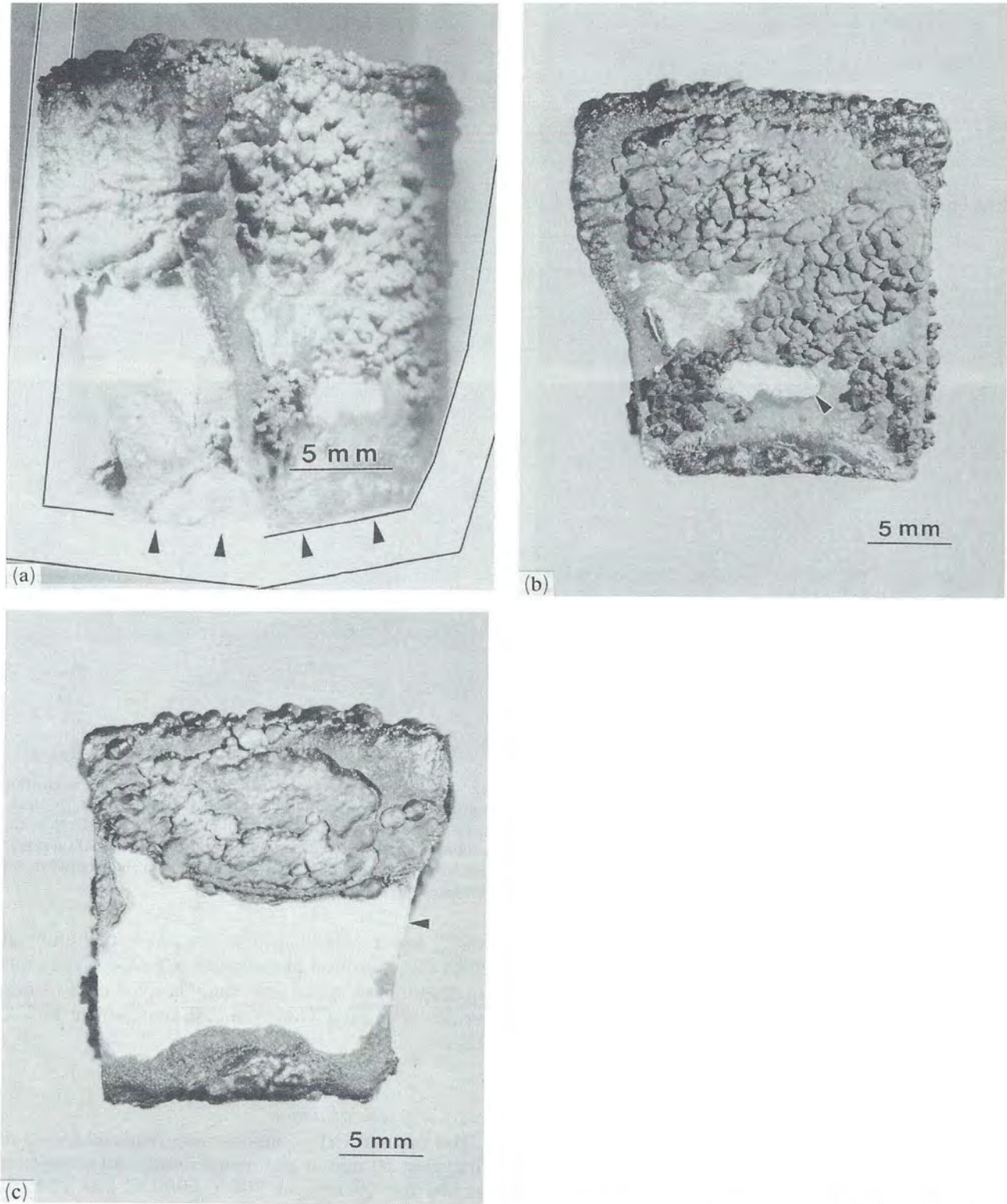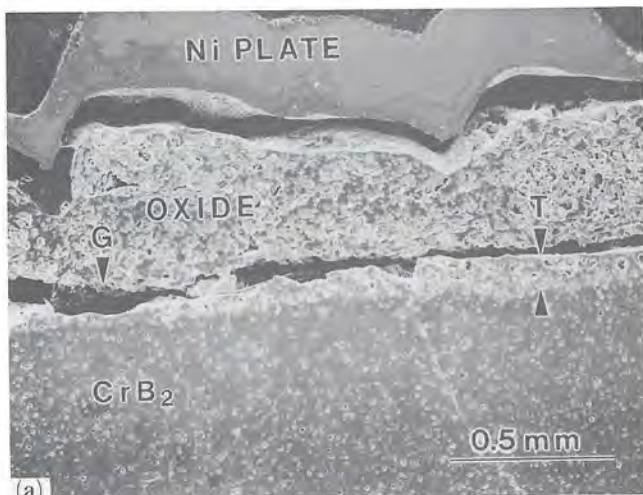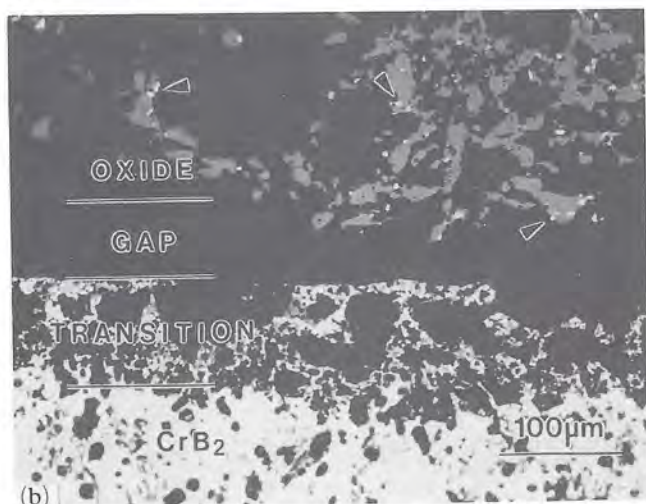
Fig. 11. (a) Photomacrograph of hot-pressed CrB$_2$ oxidized at 1100 °C in static furnace air for 100 h. The scale is massive and largely adherent. The sample was bonded to the bottom of the crucible owing to reaction with Al$_2$O$_3$ (arrows). (b) The right and (c) the left sides of the oxidation sample shown in (a). Arrows denote regions free of the massive oxide.
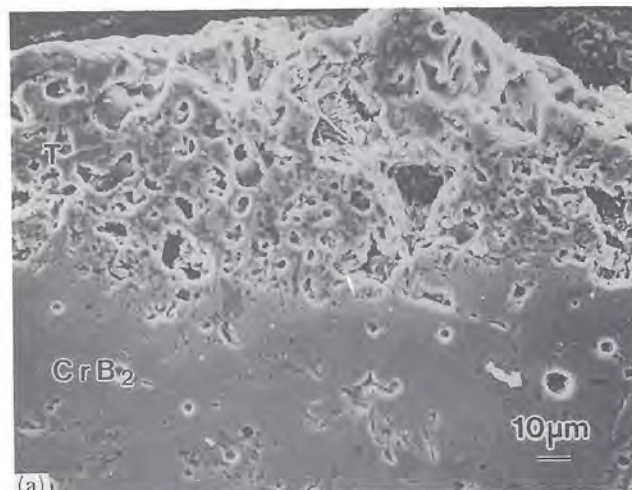
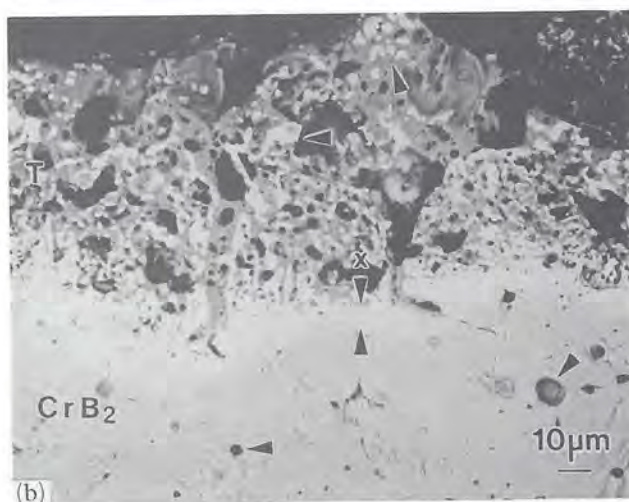Fig. 12. (a) SEM image of hot-pressed CrB$_2$ oxidized at 1100 °C in static furnace air for 100 h. Note the gap (labeled G) between the transition region (labeled T) and oxide. (b) Light micrograph of the region shown in (a). The oxidation product fractured at the transition region interface. Note the particles distributed in the oxidation product (arrows).

Fig. 13. (a) Secondary electron micrograph of the transition region (labeled T) and bulk hot-pressed CrB$_2$ below it. (b) Back-scattered electron micrograph of the area shown in (a). Note the variation in contrast between bulk CrB$_2$ and the transition region (labeled T). A continuous Cr-rich layer is present between the diboride and transition zone (labeled x).

weight loss of -0.6388 mg cm^{-2} (-0.217% weight change), presumably owing to vaporization of volatile species such as B$_2$O$_3$ [25] and CrO$_3$ [26]. Oxidation tests were performed at approximately the temperature where both B$_2$O$_3$ and CrO$_3$ begin to vaporize substantially. The surface of the oxidized sample contained a thin (less than 1 μm), granular oxide scale and pores characteristic of those found in hot-pressed CrB$_2$ (Fig. 17). Grain boundaries are revealed by thermal etching. A previous study of the oxidation resistance of CrB$_2$ at 1000 °C in static air for 150 h found a weight gain of $+2.1$ mg cm^{-2} [27].

The results of static oxidation tests at 1000 °C and 1100 °C for 100–150 h reveal at least one substantial difference. The oxidation product is massive and largely adherent after exposure to 1100 °C (Fig. 11(a)), but thin and granular when oxidized approximately

100 °C lower (Fig. 17). The precise temperature at which this transition in oxidation behavior occurs was not determined. A previous study noted the chromium borides have poor oxidation resistance above 982 °C [22].

2.2.3. Cyclic oxidation

Hot-pressed CrB$_2$ coupons were oxidized for up to 50 cycles, 50 min at high temperature and convective cooling for 10 min, at 700 °C, 900 °C and 1100 °C using a custom-built automatic cyclic oxidation test rig. The 700 °C and 900 °C test temperatures were selected to determine whether there is any unusual low temperature oxidation phenomenon in hot-pressed CrB$_2$. Samples were weighed at intervals of 2, 4, 8, 16, 32 and 50 cycles. The results are plotted in Fig. 18.
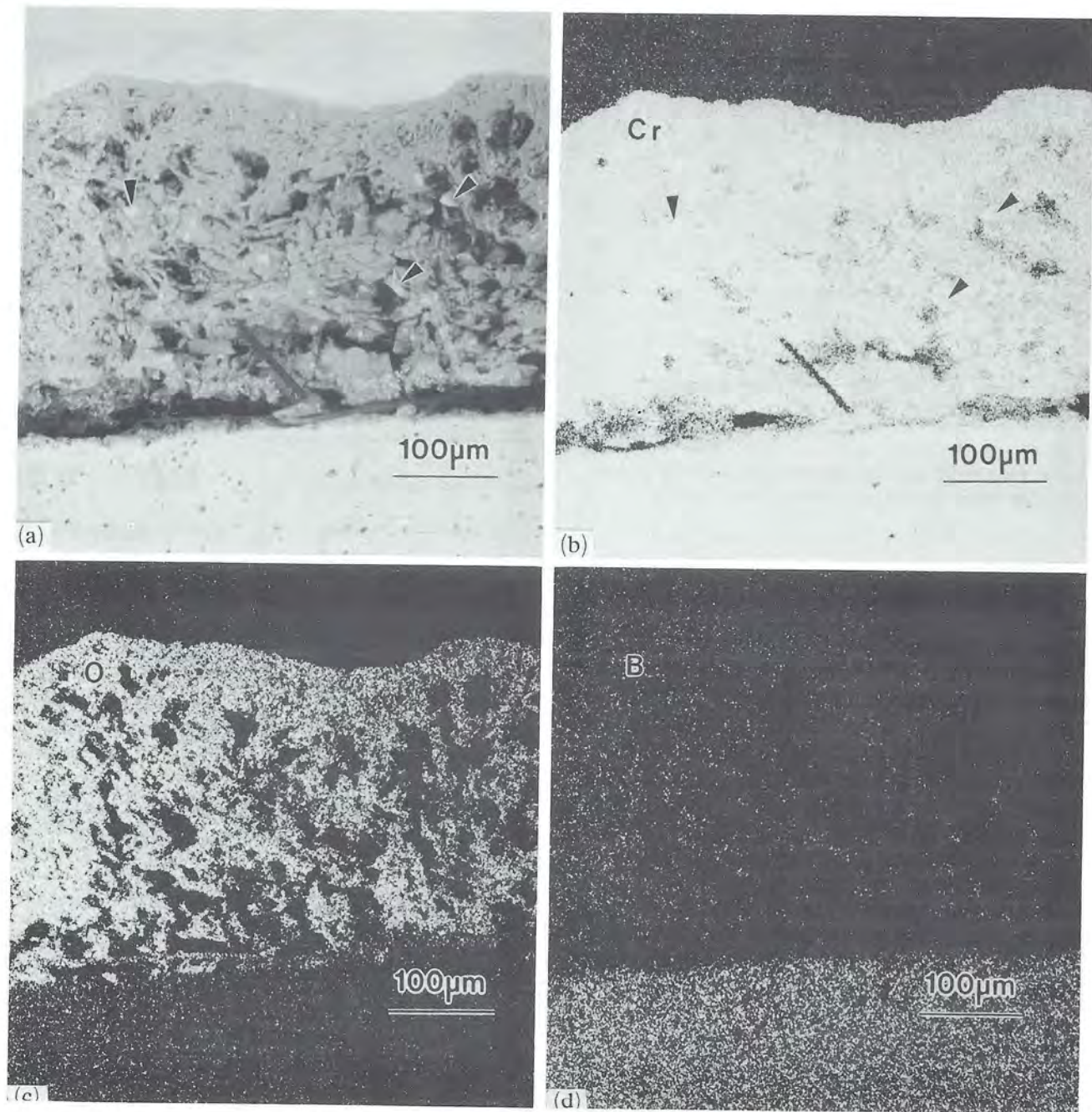
Fig. 14. SEM images of CrB$_2$ oxidized in static furnace air at 1100 °C: (a) the area mapped, (b) Cr X-ray map, (c) O X-ray map, and (d) B X-ray map. The arrows in (a) and (b) correspond to Cr-rich particles present in the oxidation product. The oxidation product and diboride are not deficient in B as part (d) indicates.

Cyclic oxidation at 700 °C resulted in nearly zero weight gain. The oxide scale was thin, adherent, and dark green in color (Fig. 19(a)). The weight gain at 900 °C is linear up to four cycles, after which it is constant. The oxide scale is again thin and adherent, but lighter green in color (Fig. 19(b)). No unusual low temperature oxidation phenomenon was observed in 700 °C and 900 °C cyclic samples. Cyclic oxidation testing was terminated after 16 cycles at 1100 °C since the sample experienced a weight gain of over about 40 mg cm^{-2} owing to the formation of a massive oxidation product (Fig. 19(c)). The scale was adherent in most areas, but non-adherent in others, and did not spall as a result of thermal cycling. Cracks were not found in any of the cyclic oxidation samples. An extensive literature survey did not produce any data on the cyclic oxidation behavior of CrB$_2$. The results therefore could not be compared with any previously published work.
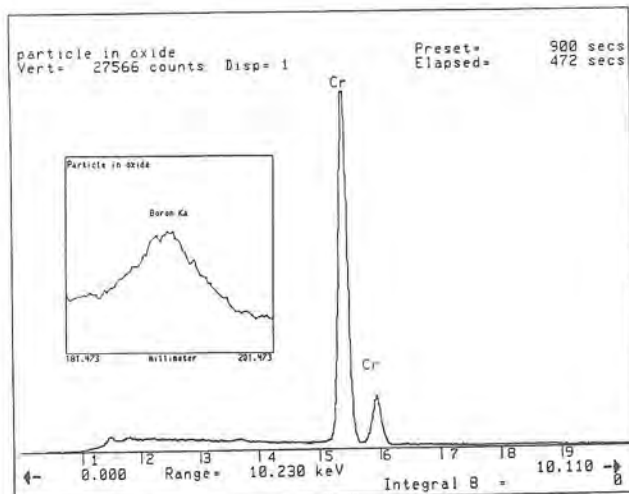
Fig. 15. Energy dispersive and wavelength dispersive (inset) spectra of the Cr-rich particles found in the oxidation product (Fig. 14(a) or 14(b)). The particles contain only Cr and B.

3. Discussion of results

3.1. Characterization of hot-pressed chromium diboride

A previous study examining CrB_2 sputtered from a hot-pressed target by XPS showed B_2O_3 was present in all coatings [8]. The initial source of boria was reported to be oxidation of the target surface caused by exposure to ambient. Sputtering for up to 120 min did not completely eliminate the B_2O_3 signal. A small amount of B_2O_3 was thought to form continuously during sputtering owing to diffusion of O adsorbed through pores in the hot-pressed sputtering target.

XPS data for the surface of as-received hot-pressed CrB_2 (Fig. 7) indicate that O is present, probably as an oxide, but is restricted to the outer 10–20 nm. Similarly, XPS spectra of a freshly fractured surface of hot-pressed CrB_2 (Fig. 8) indicate that O is confined to the near-surface. In support of this finding, AES did not detect O in hot-pressed CrB_2 approximately 300 nm below the fracture surface (Fig. 9(b)). Thus, hot-pressed CrB_2 examined in the present study does not contain B_2O_3 within the bulk.

C was consistently detected by AES at levels of approximately 2 at.% (0.7 wt.%) at depths greater than 5 nm (Table 1). In contrast, the C content of bulk hot-pressed CrB_2 was found to be 0.04 at.% (0.019 wt.%). The amount of C may therefore be higher than previously thought. Fe was detected in hot-pressed CrB_2 by EDS and therefore is thought to be in solution at a concentration of greater than or equal to 0.1 wt.%. However, it was not found by AES (Fig. 9(b)), indicating that it may be a segregated impurity. Fe may be more easily detectable by techniques sampling larger volumes such as EDS.

(a)
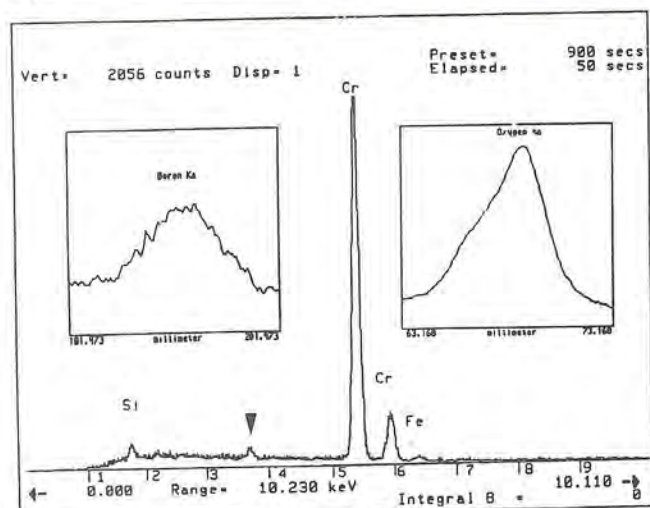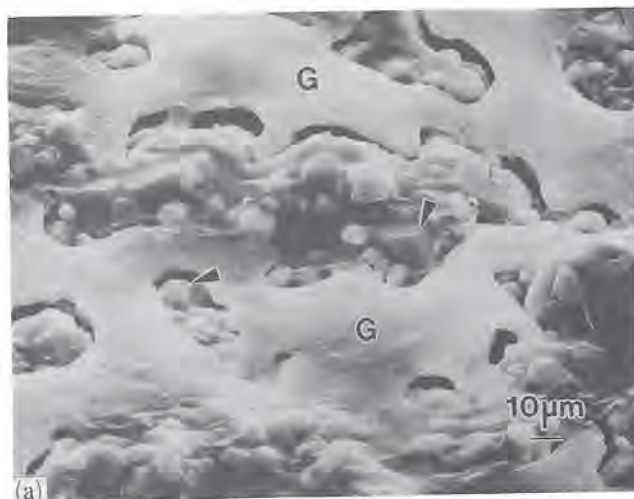
(b)

Fig. 16. (a) SEM image of the surface of the massive oxidation product shown in Fig. 11(a). It contains small faceted particles (arrows) and a glassy phase (labeled G). (b) Energy dispersive and wavelength dispersive (insets) spectra of the oxidation product shown in (a). The oxide contains primarily Cr, B and O with small amounts of silicon and iron. The latter two elements are segregated impurities previously found in hot-pressed CrB_2 (Fig. 3(a)). The small peak between Si and Cr (arrow) is the Cr escape peak.

3.2. Static oxidation

The static oxidation resistance of CrB_2 has been documented but is often contradictory [13, 27–34]. For example, chromium borides were once thought to be the only borides capable of replacing superalloys [30], but in the same publication five months later, chromium borides were said to have poor oxidation resistance above 982 °C [31]. CrB_2 was reported to be stable in air up to 1200–1300 °C as a result of the formation of a protective low-melting point borochromium glass [32].

The oxidation resistance of CrB_2 is reportedly greater than that of molybdenum diboride [13], while

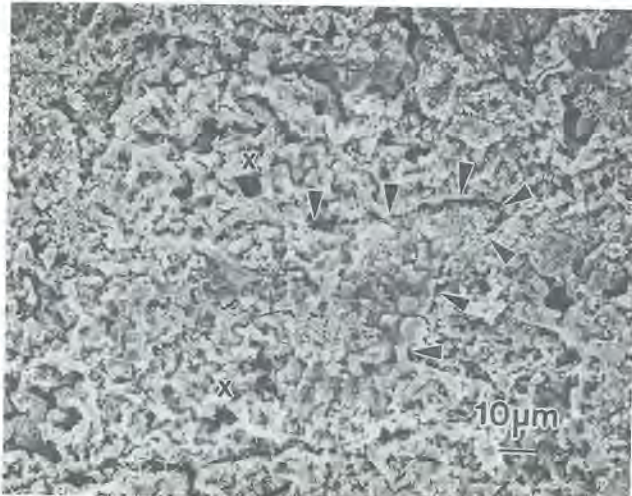Fig. 17. SEM image of hot-pressed CrB$_2$ oxidized at 1000 °C for 100 h in static furnace air. The weight loss was -0.6388 mg cm^{-2} owing to vaporization of CrO$_3$ or B$_2$O$_3$. The oxide is thin and granular. Pores are labeled x, and arrows denote a grain boundary revealed by thermal etching.

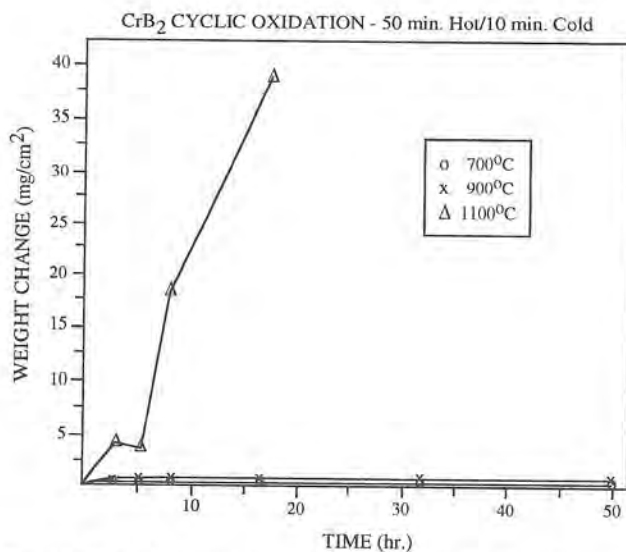Fig. 18. Plot of weight gain *vs.* number of cycles for hot-pressed CrB$_2$. The weight gain is negligible at 700 °C and less than $+2$ mg cm^{-2} at 900 °C. The formation of a massive oxide at 1100 °C resulted in a large weight gain after only 16 cycles.

neither are as great as that of titanium diboride [28]. Transition metal diborides were shown to be the most stable in oxidizing environments, yet begin to oxidize at 600–700 °C, with TiB$_2$ having the highest stability [33]. In any diboride, oxidation of the metal and B will result in the formation of a complex amorphous or crystalline oxide with varying degrees of protective capability. It is apparent that the oxidative stability of diborides is poorly understood, and probably depends on the quality and stoichiometry of the starting material.

A previous study reported a weight gain of $+2.1$ mg cm^{-2} for hot-pressed CrB$_2$ oxidized at 1000 °C for 150 h [27]. This is in contrast to the present study, where a weight loss of -0.6388 mg cm^{-2} was recorded. The discrepancy cannot be accounted for since the quality of material previously evaluated and test conditions were not reported. However, static oxidation tests performed at 1100 °C indicate that oxidation of CrB$_2$ may depend on the partial pressure of oxygen and test conditions. The weight loss found in the present study may be representative of the oxidation behavior of CrB$_2$ in which small amounts of B$_2$O$_3$ [25] and CrO$_3$ [26] vaporize at 1000 °C. This is in contrast to the cyclic oxidation data obtained for hot-pressed CrB$_2$ at 900 °C where a weight gain caused by the formation of Cr and B oxides was measured (Fig. 18).

A few studies attempting to evaluate or improve the oxidation resistance of various diborides have been performed [35, 36]. The oxidation behavior of metal boride, carbide, nitride, and silicide powders was evaluated in flowing air up to 1000 °C [35]. Diborides of Cr, Hf, Nb, Ta, V, Al, Ti and Zr began to oxidize at temperatures ranging from 400 to 700 °C. CrB$_2$ exhibited a weight gain of 35% at 1000 °C, whereas TiB$_2$ powder increased in weight by 30% at 1000 °C. Such a dramatic weight gain is predictable since powders have high surface-to-volume ratios.

The oxidation behavior of diborides of Hf, Zr and Ti was investigated in flowing air at temperatures up to 2127 °C to study the influence of stoichiometry, alloying and composition [36]. HfB$_{1.7}$ oxidized at 1727 °C formed an oxidation product approximately 100 μm thick in 1 h, compared with approximately 400 μm for HfB$_{2.2}$. Thus, metal-rich compositions exhibited greater oxidation resistance. ZrB$_2$ composites alloyed with Al were found to oxidize more rapidly than stoichiometric ZrB$_2$ above 1847 °C, while Si additions improved scale adherence. HfB$_{1.8}$ + 20 vol.% SiC oxidized at 1970 °C for 1 h had a thinner and more adherent oxide scale. Another study examined the oxidation resistance ZrB$_2$ composites containing 20 vol.% SiC by gravimetric analysis [25]. The oxidation resistance of the composite is greatly improved over the monolithic ZrB$_2$ oxidation of SiC above 1300 °C and the resultant formation of a protective SiO$_2$-rich amorphous scale. Below 1300 °C, the scale contains primarily B$_2$O$_3$ and is non-protective.

A significant result from the above studies is the effect of stoichiometry on the oxidation resistance of the diborides. Thus, Cr-rich material may have better oxidation resistance than stoichiometric CrB$_2$ [36] owing to the formation of a more continuous protective layer of Cr$_2$O$_3$. A survey of the available literature for oxidation data on Cr-rich borides was unsuccessful.
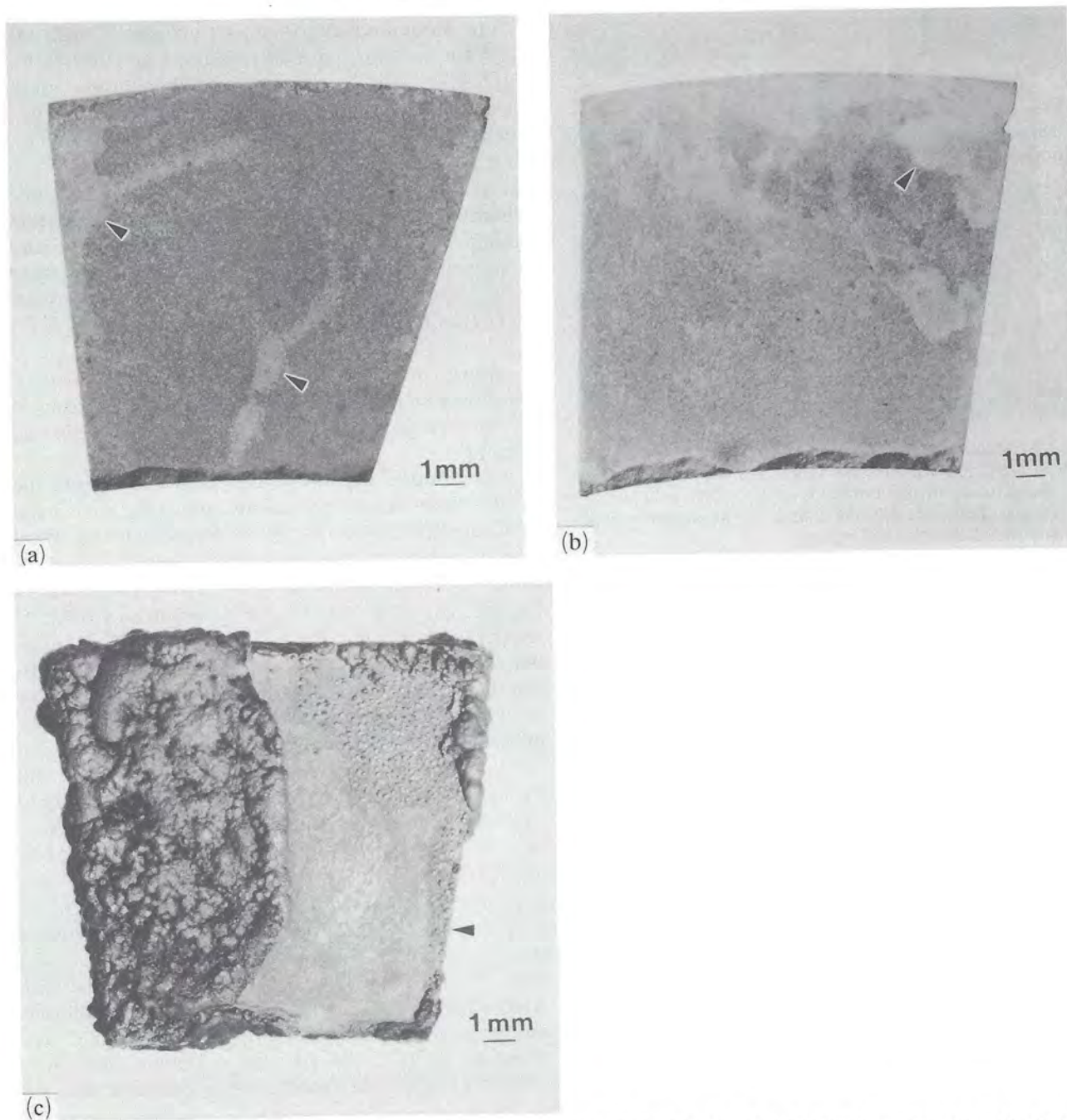
Fig. 19. Photomacrographs of CrB_2 cyclic oxidation samples: (a) 700 °C, (b) 900 °C, and (c) 1100 °C coupons. Note the discolored regions in samples oxidized at 700 °C and 900 °C (arrows). The presence of a large area free of massive oxidation product (arrow in part (c)) is similar to that found in hot-pressed CrB_2 oxidized in static air at 1100 °C for 100 h.

However, the Cr-rich particles found in the oxide scale of CrB_2 oxidized at 1100 °C for 100 h exhibit improved oxidation resistance compared with CrB_2 (Fig. 14(a)).

XRD of the oxidation product formed at 1100 °C for 100 h shows good correlation with $CrBO_3$. The calculated d-spacings from the oxidation product were shifted to slightly higher values in most peaks, suggesting that the equilibrium oxide can contain less than 20 at.% B. A study of the formation of $CrBO_3$ by solid state reaction of Cr_2O_3 with B_2O_3 did not discuss the range of solubility of boron [24].

The massive oxidation product formed on the surface of samples heated to 1100 °C has the appearance of having been a liquid scale. The melting temperature of $CrBO_3$ is not known, but forms in various quantities by solid state reaction of Cr_2O_3 and B_2O_3 from 900–1220 °C [24]. A literature search to locate

either the binary $Cr_2O_3-B_2O_3$ phase diagram of Cr–B–O ternary phase diagram was unsuccessful. The regions free of massive oxide (Figs. 11(b) and 11(c)) may be due to increased diffusivity oxygen through the liquid Cr–boron oxide [35]. This effect may be enhanced if hot-pressed CrB_2 is sensitive to local variations in oxygern partial pressure.

3.3. Cyclic oxidation

The cyclic oxidation of CrB_2 at 900 °C resulted in a weight gain of +1.75 mg cm^{-2} (Fig. 18), while static oxidation at 1000 °C resulted in a weight loss of −0.6388 mg cm^{-2}. In the former case the Cr and B appear to form relatively stable oxides that may be nominally protective and adherent. Conversely, the static oxidation test indicates that B_2O_3 [24] or CrO_3 [26] begin to vaporize at approximately 100 °C higher.

The oxidation product formed at 1100 °C was massive and similar in appearance to the CrB_2 oxidized in static air at 1100 °C (Figs. 11(c) and 19(c)). In contrast, CrB_2 oxidized in static air at 100 °C lower formed a scale that was thin and granular (Fig. 17). Thus, a temperature difference of only 100 °C resulted in the formation of a thick oxide with concurrent increase in sample weight. The weight gain exhibited at 100 °C is an average over the entire sample area, but is higher in areas where oxide is thick (Fig. 19(c)). The anomaly in the 1100 °C cyclic oxidation curve between two and four cycles is not presently understood.

It is worth emphasizing that significant oxidation effects appear to occur at selected approximately 100 °C intervals. The change from weight loss to weight gain occurs between 900 °C and 1000 °C [22], and the scale morphology changes from thin and granular to massive and irregular between 1000 °C and 1100 °C [32]. While the precise mechanism responsible for this behavior is not known, it appears to be dependent on the stoichiometry of the diboride and the relative rates of formation and evaporation of complex mixed B [24, 25] and Cr [26] oxide scales (Figs. 10(c) and 16(a)).

4. Summary and conclusions

Hot-pressed chromium diboride was extensively characterized and found to contain equiaxed grains 25–30 μm in diameter, approximately 12% porosity, and aluminosilicate inclusions. The material was characterized by AES and found to be nominally stoichiometric. The average linear thermal expansion of CrB_2 from room temperature to 600 °C is 6–8 ppm °C^{-1}, and approximately 10 ppm °C^{-1} from 800 to 1400 °C. The CTE is approximately 3–8 ppm °C^{-1} lower than that of equiatomic NiAl, depending on the

temperature, and is a significant thermal mismatch. The room temperature bend strength of hot-pressed CrB_2 is 207 MPa. However, the elastic modulus is low (76.5 GPa), and will limit its utility as a reinforcing fiber.

The thermal shock resistance of hot-pressed CrB_2 is poor, as samples quenched in water from 1100 °C contained extensive cracks. Static oxidation for up to 150 h showed that hot-pressed CrB_2 forms a thin granular oxidation product at 1000 °C, with a small weight loss. However, a massive chromium borate ($CrBO_3$) scale is formed at 1100 °C. In cyclic oxidation, CrB_2 exhibits a small weight loss at 1000 °C due to evaporation of B_2O_3 and CrO_3, and a much larger weight gain at 1100 °C due to the formation of the massive $CrBO_3$ scale. Based on these results, the maximum use temperature for CrB_2 fibers exposed to ambient is approximately 1000 °C. As a result of this study, it is apparent that CrB_2 is not a viable candidate monofilament reinforcing fiber for high thermal expansion intermetallic matrices such as NiAl.

Acknowledgment

References

1 D. L. McDanels and L. J. Westfall, *HITEMP Review 1988*, *NASA Conf. Pub. No. 10025*, 1988 (NASA. Washington, DC), pp. 205–214.

2 A. K. Misra, *NASA HITEMP Review 1988*, *NASA Conf. Pub. No. 10025*, 1988 (NASA. Washington. DC). pp. 193–203.

3 A. K. Misra, *NASA HITEMP Review 1990, NASA Conf. Pub. No. 10051*, 1990 (NASA. Washington, DC), pp. 13-3-3-13.

4 L. I. Maissel and R. Glang (eds.), *Handbook of Thin Film Technology*, McGraw-Hill, New York, 1970.

5 M. L. Emiliani, Chromium diboride monofilament fiber fabrication by hollow cathode sputtering, *NASA Rep. No. CR-187176*, July 1991 (NASA, Washington, DC).

6 *Certificate of Analysis, CrB_2 powder, Lot No. 45121-C-1*, Cerac. Inc., Milwaukee, WI, January 1990.

7 B. R. Emrich, Literature survey on the synthesis, properties, and applications of selected boride compounds, *Technical Documentary Rep. No. ASD-TDR-62-873*, US Air Force, Dayton, OH, December 1962, pp. 3–13.

8 D. R. Wheeler and W. A. Brainard, *J. Vac. Sci. Technol., 15* (1978) 24.

9 G. V. Samsonov, L. Ya. Markovskii, A. F. Zhigach and M. G. Valyashko, in G. V. Samsonov (ed.), *Boron, Its Compounds and Alloys*, Book 2, *AEC-TR-5032*, US Atomic Energy Commission, Washington, DC, 1960, pp. 388–389.

10 L. Topor and O. J. Kleppa, *J. Chem. Thermodyn.*, 17 (1985) 109.

11 G. V. Samsonov (ed.), *Boron, Its Compounds and Alloys*, Book 2, *AEC-TR-5032*, US Atomic Energy Commission, Washington, DC, 1960, pp. 358–379.

12 B. Aronsson, T. Lundstrom and S. Rundqvist, *Borides, Silicides, and Phosphides*, Wiley, New York, 1965, Chapter 1.

13 J. R. Hague, J. F. Lynch, A. Rudnick, F. C. Holden and W. H. Duckworth (eds.), *Refractory Ceramics for Aerospace*, American Ceramic Society, Columbus, OH, 1964, pp. 76–78.

14 B. R. Emrich, Literature survey on the synthesis, properties, and applications of selected boride compounds, *Technical Documentary Rep. No. ASD-TDR-62-873*, December 1962, pp. 34–39.

15 T. B. Shaffer, *Plenum Press Handbook of High Temperature Materials Number 1, Materials Index*, Plenum, New York, 1964.

16 G. V. Samsonov, *Plenum Press Handbook of High Temperature Materials Number 2, Properties Index*, Plenum, New York, 1964, p. 179.

17 Y. S. Touloukain, R. K. Kirby, R. E. Taylor and T. Y. R. Lee, *Thermophysical Properties of Matter*, Vol. 13, Plenum, New York, 1977.

18 G. V. Samsonov, *Plenum Press Handbook of High Temperature Materials Number 2, Properties Index*, Plenum, New York, 1964.

19 G. V. Samsonov (ed.), *Boron, Its Compounds and Alloys*, Book 2, *AEC-TR-5032*, US Atomic Energy Commission, Washington, DC, 1960, pp. 385–386.

20 B. Ott, Personal communication, Cerac Inc., Milwaukee, WI, 1990.

21 V. S. Neshpor and P. S. Kislyi, *Refract. Mater. (USSR)*, 24 (1959) 231.

22 P. K. Liao and K. E. Spear, *Bull. Alloy Phase Diagrams*, 7 (1986) 232.

23 J. D. Mackenzie and W. F. Clausen, *J. Am. Ceram. Soc.*, 44 (1961) 81.

24 N. C. Tombs, W. J. Croft and H. C. Mattraw, *Inorg. Chem.*, 2 (1962) 872.

25 W. C. Tripp, H. H. Davis and H. C. Graham, *Ceram. Bull.*, 52 (1973) 612.

26 C. S. Tedman, Jr., *J. Electrochem. Soc.*, 113 (1966) 766.

27 G. V. Samsonov, *Plenum Press Handbook of High Temperature Materials Number 2, Properties Index*, Plenum, New York, 1964, p. 276.

28 I. E. Campbell (ed.), *High Temperature Technology*, Wiley, New York, 1956, pp. 147–148.

29 B. R. Emrich, Literature survey on the synthesis, properties, and applications of selected boride compounds, *Technical Documentary Rep. No. ASD-TDR-62-873*, US Atomic Energy Commission, Washington, DC, December 1962, pp. 45–46.

30 F. W. Glaser, *Met. Prog.*, 67 (1955) 77.

31 R. A. Long, *Met. Prog.*, 67 (1955) 123, 5–24.

32 G. V. Samsonov (ed.), *Boron, Its Compounds and Alloys*, Book 2, *AEC-TDR-60-5032*, US Atomic Energy Commission, Washington, DC, 1960, pp. 341–342, 420–421.

30 F. W. Glaser, *Met. Prog.*, 67 (1955) 77.

31 R. A. Long, *Met. Prog.*, 67 (1955) 123, 5–24.

32 G. V. Samsonov (ed.), *Boron, Its Compounds and Alloys*, Book 2, *AEC-TDR-60-5032*, US Atomic Energy Commission, Washington, DC, 1960, pp. 341–342, 420–421.

33 G. V. Samsonov and Ya. S. Umanskiy, Hard compounds of refractory metals, *NASA Tech. Trans. TT-F-102*, June 1962 (NASA, Washington, DC), p. 240.

34 G. V. Samsonov and P. S. Kislyi, *High Temperature Non-Metallic Thermocouples and Sheaths*, Trans. S. H. Taylor, Consultants Bureau, New York, 1967, p. 34.

35 D. W. McKee, *Carbon*, 24 (1986) 331.

36 E. V. Clougherty, R. L. Pober and L. Kaufman, *Trans. Metall. Soc. AIME*, 242 (1968) 1077.